

May 2018

Applications of Nanoporous Materials in Gas Separation and Storage

Amit Sharma
amit7201@gmail.com

Follow this and additional works at: <https://digitalscholarship.unlv.edu/thesedissertations>



Part of the [Chemistry Commons](#)

Repository Citation

Sharma, Amit, "Applications of Nanoporous Materials in Gas Separation and Storage" (2018). *UNLV Theses, Dissertations, Professional Papers, and Capstones*. 3326.
<https://digitalscholarship.unlv.edu/thesedissertations/3326>

This Dissertation is brought to you for free and open access by Digital Scholarship@UNLV. It has been accepted for inclusion in UNLV Theses, Dissertations, Professional Papers, and Capstones by an authorized administrator of Digital Scholarship@UNLV. For more information, please contact digitalscholarship@unlv.edu.

APPLICATIONS OF NANOPOROUS MATERIALS IN
GAS SEPARATION AND STORAGE

By

Amit Sharma

Master of Technology – Nanotechnology
University of Rajasthan - Jaipur, India

Bachelor of Technology – Nanotechnology
University of Rajasthan - Jaipur, India

A dissertation submitted in partial fulfillment
of the requirements for the

Doctor of Philosophy – Chemistry

Department of Chemistry and Biochemistry
College of Sciences
The Graduate College

University of Nevada, Las Vegas
May 2018

Copyright 2018 by Amit Sharma

All Rights Reserved



Dissertation Approval

The Graduate College
The University of Nevada, Las Vegas

February 16, 2018

This dissertation prepared by

Amit Sharma

entitled

Applications of Nanoporous Materials in Gas Separation and Storage

is approved in partial fulfillment of the requirements for the degree of

Doctor of Philosophy – Chemistry
Department of Chemistry and Biochemistry

Paul Forster, Ph.D.
Examination Committee Co-Chair

Kathryn Hausbeck Korgan, Ph.D.
Graduate College Interim Dean

Kathleen Robins, Ph.D.
Examination Committee Co-Chair

Jun Young Kang, Ph.D.
Examination Committee Member

Satish Bhatnagar, Ph.D.
Graduate College Faculty Representative

ABSTRACT

Past decades in the field of gas separation and storage utilized the concepts of both cryogenic distillation and non-cryogenic methods such as high-pressure cylinders but few concerns – efficiency, energy intensiveness, cost associated, risk of failure always existed. Recent advances in the field focuses on using porous materials especially nanoporous materials. Nanoporous materials, due to their well-defined structure, range of pore diameters, and striking surface chemistry hold over traditional porous materials for gas separation and storage. With pore diameter less than 2 nm and abundance of energetically favorable sites (such as unsaturated metal sites, channels, cages, cavities etc.), these materials can also undergo various surface decorations to enhance the adsorbate-adsorbent interactions making them suitable for the applications using the principles of pressure swing adsorption. The objective of this study is to show the potential these materials hold in gas separation and storage studies and we provide four different nanoporous materials dedicated to deal with certain gas mixtures.

Out of the wide class of nanoporous materials, in first part of this work we show screening of 229 zeolitic frameworks in separation of radiochemically relevant noble gases mixture of Kr/Xe by Grand Canonical Monte Carlo simulations by benchmarking the model by measuring adsorption isotherms at various temperatures. Zeolites with narrow pore system and zig-zag or elliptical cross sections were found to be more selective for Xe.

To separate one of the lightest gas mixture of D_2/H_2 we examine the adsorption into a nanoporous nickel phosphate, VSB-5, which on the basis of gas sorption analysis gives one of the highest heats of adsorption (HOA) for hydrogen (16 kJ/mol). A much higher HOA for D_2 with calculated selectivities above 4 for D_2 at 140 K suggests that VSB-5 is a promising adsorbent for separations of hydrogen isotopes.

To understand the storage aspect of nanoporous materials, we utilize the principles of Inelastic Neutron Scattering (INS) to examine the lightest gas (H_2) on one of the simplest yet exciting surface of graphene where the H_2 gas corresponds to a 2D rotor with a rotational barrier of around 4 meV. This also helps in checking the validity of the model of H_2 in an anisotropic potential and thereby provides more insight on the concept of hydrogen storage. A hand-in-hand comparison with a much stronger interaction potential provided by Ni^{2+} sites in VSB-5 is also studied. A huge shift in the rotational line of hydrogen in VSB-5 represents itself as a case of Kubas complex indicating the strong affinity of the unsaturated metal sites towards H_2 .

To capture a different system of toxic gas of ammonia (NH_3), we functionalize a well-studied metal organic framework, HKUST-1 (copper trimesate) containing bound sulfuric acid tethered to the framework through terminal oxygen coordination to the accessible Cu(II) sites. Presence of sulfuric acid in the framework and the NH_3 sorption is examined by INS. Here acid modified HKUST-1 shows three times more uptake of NH_3 compared with pristine HKUST-1. A series of DFT simulation reveals adsorption of ammonia at the acid -OH site leading to a partial transfer of H^+ and giving an elongated O-H-N bond rather than a full transfer of H^+ and explaining the observed reversibility of adsorption without the destruction of framework.

Acknowledgments

The work compiled in this dissertation wouldn't be completed without the kind help from several people who always supported, guided and believed in me throughout this wonderful journey. I am thankful to Dr. Paul Forster for providing me the opportunity to be a part of his group and for his constant encouragement and expert critique on my work. His positive and kind nature always kept me motivated to go an extra mile. I will surely be missing the Saturdays lunch and the conversations on photography. I am also grateful to Dr. Keith Lawler for always being there for me and for being so patient despite how juvenile my doubts were. His comic and serious way of explaining the complicated picture helped me in understanding the basics which I couldn't get from books. It is due to the efforts of Dr. Kathleen Robins that I was always on track on my graduate program and didn't get lost in the space and time continuum. Her constant appreciation and support strengthened me to finish off my studies on time. Dr. Jun Kang's direct approach helped me in visualizing the next step of my studies and research and I am thankful for his insightful comments for my work. I thank Dr. Satish Bhatnagar for his sincere advices and kind appreciation of my work which always boosted my confidence. His sweet way of encouraging helped in concentrating and enjoying the research.

I also thank the faculty of Chemistry department for all the advices offered and I can't express my gratitude to Mark, Debbie, and Bianca for taking care of all the paperwork, positive outlook, kindness, and for always finding a solution for me.

At Oak Ridge National Laboratory, I thank team VISION (BL-16B) – Dr. Anibal Javier Ramirez-Cuesta, Dr. Luke Daemen, and Dr. Yongqiang Cheng for introducing me to the field of inelastic neutron scattering and for always being kind and patient. I am thankful to them for providing me an amazing platform for learning and for all the fun experiments.

I thank all my friends at UNLV for all the fun moments and talks, for making all TA responsibilities enjoyable, for the moral support and for all the laughs.

My deepest gratitude to my parents Indu and Virendra Sharma and my sister Mona for their unconditional love, support and enthusiasm. My final thanks to my loving wife Astha for the help, support, and for always being by my side all the time.

Table of Contents

Abstract.....	iii
Acknowledgments.....	v
List of Tables.....	xii
List of Figures.....	xiv
Chapter 1: Introduction.....	1
1.1 Nanoporous Materials.....	2
1.1.1 Zeolites.....	3
1.1.2 Metal Organic Frameworks (MOFs).....	4
1.2 Motivation.....	5
1.3 Pressure Swing Adsorption (PSA) and the Factors Associated.....	9
1.3.1 Basics of PSA.....	9
1.3.2 Factors Governing PSA.....	13
1.3.2.1 Shape or Size Exclusion.....	13
1.3.2.2 Thermodynamic Equilibrium Effect.....	13
1.3.2.3 Diffusivity.....	14
1.3.2.4 Quantum Sieving Effect.....	14
1.3.3 Measures to Determine the Performance of Nanoporous Materials for Gas Separation.....	15
1.3.3.1 Selectivity.....	15
1.3.3.2 Heat of Adsorption.....	20
1.4.1 Overview of the Dissertation.....	26
1.5 References.....	29
Chapter 2: Assessing Zeolite Frameworks for Noble Gas Separations Through a Joint Experimental and Computational Approach.....	35
2.1 Abstract.....	36
2.2 Motivation.....	36
2.2.1 Importance of Kr-Xe.....	36

2.2.2 Present Techniques to Separate Kr-Xe and the Problems Associated.....	40
2.3 Zeolites and Their Applications in Pressure Swing Adsorption.....	41
2.4 Grand Canonical Monte Carlo (GCMC) Simulation.....	43
2.4.1 Requirement of GCMC Simulation.....	43
2.5 Previous Work.....	44
2.6 Experimental.....	46
2.6.1 Materials and Methods.....	46
2.6.2 Gas Sorption Measurements.....	46
2.6.3 GCMC Details.....	47
2.6.4 Mapping the Pore Volume.....	50
2.7 Results and Discussions.....	51
2.7.1 Benchmarking the Model Chemistry.....	51
2.7.2 Screening the Zeolite.....	54
2.8 Conclusions.....	65
2.9 References.....	67
2.10 Supplementary Information.....	73
Chapter 3: Hydrogen Uptake on Coordinatively Unsaturated Metal Sites in VSB-5: Strong Binding Affinity Leading to High Temperature D ₂ /H ₂ Selectivity.....	81
3.1 Abstract.....	82
3.2 Motivation.....	82
3.2.1 Importance of hydrogen and its isotopes.....	82
3.2.2 Properties of hydrogen and its isotopes.....	83
3.2.3 Present technology to separate D ₂ /H ₂ and the problems associated.....	85
3.2.3.1 Cryogenic distillation.....	85
3.2.3.2 Non-cryogenic methods.....	85
3.3 The solution.....	86
3.3.1 Pressure Swing Adsorption (PSA).....	86
3.3.2 Quantum Sieving.....	88

3.4 Gas separation techniques and previous work.....	91
3.5 VSB-5 and structure and applications.....	94
3.6 Earlier work on VSB-5 and hydrogen interaction.....	95
3.7 Materials and Methods.....	96
3.7.1 Synthesis.....	96
3.7.2 Adsorption simulation.....	96
3.8 Results and discussion.....	99
3.8.1 Need of activation.....	99
3.8.2 Need of colder adsorption isotherms.....	102
3.8.3 Heat of adsorption measurement.....	107
3.9 Conclusions.....	114
3.10 References.....	116
Chapter 4: Using Inelastic Neutron Scattering to Probe Weak and Strong Hydrogen Binding in Graphene and VSB-5.....	123
4.1 Abstract.....	124
4.2 Introduction to neutron scattering.....	124
4.2.1 Neutron Sources.....	125
4.2.2 Beamline 16-B: VISION.....	130
4.2.3 Inelastic Neutron Scattering (INS).....	135
4.2.3.1 Why INS.....	136
4.2.3.2 The Scattering Law.....	140
4.2.3.3 How to model INS.....	143
4.3 Rotation of the dihydrogen molecule.....	143
4.3.1 ortho(o-H ₂) and para-hydrogen (p-H ₂).....	145
4.3.2 An outline of the INS spectrum of dihydrogen.....	147
4.3.3 The INS of dihydrogen in an anisotropic potential.....	148
4.4 Motivation.....	150
4.5 Earlier work on carbonaceous materials and dihydrogen interactions.....	151

4.6 Materials and Methods.....	153
4.7 Characterization.....	155
4.8 Results and discussion of para-hydrogen loadings on graphene.....	156
4.9 Results and discussion of para-hydrogen loadings on VSB-5.....	164
4.9.1 Kubas Complex.....	164
4.9.2 para-hydrogen loadings on VSB-5.....	165
4.10 Conclusions.....	168
4.11 References.....	170
Chapter 5: Three Times Higher and Reversible Ammonia Adsorption in Acid Modified HKUST-1.....	175
5.1 Abstract.....	176
5.2 Motivation.....	176
5.3 Ammonia: A brief introduction.....	177
5.4 Ammonia capture.....	179
5.4.1 Present storage technique.....	179
5.4.2 Problems with the present storage techniques.....	180
5.5 Solution.....	180
5.5.1 Porous materials for ammonia capture.....	180
5.5.2 MOFs for ammonia capture.....	183
5.5.3 Bronsted acidity for enhanced ammonia capture.....	184
5.6 MOF investigated: HKUST-1.....	190
5.6.1 Structure.....	190
5.6.2 Earlier work on HKUST-1 and ammonia capture.....	191
5.7 Experimental.....	192
5.7.1 Synthesis of HKUST-1 and acidic HKUST-1.....	192
5.7.2 Characterization of synthesized MOFs.....	193
5.8 Results and Discussions.....	195
5.8.1 Structure integrity and presence of sulfate in the framework.....	195

5.8.2 Binding of sulfate in the framework.....	197
5.8.3 Ammonia adsorption captured.....	200
5.8.4 Reversible adsorption of ammonia in acidic HKUST-1.....	206
5.9 Conclusions.....	210
5.10 References.....	212
Chapter 6: Conclusions.....	217
Appendix	
Appendix A.....	219
Curriculum Vitae.....	225

List of Tables

Table 2.1 General properties of Krypton and Xenon.....	39
Table 2.2 ^a From TraPPE-zeo. ^b From Clay-FF, charge lowered for charge neutrality. ^c From Talu and Myers. ^d Obtained from principle of corresponding states, critical parameters from the CRC. ^e Increased to match experiment. ^f From COMPASS.....	49
Table 2.3 Simulated Total Quantities Adsorbed (cm ³ /g) and Kr/Xe selectivities for initially Kr selective zeolite framework types calculated at 10,000 mmHg at both 298 K and 250 K.....	57
Table S1 Simulated total quantities adsorbed and Xe/Kr selectivities for all 229 IZA siliceous zeolite framework types.....	73
Table 3.1 Critical parameters for H ₂ and D ₂	98
Table 3.2 : Force field parameters for H ₂ . D ₂ parameters are the same. COM represents the center of mass site for the molecule, EL represents an additional electrostatic site to model the quadrupole, LJ represents an additional off-center Lennard-Jones dispersion site.....	99
Table 4.1 A brief overview on the physical properties of a neutron.....	125
Table 4.2 Brief comparison between the VISION spectrometer with corresponding Raman and IR spectrometers.....	135
Table 4.3 A list of the elements with their respective total neutron scattering cross-section (measured in barn). The higher is the cross-section, the more the element will scatter during the inelastic neutron scattering measurements.....	137

Table 4.4 Rotational peak shape parameters (shape, area, width) for all the para-hydrogen loadings on graphene. Data in the table is used to generate the figure 11. “ML” for loading represents the fraction of a full monolayer of adsorbed H ₂	160
Table 5.1 Physical properties of ammonia.....	178
Table 5.2 List of few acids with their respective conjugate base.....	186

List of Figures

Figure 1.1 A diagrammatic representation of a 1 bed pressure swing adsorption system.....	8
Figure 1.2 A graphical explanation to show the difference in energies for the process of chemisorption and physisorption. The extent of physisorption (middle) at first drops with increasing temperature following a saturation and chemisorption (right) on the other hand first increases, reaches a maxima before decreasing. x/m on the left axis is the quantity of the adsorbate adsorbed.....	9
Figure 1.3 IUPAC classification of six types of adsorption isotherms.....	10
Figure 1.4 Typical System Configuration of a PSA assembly.....	12
Figure 1.5 An example for a breakthrough curve. Breakthrough curves are beneficial as they provide information on the dynamic picture on separation performance of different adsorbents...	16
Figure 1.6 A diagrammatic explanation to show difference between the different gas laws. For Henry's law which focuses on the low-pressure regime, we need to measure adsorption isotherms in the low-pressure region. A nanoporous material typically gives a type I adsorption isotherm using which selectivities can be extracted.....	17
Figure 1.7a A general representation of a Langmuir isotherm.....	23
Figure 1.7b and c 7b (left) shows the extent of coverage when the temperature is reduced to increase the value of 'b' and figure 7c (right) where two points (P_1T_1 and P_2T_2) are picked to calculate heat of adsorption as explained in the text.....	23

Figure 1.7d Images for the corresponding steps to calculate heats of adsorption.....	25
Figure 2.1 Generation of various radioactive materials generated during a nuclear fuel cycle.....	37
Figure 2.2 A standard distillation assembly to capture Kr and Xe.(Left) A description of one column of the distillation assembly(Right).....	40
Figure 2.3 A diagrammatic description of zeolitic structure and Secondary Building Units (SBUs). The top figures in blue depict some of few secondary building units which are used to build a zeolite structure. The bottom left image shows the final structure of a zeolite which is built from different SBUs. The bottom right image shows that how sometimes Si could get replaced with Al to give a zeolitic structure with different charge configuration.....	42
Figure 2.4 Comparisons of experimental (solid) and simulated (dashed) Kr and Xe isotherms and heats of adsorption for LTA.....	52
Figure 2.5 Comparisons of experimental (solid) and simulated (dashed) Kr and Xe isotherms and heats of adsorption for BEA.....	52
Figure 2.6 Comparisons of experimental (solid) and simulated (dashed) Kr and Xe isotherms and heats of adsorption for FAU.....	53
Figure 2.7 Initial selectivities of a 90:10 Xe/Kr mixture. The dashed line indicates a selectivity of 1, below which the materials are selective for Kr instead of Xe.....	55
Figure 2.8 High loading selectivities of a 90:10 Xe/Kr mixture. The dashed line indicates a selectivity of 1, below which the materials are selective for Kr instead of Xe.....	56

Figure 2.9 Initial selectivities of a 90:10 Xe/Kr mixture as a function of the difference in the Xe and Kr heats of adsorption. The dashed line indicates a selectivity of 1, below which the materials are selective for Kr instead of Xe.....	58
Figure 2.10 Xe loading density into ATN at 10 mmHg and 298 K.....	60
Figure 2.11 Xe loading density into UFI at 10 mm Hg and 298 K.....	61
Figure 2.12 show results from selectivity simulations for each of the top zeolites as a function of percent loading, with 100% defined as the respective loading at 10,000 mmHg.....	62
Figure S1 A comparison of selectivity vs. Percent loading of a 90:10 Xe:Kr mixture (solid) and 80:20 Kr:Xe mixture (dashed) into some of the top zeolites.....	78
Figure S2 A comparison of an equivalently parameterized 12-6 Leonard-Jones potential (red) and 9-6 Leonard-Jones potential (blue). This illustrates the softer repulsion of the 9-6 potential compared to the 12-6 potential, which we believe is better for describing noble gas-noble gas interactions at high loadings.....	79
Figure 3.1 VSB-5 viewed down the c axis with octahedral nickel represented in green and tetrahedral phosphorous represented in purple.....	95
Figure 3.2 Measured X-ray Diffraction data for activated VSB-5.....	101
Figure 3.3 Measured temperature dependence of H ₂ @VSB-5 adsorption: isotherms every 10 K between 80-140 K (left), and the isosteric heats of adsorption obtained from the Clausius-Clapeyron equation for each pair of isotherms in separated by 10 K (right).....	102
Figure 3.4 The measured adsorption isotherms for H ₂ (left) and D ₂ (right).....	104

Figure 3.5 Simulated H₂ (solid) and D₂ (dashed) adsorption isotherms (left) and isosteric heats of adsorption (right) using the DL H₂ model at 120 K (red), 130 K (green), and 140 K (blue).....106

Figure 3.6 Simulated H₂ (solid) and D₂ (dashed) adsorption isotherms (left) and isosteric heats of adsorption (right) using the BSSP H₂ model without polarization at 120 K (red), 130 K (green), and 140 K (blue).....107

Figure 3.7 The measured heats of adsorption (left) and IAST determined selectivity (right) for H₂ and D₂ into VSB-5.....110

Figure 3.8 Diffuse reflectance IR spectra of adsorbed H₂ within VSB-5 at 40 K. Spectra are shown for H₂ concentrations in cm³/g of: red 6 (lowest), green 17, blue 45, and purple 80 (highest).....111

Figure 3.9 The measured IR shift as a function of the initial isosteric heat of adsorption for several MOF materials.....112

Figure 4.1 Layout of Spallation Neutron Source at Oak Ridge National Laboratory at Tennessee, USA.....129

Figure 4.2 Layout of the Target building at Spallation Neutron Sources at Oak Ridge National Laboratory housing several beamlines.....129

Figure 4.3 VISION instrument : Outside view of the spectrometer chassis, facing upstream (left), real working spectrometer with beam stop (middle), and inside view of the upstream double-focusing crystal array analyzers and corresponding beryllium filter assemblies (right).....131

Figure 4.4 Engineer drawing of the VISION Beamline showing the several components of the beamline with their specific orientation and distance from the source.....132

Figure 4.5 Schematic representation of INS showing the different interactions occurring at respective energy transfer.....139

Figure 4.6 The inelastic neutron scattering of a solid, ammonia containing material as function of energy. The energy axis is linear between -1,1 meV range (the QENS signal of ammonia) and logarithmic from 1 meV to 1000 meV where the INS data is. Note that the left axis corresponding to the QENS signal is logarithmic (goes up to 10,000) and the INS data vertical scale is up to 100. The QENS signal is two orders of magnitude higher.....141

Figure 4.7 INS Spectra of solid parahydrogen at 5K as measured in VISION) The insert in the figure shows a zoomed-in area The red trace is the forward scattering bank and the black trace is the back-scattering bank. The rotational line of dihydrogen is the main peak at 14.7 meV (118 cm^{-1}). The peak around 20 meV corresponds to the translational vibration of the center of mass (CoM) of the parahydrogen molecule. The higher rotational transitions are affected by the recoil of the dihydrogen molecule.....148

Figure 4.8 Depicts the range of a/B and how the potential changes accordingly. The values of ‘a’ determines the alignment of the dihydrogen molecule with the surface.....150

Figure 4.9 The INS spectra of parahydrogen dosed on graphene at 5K as function of loading. The arrows point to the most important features, the rotational line and the recoil features.....157

Figure 4.10 Zoomed-in spectra of para-hydrogen as function of loading.....158

Figure 4.11 Deconvolution of the rotational line of para-hydrogen for the 0.1 ML, 0.25 ML, 0.75 ML and 1.8 ML loadings. Note that the x-axis corresponds to the shift in the shift from the rotational line (14.7 meV) of dihydrogen in μeV160

Figure 4.12 Relative peak area (Area of main peak/total peak area) for all coverages.....	163
Figure 4.13 para-hydrogen loadings on VSB-5 as a function of increasing temperature.....	166
Figure 4.14 Magnified bound spectrum of para-hydrogen on VSB-5 as a function of increasing temperatures.....	167
Figure 5.1 Depicting the various ways of introducing Bronsted acidic molecules in the porous framework of MOF.....	189
Figure 5.2 Unit cell of HKUST-1 where the Cu-Cu paddlewheels are shown in blue-red and the ring of the ligand (benzene tricarboxylic acid) is shown in black.....	191
Figure 5.3 PXRD pattern for pure HKUST-1 (black) and acidic HKUST-1 (red) after activation showing that the structure is preserved even after introduction of sulfuric acid in the framework.....	196
Figure 5.4 FTIR spectra for pure HKUST-1 and acidic HKUST-1 to detect the presence of sulfuric acid and second check for structure integrity.....	197
Figure 5.5 5a (top) An unstable configuration of sulfuric acid in the framework with one -OH group being used for anchoring the molecule and leaving other OH group stereo-hindered for interaction with ammonia. Figure 5b (bottom) Most stable and favorable configuration of sulfuric acid binding as it leaves both -OH groups free to exhibit the Brønsted acidic character with a reasonable binding energy of ~ 33 kJ/mol.....	199
Figure 5.6 6(a) pure HKUST-1 activated sample before dosing ammonia with its characteristic deep-indigo color. 6b shows the interaction of ammonia with material when ammonia was initially	

dosed into the Schlenk tube showing uneven adsorption levels. 6c is another view to show clearly, the non-homogenous distribution of ammonia in the sample with next small dose of ammonia. From 6d, we can see that uniform distribution is achieved after heating the tube gently with mild shaking. This distribution is now ready for next dose of ammonia. Repetition of this method will eventually lead to a true saturation of ammonia.....201

Figure 5.7 INS spectra for ammonia loadings on pure HKUST-1. It can be observed that the material saturates between 3 and 6 NH₃/ formula unit or 1 and 2 NH₃/Cu site.....202

Figure 5.7b : Interaction of NH₃ with pure HKUST-1. Without any acid present, as expected, ammonia first goes and binds strongly with the Cu site.....203

Figure 5.8 INS spectra describing the ammonia loadings on acidic HKUST-1. It can be observed that the material doesn't saturate even at higher loadings of 3 NH₃/Cu site or 9 NH₃/ formula unit.....204

Figure 5.8b Interaction of first molecule of ammonia with the first acidic site.....205

Figure 5.8c Interaction of second molecule of ammonia with the first acidic site.....206

Figure 5.9 Comparison of the final color of the material after pumping the ammonia from the material where the left image shows the acidic material reverting back to original blue color after pumping the gas whereas the pure HKUST-1 on right doesn't show any change in color after pumping indicating chemisorption.....207

Figure 5.10 FTIR spectra for pumped acidic HKUST-1 showing the removal of gas at 50 C. The inset shows the zoomed range to compare the presence (black) and removal (red) of ammonia in acidic HKUST-1.....208

Figure 5.11a Complete loss in PXRD pattern in acidic HKUST-1 after saturating the material with ammonia. The new pattern corresponds to a monoclinic phase.....209

Figure 5.11b Regeneration of the lost PXRD pattern after pumping the ammonia from the framework.....210

Chapter 1 - Introduction

Index

1.1 Nanoporous materials

1.1.1 Zeolites

1.1.2 Metal Organic Frameworks (MOFs)

1.2 Motivation

1.3 Pressure Swing Adsorption (PSA) and the factors associated

1.3.1 Pressure Swing Adsorption

1.3.2 Factors governing pressure swing adsorption

1.3.2.1 Size or shape exclusion

1.3.2.2 Thermodynamic equilibrium effect

1.3.2.3 Diffusivity

1.3.2.4 Quantum sieving effect

1.3.3 Measures to determine the performance of nanoporous materials for gas separation

1.3.3.1 Selectivity

1.3.3.2 Heat of adsorption

1.4 Overview of the dissertation

1.5 References

1.1 Nanoporous Materials

The advent of nanoparticles i.e. the particles with lengths between 1 – 100 nm has attracted a lot of interest in scientific community due to the various fields of applications such as – catalysis, drug delivery, semiconductors etc.[1-9] Besides a high surface-to-volume ratio and high surface area, these materials exhibit size-dependent properties such as quantum confinement which are completely different from their bulk counterparts. Bulk phase gold which is a dense solid at room temperature is found to be liquid in its nanophase.[10-12] Similarly, nanophase silicon is conductor of electricity whereas bulk phase is an insulator.[13, 14] The list of such cases is quite long and we are focused on a subset of nanoparticles – nanoporous materials which have a pore diameter ranging from 1 – 100 nm.

Simply put, a porous material contains a main frame (organic/inorganic/mixed) connected by the voids (pores). International Union of Pure and Applied Chemistry (IUPAC) classifies the nanoporous materials into three further classes on the basis of pore diameter as[15]:

Microporous materials – Pore diameter less than 2 nm

Mesoporous materials – Pore diameter with 2 – 50 nm

Macroporous materials – Pore diameter greater than 50 nm

Beside the IUPAC classification on size, the nanoporous materials are also classified on the basis of the framework as (a) Inorganic – As expected, the framework here consists primarily of metals/non-metals such as Al, Si, Na, Cs etc and zeolites represent an exceptional example of inorganic nanoporous materials. (b) Organic – Here the framework consists of organic ligands and present a vast class of organic porous polymers and organic framework cages. (c) Mixed – These materials have metal nodes connected by the organic ligands and Metal Organic Frameworks (MOFs) represent the mix or hybrid type nanoporous materials.

Similar to nanoparticles, these materials have exceptionally high surface area and also provide a highly porous network or porosity. For a porous material, the porosity is defined as

$$\text{Porosity} = \frac{\text{Total Volume of the Voids}}{\text{Total Volume of the Material}}$$

1.1.1 Zeolites

An elaborated description on zeolites is provided in Chapter 1 section 4. Zeolites also called as molecular sieves are aluminosilicates which were discovered in 1750s' by Swedish mineralogist Axel Fredrik Cronstedt who observed large steam of water escaping from a stone (silicate) while heating indicating the adsorptive properties. The water which got trapped in the pores of the rock escaped only during the heating process which led him to coin the term zeolite meaning boiling (zeo) the stones (lithos). Till date the same word is used to describe an ever-growing library of zeolites comprising close to 250 different type of zeolitic structures (IZA database).[16] Naturally, the zeolites are deposited slowly at the beds of volcanic rocks where the sand and the ash reacts with alkaline water to form the crystalline structure containing different cations (Ca^{2+} , Mg^{2+} , Na^+ , K^+) acting as impurities. These materials exhibit significant surface area ranging from 700 – 1500 m^2/g and the crystalline structure consists of cages, long cavities and pores interlinked by the building units – $[\text{SiO}_4]^{-4}$ and $[\text{AlO}_4]^{-5}$.[17, 18] High surface area with high tolerance to temperatures, high pressures and harsh chemical environment make zeolites to be used in various sectors of industry. Commercially, the mining of natural zeolites is considered as a cost-effective mean to obtain zeolite which needs further purification to obtain pure zeolite. Various sectors of industries have started to commercialize zeolites in the daily life because of the ease in synthesis,

low cost associated with synthesis, easy scale-up, robustness and a variety of applications possible by simple modifications in the structure. At present, Linde type A is used as a laundry detergent and Fauasite type X and Y are used in oil-processing.[19-22] From the library of International Zeolitic Association, a few topologies: mordenite, chabazite, and clinoptilite are studied extensively in the field of academia.[23-27]

1.1.2 Metal Organic Frameworks (MOFs)

Metal Organic Frameworks or MOFs are a subclass of coordination polymers constituting a metal node and an organic ligand.[28] The metal node is usually picked from transition series due to ability to achieve higher coordination number. The empty *d* orbitals in the transition metals act as Lewis acid acceptors and form a coordination bond with the ligands. For a MOF, coordination number is the total number of ligands it is linked to. So, the angles of binding of ligand with the coordination number determines the dimensionality of the MOF. The other properties such as specific surface area, porosity can be tuned by choosing a proper organic ligand from the huge library. There are innumerable available options for organic ligand and so the combination of metals with the ligand generates a huge library of the MOFs. According to The Cambridge Crystallographic Data Centre (CCDC) and a recent work, there are more than 70,000 entries for MOFs when compared to the International Zeolitic Association which has 229 zeolitic frameworks.[29] MOFs have much higher surface area $>10,000 \text{ m}^2/\text{g}$, meaning half a gram of such MOFs is sufficient to cover the entire football field.[30] These vast number of MOFs have found their application in various sectors of industries such as – drug delivery, catalysis, luminescence, electrical conductivity, and gas storage.[31-37]

1.2 Motivation

The work here focuses on four different systems of gas separation and storage and each chapter is provided with its individual problems encountered and the solutions. Here we provide a brief course on the problems associated with the current gas separation and storage techniques followed by the solution using nanoporous materials.

For gases with low abundance and their heavy use in numerous sectors of industries require a meaningful process of separation and storage. For instance, hydrogen is the most abundant element on the Earth but its abundance as hydrogen gas (H_2) is quite low (~ 1 ppm). Despite its low concentration it is heavily used as a replacement for fossil fuels such as oil, coal, natural gas and an era of hydrogen powered automobiles is emerging.[38-40] Due to its high heat of combustion, it is also used in rocket fuel technology and its ‘zero-emission’ property makes it a favorite as an alternate to the fossil fuels. Applications of hydrogen gas aren’t limited to the automobile industry and it is also used in petroleum and chemical industry as a hydrogenating agent. It is also known as shielding gas in the welding processes and its liquid form is heavily used in cryogenic research such as in cooling of neutrons in neutron production or in superconductivity studies.[41, 42]

Other important gases which are of prime concern and are low in concentration are Krypton, Xenon, Deuterium, Tritium, etc and their list of applications is quite long. Krypton is used in electric arc lights, headlights of automobiles, other electric devices such as lamp bulbs and also in the field of magnetic resonance imaging.[43, 44] Xenon is used as an anesthetic, cardioprotectant, radiation detection, and in ion thrusters for spacecrafts.[45] Deuterium finds its use as a moderator in nuclear reactors, in drug synthesis and also in the field of neutron scattering research where the deuterated compounds are required for comparison with the protonated

ones.[46, 47] Tritium beside being used in military applications is tested as a source of sustainable energy in International Thermonuclear Experimental Reactor in France.[48]

The low abundance of these gases (less than 1 ppm) and their source (such as tritium in upper layers of stratosphere) motivated researchers to design processes for the capture or separation. Most of these gases are separated from a mixture of air by the process called as cryogenic distillation. In a regular cryogenic distillation set-up, the gas mixture is liquified by cooling it at low temperatures and then slowly boiling the liquid to selectively separate the pure gas components on the basis of difference in their boiling points. As can be imagined, this set-up is not only costly but also energy intensive.[49, 50] The process of distillation at low temperatures is a multi-step process which requires the gas mixtures to undergo refrigeration cycle without going under any change in temperature. Since these plants are built on a large scale, the large amount of energy required to keep the temperature constant is provided by large air compressors, expansion turbines or other sophisticated machinery. Mostly the components in a gas mixture have close boiling points such as nitrogen (77 K), argon (87 K), oxygen (90 K) which affects the efficiency of this process. Cryogenic distillation for krypton and xenon still struggles to keep ^{85}Kr separated from xenon feed. The complexity of cryogenic process, the scale of set-up, and the energy investment required to achieve a significant efficiency varies with the number of components in the feed and so one set-up can't be used to separate all the gas mixtures. There are few non-cryogenic options available for separation and storage purposes as well for instance high pressure cylinders but the threat of their failure (leakage) is always of concern and can't be avoided. Chemical methods to generate gas such as hydrogen which is based on electrolysis of water are available but again they suffer from the efficiency aspect. Isotopic separation of gas mixtures for instance for D_2/H_2 is also based on cryogenic distillation but the end product is D_2O

rather than D₂. [51, 52] Wet scrubbing is yet another non-cryogenic method available for separation and storage but the end product is obtained as a salt which makes the product recovery low, for instance ammonia is recovered as ammonium sulfate using sulfuric acid as the scrubbing liquid. [53, 54]

Due to these concerns, researchers started to explore other directions and Pressure Swing Adsorption (PSA) so far has proven to be one of the most successful method. The concepts of adsorption and PSA are discussed in following section but to simply put, PSA is used to separate gas mixtures under pressure. PSA works on the concept that different gases interact differently with the same surface and so, since the interaction of one gas will be different or preferred at a surface, we can look for separation or capture. In order for PSA to work, a constant temperature is required along with an adsorbent bed filled with the nanoporous material. PSA utilizes the concept of swinging pressure high i.e. the gas being adsorbed followed by lowering the pressure to remove the adsorbed gas also known as desorption. [55-57] The simplest design of such an adsorbent bed is shown below –

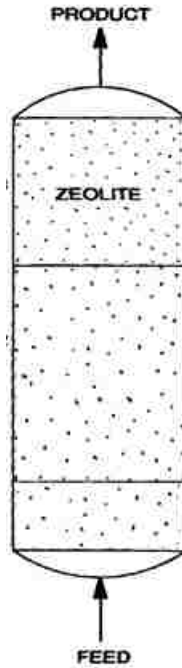


Figure 1.1: A diagrammatic representation of a 1 bed pressure swing adsorption system.

Here, a gas mixture is fed into the adsorbent bed and the pressure is increased so that one of the gas which is selective to the adsorbent will be adsorbed. Soon the pressure will be high to saturate the entire bed and the remaining gas feed will pass through. In order for the next cycle of gas feed to enter, the bed needs to be regenerated which is carried out by decreasing the pressure and removing the adsorbed gas. Once regenerated, the bed is ready to separate the next cycle of the gas feed. To improve the efficiency of such system, multi-bed designs are being used where in some bed, the gas feed is entering and in the remaining the regeneration or lowering down of the pressure is carried. The choice of adsorbent is based on the gas to store and these beds are comparatively easy to replace if needed.

1.3 Pressure Swing Adsorption and the factors associated

1.3.1 Basics of PSA

Before talking about the principles of PSA, a brief introduction on adsorption and the mechanics is provided. Simply put, adsorption is gathering of gas molecules by some interactions on the surface of a solid. The solid surface is referred to as adsorbent and the gas/fluid molecules are called as adsorbates. The interaction between adsorbate and adsorbent is governed by surface energy and the energy evolved (heat of adsorption) is needed to further assess the performance of one adsorbent over the other. Adsorption is classified into two classes based on the strength of the interactions between adsorbate and adsorbent as – physisorption, which is a weak interaction and there is no formation of a chemical bond. Weak van der Waals forces hold the gas molecules closer to the surface of adsorbent and it occurs at low temperature and decreases with increase in temperature. The typical physisorption interaction ranges from 3-50 kJ/mol. Chemisorption on other hand involves formation of stronger chemical covalent bond leading to an irreversible interaction. The typical chemisorption interaction range begins around 70 kJ/mol. [58]

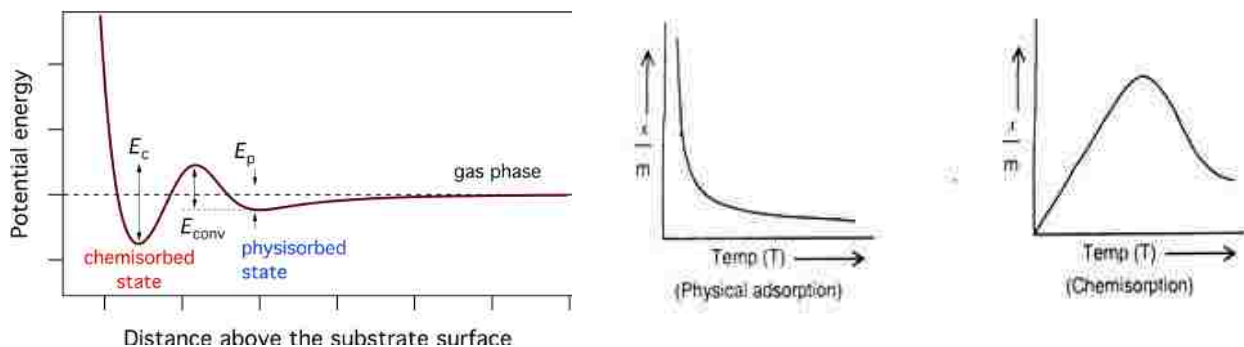


Figure 1.2: (left) A graphical explanation to show the difference in energies for the process of chemisorption and physisorption. The extent of physisorption (middle) at first drops with increasing temperature following a saturation and chemisorption (right) on the other hand first increases, reaches a maxima before decreasing. x/m on the left axis is the quantity of the adsorbate adsorbed.[59]

These sorption behaviors are studied by measuring adsorption isotherms which are also known as equilibrium isotherms. These are a measure of the amount of gas molecules (adsorbate) being adsorbed on a solid surface (adsorbent) against relative pressures (P/P_0 ; P is the absolute pressure, P_0 is the saturated pressure of gas) at constant temperature. Adsorption is followed by desorption which takes place upon lowering of pressure. [60] As per IUPAC, there are six types of isotherms which are classified on the basis of the interaction and the shape of the isotherm. We are interested in zeolites which are microporous materials and so these materials exhibit filling of the micropores first at lower gas loading (low partial pressure $P/P_0 < 0.1$) followed by inflection into a long plateau meaning the saturation of micropores and diffusion of gas in the other possible sites.

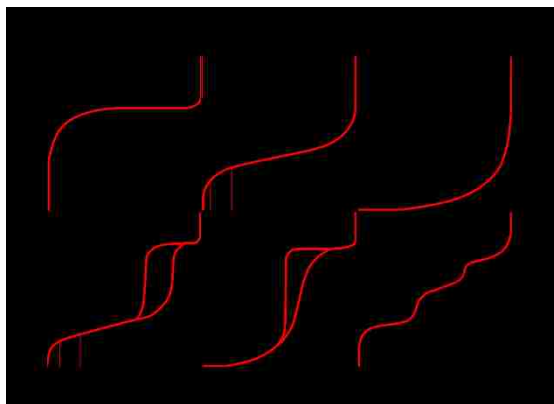


Figure 1.3: IUPAC classification of six types of adsorption isotherms[61]

If potential energy of the entire system is taken into consideration, the interaction can be further studied by considering the second term of the following equation since adsorbent has a secondary effect on the total potential of adsorbate-adsorbent interactions.

$$\Theta_{\text{total}} = \Theta_{(\text{adsorbate-adsorbate})} + \Theta_{(\text{adsorbate-adsorbent})}$$

The contribution from the first term is zero at low coverages and it arises from the interactions within the adsorbate molecules even though when the molecules are non-polar and adsorbent does not have an electric field. At high coverages, it can be observed with an increase in the heat of adsorption.

Heat of adsorption is the measure of the strength of adsorbate-adsorbent interactions and the adsorption affinity of the adsorbate. For adsorption process which is spontaneous, ΔG is negative. Since the translational degree of freedom is lost during the adsorption, ΔS is also negative. Since we have $\Delta G = \Delta H - T\Delta S$, the enthalpy of adsorption, ΔH is also negative. This evolved heat is called as heat of adsorption and we measured the isosteric heats of adsorption by using the Clausius-Clayperon equation:

$$\left(\frac{\partial \ln P}{\partial \frac{1}{T}} \right)_{\theta} = \frac{\Delta H_{ads}}{R}$$

Where “ θ ” is the fraction of adsorbed sites at pressure P and temperature T and R is the universal gas constant. ΔH_{ads} is obtained by multiplying the slope of $\ln P$ against $1/T$ with R . [62-64]

PSA relies on the concept of separating certain gas molecules from a feed where the particles are separated based on their affinity towards the adsorbent. With increasing pressure, gas molecules are forced to interact with the solid surface (adsorbent) and they reach an equilibrium or saturation with higher pressures. Following saturation, the pressure is decreased or it swings back to slowly release the gas molecules from the surface. Elaborating on PSA, the adsorbents are

shaped specifically to reduce the pressure drop during the adsorption cycle. These adsorbents are then packed closely to form a series of beds through which the feed containing a mix of gases is passed. Particles with higher affinity towards adsorbent such as smaller particles will diffuse faster compared to others and need to be separated or removed before the next type of molecules break into the column. This is referred to as the regeneration of the adsorbent which is achieved by lowering the pressure thereby forcing the adsorbed molecules to be removed. Since the total pressure of the system swings between high pressure in feed and low pressure in regeneration, this “heatless” separation process is called as pressure swing adsorption. The other variable to remove the adsorbed species is temperature where a gradual change in temperature affects the adsorbate-adsorbent interactions.[65] To enhance the mentioned interactions, the choice of adsorbent is crucial and in the past decades, the porous materials such as zeolites, metal organic frameworks, zeolitic imidazoles, porous organic polymers, activated carbons, molecular sieves and many other have been utilized.

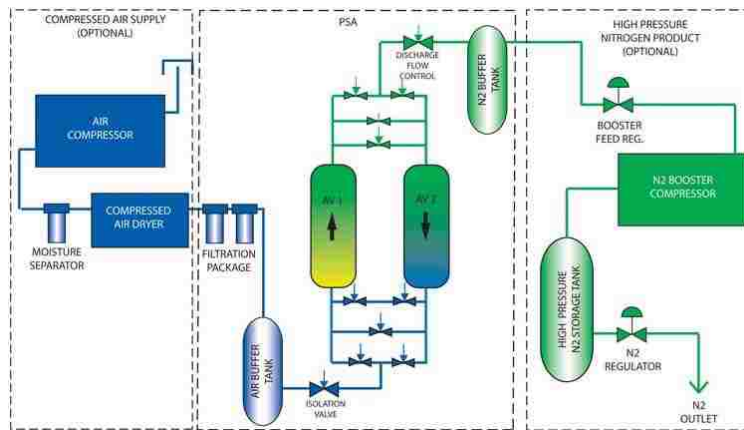


Figure 1.4: Typical System Configuration of a PSA assembly [66]

1.3.2 Factors Governing PSA [55, 62-64]

1.3.2.1 Size or Shape Exclusion

Also called as molecular sieving effect or steric separation, this method separates gas molecules based on their difference in size or shape. As mentioned earlier that the adsorbents for pressure swing adsorption are porous, have high surface area, and uniform pore size, they offer various sites for gas molecules to sieve through because the pore size is of the order of the gas molecules. So, when a mixture of gas is passed through series of beds/columns, the smaller molecules will pass through the numerous sieves and remain entrapped with heavier or larger particles being occupied near surface. When the pressure is reduced in the desorption step, the heavier or larger molecules leave the bed first followed by smaller molecules from the small cavities. For steric separation, kinetic diameter and the shape of the molecule govern the selective adsorption. Kinetic diameter for a gas is defined as the collision diameter or the intermolecular distance of the closest approach for two molecules colliding with zero initial kinetic energy. If temperature is affecting pore opening/closing, or the size of the pore, then the selective adsorption is affected by temperature as well.

1.3.2.2 Thermodynamic Equilibrium Effect

Due to the difference in the interaction between gas molecules and the surface, preferential adsorption of certain molecules takes place over other leading to another extent of selective gas separation. For instance, if the pores are wide enough to accommodate the flow of all gas molecules, then factors such as magnetic susceptibility, polarizability, quadrupole moment, and dipole moment, etc. govern the adsorbate-adsorbent interaction and hence the separation.

1.3.2.3 Diffusivity

Also known as kinetic effect or partial molecular sieve action dictates that due to difference in the rates of diffusion, certain molecules will ‘flow’ through the channels and cavities faster and end up being adsorbed faster than others. For example, in separation of N₂ from air, a carbon molecular sieve is used where O₂ diffuses 30 times faster than N₂ with similar quantities adsorbed at equilibrium. In other instances, propane is separated from propylene by AlPO₄-14, nitrogen from methane by Zeolite 4A.

1.3.2.4 Quantum sieving effect

In some cases for lighter molecules such as H₂, D₂, T₂, and He, certain adsorbents have micropores which allow these gases to penetrate and so gas separation gets difficult. But at lower temperatures, the de Broglie wavelength of these molecules gets comparable to the pore diameter leading to separation based on diffusion speed. First reported by Beenakker *et al*, this effect mentions that a high diffusion barrier is built up for the lighter molecules when the de Broglie wavelength is comparable to the pore diameter which causes the heavier molecules to diffuse rapidly in the micropores resulting in selective separation. Another variant, chemical affinity quantum sieving, occurs when the certain gas molecules are adsorbed at the active site or the primary site due to their difference in masses giving a different heat of adsorption and hence preferential adsorption.

1.3.3 Measures to Determine the Performance of Nanoporous Materials for Gas Separation

1.3.3.1 Selectivity [63]

For an adsorbent for a separation process, the multi-component adsorption equilibria, heats of adsorption, and kinetics are studied. So far advancement in studying the multi-component adsorption equilibria isn't observed due to the difficulty associated in measuring it experimentally. Therefore, for simplicity, separation factor or selectivity ($S_{i,j}$) is used to express the multi-component adsorption equilibria which is defined as

$$S_{i,j} = \left(\frac{x_i}{y_i}\right) / \left(\frac{x_j}{y_j}\right) \quad (1)$$

where x_i and y_i are the mole fractions of the gas in the adsorbed and bulk phase respectively. For selectivity calculations, an initial selectivity is reported by breakthrough measurements. Here, researchers use their own custom-built set up to evaluate the material for separation process but the underlying principle of these set up is that a breakthrough curve is generated by a gas flow containing a well-defined concentration of adsorptive in a carrier gas which passes through a column which contains the adsorbent to be evaluated. When the adsorbent is saturated with the adsorbed gas, no additional gas can be adsorbed. Additional increment of adsorptive gas in the column passes through the column and is observed at the end of the column. This travel to the other end upon saturation is referred to as the breakthrough of the gas and a breakthrough curve (an example shown in Figure 1.5) is generated which exhibits the quantity of adsorptive adsorbed by the adsorbent in the presence of other gas components thereby giving an indication of selectivity. The concentrations of each gas component of the mixture is detected in a time resolved manner. An inert material which is unresponsive to the adsorptive gas is also used for dead volume correction.

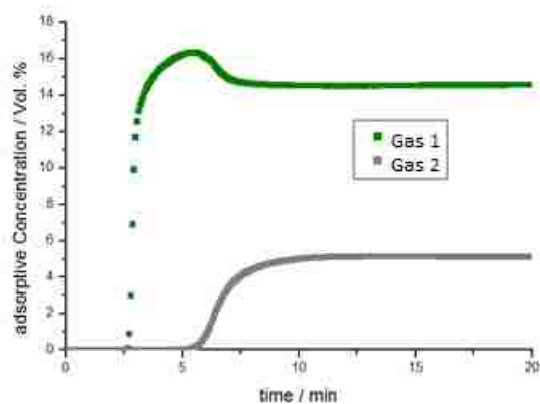


Figure 1.5: An example for a breakthrough curve. Breakthrough curves are beneficial as they provide information on the dynamic picture on separation performance of different adsorbents.

Other possibility to determine the initial selectivity of an adsorbent is from Henry's law approximation. Henry's law states that at a constant temperature, the amount of a given gas that dissolves in a given type and volume of a liquid is directly proportional to the partial pressure of that gas in equilibrium with that gas in equilibrium with that liquid. In other words, solubility of a gas in a liquid is directly proportional to the partial pressure of the gas above the liquid. But the gas separation applications depend on the selectivities across a range of loadings and Henry's law can only help in determining the initial selectivity, so other methods need to be explored.

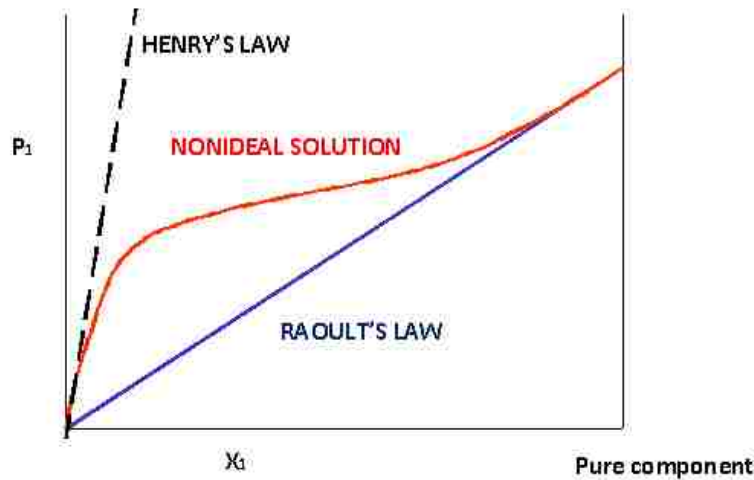


Figure 1.6: A diagrammatic explanation to show difference between the different gas laws. For Henry's law which focuses on the low-pressure regime, we need to measure adsorption isotherms in the low-pressure region. A nanoporous material typically gives a type I adsorption isotherm using which selectivities can be extracted. Image taken from the reference - [67]

A useful approach is by using the single gas experiments using Ideal Adsorbed Solution Theory (IAST). Developed in 1965 by Myers and Prausnitz, IAST is used to predict multi-component adsorption isotherms from the single gas experiment adsorption isotherm at the same temperature and on the same adsorbent.[68] IAST is based on reasonable approximations that (a) adsorbed gas molecules form an ideal mixture, meaning that the mean strength of interaction is equal between all molecules of the mixture, (b) same surface area is available to all gas molecules, and (c) that the adsorbent is inert. IAST is similar to Raoult's law for vapor-liquid equilibrium and through IAST, the mixture loading can be derived from (a) the system pressure P , (b) the fugacity coefficient of component i at pressure P : ϕ_i , (c) the original mole-fraction of component i in the feed gas: y_i , and (d) the loading as a function of fugacity. According to Myers, "the partial pressure of the adsorbed component is given as the product of its mole fraction in the adsorbed phase and

the pressure which it would exert as a pure adsorbed component at the same temperature and spreading pressure as those of the mixture.” Here, the gas adsorbed onto the adsorbent is considered as adsorbed phase and the gas in the theoretical bath surrounding the simulation system can be termed as vapor phase.

The mole fraction of adsorbed phase x_i and the vapor phase y_i are related as:

$$y_i \phi_i P = x_i f_i^0 \quad (2)$$

Here ϕ_i is the fugacity coefficient of component i at pressure P , and fugacity of component i in the adsorbed phase is given as f_i^0 . y_i and P are pre-decided by the experimental conditions and ϕ_i depends on P and the gas type. x_i is calculated upon deduction of f_i^0 and is used to calculate the total number of molecules being adsorbed:

$$\frac{1}{n_t} = \sum_{i=1}^{n_i} \frac{x_i}{n_i^p} \quad (3)$$

Where n_t is the total number of adsorbed gas molecules and n_i^p is the pure loading of the component on the surface, described by Freundlich isotherm. The number of molecules of adsorbate i adsorbed on the surface is given as

$$\eta_i = x_i n_t \quad (4)$$

From here on, f_i^0 can be calculated as follows:

For each component i , the spreading pressure of adsorbate is given as

$$\pi_i = \int_0^{f_i^0} \frac{n_i^p}{f_i} df_i \quad (5)$$

Where f_i is the fugacity of the vapor phase component i and so in the case of Freundlich isotherm $n_i^p = a f_i^b$, the spreading pressure is

$$\pi_i = \frac{a}{b} (f_i^0)^b \quad (6)$$

Since the spreading pressure must be same for all adsorbed components, an appropriate value for f_i^0 (determined through iteration, subject to the result satisfying the constraint that the mole-fraction sum to one) the mixture loading can be predicted.

So, we have

$$P_i = P_i^0 (\pi_i) x_i \quad (7)$$

where, π_i is the spreading pressure and x_i is the mole fraction of the component i in the adsorbed phase. Now, at adsorption equilibrium, for each component and the mixture must be having same reduced spreading pressures:

$$\pi_i^* = \frac{\pi_i}{RT} = \int_0^{P_i^0} \frac{n_i^0(P)}{P} dP \quad i = 1, 2, 3, \dots, N \quad (8)$$

$$\pi_1^* = \pi_2^* = \pi_3^* = \dots = \pi^*$$

The pure component equilibrium capacity is given by $n_i^0(P)$ and pure component hypothetical pressure is given by P_i^0 which gives the same spreading pressure as that of mixture. And by assumption of ideal mixing at constant spreading pressure (π) and temperature (T), the amount adsorbed (n_t) is given as:

$$\frac{1}{n_t} = \sum_{i=1}^N \left[\frac{x_i}{n_i^0(P_i^0)} \right] \quad (9)$$

where the constraint is

$$\sum_{i=1}^N x_i = 1 \quad (10)$$

1.3.3.2 Heat of adsorption [62, 63, 69-71]

Heat of adsorption, or integral heat, or differential heat, or isosteric heat of adsorption is one of the basic quantities in measuring the performance of adsorbent for gas separation studies. It is the ratio of infinitesimal change in the adsorbate enthalpy to the infinitesimal change in the amount adsorbed. The heat released by adsorption is partly adsorbed by the adsorbent and partly dissipated to the surroundings. As the gas molecules are adsorbed by the solid surface, it raises the molecule temperature and this increase in temperature slows down the further adsorption kinetics as the uptake in mass is governed by the rate of cooling of the molecule and so measurement of heat of adsorption is required in adsorption studies.

The heat of adsorption might vary with loading and can be calculated by the thermodynamic van't Hoff equation:

$$\frac{\Delta H}{RT^2} = - \left(\frac{\partial \ln P}{\partial T} \right)_{c_{\mu}} \quad (11)$$

For Langmuir isotherm, if the total differential is taken and substituted in the above equation, we get:

$$\frac{\Delta H}{RT^2} = \frac{Q}{RT^2} + \delta(1 + bP) \quad (12)$$

Here we have the assumption that the maximum concentration ($C_{\mu s}$), to vary with temperature and to take the following form:

$$\frac{1}{C_{\mu s}} \frac{dC_{\mu s}}{dT} = -\delta \quad (13)$$

And taking $(1+bP) = 1/(1-\Theta)$, the above substituted equation yields the heat of adsorption:

$$-\Delta H = -Q + \frac{\delta RT^2}{1 - \theta}$$

(14)

The negative sign for adsorption enthalpy here signifies that the adsorption is an exothermic process. Assuming that maximum adsorbed concentration, decreases with increase in temperature, the isosteric heat of adsorption, will increase with the loading due to the second term on equation. For the isosteric heat of adsorption to take a finite value at higher coverage ($\Theta \rightarrow 1$) the parameter for thermal expansion δ , must be zero meaning that the saturation capacity is independent of temperature, and as a result the heat of adsorption is constant, independent of loading.

To explain the concept in a different way, assume a well-insulated, constant temperature bath containing a box with a partition which is separating an ideal gas from an adsorbent under vacuum. Upon removing the partition, the equilibrium is established with gas molecules redistributing and becoming adsorptive, the integral heat of adsorption is equal to the internal energy change of the surroundings which is equal to the internal change of the adsorbed gas multiplied by the amount of the gas adsorbed:

$$q_{int} = \Delta U_{surr} = n^s(\mu_g - \mu_s)$$

(15)

Differentiating w.r.t to the amount adsorbed n^s , we get the differential heat:

$$q_d = \frac{\partial q_{int}}{\partial n^s}$$

(16)

The isosteric heat of adsorption can be defined by analogy to the Clausius-Clapeyron equation for the vapor-liquid equilibrium:

$$q_{st} = T(v_g - v_s) \left. \frac{\partial p}{\partial T} \right|_{n^s} \quad (17)$$

The differential heat arises from a change in internal energy and the isosteric heat from a change in enthalpy, then by neglecting the adsorbed phase volume (v_s):

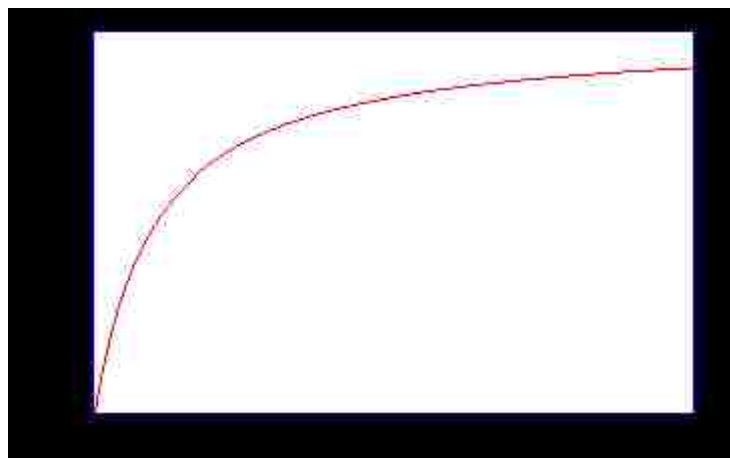
$$q_{st} = q_d + pv_g = q_d + ZRT \quad (18)$$

where R is the ideal gas constant and Z is the gas phase compressibility factor.

To understand this indirect method of measuring the adsorption isotherms at different temperatures, extrapolating the points of adsorption or coverage from isotherms, let's work with Langmuir isotherm where the monolayer adsorption is given as

$$\theta = \frac{bP}{1 + bP} \quad (19)$$

Where $b = b(T)$ and the Langmuir variation of monolayer adsorption with pressure can be shown as:



$\theta \rightarrow bP$ at low pressures and
 $\theta \rightarrow 1$ at high pressures

Figure 1.7a: A general representation of a Langmuir adsorption

At any given pressure the extent of adsorption is determined by the 'b' which is a function of temperature and depends on the strength of adsorption or heat of adsorption. The affinity of the adsorbate to the substrate can be observed by the magnitude of adsorption enthalpy, negative quantity itself (spontaneous process). So, value of b can be increased by (a) reducing the system temperature and (b) increasing the adsorbate-adsorbent interaction which is shown in the curves below:

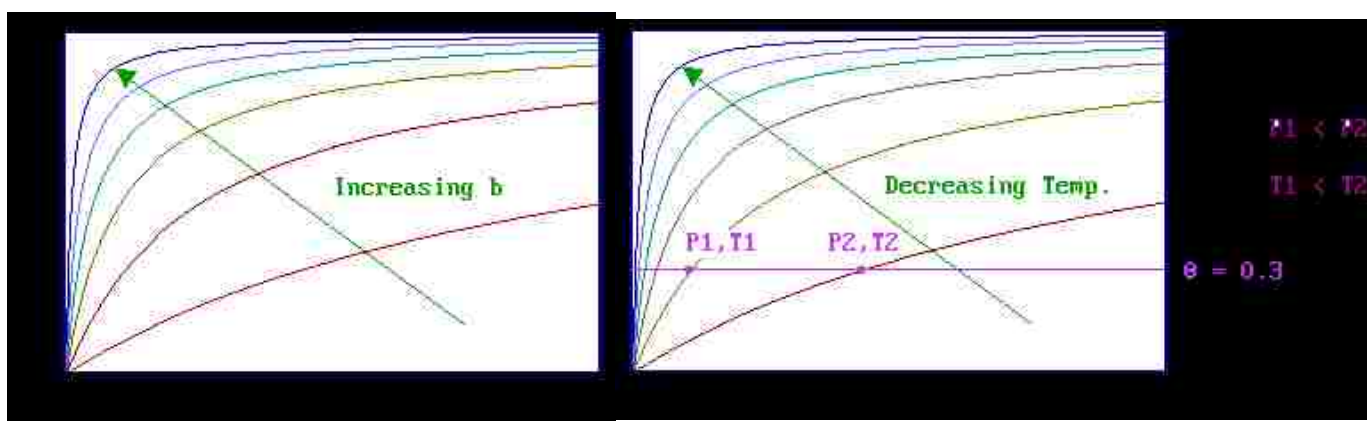


Figure 1.7b (left) shows the extent of coverage when the temperature is reduced to increase the value of 'b' and figure 1.7c (right) where two points (P_1T_1 and P_2T_2) are picked to calculate heat of adsorption as explained in the text.

This dependency of b on temperature and the adsorption enthalpies can be used in many ways, one of which is discussed briefly here:

Step 1: Determine the number of adsorption isotherms where a single isotherm is a coverage/pressure curve at a constant temperature.

Step 2: Pick the pairs of values of temperature and pressure which provide the same coverage.

Step 3: Use Clausius-Clapeyron equation

$$\left(\frac{\partial \ln P}{\partial \frac{1}{T}} \right)_{\theta} = \frac{\Delta H_{ads}}{R}$$

to this P-T data and the plot of $\ln P$ vs $1/T$ will give a straight line, the slope of which will yield heat of adsorption. The steps 2 and 3 can be repeated for various surface coverages to calculate heat of adsorption over the entire range of coverage for a reversible process.

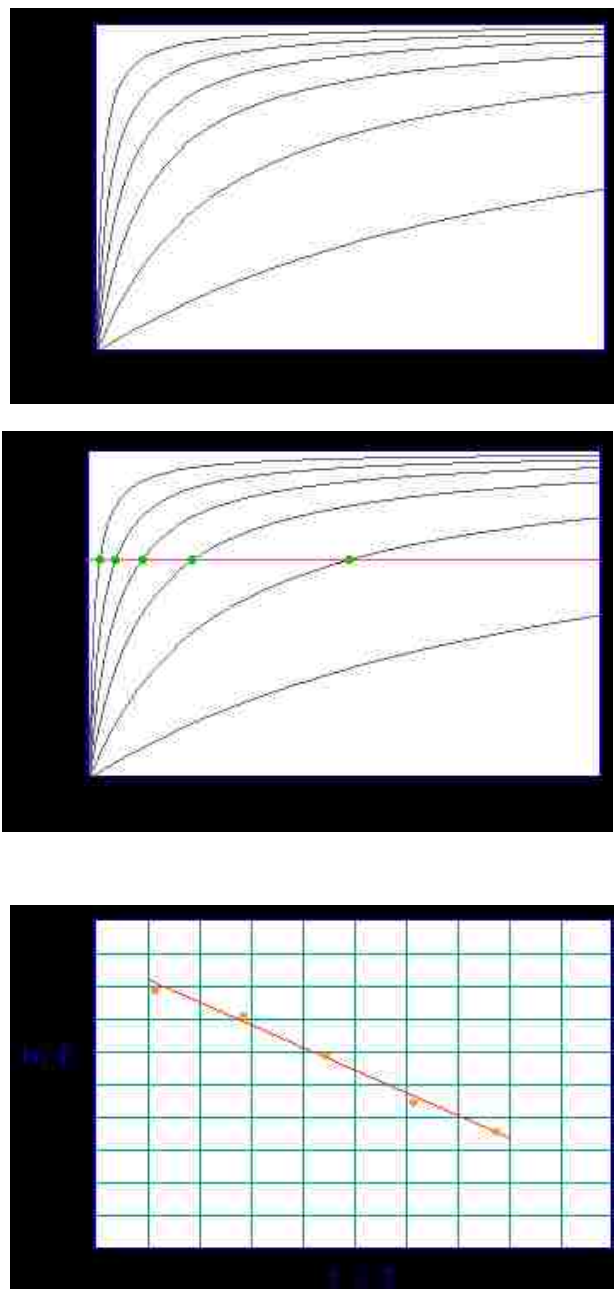


Figure 1.7d: Images for the corresponding steps to calculate the heats of adsorption.

These parameters are measured experimentally and using computational tools such as Grand Canonical Monte Carlo (GCMC) simulations. In our studies, we have used both parameters to assess the nanoporous materials for their storage and separation capabilities and the results are discussed in the respective chapters.

1.4.1 Overview of the Dissertation

The work compiled in this dissertation focuses on applications of the microporous materials i.e. materials with pore diameter less than 2 nm, in the field of gas separation and storage. This dissertation is divided into two parts where chapter 1 and 2 focus on the mechanism of gas separation and chapter 3 and 4 look into the storage capability of microporous materials. Each chapter has its separate focus on the problems with the current technology followed by the solution and conclusion.

Chapter 1 deals with the joint experimental and computational approach to assess the zeolitic frameworks for Kr and Xe gas separation. Here, an introduction on the present technique used for gas separation – Pressure Swing Adsorption (PSA) is provided along with the computational approach – Grand Canonical Monte Carlo (GCMC) simulation, which was used for screening purposes. Experimental adsorption isotherms and heat of adsorption were used to benchmark an accurate model for Kr-Xe gas separation and the selectivity of all zeolites (ISA database of year 2014) was screened across a range of pressures.

In chapter 2, we utilize the concepts of PSA to selectively separate hydrogen (H_2) from one of its isotope – deuterium (D_2). Here, since the gas molecules are quite small, we focus on the effects of quantum sieving and describe how it controls the selective separation process. We measured adsorption isotherms and the corresponding heats of adsorption at varying temperatures to determine the efficiency of the substrate – VSB-5 which is a nickel phosphate. So far, we have

measured the second highest heat of adsorption for hydrogen with VSB-5 indicating the strong binding sites it contains.

In chapter 3 we have compiled the Inelastic Neutron Scattering (INS) data to assess one of the simplest yet the most exciting material or the surface – graphene, to capture hydrogen (H_2). Being the only 2-D material (crystal) in the periodic table, graphene has measured interesting electrical, mechanical, optical, and thermal properties. Since graphene only consists of carbon, it provides a weak binding site for hydrogen gas which is required to validate the interaction of hydrogen in an anisotropic potential. Here we provide a brief introduction on the technique, INS, and the instrument VISION which was used to measure the dynamic adsorbate-adsorbent interactions. We also provide a brief summary on the vibrational spectroscopy with hydrogen and for a more detailed review, ‘Vibrational Spectroscopy with Neutrons, with applications in Chemistry, Biology, Materials Science and Catalysis’ by PCH Mitchell, SF Parker, AJ Ramirez-Cuesta and J Tomkinson is recommended. A brief comparison with a strong binding site, as observed in VSB-5 is also measured as a function of increasing temperature by the help of VISION instrument.

Chapter 4 focuses on one of the most extensively studied Metal Organic Frameworks (MOFs) – HKUST-1 also known as Copper Trimesate, which here was used to capture ammonia. To increase the amounts of ammonia in the microporous cavities, cages, and channels of the MOF, Bronsted acidic character was introduced post-synthesis. Extra Bronsted acidic character in HKUST-1 attracts three times more ammonia compared to the pristine HKUST-1 and makes the process of adsorption reversible as reported for the first time. INS measurements were used to

study the interaction of ammonia with HKUST-1 and at the acidic sites in acid modified HKUST-1. Molecular dynamics calculations were used to study the binding of the acidic (sulfuric acid) moiety in the HKUST-1 framework and also to study the interactions between ammonia and acidic sites.

1.5 References

1. Fedlheim, D.L. and C.A. Foss, *Metal nanoparticles: synthesis, characterization, and applications*. 2001: CRC press.
2. Correa-Duarte, M.A., M. Giersig, and L.M. Liz-Marzan, *Stabilization of CdS semiconductor nanoparticles against photodegradation by a silica coating procedure*. *Chemical Physics Letters*, 1998. **286**(5-6): p. 497-501.
3. Georgakilas, V., et al., *Decorating carbon nanotubes with metal or semiconductor nanoparticles*. *Journal of Materials Chemistry*, 2007. **17**(26): p. 2679-2694.
4. Bandaranayake, R., et al., *Structural phase behavior in II–VI semiconductor nanoparticles*. *Applied physics letters*, 1995. **67**(6): p. 831-833.
5. Johnson, B.F., *Nanoparticles in catalysis*. *Topics in Catalysis*, 2003. **24**(1-4): p. 147-159.
6. Hinnemann, B., et al., *Biomimetic hydrogen evolution: MoS₂ nanoparticles as catalyst for hydrogen evolution*. *Journal of the American Chemical Society*, 2005. **127**(15): p. 5308-5309.
7. Cho, K., et al., *Therapeutic nanoparticles for drug delivery in cancer*. *Clinical cancer research*, 2008. **14**(5): p. 1310-1316.
8. Soppimath, K.S., et al., *Biodegradable polymeric nanoparticles as drug delivery devices*. *Journal of controlled release*, 2001. **70**(1-2): p. 1-20.
9. Jain, A., et al., *Single-walled carbon nanotubes as near-infrared optical biosensors for life sciences and biomedicine*. *Biotechnology journal*, 2015. **10**(3): p. 447-459.
10. Brust, M., et al., *Synthesis of thiol-derivatised gold nanoparticles in a two-phase liquid–liquid system*. *Journal of the Chemical Society, Chemical Communications*, 1994(7): p. 801-802.
11. Daniel, M.-C. and D. Astruc, *Gold nanoparticles: assembly, supramolecular chemistry, quantum-size-related properties, and applications toward biology, catalysis, and nanotechnology*. *Chemical reviews*, 2004. **104**(1): p. 293-346.

12. Brust, M., et al., *Synthesis and reactions of functionalised gold nanoparticles*. Journal of the Chemical Society, Chemical Communications, 1995(16): p. 1655-1656.
13. Lee, J.K., et al., *Silicon nanoparticles–graphene paper composites for Li ion battery anodes*. Chemical Communications, 2010. **46**(12): p. 2025-2027.
14. Wu, H., et al., *Stable Li-ion battery anodes by in-situ polymerization of conducting hydrogel to conformally coat silicon nanoparticles*. Nature communications, 2013. **4**: p. 1943.
15. Max, L.G. and Z.X. Song, *Nanoporous materials: science and engineering*. Vol. 4. 2004: World Scientific.
16. *International Zeolite Association*. Available from: <http://www.iza-online.org/>.
17. Chae, H.K., et al., *A route to high surface area, porosity and inclusion of large molecules in crystals*. Nature, 2004. **427**(6974): p. 523.
18. Matsuoka, K., et al., *Extremely high microporosity and sharp pore size distribution of a large surface area carbon prepared in the nanochannels of zeolite Y*. Carbon, 2005. **43**(4): p. 876-879.
19. Fruijtier-Pöllöth, C., *The safety of synthetic zeolites used in detergents*. Archives of toxicology, 2009. **83**(1): p. 23-35.
20. Primo, A. and H. Garcia, *Zeolites as catalysts in oil refining*. Chemical Society Reviews, 2014. **43**(22): p. 7548-7561.
21. Corma, A., et al., *A large-cavity zeolite with wide pore windows and potential as an oil refining catalyst*. Nature, 2002. **418**(6897): p. 514.
22. Weitkamp, J. and L. Puppe, *Catalysis and zeolites: fundamentals and applications*. 2013: Springer Science & Business Media.
23. Lee, G., et al., *Shape selective alkylation of polynuclear aromatics with mordenite-type catalysts: A high yield synthesis of 4, 4'-Diisopropylbiphenyl*. Catalysis letters, 1989. **2**(4): p. 243-247.
24. Song, C. and S. Kirby, *Shape-selective alkylation of naphthalene with isopropanol over mordenite catalysts*. Microporous Materials, 1994. **2**(5): p. 467-476.

25. Regli, L., et al., *Hydrogen storage in chabazite zeolite frameworks*. Physical Chemistry Chemical Physics, 2005. **7**(17): p. 3197-3203.
26. Jha, V.K. and S. Hayashi, *Modification on natural clinoptilolite zeolite for its NH₄⁺ retention capacity*. Journal of Hazardous Materials, 2009. **169**(1-3): p. 29-35.
27. Camacho, L.M., S. Deng, and R.R. Parra, *Uranium removal from groundwater by natural clinoptilolite zeolite: effects of pH and initial feed concentration*. Journal of hazardous Materials, 2010. **175**(1-3): p. 393-398.
28. Li, H., et al., *Design and synthesis of an exceptionally stable and highly porous metal-organic framework*. nature, 1999. **402**(6759): p. 276.
29. (CCDC), T.C.C.D.C.; Available from: <https://www.ccdc.cam.ac.uk/support-and-resources/support/case/?caseid=9833bd2c-27f9-4ff7-8186-71a9b415f012>.
30. Farha, O.K., et al., *Metal-organic framework materials with ultrahigh surface areas: is the sky the limit?* Journal of the American Chemical Society, 2012. **134**(36): p. 15016-15021.
31. Horcajada, P., et al., *Porous metal-organic-framework nanoscale carriers as a potential platform for drug delivery and imaging*. Nature materials, 2010. **9**(2): p. 172.
32. Horcajada, P., et al., *Metal-organic frameworks as efficient materials for drug delivery*. Angewandte chemie, 2006. **118**(36): p. 6120-6124.
33. Lee, J., et al., *Metal-organic framework materials as catalysts*. Chemical Society Reviews, 2009. **38**(5): p. 1450-1459.
34. Wu, C.-D., et al., *A homochiral porous metal-organic framework for highly enantioselective heterogeneous asymmetric catalysis*. Journal of the American Chemical Society, 2005. **127**(25): p. 8940-8941.
35. Allendorf, M., et al., *Luminescent metal-organic frameworks*. Chemical Society Reviews, 2009. **38**(5): p. 1330-1352.
36. Talin, A.A., et al., *Tunable electrical conductivity in metal-organic framework thin-film devices*. Science, 2013: p. 1246738.

37. Ma, S. and H.-C. Zhou, *Gas storage in porous metal–organic frameworks for clean energy applications*. Chemical Communications, 2010. **46**(1): p. 44-53.
38. Bleakney, W. and A.J. Gould, *The relative abundance of hydrogen isotopes*. Physical Review, 1933. **44**(4): p. 265.
39. Dicks, A.L., *Hydrogen generation from natural gas for the fuel cell systems of tomorrow*. Journal of power sources, 1996. **61**(1-2): p. 113-124.
40. Sharma, S. and S.K. Ghoshal, *Hydrogen the future transportation fuel: from production to applications*. Renewable and sustainable energy reviews, 2015. **43**: p. 1151-1158.
41. Durgutlu, A., *Experimental investigation of the effect of hydrogen in argon as a shielding gas on TIG welding of austenitic stainless steel*. Materials & design, 2004. **25**(1): p. 19-23.
42. Tools, H.; Available from: <https://www.h2tools.org/bestpractices/h2introduction/basics/applications>.
43. Laboratories, A.K.; Available from: https://www.amglo.com/krypton_arc_laser.html.
44. Pavlovskaya, G.E., et al., *Hyperpolarized krypton-83 as a contrast agent for magnetic resonance imaging*. Proceedings of the National academy of Sciences of the United States of America, 2005. **102**(51): p. 18275-18279.
45. Cullen, S.C. and E.G. Gross, *The anesthetic properties of xenon in animals and human beings, with additional observations on krypton*. Science, 1951. **113**(2942): p. 580-582.
46. Seelig, J., *Deuterium magnetic resonance: theory and application to lipid membranes*. Quarterly reviews of biophysics, 1977. **10**(3): p. 353-418.
47. Ageron, P., et al., *Experimental and theoretical study of cold neutron sources of liquid hydrogen and liquid deuterium*. Cryogenics, 1969. **9**(1): p. 42-50.
48. ITER. Available from: <https://www.iter.org/org/ITERinFrance>.
49. Smith, A. and J. Klosek, *A review of air separation technologies and their integration with energy conversion processes*. Fuel processing technology, 2001. **70**(2): p. 115-134.

50. Agrawal, R. and B.E. Farrell, *Cryogenic production of krypton and xenon from air*. 1992, Google Patents.
51. Mitsui, J., et al., *Separation of hydrogen isotopes by an advanced thermal diffusion column using cryogenic-wall*. *Fusion technology*, 1991. **19**(3P2B): p. 1646-1650.
52. Neuburg, H.J., J. Atherley, and L. Walker, *Girdler-Sulfide Process Physical Properties*. 1977: Atomic Energy of Canada Limited, Chalk River Nuclear Laboratories.
53. Chien, T.-W. and H. Chu, *Removal of SO₂ and NO from flue gas by wet scrubbing using an aqueous NaClO₂ solution*. *Journal of Hazardous Materials*, 2000. **80**(1-3): p. 43-57.
54. Resnik, K.P. and H.W. Pennline, *Study of an ammonia-based wet scrubbing process in a continuous flow system*. *Fuel*, 2013. **105**: p. 184-191.
55. Sircar, S., *Pressure swing adsorption*. *Industrial & engineering chemistry research*, 2002. **41**(6): p. 1389-1392.
56. Knaebel, K.S., *Pressure swing adsorption*. 1991, Google Patents.
57. Sircar, S. and T. Golden, *Purification of hydrogen by pressure swing adsorption*. *Separation Science and Technology*, 2000. **35**(5): p. 667-687.
58. IUPAC. *MANUAL OF SYMBOLS AND TERMINOLOGY FOR PHYSICOCHEMICAL QUANTITIES AND UNITS*. Available from: http://old.iupac.org/reports/2001/colloid_2001/manual_of_s_and_t/manual_of_s_and_t.html.
59. Toth, M., et al., *Continuum models of focused electron beam induced processing*. *Beilstein journal of nanotechnology*, 2015. **6**: p. 1518.
60. Brunauer, S., P.H. Emmett, and E. Teller, *Adsorption of Gases in Multimolecular Layers*. *Journal of the American Chemical Society*, 1938. **60**(2): p. 309-319.
61. Connelly, A.; Available from: <https://andyjconnelly.wordpress.com/2017/03/13/bet-surface-area>.
62. Myers, A. and P. Monson, *Adsorption in porous materials at high pressure: theory and experiment*. *Langmuir*, 2002. **18**(26): p. 10261-10273.

63. Myers, A., *Thermodynamics of adsorption in porous materials*. AIChE Journal, 2002. **48**(1): p. 145-160.
64. Siperstein, F.R. and A.L. Myers, *Mixed-gas adsorption*. AIChE journal, 2001. **47**(5): p. 1141-1159.
65. Cavenati, S., C.A. Grande, and A.E. Rodrigues, *Removal of carbon dioxide from natural gas by vacuum pressure swing adsorption*. Energy & fuels, 2006. **20**(6): p. 2648-2659.
66. Generon. *PSA Nitrogen Generator*. [cited 2018; Available from: https://www.generon.com/product_type/psa-nitrogen-generator/].
67. Yamuni, K. *Henry's law*. 2017 [cited 2018; Available from: https://chem.libretexts.org/Core/Physical_and_Theoretical_Chemistry/Physical_Properties_of_Matter/Solutions_and_Mixtures/Ideal_Solutions/Dissolving_Gases_In_Liquids%2C_Henry%27s_Law].
68. Myers, A.L. and J.M. Prausnitz, *Thermodynamics of mixed-gas adsorption*. AIChE Journal, 1965. **11**(1): p. 121-127.
69. Myers, A. and J.M. Prausnitz, *Thermodynamics of mixed-gas adsorption*. AIChE Journal, 1965. **11**(1): p. 121-127.
70. Pan, H., J.A. Ritter, and P.B. Balbuena, *Examination of the approximations used in determining the isosteric heat of adsorption from the Clausius– Clapeyron equation*. Langmuir, 1998. **14**(21): p. 6323-6327.
71. Cimino, R.T., et al., *Determination of isosteric heat of adsorption by quenched solid density functional theory*. Langmuir, 2017. **33**(8): p. 1769-1779.

CHAPTER 2 – Assessing Zeolite Frameworks for Noble Gas Separations Through a Joint Experimental and Computational Approach

Index

2.1 Abstract

2.2 Motivation

2.2.1 Importance of Kr-Xe

2.2.2 Present techniques to separate Kr-Xe and the problems associated

2.3 Zeolites and their application in Pressure Swing Adsorption

2.4 Grand Canonical Monte Carlo (GCMC) simulation

2.4.1 Requirement of GCMC simulation

2.5 Previous Work

2.6 Experimental

2.6.1 Materials and Methods

2.6.2 Gas sorption measurements

2.6.3 GCMC details

2.6.4 Mapping the pore volume

2.7 Results and Discussions

2.7.1 Benchmarking the model chemistry

2.7.2 Screening the zeolite

2.8 Conclusions

2.9 References

2.10 Supplementary Information

2.1 Abstract

All 229 identified zeotype frameworks are screened in their siliceous form by grand canonical Monte Carlo simulation for their ability to separate a radiochemically relevant Kr/Xe mixture in a pressure swing adsorption process. Prior to screening, our model was benchmarked against experimental single gas adsorption measurements, and it was found that for Kr and Xe, a Lennard-Jones 9-6 potential with a softer repulsion than an equivalently parameterized Lennard-Jones 12-6 potential was necessary to accurately model fluid-fluid interactions. By examination of the most promising candidate materials, we concluded that zeolites with small, accessible cages about the size of a Xe atom performed the best initially. Zeolites with narrow pore channels with spots along the pore wall with high local surface area are the best performers across all loadings.

2.2 Motivation for separation Kr-Xe

2.2.1 Importance of Kr-Xe

Depletion of fossil fuels at a faster rate has attracted interest towards other possible alternatives and the current focus is in harnessing the field of nuclear energy. U-235 nuclear fission reaction generates two-three millions times more energy than the conventional sources and the research focuses towards recycling as well.[1, 2] The fission energy industry (nuclear power plants) generates enormous amounts of energy and utilizes Uranium and Plutonium as the source for generation.

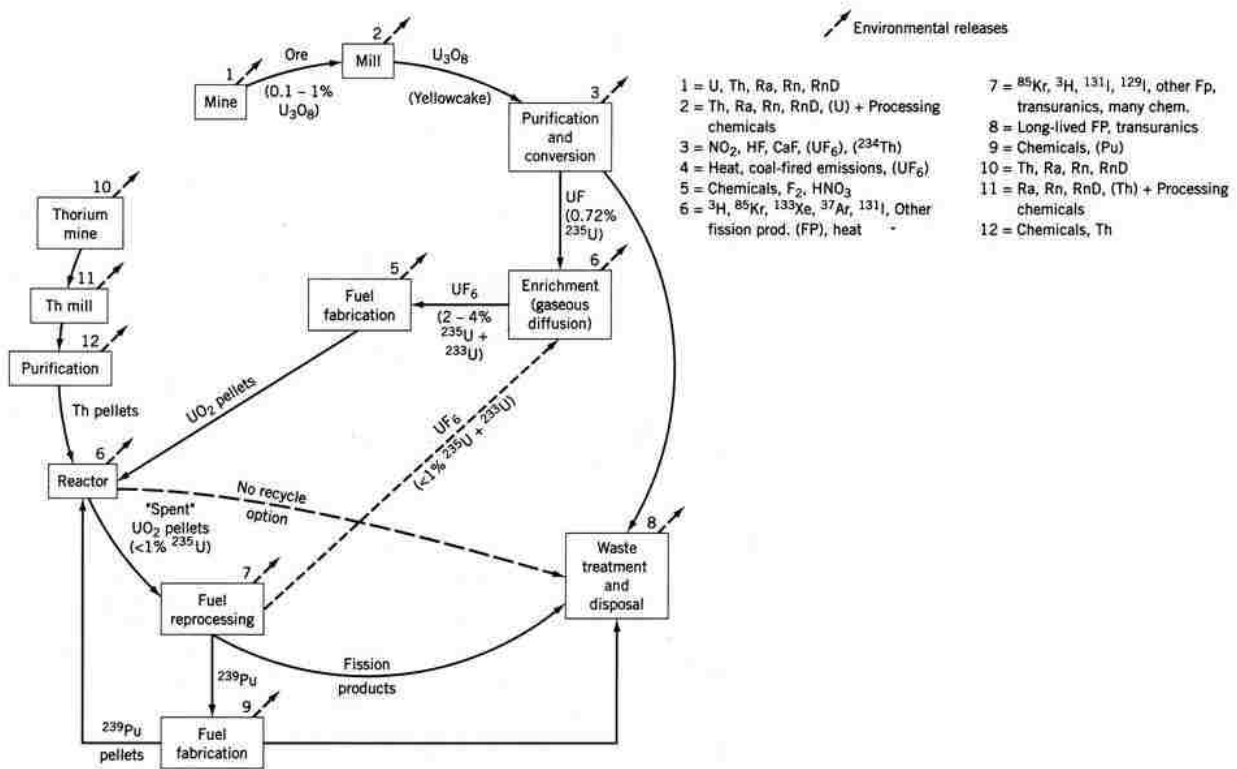


Figure 2.1 : Generation of various radioactive materials generated during a nuclear fuel cycle[3]

The low abundance of these sources requires reprocessing cycle where the reusable fissionable materials are recovered.[4, 5] Additionally, the by-products (³H, ¹⁴C, ¹²⁹I, ⁸⁵Kr) need to be stored safely until they don't possess a radiation hazard. Recent efforts on practical separation and waste forms for ³H and ¹⁴C have been identified and storage and separation of ⁸⁵Kr is still in its infancy. So development of a viable process has implications for separation of Kr and Xe from air and this mixture has an 80:20 Kr:Xe molar ratio after the noble gases have been isolated. The other process of interest is encountered during the mentioned processing of the spent radioactive fuel.[6, 7] Once all other gases are purged, the noble gas fraction consists of 90:10 Xe:Kr. As the Xe present in fission gas has no radioactive isotopes with half-lives longer than 30 days, Xe is expected to contain essentially no radioactive isotopes at the time of separation. In the Kr fraction

however, some radioactive ^{85}Kr is present. Storage of entire mixture is impractical when only the Kr fraction needs to be sequestered. In addition, this separation could serve as a new source for commercial Xe which has a high cost \$5000/L owing to its rarity as a minor byproduct from cryogenic distillation of air.[8]

Besides the reprocessing cycle, Kr and Xe (additional information in Table 1) need to be stored and separated due to their specific properties in numerous applications. For instance, the ionized Krypton, emits a white discharge due to the multiple sharp line emission and is used as a “white-light” source. [9] This white discharge is often mixed with other trace amounts of gases (Ne, Br, I) for multiple colored high efficiency lasers. The efficiency of various light sources is enhanced along with simultaneous increase in operating voltage because of reduced filament evaporation. Its medicinal usage is seen in magnetic resonance imaging and it is used to prepare the anesthetic mixtures as well. [10] ^{85}Kr is also used in military sector to detect the presence of any clandestine nuclear fuel reprocessing. [11] Natural (atmospheric) concentration of Kr is ~1 ppm which contains the five isotopes.

Discharge or emission of Xenon has a color temperature profile close to daylight and so its heavily used in the digital movie projections, vehicle headlights and other areas requiring daylight light source. Besides being an established anesthetic, Xe is also used as a neuro/cardioprotectant in medicinal field. [12-14] Similar to Kr, Xe is used in imaging technology to monitor blood flow. The natural occurrence of Xe is less than 1 ppm and so there is a huge demand to store these two noble gases.

Property	Krypton	Xenon
Atomic number	36	54
Atomic mass	83.798 amu	131.293 amu
Melting point	115.78 K	161.40 K
Boiling point	119.93 K	165.05 K
Critical point	209.48 K	289.73 K
Triple point	115.775 K	161.405 K
Density	3.74 g/L	5.89 g/L
Common oxidation states	0, +2	0, +1, +2
Van der Waals radius	202 pm	216 pm
Covalent radius	116 pm	140 pm
Kinetic diameter	3.9 Å	4.1 Å
Isotopes	⁷⁸⁻⁸⁶ Kr	¹²⁴⁻¹³⁶ Xe
Appearance	Colorless gas	Colorless gas

Table 2.1: General properties of Krypton and Xenon[15]

Besides the low natural occurrence, both gases are obtained as a by-product of fractional distillation of air which occurs at cryogenic temperatures. Unfortunately, here too, the concentration of the gases is too low and they are obtained as a mixture and therefore separating these two gases will positively affect numerous sectors of industry. This research focuses on storing and separating Kr and Xe from a gas mixture by a special class of microporous materials – zeolites.

2.2.2 Present techniques to separate Kr-Xe and the problems associated

Present technology dealing with capture focus on cryogenic and non-cryogenic processes. The cost associated and the efficiency of cryogenic fractional distillation of air has been reported multiple times where besides the cost of set-up of the plant, the energy required to separate the gases play a crucial role.[16, 17] The boiling points of Kr (-153 °C) and Xe (-108 °C) are too low for the cryogenic process to begin with thereby needing high energy input. Also, the final product obtained contains contamination of Xe in the stream of ^{85}Kr . Besides the energy input, the cost, and purity concern of the gas, the height of the column also poses distillation issues as the height of the column always determine the efficiency of distillation process.[16, 17] There are efforts still being put into the design of the column but they all require non-ambient conditions for the separation.



Figure 2.2: (left) A standard distillation assembly to capture Kr and Xe. (Right) A description of one column of the distillation assembly.[18]

Other alternative- high pressure cylinders, are non-ideal for the non-reliability for long period storage and the safety threat they pose if they were to fail miserably. Other mechanical

devices aren't suitable for similar reasons such as – decay heat and radiation leak along with other variables.

For non-cryogenic methods, Pressure Swing Adsorption (PSA) techniques – adsorption by various adsorbents has been utilized, such as – fluorinated organic solvents, silicone rubber membranes, activated charcoal and zeolites. [19, 20]

2.3 Zeolites and their applications in Pressure Swing Adsorption

As per IUPAC nomenclature, zeolites are considered as microporous materials as the average pore diameter is less than 2 nm (2 Å). A zeolitic network has a stoichiometry of TO_2 (T: metal/metalloid atoms) where the T-atoms are connected by two coordinated oxygen. The crystalline network is obtained by the aluminum tetrahedra $[AlO_4]^{5-}$ and silica tetrahedra $[SiO_4]^{4-}$ bonded to form a tetrahedron where the oxygen atoms are pushed in the corners for sharing with the adjacent tetrahedron. Typically, the quadri-charged silicon cations are replaced by triply charged aluminum cations which leads to deficiency in the positive charge. This imbalance in charge is compensated by presence of other singly/doubly charged cations which could be found elsewhere in the structure. Besides, inclusion of extra cations modifies the surface chemistry and the pore size distribution and affects the performance of zeolite in specific application. This arrangement of cations gives a general formula of zeolite as $M_{x/n}[(AlO_2)_x.(SiO_2)_y].zH_2O$, where the metal (M) could be any group I or II element with a valency n , x and y being the integers with a range Si/Al : 1(polymorph of silica) to infinity. So, the overall structure presents itself as Si or Al atoms in center and oxygen atoms occupying the corners. The $[AlO_4]^{5-}$ and $[SiO_4]^{4-}$ are called as primary building units (PBUs) and the oxygen atoms link the silicon or aluminum tetrahedra to give secondary building units (SBUs) which are rings and channels of specific lengths and dimensions. These SBUs (corner sharing tetrahedras) are linked to form inter-crystalline cavities

and cages called as Tertiary Building Units (TBUs) or pores which are specific to a certain type of zeolite. The long-range ordering of these building units give rise to the highly crystalline microporous framework of zeolite. Their stability in non-ambient conditions, abundance, ease in synthesis, low cost, and low toxicity have made zeolites an attractive material for the various applications. Since the pore size falls under the micropore range, these materials are often used as molecular sieves and are used in gas-phase separation studies.

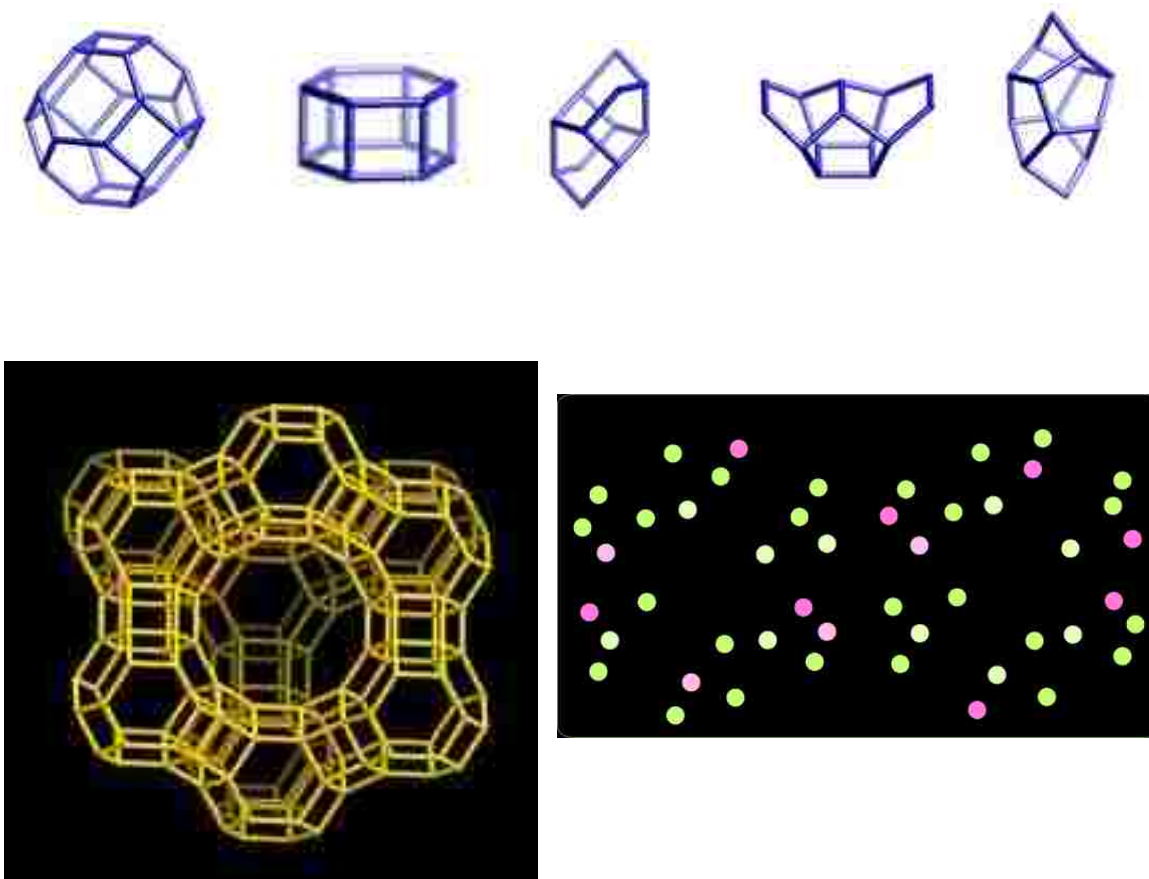


Figure 2.3: A diagrammatic description of zeolitic structure and Secondary Building Units (SBUs). The top figures in blue depict some of few secondary building units which are used to build a zeolite structure. The bottom left image shows the final structure of a zeolite which is built from different SBUs. The bottom right image shows that how sometimes Si could get replaced with Al to give a zeolitic structure with different charge configuration. Images

taken from - [21]

Zeolite enhances the adsorbate-adsorbent interactions which are the governing force of PSA process and zeolites have extra-framework cations which act as the primary site for gas adsorption. Mostly these sites are inaccessible due to the presence of water molecules (from the synthesis) which are removed by heating the material at optimum temperature. Here the robust nature of zeolite allows to have a higher activation temperature compared to other porous materials such as coordination polymers, leading to a better activated material. The electrostatic interaction between the gas and the cations are more pronounced after removal of water molecules. Other parameters such as – availability of cations in the framework, type of gas, pore size of the cages, access to the primary sites, connectivity of the cavities, effective charge at a particular site and several other factors also affect the adsorption process.

Since zeolites can act as molecular sieve by offering limiting pore structure and the separation process or the difference in adsorption capacities can be controlled by several parameters, zeolites can be effectively used as the adsorbents. The kinetic diameters of Kr and Xe are $\sim 3.6 \text{ \AA}$ and $\sim 3.96 \text{ \AA}$ and therefore zeolites with pore apertures in this range would be the ideal candidates for separation studies as Kr will “sieve” over Xe or in other terms, Kr molecules will diffuse in rapidly thereby proceeding for the first step of PSA followed by a slow diffusion of Xe giving rise to size exclusion by zeolites. The preferential adsorption of Kr over Xe by zeolites would also help in screening the suitable material for separation studies. Other mentioned porous materials exhibiting these properties can also be used but here we will focus on zeolites.

2.4 Grand Canonical Monte Carlo (GCMC)

2.4.1 GCMC requirement for screening zeolites

To screen the zeolites, an experimental approach is not optimal for practical reasons. Assessing one specific zeolite is quite labor intensive as far as synthesis, ion exchange,

characterization and adsorption analysis is considered. An average synthesis of zeolite takes 4-5 days followed by few days for ion-exchange before the material is ready for basic characterization. Our gas adsorption analysis (explained later) require at least 8 days to assess the potential of one adsorbent for Kr and Xe separation. Also from the initial experimental data for a promising zeolite, it is not clear and lack of information makes it difficult to explain a preferred selectivity by a zeolite without going for advanced characterization for instance *in-situ* crystallography with gas loading. An atomistic picture of gas adsorption will provide a straightforward approach to take a positive result for one zeolite and use that to assess the others. Modelling techniques such as grand canonical Monte Carlo (GCMC) simulations, help to provide a better atomistic picture of adsorption leading to an understanding of the adsorption behavior in adsorbents which are known to perform well for gas separation and thereby guiding the screening process for better adsorbents. Introduction on GCMC simulations is provided in Appendix A.

2.5 Previous work on Kr-Xe gas separation:

Previous studies focused on separating Kr-Xe using porous adsorbents have shown remarkable efficiency. Metal formates are considered for Kr-Xe gas separation due to their robustness and microporosity. Monte Carlo simulations on metal formates, $M(\text{HCOO})_2$ (where $M = \text{Fe, Co, Ni}$) showed that Xe is located close to the center of the cages/pores and Kr is found closer (0.21 \AA) to the wall. Here Xe is surrounded by eight formates such that their “pi” faces points into the pore. This suggests that interaction of Xe is with all the regions of the pores whereas Kr stays close to the pockets. Xe-Kr selectivities calculated from single gas adsorption isotherms is 22 with isosteric heat of adsorption $\sim 30 \text{ kJ/mol}$ and 22 kJ/mol for Xe and Kr respectively.[22] Similar studies on UTSA-49, which has two 6-membered rings of pore sizes $2.9 \text{ \AA} \times 3.6 \text{ \AA}$ and $3.6 \text{ \AA} \times 4.0 \text{ \AA}$ showed that thermal motions of atoms are sufficiently broad to have both gases to diffuse

into. Again, the heat of adsorption for Xe (23 kJ/mol) was much higher than Kr (16 kJ/mol) to effectively separate the two gases.[23] Effect of difference in polarization on separation was studied on SBMOF-2 (Ca cation and 1,2,4,5-tetrakis(4-carboxyphenyl)-benzene) with pore apertures 6.34 Å and 6.66 Å and it was found that channels with hydroxyl groups (polar) attracted more Xe or Kr molecules than non-polar channels.[24] High heat of adsorption for Xe (26 kJ/mol) suggests strong interaction with the wall when compared with Kr (21 kJ/mol). SBMOF-1 (Ca cations and 4,4'-sulfonyldibenzoate) with square shaped channels and pore dimensions 5.8 Å x 5.9 Å again showed a high affinity of Xe for the material when Xe isotherm saturated at low partial pressures and Kr didn't saturate at 1 bar.[25] Bae *et al* also focused on the adsorption within small pores of HKSUT-1 and MOF-505 and observed a clear difference in breakthrough time with Xe filling in the pores first and also pushing Kr molecules from the small pores. Based on their breakthrough measurement and GCMC calculations, MOF-505 performs better for the separation studies.[26] Zeolites NaA and NaX are also studied for Kr-Xe gas separation and showed higher preference towards Xe gas adsorption. Munakata *et al* worked with silver mordenite and mentioned the effect of ion-exchange leading to change in electrostatic potential on the surface of zeolite and increment in the affinity of surface towards noble gases. [27] Activated charcoals which have high surface area and thermal stability with low cost are also studied along with porous organic cages as in CC3.[28] A silicoaluminophosphate SAPO-34, $\text{Si}_x\text{Al}_y\text{P}_z\text{O}_2$ with average pore size of 3.8 Å was studied by Feng *et al* while focusing on separating Kr-Xe gas mixtures at industrially relevant compositions. They reported membrane thickness and crystal size as the key parameters in separating the mixture. High Kr permeances and high separation selectivities by SAPO-34 are interesting from industry's point of view.[29]

2.6 Experimental

2.6.1 Materials and Methods

We obtained a sample of calcined and activated siliceous LTA (ITQ-29) from Avelino Corma's group. We obtained a sample of siliceous FAU from Joseph Hriljac. We obtained a sample of siliceous BEA from Laszlo Nemeth that was synthesized, calcined, activated, and characterized using a modification of a previously published procedure with tetraethylorthosilicate as the only silica metal source.

2.6.2 Gas sorption measurements

About 150 mg of each sample was initially activated under dynamic turbopump vacuum at 400 °C for 24 h. Gas adsorption isotherms were measured using a Micromeritics ASAP 2020 instrument fitted with a He cryostat purchased from ColdEdge technologies. The cryostat interfaces with the analysis port on the analyzer through a specially designed joint with an isolation valve which enables removal of the tube from cryostat without exposing the sample to the atmosphere. Samples are loaded inside glass tubes which are attached to this joint and fitted inside a sample well area of the cryostat. The inside of the sample well is purged with a constant positive flow of He to prevent the condensation of gases on or around the sample tube and to enable efficient heat transfer to the sample tube. The bottom bulb of the sample tube is surrounded by aluminum heat shields in order to ensure a large region of stable temperature control around the sample. A LakeShore model 336 temperature controller provides stability of better than ± 0.01 K within the range of 25-350 K. Actual temperatures in the sample tubes are determined to high precision through a calibration curve constructed by the measurement of condensation pressures of various gases using the ASAP 2020 instrument. Freespace calibrations for specific sample tubes are performed by measuring the blank tube isotherms at 20 K intervals over the entire temperature

range. This removes the need for the typical He freespace measurement at the beginning of the isotherm, which could result in He contamination. The volume occupied by the sample was subtracted based on the sample mass and the density calculated from the crystal structure. Isotherms were collected up to ~710 mmHg with 5 cm³/g incremental volumetric doses and long equilibration times. Desorption measurements were taken at the end of each isotherm. Each measurement displayed negligible hysteresis, indicating equilibrium had been achieved. Samples were reactivated for an hour under dynamic vacuum at 150 °C and allowed to equilibrate in the cryostat for an hour between each measurement. Kr isotherms were measured at 230 K, 240 K, and 250 K. Xe isotherms were measured at 280 K, 290 K, and 300 K.

2.6.3 GCMC details

Gas adsorption was simulated with Monte Carlo in the grand canonical ensemble using the multi-component Peng-Robinson equation of state for fugacities.[30, 31] GCMC simulations were done with a modified version of the MUSIC package. The binary mixing parameters are found using the form of Coutinho *et al.* In addition to the normal GCMC moves, swap and exchange moves were moved to improve equilibration in the binary gas simulations. Each simulation employed 200,000 equilibration cycles and 300,000 production cycles. A cycle here consists of N moves, where N is the number of adsorbed particles (minimum 20). The zeolites are held as rigid during the simulations. [32-35]

We carefully considered potential options for obtaining crystal structures for the 229 zeolites. While experimental structures are attractive in some respects, they are not available for the majority of SiO₂ zeolites and vary in accuracy. For a comparative screening effort, we anticipate that a self-consistent set of structure would provide the best means of comparing zeolitic topologies directly. Computational lattice energy minimization is particular well-developed in the

case of SiO₂ zeolites, and should provide reasonably accurate structures that are fully self-consistent with each other. We used structures taken from the IZA-SC Database of Zeolite Structures. Those structures were optimized using the DLS76 program for a pure SiO₂ composition in a pre-dominant symmetry of the zeolite. Some of the frameworks (CHI, CLO, EWT, IRY, ITN, ITV, LIT, PAR, RON, SSO, SVR, and WEN) are acknowledged by the IZA-SC as interrupted frameworks that cannot be made as four-connected frameworks and therefore have dangling oxygens around the broken tetrahedra. For these frameworks, Olex2 was used to place the hydrogens to form silanol groups to terminate the dangling oxygens which would be the calcined form of the framework. The hydrogen positions in the primitive cell were refined with a selective dynamics plane-wave density functional theory optimization with the Vienna ab-initio Simulation Package 5.3.5 (VASP) using the projector-augmented wave (PAW) method and the generalized gradient approximation (GGA) exchange-correlation functional of Perdew, Burke, and Ernzerhof (PBE). [36-40] Just the Γ point was used to describe k-space. The WEN structure in the database does not include the experimental disorder and omits two of the would be silanol oxygens. To solve this, we constructed both symmetry inequivalent forms of the original reported WEN experimental crystal structure, and the lower energy ‘trans’ form is used in the screening. [41]

Table 2 includes all of the single species parameters used in this work. The framework-fluid potential was computed using a 12-6 Lennard-Jones with a low cutoff of 1.5 Å and a high cutoff at 15 Å. The atomic parameters for the framework-fluid potential are from the first two sections of Table 2 and combined using the Lorentz-Berthelot mixing rules. The framework Si and O parameters come from the recently developed TraPPE-zeo force field , and the silanol hydrogen parameters are taken from ClayFF with the charge lowered to ensure charge neutral unit cells. The Kr and Xe parameters were found using the principle of corresponding states using the Ar parameters of Talu and Myers and the critical parameters from the CRC as the starting point.

Explicit fluid point dipole polarizability was included as “ U_{pol} ” using the polarizability volumes in Table 2. The electric field is computed with the Wolf Coulomb potential truncated at 15 Å, a damping parameter of 0.1 Å⁻¹, and both the force and potential shifted.[42-49] In our own experiments, we have found that high loading regimes of isotherms for Kr and Xe are better modeled with a 9-6 Lennard-Jones potential, therefore the fluid-fluid potential interactions were modeled with the 9-6 Lennard-Jones COMPASS force field cutoff at 15 Å and combined with 6th order mixing rules. [50]

Framework parameters for framework-fluid interactions

	LJ-Type	$R_o(\text{Å})$	ϵ (K)	Charge (e)
Si ^a	12-6	2.5817	22.0	+1.500
O ^a	12-6	3.7041	53.0	-0.750
H ^b	12-6	0.0	0.0	+0.375

Noble gas parameters for framework-fluid interactions

	LJ-Type	$R_o(\text{Å})$	ϵ (K)	$\alpha(\text{Å}^3)$	$T_c(\text{K})$	$P_c(\text{MPa})$	V_c
Ar ^c	12-6	3.8220	119.80	1.6411	150.687	4.863	75
Kr ^d	12-6	4.0768	180.00	2.4844	209.48	5.525	91
Xe ^d	12-6	4.4449	230.30	4.0440	289.733	5.842	118

Noble gas parameters for fluid-fluid interactions

	LJ-Type	$R_o(\text{Å})$	ϵ (K)	$\alpha(\text{Å}^3)$	$T_c(\text{K})$	$P_c(\text{MPa})$	V_c
Kr ^f	9-6	4.3000	140.90	2.4844	209.48	5.525	91
Xe ^f	9-6	4.2600	196.26	24.0440	289.733	5.842	118

Table 2.2: ^a From TraPPE-zeo. ^b From Clay-FF, charge lowered for charge neutrality. ^c From Talu and Myers. ^d Obtained from principle of corresponding states, critical parameters from the CRC. ^e Increased to match experiment. ^f From COMPASS.

2.6.4 Mapping the pore volume:

In zeolites, there are pores that are known experimentally to be accessible to guests while there are cages that are kinetically inaccessible. To correctly model the accessible volume within a zeolite, we developed our own void volume mapping program which is very similar to a recently developed program.[51] Our program lays down a uniform grid of parallelepiped voxels laid in each crystallographic dimension, evaluates the energy of the adsorbate-framework Lennard-Jones interaction for the center of each voxel, and uses a six way (no diagonal connections) 3-D flood fill algorithm connecting neighboring points that allows for the crossing of periodic boundaries. If a voxel has an energy below a certain threshold it is initially considered accessible and could be connected to other voxels; otherwise it is considered as belonging to the volume of the framework and could not be connected to other voxels. A void was determined to be part of a pore network if a path within the connected void volume could be made from 0 to 1 along any crystallographic dimension including crossing other dimension's PBCs, if no such path could be made that connected volume was considered a closed-off cavity. Our pore volumes are taken as the sum of the volume of all accessible parallelepipeds. We found that a grid spacing of 0.15 Å and an energy cut off of 14 kcal/ mol was sufficiently small to close off all CBUs that should be considered inaccessible. The pores produced in this manner have accessible pore volumes that typically agree to within 0.5% of those presented in the IZA-SC database.[52] The GCMC moves were modified to have an auxiliary move rejection for use with the void maps. If the move placed the center of mass of the particle in a voxel within an open pore, the move is accepted by the conventional Metropolis algorithm. If the voxel is not part of an open pore, then the GCMC program checks whether the voxel is less than a certain number of voxels away (including diagonally). If any of the checked voxels are open, the move is accepted by the conventional Metropolis algorithm;

otherwise the move is outright rejected. We used a depth of 3 voxels away to resemble a translation move that has walked the particle into the wall of a framework.

2.7 Results and Discussions

2.7.1 Benchmarking a model chemistry

To screen all of the siliceous zeolites for their ability to separate Kr/Xe, an appropriate parametrization needs to be done against experimental single gas adsorption data. Figures 2.4-2.6 contain our experimental and simulated isotherms and heats of adsorption for LTA, BEA, and FAU plotted on the same scales for easy visual comparison. The simulated heats of adsorption were found using fluctuation theory at the same median temperature used in the determination of the experimental heats of adsorption. It is important to carefully select the 12-6 Kr/Xe parameters for the framework-fluid interaction to correctly model the Henry's law region of the isotherm. Very good results have been observed in MOFs using force fields derived from the two-parameter principle of corresponding states ($\epsilon \propto T_c$ and $\sigma \propto V_c^{1/3}$). [44] We found that the Kr force field produced in this matter predicted the HOA very well but under-predicted adsorption for these zeolites. To improve the fit, we increased the value of ϵ within 3 significant figures until a reasonable fit was found. Table 2 contains the determined force field parameters and the critical parameters.[45] We have also found that the softer repulsion term of a 9-6 Lennard-Jones for fluid-fluid interactions works well to describe the whole experimental Kr/Xe isotherm at higher loadings.[53] That result is the same here as a significant underestimation of adsorption at higher pressure (especially for Xe) when the same 12-6 potential used to build the fluid-framework interactions is used for the fluid-fluid interactions.

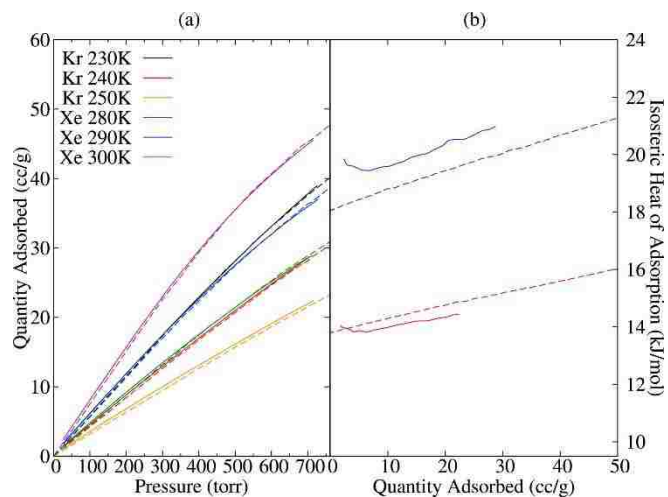


Figure. 2.4. Comparisons of experimental (solid) and simulated (dashed) Kr and Xe isotherms and heats of adsorption for LTA.

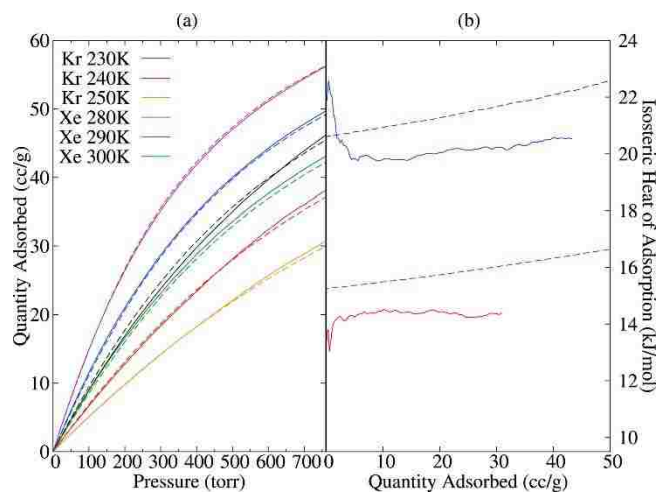


Figure.2.5. Comparisons of experimental (solid) and simulated (dashed) Kr and Xe isotherms and heats of adsorption for BEA.

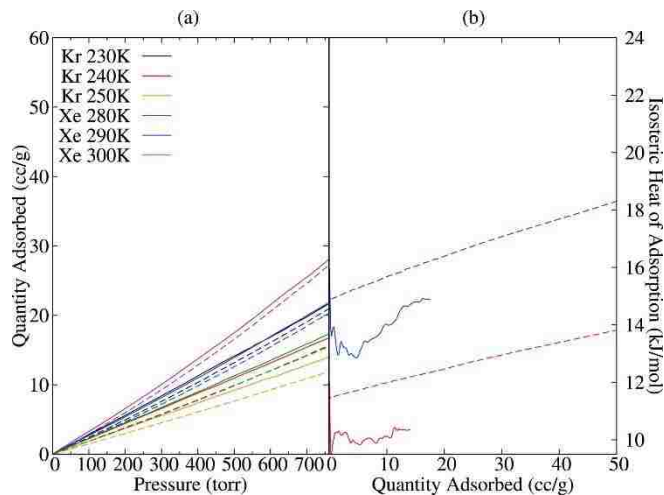


Figure.2.6 Comparisons of experimental (solid) and simulated (dashed) Kr and Xe isotherms and heats of adsorption for FAU.

BEA is known to be polymorphic, and we only performed simulations using the structure of polymorph A, the most representative polymorph. Given the similarity between the BEA polymorphs, we did not anticipate large differences with this approximation, as confirmed by the close agreement encountered. FAU is known to be a difficult material to produce in its siliceous form, as the process require dealumination and can lead to mesoporosity and aggregates of amorphous silica. This FAU sample seems to be high quality as a 77 K N₂ pore size distribution (over the default range in the Micromeritics software) is trimodal, which is in line with the three primary topological features of FAU: the a cage (t-fau), sod (t-toc) the sodalite or b cage, and d6r (t-hpr) connecting the sodalite cages. The agreement between the FAU HOAs is of comparable quality to that of LTA and BEA, however the simulation model under-predicts total adsorption by 5-10%. We believe the discrepancy arises from two factors: the mass of the measured sample being too low giving too high measured quantities adsorbed, and the COMPASS fluid-fluid parameters being too weak as FAU is a large pore system where correctly describing fluid-fluid interactions will be more critical. The finalized model we employed yields excellent agreement for the isotherm

and heat of adsorption for both gases at all tested temperatures. The predicted and measured heats of adsorption are both fairly flat, as expected of the relatively homogenous surface inside these zeolites. What is surprising is the similarity of the predicted heats of adsorption for Kr and Xe in both materials. A lack of small accessible pockets in the cells and a surface covered in 4-ring to 6-ring provides an easy explanation for the flatness and similarities in the heats of adsorption between these materials. The difference in heat of adsorption is consistent across all loadings which we have shown indicates a fairly uniform Xe/Kr selectivity at all loadings will be observed. We recognize that our approach neglects structural changes in response to gas uptake, as are known to occur in MFI, for example.[54, 55] However, the initial selectivities obtained from our calculations should still be valid.

2.7.2 Screening the zeolite

We carried out our screening at 298 K at five pressures on a logarithmic scale spanning the Henry's law region (1 mmHg) to PSA useful pressures (10,000 mmHg). In Table 1 of the Supplementary information, we plot 1) the percent accessible pore volume of the framework, 2) the total loading at each point, 3) and the Xe/Kr selectivity at each point. Figs. 2.7 and 2.8 summarize the screening results for both the initial adsorption (1 mmHg) and high loading (10,000 mmHg). The selectivities presented are for Xe over Kr, and the material's percent accessible pore volume is used to shade the plotted points. In figures a strong correlation between total loading and selectivity is evident, persisting to high loadings although with considerably more scatter. At low loadings, quantity adsorbed is primarily determined by the affinity of the zeolite for noble gases- frameworks with high HOAs for Kr and Xe also tend to have high selectivities. It is promising that zeolites with the highest selectivities tend to have relatively high adsorption for Kr and Xe as well. It is noteworthy that 10 zeolites have selectivities in excess of 10 - a value

comparable to the most promising MOFs studied so far. At higher pressures, the zeolites stratify dramatically, as can be seen in Figure 2.8. The zeolites with relatively low capacity (20-60 cm³/g) tend to be the most selective which is mainly due to a narrow small pore system. The zeolites with large capacity (≥ 100 cm³/g) are only moderately selective (~ 4 , the same as observed for HKUST-1 at high loadings). This is to be expected for large pore systems as they have space to accommodate large amounts of noble gas, but most of that gas cannot come into close enough contact with the unique framework topologies that provide sufficient dispersive interactions to make the material selective.

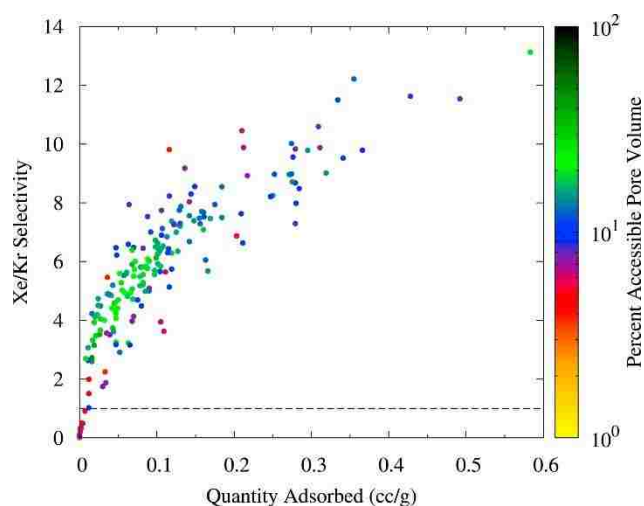


Figure.2.7. Initial selectivities of a 90:10 Xe/Kr mixture. The dashed line indicates a selectivity of 1, below which the materials are selective for Kr instead of Xe.

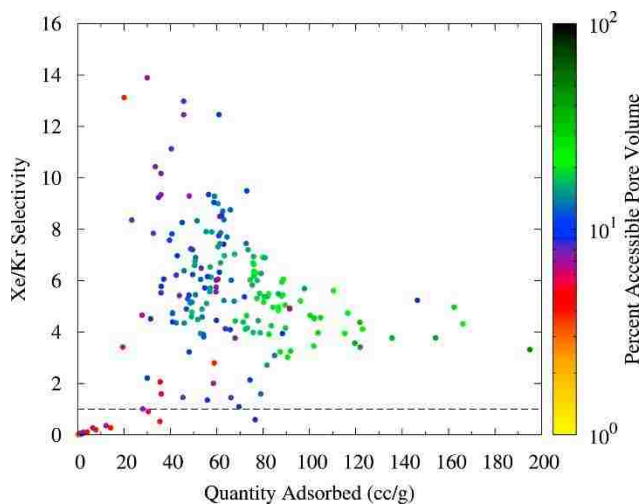


Figure.2.8. High loading selectivities of a 90:10 Xe/Kr mixture. The dashed line indicates a selectivity of 1, below which the materials are selective for Kr instead of Xe.

For some separations, a selectivity in favor of Kr is desirable. A recent review of MOF applicability to this problem highlighted FMOFCu, which could go from being Xe selective to Kr selective by lowering the temperature below 0 °C.[56, 57] A few siliceous zeolites appear selective for Kr (Xe/Kr selectivity less than 1), but none appear practical overall. At 298 K, four Kr-selective materials exhibited reasonable total gas loadings ($\geq 40 \text{ cm}^3/\text{g}$), yet they are only slightly selective for Kr. More selective frameworks all have low porosity and either modest uptake or low Kr selectivity at the highest pressures measured. Additional simulations at a lower, yet potentially realistic PSA temperature (250 K), were performed to see if the loadings of the Kr selective materials could be improved. Table 3 shows the results for quantity adsorbed and Kr selectivity at the highest loading point (10,000 mmHg) for both temperatures evaluated. When cooled, the quantity adsorbed improved by no more than a factor of 5 for each of the zeolites examined. The Kr selectivity did not change appreciably for any materials with reasonable loadings. Remarkably high Kr selectivity is suggested in several topologies, including CHI and NPO, but the predicted

total uptake is so small that these materials would be impractical for applications. Our simulations strongly suggest no siliceous zeolites would be competitive with FMOFCu.

	298 K 10,000 mmHg		250 K 10,000 mmHg	
	N(cm ³ /g)	S(Kr/Xe)	N(cm ³ /g)	S(Kr/Xe)
ABW	1.42	48.44	5.84	39.85
ACO	76.58	1.68	134.68	1.30
AEN	2.46	9.12	10.09	8.97
APC	4.15	9.48	18.36	10.66
BIK	2.01	13.85	7.66	15.59
CHI	0.11	214.98	0.29	470.88
CZP	14.27	3.59	36.22	3.88
JBW	7.89	5.13	26.62	5.43
LTJ	2.30	11.41	10.34	12.94
MON	2.44	14.27	10.38	14.61
NAB	0.98	16.42	2.35	107.50
NAT	69.63	0.91	101.08	0.74
NPO	0.30	76.32	0.84	148.52
NSI	0.56	43.63	1.87	75.53
PAR	0.99	14.46	3.34	14.69
RRO	12.26	2.78	33.97	2.85
RWR	35.48	1.91	83.39	1.53
VSV	6.50	3.68	19.94	4.04
WEI	1.93	20.88	7.59	18.39
YUG	30.52	1.11	43.57	1.03

Table 2.3: Simulated Total Quantities Adsorbed (cm³/g) and Kr/Xe selectivities for initially Kr selective zeolite framework types calculated at 10,000 mmHg at both 298 K and 250 K.

Figure 2.9 shows a strong correlation between the initial selectivities compared against the difference in the Xe and Kr heats of adsorption into the material. The heats of adsorption were computed with multi-component fluctuation theory. [57] There appears to be a maximal initial selectivity possible for a given difference in initial HOA, although many materials show lower selectivities than this. Normalizing the difference in heat of adsorption to either the Kr, Xe, or total heat of adsorption does not yield a more linear or tightly correlated data set. The same effect is observed at all loadings with a similarly narrow spread in the results. This plot directly demonstrates the established rule of thumb for using single gas adsorption measurements to estimate a material's selectivity. Figures above indicate that, for a material to have a Xe selectivity ≥ 10 , the difference in heat of adsorption needs to be at least ≥ 8 kJ/mol.

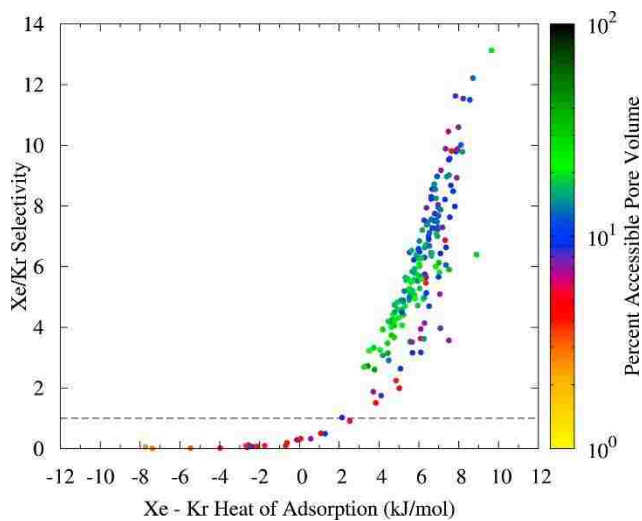


Figure.2.9 Initial selectivities of a 90:10 Xe/Kr mixture as a function of the difference in the Xe and Kr heats of adsorption. The dashed line indicates a selectivity of 1, below which the materials are selective for Kr instead of Xe.

Compiling the most selective materials at both initial and high loadings, we selected 23 frameworks for more detailed study: AFO, **ATN**, ATO, BOF, CAN, **CDO**, EAB, EDI, EON, EPI, ESV, **FER**, **LAU**, LTF, MAZ, **MRE**, MTF, OFF, OWE, **PCR**, **PSI**, UFI, and **ZON** (those in bold are among the most selective at both initial and high loading). Examining these structures, we have

identified two different sets of adsorption behavior that correspond with distinct structural motifs responsible for the high selectivity. The first category of selective zeolite frameworks, comprising the majority of the best performers, exhibits flat or slightly increasing selectivity and is associated with a narrow pore system. The remaining highly selective zeolites exhibit a high initial selectivity which drops, often dramatically, as loading increases. This type of behavior is associated with the presence of small pockets capable of adsorbing a single gas atom that are accessible off larger channels.

The first group, where selectivities increase or remain nearly constant as a function of loading, contain narrow pore systems. Snurr and coworkers, conducting a survey of 137,000 hypothetical MOFs, concluded that this mechanism lead to the best selectivities for this separation.[58] We later showed that porous transition metal formates exhibit among the highest Xe/Kr selectivities reported, and that this selectivity gently improves with increased loading, due to this mechanism[22]. This result was further enforced by a recent survey of 670,000 materials by Smit and coworkers, which did analyze the IZA zeolites but only for initial selectivity.[59] ATN is an example of a narrow channel pore system with 1-D ~ 6 Å diameter pores. The Xe loading is centralized in the t-ocn (atn) composite building unit (CBU) maximizing the Xe atoms dispersion interaction with the 2 8-ring windows of the t-ocn (Figure 2.10). The constricted pores provide a site (or sites) with a large amount of contact between the pore wall and the adsorbed gas, leading to high dispersive interactions and a good selectivity[22, 58, 59]. Typically, only one or several crystallographically distinct gas adsorption sites are present in compounds with this type of adsorption. If only one site is present, the only energetic difference between the first gas molecule to adsorb and the last are fluid-fluid interactions, resulting in a gradual increase in HOA and selectivity. While slightly more complicated, similar overall behavior generally occurs when several adsorption sites are present, especially when the sites are chemically similar. 8-ring pores

are common in this group with examples of cylindrical, elliptical or zigzag cross sections. 10-ring pores tend to be distorted. The zeolites EPI, ESV, MTF, and OWE show fall-offs in selectivity at high loadings. OWE and EPI are 2-dimensional materials with limited wall surface for adsorption whereas ESV and MTF have undulating pore volumes that resemble a series of pockets connected by smaller windows. As these features saturate, the decrease in selectivity is observed.

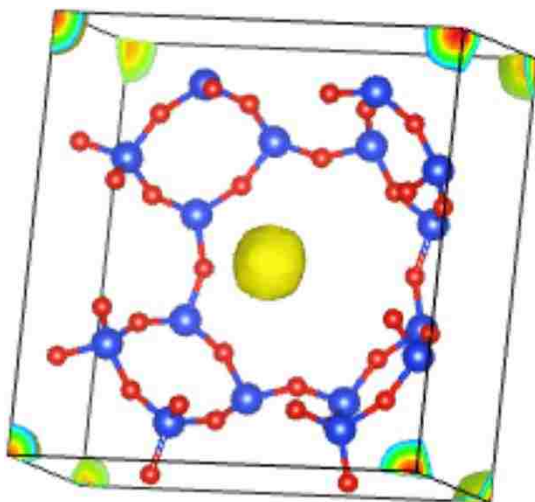


Figure.2.10 Xe loading density into ATN at 10 mmHg and 298 K.

The second category of topological features leading to high selectivity are small pockets or secondary pores connected to larger pores. Features comparable in size to Xe provide a region with very high dispersive interactions favoring Xe. We have previously shown that this is the mechanism behind high initial HOAs and selectivities for Kr and Xe in HKUST-1, but that it also leads to lower HOAs and selectivities at higher loadings. In our survey, this mechanism leads to the highest initial selectivities, but these may not be ideal adsorbents for PSA-type processes as the selectivities drop as loading increases. We illustrate this mechanism with UFI, which has the highest predicted initial selectivity for siliceous zeolites. UFI has a 2D pore system consisting of large lta (t-grc) cages connected through 8-ring pores. A number of t-ufi cages are accessible

through this pore system; this is where the simulations show gas density building up at low loadings (Figure 2.11). This is analogous to the mechanism for high initial selectivity observed in HKUST-1.[60, 61]

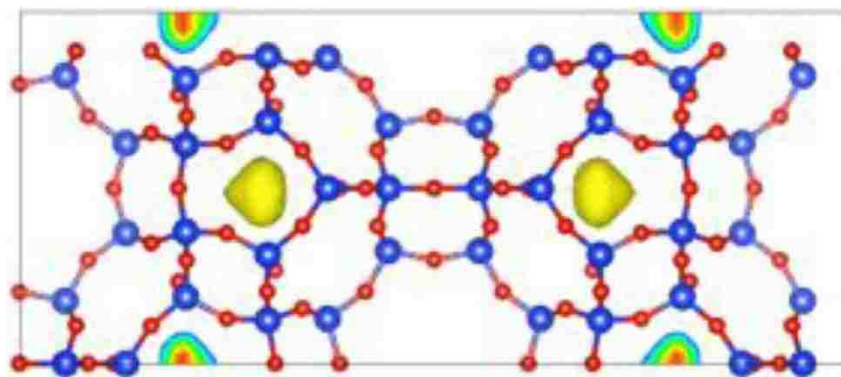
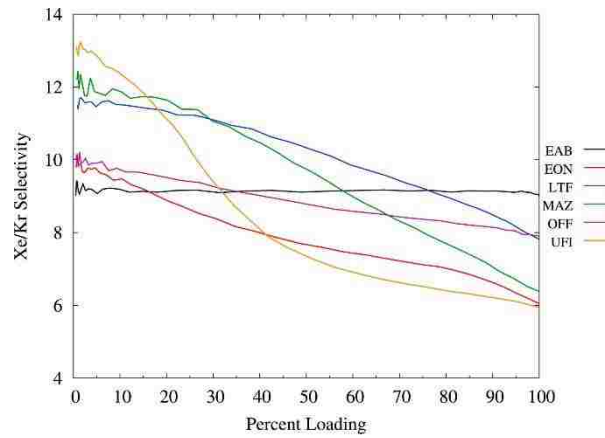
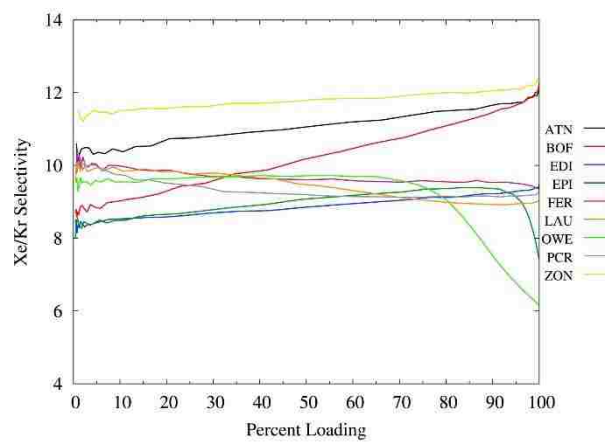


Fig. 2.11 Xe loading density into UFI at 10 mmHg and 298 K.

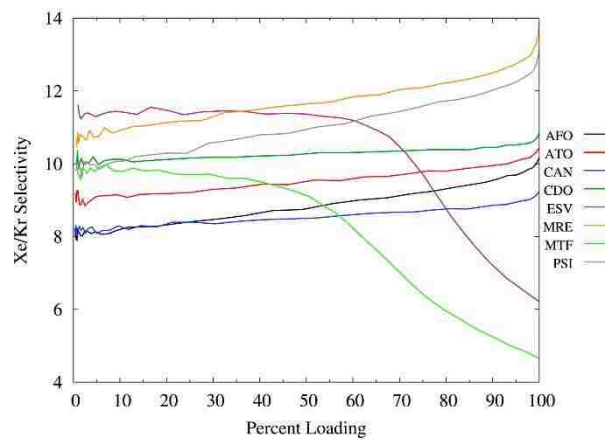
Figure 2.12 shows the results from the more thorough selectivity simulations for each of the top zeolites as a function of percent loading, with 100% defined as the respective loading at 10,000 mmHg. As all of the simulated adsorption data has been corrected to reflect the excess adsorption, a turnover in the isotherm should be expected when the density of the adsorbed fluid very closely matches that of the bulk fluid [76]. By collecting some data points beyond 10,000 mmHg, we have determined that this turnover occurs around 10,000 mmHg in almost all of these zeolites thus indicating the loading at 10,000 mmHg is close to the asymptotic limit. The results have been divided into two sets corresponding to either narrow pores or cavities off larger pores, and for visual clarity the narrow pore materials have been further subdivided based off of their loading at 10,000 mmHg. Note that the noise at low loadings is due to very low total Kr uptake.



(a) Zeolites with small cages



(b) Zeolites with channels and loading $\geq 45 \text{ cm}^3/\text{g}$



(c) Zeolites with channels and loading $\leq 45 \text{ cm}^3/\text{g}$

Figure 2.12 show results from selectivity simulations for each of the top zeolites as a function of percent loading, with 100% defined as the respective loading at 10,000 mmHg.

Each of the materials with a small pocket adsorption mechanism are shown in figure. In these materials, small cages accessible from larger channels result in high initial selectivities as these pockets fill. Once the majority of the pockets have filled, larger fractions of adsorbed gas atoms occupy less selective sites in the larger pores, leading to lower selectivities at higher loadings. For example, the t-ufi cages in UFI are nearly saturated at 10-20% of the total possible loading. Once the t-ufi cages are close to saturated, the majority of the adsorption occurs in the t-grc cages. These t-grc cages are not expected to be as selective based on our screening results for LTA, which only can adsorb into t-grc CBUs and has a selectivity of ~ 4.5 at all loadings. Interestingly enough, UFI had the highest capacity of any of the zeolites closely examined at $88.0 \text{ cm}^3/\text{g}$. An exception to dramatically falling selectivities is EAB where the selectivity remains essentially flat across all selectivities studied. As EAB contains large channels that connect smaller t-gme pockets off the main pores, this behavior came as a surprise. Examining predicted adsorption sites, Xe indeed occupies the t-gme pocket as anticipated, but also occupies two well-defined sites in the larger t-eab cavities of the main pore. This is the only instance we are aware of where a pocket large enough to accommodate two Xe atoms provides comparable selectivities to a pocket which only accommodates one.

The GCMC results presented above represent a significant step towards identifying zeolitic adsorbents for practical separations, although more than was determined above will ultimately be required. Practical adsorbents need to be available economically and show reasonable kinetics. While the selectivities over useful loading ranges are most promising with narrow pore zeolites, these zeolites may also show much lower adsorption/desorption kinetics compared with zeolites containing larger pores and selective pockets. EAB represents a potentially important framework as it has both large channels, which should lead to superior kinetics, and also flat selectivity at all

loadings. Further experimental studies are needed to determine whether these zeolites would be practical in real-world separations.

We are also well-aware that most zeolite frameworks have not been synthesized in purely siliceous forms. To our surprise, a number of zeolites do exhibit selectivities that are competitive with the best MOF adsorbents studied so far. One of the promising structures to emerge from this effort is FER, which is well-known in a pure silica form. Other frameworks (e.g. MRE, UFI) occur in high Si/Al ratios, as germanosilicates (e.g. PCR), or as an AlPO (e.g. ATO, ZON), where performance may be comparable to the pure silica form. The promising germanosilicates and pure AlPO results here should be transferable as they have no mobile cations, the dispersion interactions should be similar (especially if the T-atom approximation is made), and the distribution of framework partial charges will have little effect on the adsorption of noble gases as polarizability only accounted for 1-2% of the total energetics in this study (owing to the cancellation of electric fields caused by neighboring charges). Additionally, H-exchanged versions of these frameworks are likely to offer similar overall performance. Even in cases where compounds resembling the SiO₂ form do not exist, such frameworks remain promising for follow-up studies where mobile cations are present. A final substantial advantage that siliceous zeolites have over aluminosilicates is that they are sufficiently hydrophobic that separations could be run in the presence of humidity without need for periodic reactivation.

The screening results presented here are a first step towards screenings with cations present. For realistic results from such screenings, cation mobility must be included, which represents a considerable challenge on its own. Good agreement between our experimental and simulated data on several SiO₂ structures provides important validation that our model is indeed sufficiently accurate. The screening has also provided important clues as to which frameworks may be promising as cations are included in later simulations. Finally, in order to correlate our

results with the recent study by Smit[59], we compared our predicted performance for air separation ($\text{Xe}/\text{Kr} = 20:80$) to results for the radiochemical separation. The Xe selectivities remained comparable, except in compounds showing high selectivity due to small pockets, where the high loading selectivity greatly improved for the 20:80 ratio. Figures are presented in the SI.

2.8 Conclusions:

An initial screening demonstrated that many siliceous zeolites have promise for a Kr/Xe separation. In the case of EAB, EON, LTF, MAZ, OFF, and UFI, a high initial selectivity results from the presence of a small cage off of the main pore system that is about the right size to adsorb a single Xe atom. However, these small cages quickly saturate with increased gas loading. Zeolites with only small cages are expected to have limited utility as practical PSA sorbents as their selectivity is limited by the adsorption into the small cages. The most promising zeolites for selective Xe adsorption at PSA relevant pressures were ones that contained narrow pore systems with either zig-zags or elliptical cross sections. We suggest the most promising topologies for further study are CDO, MRE, and PSI as they have selectivities greater than 10 at all loadings and high capacities. CDO, FER, MRE, and MTF are of particular interest as these frameworks can be made as pure SiO_2 . AFO, ATO, PSI, and ZON are also of interest as they can be made as pure AlPOs to test the transferability of the pure silica results. It is also important to note that a good parametrization of the force field is essential to using multi-component GCMC as a screening tool. TraPPE-zeo provides an excellent transferable description of fluid-framework interactions. The fluid-fluid interactions need to be correctly modeled to get good isothermal agreement at both low and high loadings, in particular for Kr/Xe a softer repulsion term than that of a 12-6 Lennard-Jones is needed. This problem is not unique to this work, and can be seen in many of the previously published Kr/Xe adsorption isotherms into MOFs and zeolites. In the future, we intend to extend

our findings to some of the more complex zeolitic topologies, i.e. cation containing aluminosilicates, and to include framework flexibility to better describe materials known to distort on adsorption like MFI.

2.9 References

1. Society, E.N. *Fuel Comparison*. 1975; Available from: <https://www.euronuclear.org/info/encyclopedia/f/fuelcomparison.htm>.
2. Energy, D.o. *Fuel Cycle Research and Development*. Available from: <https://energy.gov/ne/fuel-cycle-technologies/fuel-cycle-research-development>.
3. Richards, J., *Nuclear energy and Nuclear power*. 2015.
4. Simpson, M.F. and J.D. Law, *Nuclear Fuel, Reprocessing of*, in *Nuclear Energy: Selected Entries from the Encyclopedia of Sustainability Science and Technology*, N. Tsoulfanidis, Editor. 2013, Springer New York: New York, NY. p. 153-173.
5. R., J. *Spent Fuel Reprocessing*. in *Introduction to Nuclear Chemistry and Fuel Cycle Separation Course* 2008. Consortium for Risk Evaluation With Stakeholder Participation.
6. Soelberg, N.R., et al., *Radioactive Iodine and Krypton Control for Nuclear Fuel Reprocessing Facilities*. Science and Technology of Nuclear Installations, 2013. **2013**: p. 12.
7. Izumi, J., *Waste gas treatment using zeolites in nuclear-related industries*, in *Handbook of Zeolite Science and Technology*, K.C. Scott Auerbach, Prabir Dutta, Editor. 2003: New York.
8. Lawler, K.V., et al., *Assessing zeolite frameworks for noble gas separations through a joint experimental and computational approach*. Microporous and Mesoporous Materials, 2016. **222**(Supplement C): p. 104-112.
9. *Mercury in lighting*. 2007; Available from: <http://www.capecodextension.org/pdfs/MercuryLighting.pdf>.
10. Bogaerts, A., et al., *Gas discharge plasmas and their applications*. Spectrochimica Acta Part B: Atomic Spectroscopy, 2002. **57**(4): p. 609-658.
11. Sanger, D. 2003; [Clandestine nuclear fuel processing]. Available from: http://intellit.muskingum.edu/alpha_folder/S_folder/sanger.html.

12. Tonner, P.H., *Xenon: one small step for anaesthesia... ?* Curr Opin Anaesthesiol, 2006. **19**(4): p. 382-4.
13. Mellor, D., *Sound Persons's guide to video*. 2000: Focal Press.
14. Burke, J., *Twin Tracks: The unexpected origins of the modern world*. 2003: Simon & Schuster
15. Lenntech. *Properties of Krypton and Xenon*. [cited 2018; Available from: <https://www.lenntech.com/periodic/elements/kr.htm>.
16. Waggoner, R.C., *Technical and economic evaluation of processes for krypton-85 recovery from power fuel-reprocessing plant off-gas*. 1982.
17. Koros, W.J., *Evolving beyond the thermal age of separation processes: Membranes can lead the way*. AIChE Journal, 2004. **50**(10): p. 2326-2334.
18. Aprile, E., et al., *Removing krypton from xenon by cryogenic distillation to the ppq level*. The European Physical Journal C, 2017. **77**(5): p. 275.
19. Moore, E.B., *Control Technology for Radioactive Emissions to the Atmosphere at U.S. Department of Energy Facilities*. 1984: Pacific Northwest National Laboratory. p. 632.
20. R.H. Rainey, W.L.C., S. Blumkin, *Completion report: Evaluation of the use of permselective membranes in the nuclear industry for removing radioactive xenon and krypton from various off gas streams* 1971.
21. *International zeolite association-structure commission database of zeolite structures*. Available from: <http://www.iza-structure.org/databases/>.
22. Lawler, K.V., Z. Hulvey, and P.M. Forster, *Nanoporous metal formates for krypton/xenon separation*. Chemical Communications, 2013. **49**(93): p. 10959-10961.
23. Adil, K., et al., *Gas/vapour separation using ultra-microporous metal-organic frameworks: insights into the structure/separation relationship*. Chemical Society Reviews, 2017. **46**(11): p. 3402-3430.

24. Chen, X., *Direct Observation of Xe and Kr Adsorption in a Xe-Selective Microporous Metal–Organic Framework*. Journal of the American Chemical Society, 2015. **137**(22): p. 7007-7010.
25. Banerjee, D., et al., *Metal–organic framework with optimally selective xenon adsorption and separation*. Nature Communications, 2016. **7**: p. ncomms11831.
26. Bae, Y.-S., et al., *High xenon/krypton selectivity in a metal-organic framework with small pores and strong adsorption sites*. Microporous and Mesoporous Materials, 2013. **169**(Supplement C): p. 176-179.
27. Munakata, K., et al., *Adsorption of Noble Gases on Silver-mordenite*. Journal of Nuclear Science and Technology, 2003. **40**(9): p. 695-697.
28. Chen, L., et al., *Separation of rare gases and chiral molecules by selective binding in porous organic cages*. Nature Materials, 2014. **13**: p. 954.
29. Feng, X., et al., *Kr/Xe Separation over a Chabazite Zeolite Membrane*. Journal of the American Chemical Society, 2016. **138**(31): p. 9791-9794.
30. Gupta, A., et al., *Object-oriented Programming Paradigms for Molecular Modeling*. Molecular Simulation, 2003. **29**(1): p. 29-46.
31. Metropolis, N., et al., *Equation of State Calculations by Fast Computing Machines*. The Journal of Chemical Physics, 1953. **21**(6): p. 1087-1092.
32. Coutinho, J.A.P., G.M. Kontogeorgis, and E.H. Stenby, *Binary interaction parameters for nonpolar systems with cubic equations of state: a theoretical approach 1. CO₂/hydrocarbons using SRK equation of state*. Fluid Phase Equilibria, 1994. **102**(1): p. 31-60.
33. Snurr, R.Q., A.T. Bell, and D.N. Theodorou, *Prediction of adsorption of aromatic hydrocarbons in silicalite from grand canonical Monte Carlo simulations with biased insertions*. The Journal of Physical Chemistry, 1993. **97**(51): p. 13742-13752.

34. Cracknell, R.F., P. Gordon, and K.E. Gubbins, *Influence of pore geometry on the design of microporous materials for methane storage*. The Journal of Physical Chemistry, 1993. **97**(2): p. 494-499.
35. Jeffroy, M., et al., *Evidence of a framework induced cation redistribution upon water adsorption in cobalt exchanged X faujasite zeolite: A joint experimental and simulation study*. Microporous and Mesoporous Materials, 2011. **138**(1): p. 45-50.
36. Dolomanov, O.V., et al., *OLEX2: a complete structure solution, refinement and analysis program*. Journal of Applied Crystallography, 2009. **42**(2): p. 339-341.
37. Hohenberg, P. and W. Kohn, *Inhomogeneous Electron Gas*. Physical Review, 1964. **136**(3B): p. B864-B871.
38. Kohn, W. and L.J. Sham, *Self-Consistent Equations Including Exchange and Correlation Effects*. Physical Review, 1965. **140**(4A): p. A1133-A1138.
39. Blöchl, P.E., *Projector augmented-wave method*. Physical Review B, 1994. **50**(24): p. 17953-17979.
40. Perdew, J.P., K. Burke, and M. Ernzerhof, *Generalized Gradient Approximation Made Simple*. Physical Review Letters, 1996. **77**(18): p. 3865-3868.
41. Merlino, S., *The crystal structure of wenkite*. Acta Crystallographica Section B, 1974. **30**(5): p. 1262-1266.
42. Bai, P., M. Tsapatsis, and J.I. Siepmann, *TraPPE-zeo: Transferable Potentials for Phase Equilibria Force Field for All-Silica Zeolites*. The Journal of Physical Chemistry C, 2013. **117**(46): p. 24375-24387.
43. Cygan, R.T., J.-J. Liang, and A.G. Kalinichev, *Molecular Models of Hydroxide, Oxyhydroxide, and Clay Phases and the Development of a General Force Field*. The Journal of Physical Chemistry B, 2004. **108**(4): p. 1255-1266.

44. Talu, O. and A.L. Myers, *Reference potentials for adsorption of helium, argon, methane, and krypton in high-silica zeolites*. Colloids and Surfaces A: Physicochemical and Engineering Aspects, 2001. **187-188**(Supplement C): p. 83-93.
45. Physics, C.H.o.C.a. *CRC Handbook*. 2014-2015 [cited 2018; Available from: <http://www.hbcnetbase.com>].
46. Wolf, D., et al., *Exact method for the simulation of Coulombic systems by spherically truncated, pairwise r^{-1} summation*. The Journal of Chemical Physics, 1999. **110**(17): p. 8254-8282.
47. Zahn, D., B. Schilling, and S.M. Kast, *Enhancement of the Wolf Damped Coulomb Potential: Static, Dynamic, and Dielectric Properties of Liquid Water from Molecular Simulation*. The Journal of Physical Chemistry B, 2002. **106**(41): p. 10725-10732.
48. Yu, H. and W.F. van Gunsteren, *Accounting for polarization in molecular simulation*. Computer Physics Communications, 2005. **172**(2): p. 69-85.
49. Fennell, C.J. and J.D. Gezelter, *Is the Ewald summation still necessary? Pairwise alternatives to the accepted standard for long-range electrostatics*. The Journal of Chemical Physics, 2006. **124**(23): p. 234104.
50. Yang, J., et al., *COMPASS Force Field for 14 Inorganic Molecules, He, Ne, Ar, Kr, Xe, H₂, O₂, N₂, NO, CO, CO₂, NO₂, CS₂, and SO₂, in Liquid Phases*. The Journal of Physical Chemistry B, 2000. **104**(20): p. 4951-4957.
51. Martin, R.L., et al., *Accelerating analysis of void space in porous materials on multicore and GPU platforms*. The International Journal of High Performance Computing Applications, 2012. **26**(4): p. 347-357.
52. Foster, M.D., et al., *A geometric solution to the largest-free-sphere problem in zeolite frameworks*. Microporous and Mesoporous Materials, 2006. **90**(1): p. 32-38.

53. Lawler, K.V., Z. Hulvey, and P.M. Forster, *On the importance of a precise crystal structure for simulating gas adsorption in nanoporous materials*. *Physical Chemistry Chemical Physics*, 2015. **17**(29): p. 18904-18907.
54. Hay, D.G., H. Jaeger, and G.W. West, *Examination of the monoclinic/orthorhombic transition in silicalite using XRD and silicon NMR*. *The Journal of Physical Chemistry*, 1985. **89**(7): p. 1070-1072.
55. García-Pérez, E., et al., *Unraveling the Argon Adsorption Processes in MFI-Type Zeolite*. *The Journal of Physical Chemistry C*, 2008. **112**(27): p. 9976-9979.
56. Banerjee, D., et al., *Potential of Metal–Organic Frameworks for Separation of Xenon and Krypton*. *Accounts of Chemical Research*, 2015. **48**(2): p. 211-219.
57. Karavias, F. and A.L. Myers, *Isosteric heats of multicomponent adsorption: thermodynamics and computer simulations*. *Langmuir*, 1991. **7**(12): p. 3118-3126.
58. Sikora, B.J., et al., *Thermodynamic analysis of Xe/Kr selectivity in over 137 000 hypothetical metal-organic frameworks*. *Chemical Science*, 2012. **3**(7): p. 2217-2223.
59. Simon, C.M., et al., *What Are the Best Materials To Separate a Xenon/Krypton Mixture?* *Chemistry of Materials*, 2015. **27**(12): p. 4459-4475.
60. Hulvey, Z., et al., *Noble Gas Adsorption in Copper Trimesate, HKUST-1: An Experimental and Computational Study*. *The Journal of Physical Chemistry C*, 2013. **117**(39): p. 20116-20126.
61. Myers, A.L. and P.A. Monson, *Adsorption in Porous Materials at High Pressure: Theory and Experiment*. *Langmuir*, 2002. **18**(26): p. 10261-10273.

2.10 Supplementary information:

Table 1 contain the results for a 5 pressure point screening Xe/Kr selectivities for each of the 229 IZA identified siliceous zeolite frameworks. The frameworks are identified by their three-letter code, and the largest T-atom ring size and estimated accessible pore volume are the second and third columns, respectively. The pressure points were picked along a logarithmic scale to span the Henry's law regime to the mostly loaded regime likely encountered in PSA applications (1-10 atm). For each pressure point we report the total loading and the Xe/Kr selectivity. These simulations are done with full binary GCMC as described in the simulation methodology. These simulations include the full set of sorbate-framework dispersion-repulsion, sorbate-sorbate dispersion-repulsion, and sorbate induction from framework partial charges as described in the main text.

Table 1 Simulated Total Quantities Adsorbed (cm³/g) and Xe/Kr selectivities for all 229 IZA siliceous zeolite framework types.

IZA Code	Max Ring Size	% Acc. Pore Vol.	1 mmHg		10 mmHg		100 mmHg		1,000 mmHg		10,000 mmHg	
			N	S _{Xe/Kr}	N	S _{Xe/Kr}	N	S _{Xe/Kr}	N	S _{Xe/Kr}	N	S _{Xe/Kr}
ABW	8	5.095	0.000	0.022	0.002	0.032	0.015	0.028	0.152	0.027	1.426	0.021
ACO	8	8.901	0.004	0.493	0.038	0.481	0.386	0.486	4.082	0.489	76.569	0.593
AEI	8	17.672	0.105	5.837	1.038	5.869	9.042	5.841	42.952	5.227	89.664	4.157
AEL	10	6.956	0.129	7.224	1.265	7.070	10.484	7.498	30.363	8.641	35.909	9.346
AEN	8	4.132	0.000	0.101	0.003	0.111	0.027	0.116	0.265	0.118	2.461	0.110
AET	14	13.215	0.016	4.231	0.163	4.343	1.632	4.275	14.699	4.618	40.885	4.744
AFG	6	0.000	0.000	0.000	0.000	0.000	0.000	0.000	0.000	0.000	0.000	0.000
AFI	12	14.230	0.038	4.880	0.373	5.075	3.556	5.118	21.486	5.136	45.979	4.345
AFN	8	4.010	0.036	5.462	0.349	5.465	2.870	5.350	11.045	4.609	19.484	3.417
AFO	10	7.454	0.142	8.039	1.382	8.085	11.171	8.483	30.615	9.426	35.913	10.167
AFR	12	19.964	0.049	4.412	0.485	4.555	4.843	4.575	38.690	4.681	90.552	3.016
AFS	12	21.985	0.047	4.067	0.471	4.409	4.774	4.461	47.717	4.970	110.408	5.606
AFT	8	17.626	0.097	5.556	0.969	5.720	8.900	5.656	43.268	5.556	72.398	4.111
AFV	8	15.591	0.250	8.249	2.412	8.379	17.663	8.445	43.253	8.269	50.480	6.580
AFX	8	17.645	0.097	5.698	0.946	5.488	8.733	5.520	43.489	5.473	73.137	4.154
AFY	12	22.397	0.047	3.255	0.471	3.235	4.855	3.279	70.300	3.741	166.190	4.321
AHT	10	0.000	0.000	0.000	0.000	0.000	0.000	0.000	0.000	0.000	0.000	0.000
ANA	8	0.000	0.000	0.000	0.000	0.000	0.000	0.000	0.000	0.000	0.000	0.000
APC	8	4.749	0.000	0.118	0.004	0.110	0.042	0.111	0.423	0.112	4.161	0.106
APD	8	5.790	0.109	3.626	1.102	3.666	12.366	3.855	78.722	4.863	91.424	4.902
AST	6	0.000	0.000	0.000	0.000	0.000	0.000	0.000	0.000	0.000	0.000	0.000
ASV	12	7.389	0.217	8.929	2.111	8.968	15.418	9.003	34.572	8.252	43.841	5.419
ATN	8	7.418	0.309	10.594	3.087	10.323	23.830	11.091	43.645	11.733	45.740	12.452
ATO	12	7.248	0.136	9.177	1.314	9.009	9.990	9.295	26.781	9.797	33.510	10.430

Continued on next page

IZA Code	Max Ring Size	% Acc. Pore Vol.	1 mmHg		10 mmHg		100 mmHg		1,000 mmHg		10,000 mmHg	
			N	$S_{Xe/Kr}$	N	$S_{Xe/Kr}$	N	$S_{Xe/Kr}$	N	$S_{Xe/Kr}$	N	$S_{Xe/Kr}$
ATS	12	15.895	0.045	4.584	0.442	5.015	4.385	5.110	32.860	5.595	57.440	6.138
ATF	8	9.390	0.209	7.629	2.097	7.623	20.307	8.027	55.767	8.435	61.107	6.329
ATV	8	3.870	0.033	2.247	0.334	2.211	3.464	2.265	33.604	2.620	58.915	2.797
AVL	8	14.720	0.271	8.964	2.596	8.591	19.254	8.579	48.000	8.312	60.521	7.317
AWO	8	5.342	0.203	6.869	2.077	6.771	22.388	7.459	57.414	8.471	61.271	8.505
AWW	8	12.240	0.274	8.978	2.581	9.185	15.647	9.134	29.936	8.042	40.940	4.720
BCT	8	0.000	0.000	0.000	0.000	0.000	0.000	0.000	0.000	0.000	0.000	0.000
BEA	12	20.902	0.086	5.844	0.862	5.897	8.246	6.038	47.675	6.436	79.945	6.902
BEC	12	21.576	0.088	6.089	0.869	6.014	7.979	6.064	44.490	6.222	75.695	6.695
BIK	8	3.882	0.000	0.101	0.002	0.085	0.022	0.080	0.220	0.079	2.010	0.072
BOF	10	9.389	0.279	8.681	2.809	8.853	25.394	9.876	57.086	11.590	60.931	12.455
BOG	12	18.500	0.068	5.066	0.687	5.182	6.770	5.331	43.941	5.886	74.390	6.026
BOZ	10	22.924	0.046	4.316	0.460	4.177	4.487	4.189	35.298	4.099	115.289	3.950
BPH	12	22.018	0.055	5.024	0.547	4.990	5.413	4.967	40.119	5.185	86.698	4.973
BRE	8	0.000	0.000	0.000	0.000	0.000	0.000	0.000	0.000	0.000	0.000	0.000
BSV	12	7.171	0.090	5.092	0.897	5.220	8.830	5.407	45.701	5.725	59.769	5.750
CAN	12	8.558	0.116	8.233	1.123	8.233	8.940	8.396	26.911	8.729	34.873	9.230
CAS	8	0.000	0.000	0.000	0.000	0.000	0.000	0.000	0.000	0.000	0.000	0.000
CDO	8	8.001	0.279	9.832	2.699	10.087	18.781	10.235	37.618	10.513	40.424	11.127
CFI	14	13.500	0.027	4.486	0.266	4.581	2.576	4.644	17.913	4.719	42.531	4.358
CGF	10	0.000	0.000	0.000	0.000	0.000	0.000	0.000	0.000	0.000	0.000	0.000
CGS	10	10.953	0.160	7.675	1.576	7.760	13.460	7.913	39.458	8.207	45.106	8.263
CHA	8	17.646	0.119	6.292	1.185	6.169	10.668	6.302	45.671	6.203	67.982	4.434
CHI	9	2.546	0.000	0.056	0.000	0.005	0.001	0.005	0.012	0.005	0.111	0.005
CLO	20	34.273	0.099	6.128	0.957	6.038	7.665	5.688	36.088	4.573	135.633	3.766
CON	12	19.564	0.088	5.759	0.877	5.775	8.589	5.888	48.180	6.317	76.051	6.358
CSV	10	18.324	0.078	5.490	0.785	5.552	7.588	5.595	43.910	5.818	77.330	5.311
CZP	12	4.193	0.002	0.326	0.020	0.291	0.199	0.301	1.912	0.296	14.249	0.279
DAC	10	9.741	0.211	6.632	2.098	6.723	20.001	6.921	56.128	6.778	65.793	4.091
DDR	8	9.350	0.149	8.555	1.399	8.467	9.310	8.229	24.385	7.248	36.050	5.777
DFO	12	22.444	0.071	5.730	0.710	5.488	6.728	5.462	43.052	5.483	87.879	5.397
DFT	8	6.461	0.105	3.946	1.064	3.735	12.007	3.965	78.453	4.875	91.351	4.924
DOH	6	0.000	0.000	0.000	0.000	0.000	0.000	0.000	0.000	0.000	0.000	0.000
DON	14	15.840	0.020	4.119	0.202	4.292	2.033	4.240	19.114	4.607	53.631	4.887
EAB	8	14.555	0.319	9.013	3.092	9.071	22.334	9.144	53.293	9.141	60.548	8.994
EDI	8	9.589	0.284	8.487	2.837	8.382	25.724	8.741	66.694	9.229	72.949	9.493
EEI	8	0.000	0.000	0.000	0.000	0.000	0.000	0.000	0.000	0.000	0.000	0.000
EMT	12	27.737	0.021	3.473	0.213	3.571	2.127	3.549	22.064	3.701	102.050	4.524
EON	12	12.634	0.274	10.016	2.499	9.773	14.282	8.526	37.848	7.194	53.042	6.046
EPI	8	9.275	0.280	7.985	2.805	8.416	25.991	8.928	57.652	9.352	63.014	7.412
ERI	8	15.337	0.169	7.467	1.664	7.693	13.891	7.784	43.864	7.819	57.843	7.890
HSV	8	8.581	0.428	11.625	3.904	11.442	19.439	11.385	31.195	9.987	42.578	6.211
ETR	18	15.250	0.011	3.072	0.109	3.278	1.102	3.242	12.441	3.469	52.991	3.944
EUO	10	12.445	0.107	7.125	1.042	7.138	8.405	6.922	31.768	6.582	47.543	5.291
EWI	21	22.528	0.059	4.929	0.590	4.964	5.811	5.018	40.757	5.329	88.501	5.440
EZT	12	13.428	0.142	7.562	1.401	7.715	12.073	7.856	45.246	8.443	58.999	9.282
FAR	6	0.000	0.000	0.000	0.000	0.000	0.000	0.000	0.000	0.000	0.000	0.000
FAU	12	27.768	0.017	3.324	0.175	3.210	1.795	3.255	20.531	3.488	104.744	4.558
FER	10	10.224	0.366	9.792	3.457	9.854	22.152	9.640	47.496	9.537	56.473	9.348
FRA	6	0.000	0.000	0.000	0.000	0.000	0.000	0.000	0.000	0.000	0.000	0.000
GIS	8	9.711	0.047	3.175	0.471	3.315	4.863	3.394	51.162	3.760	88.322	3.940
GIU	6	0.000	0.000	0.000	0.000	0.000	0.000	0.000	0.000	0.000	0.000	0.000

IZA Code	Max Ring Size	% Acc. Pore Vol.	1 mmHg		10 mmHg		100 mmHg		1,000 mmHg		10,000 mmHg	
			N	S _{Xe/Kr}	N	S _{Xe/Kr}	N	S _{Xe/Kr}	N	S _{Xe/Kr}	N	S _{Xe/Kr}
GME	12	17.678	0.069	4.717	0.687	4.643	6.585	4.661	40.498	4.743	78.715	3.969
GON	12	8.314	0.088	7.534	0.855	7.546	7.007	7.547	22.570	7.179	35.949	5.525
GOO	8	4.911	0.012	1.507	0.117	1.605	1.157	1.614	10.253	1.622	36.070	1.597
HEU	10	9.650	0.247	8.214	2.444	8.211	21.013	8.473	55.629	9.088	62.167	8.534
IFO	16	17.528	0.023	4.195	0.235	4.346	2.357	4.309	20.437	4.661	49.323	4.770
IFR	12	15.868	0.130	7.205	1.303	7.021	11.758	7.285	39.418	7.736	50.591	6.745
IFW	10	18.276	0.061	5.595	0.603	5.272	5.858	5.300	40.257	5.627	77.386	6.002
IFY	8	10.898	0.114	6.300	1.133	6.230	10.066	6.551	36.674	6.784	47.992	5.434
IHW	8	9.960	0.144	8.303	1.392	8.144	10.341	8.075	27.539	7.309	37.159	6.061
IMF	10	12.403	0.175	7.944	1.731	7.833	15.202	8.104	49.720	8.750	65.858	8.754
IRN	8	16.341	0.061	5.636	0.609	5.224	5.924	5.306	38.292	5.652	75.331	5.827
IRR	18	38.221	0.026	3.525	0.263	4.074	2.540	3.952	19.836	3.655	119.540	3.566
IRY	16	41.359	0.016	2.601	0.157	2.815	1.572	2.877	16.687	2.935	154.454	3.773
ISV	12	21.700	0.070	5.504	0.701	5.531	6.722	5.592	42.878	5.901	76.677	6.305
IIE	8	16.717	0.101	5.922	1.004	6.017	9.144	5.994	48.677	5.970	86.504	5.485
ITG	12	16.081	0.098	6.728	0.966	6.785	8.528	6.822	36.391	6.674	55.618	5.111
ITH	10	11.883	0.129	7.746	1.265	7.364	10.870	7.472	35.674	6.927	54.262	3.903
ITN	12	17.193	0.102	6.275	1.014	6.189	9.382	6.183	47.101	6.324	76.059	6.193
ITR	10	12.072	0.130	7.299	1.279	7.426	10.888	7.530	35.556	7.014	54.382	3.810
ITT	18	33.466	0.068	5.903	0.667	5.831	5.806	5.770	30.671	4.768	121.711	4.373
ITV	30	38.468	0.019	3.149	0.195	3.249	1.955	3.269	18.912	3.273	121.870	3.415
ITW	8	8.067	0.030	1.748	0.261	1.803	2.401	1.763	18.059	1.683	66.101	1.450
IWR	12	19.717	0.090	6.016	0.900	5.970	8.512	5.971	46.422	6.226	75.183	6.195
IWS	12	23.576	0.054	5.279	0.539	5.027	5.128	5.075	35.424	5.090	80.239	5.157
IWV	12	22.579	0.032	4.003	0.321	4.053	3.256	4.090	33.762	4.495	96.098	5.211
IWW	12	15.572	0.101	6.625	1.004	6.638	9.002	6.694	39.802	6.698	61.555	6.693
JBW	8	4.085	0.001	0.196	0.009	0.197	0.094	0.204	0.919	0.206	7.872	0.195
JNT	8	0.000	0.000	0.000	0.000	0.000	0.000	0.000	0.000	0.000	0.000	0.000
JOZ	8	7.510	0.039	3.510	0.394	3.582	3.919	3.555	32.785	3.718	67.897	3.764
JRY	10	6.976	0.034	1.879	0.340	1.804	3.355	1.831	26.722	1.948	58.532	2.008
JSN	8	8.301	0.279	7.296	2.695	7.265	20.125	7.388	44.432	6.749	63.705	4.124
JSR	11	28.881	0.043	3.740	0.431	3.890	4.356	3.879	45.794	4.150	162.393	4.971
JST	10	15.312	0.044	3.615	0.444	3.665	4.331	3.624	32.992	3.481	81.668	2.707
JSW	8	0.000	0.000	0.000	0.000	0.000	0.000	0.000	0.000	0.000	0.000	0.000
KFI	8	18.143	0.082	5.281	0.803	5.441	7.187	5.419	37.901	5.197	71.469	4.390
LAU	10	9.972	0.276	9.561	2.649	9.921	17.589	9.794	44.540	9.043	58.782	9.043
LEV	8	14.595	0.275	8.718	2.634	8.761	18.008	8.739	38.134	8.081	48.557	5.130
LIO	6	0.000	0.000	0.000	0.000	0.000	0.000	0.000	0.000	0.000	0.000	0.000
LIT	8	0.000	0.000	0.000	0.000	0.000	0.000	0.000	0.000	0.000	0.000	0.000
LOS	6	0.000	0.000	0.000	0.000	0.000	0.000	0.000	0.000	0.000	0.000	0.000
LOV	9	7.770	0.068	3.968	0.668	3.934	6.090	3.855	28.603	3.371	45.426	1.455
LTA	8	21.677	0.042	4.420	0.421	4.261	4.242	4.309	37.480	4.675	86.514	4.841
LTF	12	11.335	0.334	11.499	3.022	11.629	15.557	10.852	31.762	9.072	40.705	7.814
LTJ	8	3.466	0.000	0.096	0.002	0.094	0.024	0.094	0.238	0.093	2.297	0.087
LTL	12	15.531	0.036	4.900	0.359	4.707	3.564	4.791	28.748	5.257	57.207	5.707
LTN	8	0.000	0.000	0.000	0.000	0.000	0.000	0.000	0.000	0.000	0.000	0.000
MAR	6	0.000	0.000	0.000	0.000	0.000	0.000	0.000	0.000	0.000	0.000	0.000
MAZ	12	12.874	0.355	12.212	3.162	11.770	15.336	10.911	31.791	8.359	45.909	6.381
MEI	12	21.463	0.066	4.939	0.662	5.088	6.702	5.030	53.604	5.674	88.740	6.049
MEL	10	12.943	0.158	7.702	1.566	7.548	14.211	7.857	47.446	8.532	62.563	8.702
MEP	6	0.000	0.000	0.000	0.000	0.000	0.000	0.000	0.000	0.000	0.000	0.000
MER	8	10.581	0.080	4.488	0.793	4.633	7.670	4.668	35.451	4.568	48.120	3.223

LZA Code	Max Ring Size	% Acc. Pore Vol.	1 mmHg		10 mmHg		100 mmHg		1,000 mmHg		10,000 mmHg	
			N	$S_{Xe/Kr}$	N	$S_{Xe/Kr}$	N	$S_{Xe/Kr}$	N	$S_{Xe/Kr}$	N	$S_{Xe/Kr}$
MFI	10	10.163	0.119	5.745	1.179	5.885	10.771	5.969	42.664	6.106	59.783	6.020
MFS	10	11.133	0.122	7.278	1.195	7.563	10.462	7.850	35.104	8.067	49.655	6.235
MON	8	5.970	0.000	0.079	0.003	0.076	0.026	0.077	0.256	0.076	2.428	0.070
MOR	12	12.430	0.163	6.053	1.611	6.447	13.976	6.495	48.725	6.662	66.308	6.016
MOZ	12	13.330	0.131	7.879	1.258	7.820	9.423	7.580	34.387	7.034	50.901	6.896
MRE	10	6.656	0.210	10.455	2.018	10.991	13.056	11.565	26.461	12.440	29.951	13.890
MSE	12	16.717	0.098	6.495	0.972	6.553	8.966	6.599	40.604	6.878	63.295	6.968
MSO	6	0.000	0.000	0.000	0.000	0.000	0.000	0.000	0.000	0.000	0.000	0.000
MTF	8	6.803	0.212	9.886	1.944	9.977	10.237	9.598	18.595	7.414	27.807	4.658
MTN	6	0.000	0.000	0.000	0.000	0.000	0.000	0.000	0.000	0.000	0.000	0.000
MTT	10	8.084	0.106	7.743	1.053	7.721	8.926	7.894	26.527	8.422	32.626	7.839
MTW	12	9.649	0.070	6.480	0.693	6.674	6.035	6.546	23.585	6.189	40.932	4.391
MVY	10	0.000	0.000	0.000	0.000	0.000	0.000	0.000	0.000	0.000	0.000	0.000
MWW	10	17.726	0.160	7.090	1.566	7.085	12.375	6.854	45.691	5.730	78.443	5.505
NAB	9	7.443	0.000	0.038	0.001	0.060	0.010	0.065	0.103	0.064	0.988	0.061
NAT	9	9.227	0.012	1.025	0.121	0.999	1.208	1.008	12.012	1.027	69.552	1.097
NES	10	15.150	0.079	5.811	0.785	6.009	7.382	5.994	35.932	6.285	56.985	5.565
NON	6	0.000	0.000	0.000	0.000	0.000	0.000	0.000	0.000	0.000	0.000	0.000
NPO	12	2.971	0.000	0.006	0.000	0.016	0.003	0.013	0.030	0.014	0.301	0.013
NPT	8	19.655	0.082	5.812	0.809	5.975	7.590	5.940	42.933	5.541	84.229	4.968
NSI	8	3.340	0.000	0.019	0.001	0.022	0.006	0.025	0.058	0.024	0.560	0.023
OBW	10	23.339	0.072	6.004	0.712	5.685	6.724	5.521	43.522	4.982	116.535	4.735
OFF	12	15.323	0.295	9.784	2.764	9.907	17.422	9.214	43.779	8.319	55.422	7.904
OKO	12	14.671	0.119	7.375	1.172	7.124	10.040	7.194	40.285	7.285	61.359	7.431
OSI	12	9.735	0.047	6.469	0.461	6.011	4.154	6.062	18.562	6.070	31.493	4.512
OSO	14	20.626	0.047	4.229	0.465	4.218	4.541	4.250	34.396	4.239	101.852	3.454
OWE	8	10.617	0.341	9.526	3.293	9.545	22.440	9.721	44.038	9.175	56.008	6.158
PAR	10	3.939	0.000	0.071	0.001	0.082	0.011	0.079	0.109	0.080	0.993	0.069
PAU	8	12.715	0.090	5.005	0.890	4.889	7.882	4.661	38.583	3.429	78.954	1.593
PCR	12	7.064	0.311	9.880	2.856	9.879	17.993	9.263	41.698	9.159	48.146	9.296
PHI	8	10.216	0.104	5.660	1.018	5.838	9.045	5.728	36.079	4.203	55.932	1.351
PON	10	7.332	0.070	4.137	0.696	4.106	7.060	4.299	43.963	5.217	59.643	5.561
POS	12	20.224	0.106	6.449	1.046	6.552	9.188	6.427	45.698	6.347	75.949	6.630
PSI	10	3.976	0.116	9.812	1.130	9.849	8.049	10.798	17.738	11.952	20.058	13.121
PUN	12	15.644	0.085	4.988	0.856	4.982	8.761	5.187	58.397	5.942	79.080	6.276
RHO	8	21.009	0.063	3.233	0.625	3.154	6.430	3.226	62.372	3.661	122.880	4.115
RON	12	7.671	0.082	6.456	0.816	6.456	7.487	6.678	35.341	7.097	48.738	7.232
RRO	10	7.253	0.001	0.325	0.015	0.374	0.150	0.381	1.481	0.377	12.273	0.359
RSN	9	7.244	0.035	3.566	0.345	3.470	3.143	3.411	14.917	2.697	28.107	1.006
RTE	8	11.940	0.252	8.969	2.387	8.821	15.118	8.731	31.421	7.439	46.914	4.893
RTH	8	16.283	0.108	6.526	1.062	6.026	9.061	5.960	39.586	5.396	77.872	4.438
RUT	6	0.000	0.000	0.000	0.000	0.000	0.000	0.000	0.000	0.000	0.000	0.000
RWR	8	4.415	0.003	0.506	0.034	0.484	0.345	0.486	3.529	0.493	35.489	0.524
RWY	12	46.153	0.016	2.723	0.161	2.631	1.626	2.576	17.391	2.623	194.990	3.318
SAF	12	10.038	0.048	6.222	0.473	6.338	4.453	6.390	23.643	6.934	39.633	7.566
SAO	12	26.148	0.046	4.594	0.459	4.418	4.583	4.480	38.879	4.809	89.498	5.049
SAS	8	18.358	0.082	5.551	0.812	5.448	7.454	5.543	38.658	5.336	72.819	4.632
SAT	8	13.246	0.184	8.547	1.805	8.178	14.427	8.440	40.323	8.634	51.536	8.328
SAV	8	18.205	0.078	5.173	0.767	5.279	7.063	5.244	38.846	5.041	83.553	4.241
SBE	12	26.689	0.068	6.390	0.664	5.879	5.467	5.405	28.964	4.055	103.694	3.968
SBN	8	9.188	0.065	3.163	0.669	3.161	7.472	3.259	125.277	5.000	146.551	5.235
SBS	12	27.598	0.027	3.665	0.271	3.792	2.710	3.794	27.412	3.936	100.283	4.644

IZA Code	Max Ring Size	% Acc. Pore Vol.	1 mmHg		10 mmHg		100 mmHg		1,000 mmHg		10,000 mmHg	
			N	$S_{Xe/Kr}$	N	$S_{Xe/Kr}$	N	$S_{Xe/Kr}$	N	$S_{Xe/Kr}$	N	$S_{Xe/Kr}$
SBT	12	27.599	0.027	4.050	0.269	3.788	2.678	3.796	26.676	3.908	101.986	4.547
SEW	12	15.438	0.125	7.001	1.246	6.845	12.165	7.044	51.911	7.575	73.498	7.200
SFE	12	13.478	0.043	5.194	0.422	5.075	4.083	5.189	27.817	5.502	50.824	5.450
SFF	10	14.332	0.113	6.844	1.105	6.942	9.059	6.791	33.549	6.202	67.485	5.190
SFG	10	11.361	0.092	7.008	0.918	6.952	8.276	7.060	33.340	7.269	49.525	7.204
SFH	14	16.053	0.024	4.506	0.243	4.384	2.430	4.325	20.845	4.649	49.119	4.600
SFN	14	15.969	0.024	4.739	0.245	4.200	2.451	4.320	20.836	4.604	51.791	4.486
SFO	12	19.928	0.050	4.697	0.497	4.649	4.920	4.688	36.124	4.684	87.391	3.237
SFS	12	16.307	0.102	6.447	1.010	6.200	9.331	6.304	47.347	6.730	75.831	6.936
SFV	12	12.657	0.156	7.286	1.548	7.409	13.985	7.690	47.336	8.304	63.041	8.372
SFW	8	17.552	0.082	5.206	0.803	5.139	7.524	5.175	41.300	5.045	75.735	3.985
SGT	6	0.000	0.000	0.000	0.000	0.000	0.000	0.000	0.000	0.000	0.000	0.000
SIV	8	10.039	0.075	4.693	0.742	4.661	7.084	4.500	44.701	3.868	74.317	2.138
SOD	6	0.000	0.000	0.000	0.000	0.000	0.000	0.000	0.000	0.000	0.000	0.000
SOF	12	13.111	0.052	2.910	0.528	2.827	5.361	2.913	45.457	3.190	84.894	3.082
SOS	12	10.067	0.011	2.637	0.108	2.495	1.055	2.470	8.937	2.465	30.006	2.209
SSF	12	15.895	0.041	4.843	0.403	5.100	4.043	5.219	31.018	5.851	57.188	6.527
SSO	18	13.477	0.057	5.526	0.573	5.761	5.453	5.703	29.409	5.694	53.726	4.588
SSY	12	13.588	0.038	4.894	0.382	5.006	3.706	5.079	24.610	5.240	49.381	5.158
STF	10	15.677	0.104	6.380	1.031	6.215	9.159	6.192	43.503	6.020	81.862	5.382
STI	10	13.621	0.184	7.501	1.809	7.640	15.014	7.854	45.830	7.918	61.656	7.861
STO	12	10.156	0.063	6.585	0.620	6.607	5.626	6.779	25.565	6.948	42.975	6.965
STT	9	14.226	0.148	7.389	1.446	7.112	11.903	7.177	41.264	6.722	63.032	5.226
STW	10	14.364	0.166	5.677	1.661	5.615	16.574	5.810	70.263	6.250	97.793	5.691
SVR	10	11.072	0.161	7.525	1.601	7.291	14.079	7.598	45.398	7.987	60.864	7.744
SVV	6	0.000	0.000	0.000	0.000	0.000	0.000	0.000	0.000	0.000	0.000	0.000
SZR	10	9.440	0.106	6.897	1.027	7.290	7.948	7.267	27.303	6.274	54.828	5.715
TER	10	13.060	0.142	6.678	1.420	6.528	13.307	6.712	53.565	7.239	72.679	7.440
THO	8	10.144	0.116	5.134	1.158	5.114	11.318	5.182	56.116	5.512	71.929	5.369
TOL	6	0.000	0.000	0.000	0.000	0.000	0.000	0.000	0.000	0.000	0.000	0.000
TON	10	8.142	0.122	7.255	1.190	7.514	9.909	7.664	33.164	7.504	53.262	6.481
TSC	8	28.124	0.019	3.930	0.187	3.326	1.881	3.389	18.012	3.421	91.884	3.261
TUN	10	13.249	0.155	7.480	1.528	7.501	13.183	7.646	46.581	7.973	64.432	7.697
UEI	8	6.596	0.111	5.646	1.124	5.597	11.583	5.710	51.635	6.083	60.562	6.058
UFI	8	19.975	0.583	13.123	4.962	12.774	20.903	10.545	53.867	6.869	88.012	5.945
UOS	10	9.240	0.115	6.433	1.127	6.525	9.704	6.322	39.966	5.561	59.824	4.457
UOV	12	17.459	0.101	6.272	0.999	6.454	9.414	6.573	44.929	7.013	67.684	7.026
UOZ	6	0.000	0.000	0.000	0.000	0.000	0.000	0.000	0.000	0.000	0.000	0.000
USI	12	18.008	0.062	4.818	0.617	4.745	6.115	4.844	43.659	5.114	80.404	5.373
UTL	14	22.246	0.052	5.596	0.518	5.313	4.970	5.241	35.724	5.222	82.342	5.490
UWY	12	16.495	0.127	6.350	1.256	6.306	11.278	6.311	50.779	6.590	80.801	6.887
VET	12	8.086	0.064	7.941	0.628	7.698	5.253	7.782	17.559	8.152	23.357	8.359
VFI	18	25.745	0.008	2.695	0.080	2.682	0.809	2.811	8.925	2.894	82.545	3.914
VNI	8	4.663	0.012	1.996	0.123	2.260	1.217	2.258	10.107	2.241	35.544	2.060
VSV	9	6.645	0.001	0.290	0.008	0.294	0.077	0.295	0.755	0.294	6.504	0.271
WEI	10	8.379	0.000	0.071	0.002	0.060	0.021	0.057	0.204	0.056	1.924	0.048
WEN	10	0.000	0.000	0.000	0.000	0.000	0.000	0.000	0.000	0.000	0.000	0.000
YUG	8	5.703	0.007	0.909	0.069	0.944	0.679	0.933	6.334	0.934	30.503	0.904
ZON	8	8.283	0.492	11.541	4.682	11.509	27.271	11.841	43.911	12.087	45.711	12.977

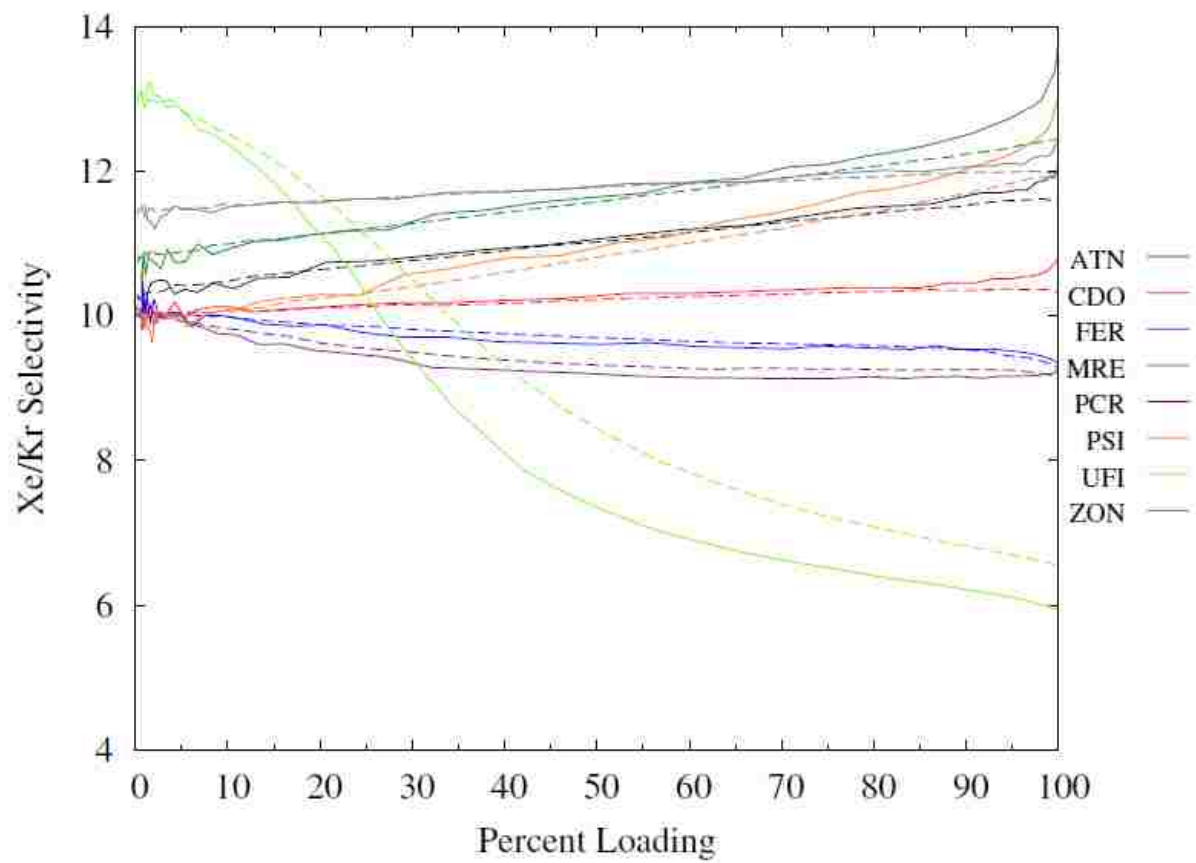


Fig. 1 A comparison of selectivity vs. Percent Loading of a 90:10 Xe:Kr mixture (solid) and an 80:20 Kr:Xe mixture (dashed) into some of the top zeolites.

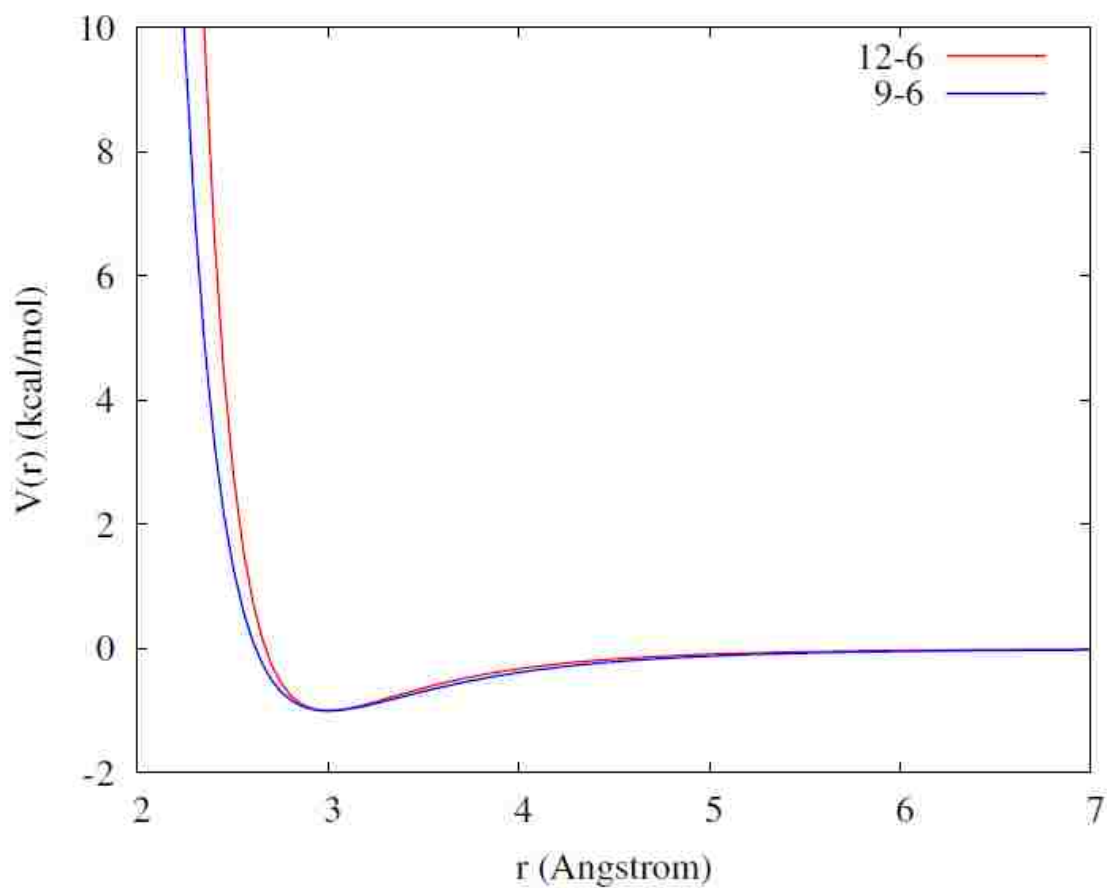


Fig. 2 A comparison of an equivalently parameterized ($R_0=3.0\text{\AA}$, $\epsilon=1$ kcal/mol) 12-6 Lennard-Jones potential (red) and 9-6 Lennard-Jones potential (blue). This illustrates the softer repulsion of the 9-6 potential compared to the 12-6 potential, which we believe is better for describing noble gas-noble gas interactions at high loadings.

Note:

The work compiled in this chapter is a joint effort by our group where all the GCMC simulations were performed by Dr. Keith V Lawler. Jarod J Wolffis helped in explaining the GCMC calculations to Amit Sharma. Breetha Algappan helped in measuring gas adsorption isotherms for few zeolites before graduating and Amit took over this project in Fall 2013 and since then he measured all the gas adsorption isotherms required for completing this study. Amit also participated in the synthesis of zeolites under the joint supervision of Dr. Keith V Lawler and Dr. Laszlo Nemeth. He also helped in gathering the initial data for all the 229 zeolites from IZA database which was needed for the GCMC calculations.

Chapter 3 - Hydrogen uptake on coordinatively unsaturated metal sites in VSB-5: Strong binding affinity leading to high temperature D₂/H₂ selectivity

Index:

- 3.1 Abstract
- 3.2 Motivation
 - 3.2.1 Importance of hydrogen and its isotopes
 - 3.2.2 Properties of hydrogen and its isotopes
 - 3.2.3 Present technology to separate D₂/H₂ and the problems associated
 - 3.2.3.1 Cryogenic distillation
 - 3.2.3.2 Non-cryogenic methods
- 3.3 The solution
 - 3.3.1 Pressure Swing Adsorption
 - 3.3.2 Quantum Sieving
- 3.4 Gas separation techniques and previous work
- 3.5 VSB-5 and structure and applications
- 3.6 Earlier work on VSB-5 and hydrogen interaction
- 3.7 Materials and Methods
 - 3.7.1 Synthesis
 - 3.7.2 Adsorption simulation
- 3.8 Results and discussion
 - 3.8.1 Need of activation
 - 3.8.2 Need of colder adsorption isotherms
 - 3.8.3 Heat of adsorption
- 3.9 Conclusions
- 3.10 References

3.1 Abstract

We examine the adsorption of hydrogen and deuterium into the nanoporous nickel phosphate, VSB-5. On the basis of gas sorption analysis, VSB-5 exhibits one of the highest measured H₂ heats of adsorption (HOA) for hydrogen (16 kJ/mol) yet reported. This high HOA is consistent with an unusually large red shift in the Q(1) and Q(0) hydrogen vibrational modes as measured with in situ infrared spectroscopy. The HOA for D₂ is measured to be 2 kJ/mol higher than that for H₂. “Ideal adsorbed solution theory” analysis of H₂ and D₂ isotherms provides selectivities above 4 for deuterium at 140 K, suggesting that VSB-5 is a promising adsorbent for pressure-swing adsorption-type separations of hydrogen isotopes.

3.2 Motivation

3.2.1 Importance of hydrogen and its isotopes

Importance of hydrogen and its isotopes is realized the most when we consider transitioning into the “zero-emission” era of fuels for automobiles. Hydrogen is one of the cleanest, efficient, reliable, and renewable source of energy. Due to its highest energy content by weight (or in other words, highest combustion energy per round), which is approximately three times higher than the conventional fuels, it could conceivably replace conventional fuel if technological and economic hurdles are overcome by improved technologies. Besides being used as rocket fuel, hydrogen is used in petroleum industry for refining purposes, in chemical industry for synthesis of numerous compounds, and also in food processing.[1-3] Hydrogen as a gas does not occur naturally on Earth and is synthesized artificially. [4-6]

Deuterium is the naturally occurring isotope and is used in various fields. One of its main usage is in nuclear magnetic resonance studies where it is used for accurate analysis of spectra due to the difference in nuclear spin with hydrogen.[7, 8] Neutron scattering studies often use deuterated materials for the similar purposes owing to difference in the neutron scattering cross section area. It is also used in the field of biochemistry and environmental sciences as a stable non-radioactive tracer to study the mechanisms of various reactions.[9] In the field of pharmaceuticals, deuterium is used often to increase the drug's shelf life and drug's half-life in the blood stream. [10]

Tritium is not only an important radionuclide to capture in treatment of fission gas, but serves as a valuable isotope worth roughly ~ \$30,000/g. Its decay product, ^3He also has numerous critical functions, especially in neutron production. At the International Thermonuclear Experimental Reactor (ITER), fusion reaction between deuterium and tritium is planned to carry out to liberate enormous amounts of energy (500 MW) to be used as a sustainable source. Improved tritium capture technologies may indirectly lead to a more stable supply of this critical isotope.

3.2.2 Properties of hydrogen and its isotopes

Hydrogen, the first element of the periodic table is one of most abundant element in the universe. Its overall natural isotopic abundance of 99.985% for ^1H leaves a relatively small fraction for the other stable isotope, ^2H . [11] Its molar mass 1.0078 g/mol makes it the lightest element known. It has one electron in the shell orbiting around the one proton in the nucleus giving the simplest electronic configuration as $1s^1$. At standard temperature and pressure, hydrogen exists as a colorless, odorless, and highly combustible gas. As gas, its atmospheric concentration is ~1 ppm

and is synthesized artificially by electrolysis of water and primarily steam reforming. [12] Hydrogen molecules exist in two forms depending on the nuclear spin – ortho and para. In ortho hydrogen, the nuclear spins in both atoms are aligned parallel (same direction) and are anti-parallel (opposite direction) in para-hydrogen. The chemical properties of both the forms are same but the physical and thermodynamic properties depend on the spin orientation. At room temperature, the two forms exist in an equilibrium ratio 3:1 (ortho:para) and the equilibrium shifts to para-hydrogen at very low temperatures. The change in spin can also be caused by presence of a strong magnetic moment. A more detailed course on ortho- and para-hydrogen is provided in chapter 3.

Among the three isotopes, deuterium is 0.0015% abundant and was discovered in 1931 by Harold Urey. Unlike hydrogen, it has one proton and one neutron in nucleus being orbited by one electron in the shell. Deuterium can replace hydrogen in compounds such as water, yielding slightly different physical properties. For instance, heavy water (D_2O) is heavy as it is ~10% denser than normal water. [12]

Tritium is the radioactive isotope of hydrogen with one proton and two neutrons giving a molar mass of 3.01604 g/mol. Tritium doesn't occur naturally in significant quantities on Earth, but trace amounts may be found in upper layers of atmosphere due to collisions with cosmic rays. 3H (or 3T) was first prepared by Rutherford in 1934 by bombarding energetic deuterons on deuterated acid. At ambient conditions, tritium exists as gas and reacts with oxygen to give highly radioactive tritiated water. [12-14]

3.2.3 Present technology to separate hydrogen and isotopes

3.2.3.1 Cryogenic distillation

Cryogenic distillation to separate hydrogen isotopes was first discussed by J.R. Bartlit and coworkers at Los Alamos National Laboratory in United States for fusion reactors. Based on the principle of distillation, where the components are separated on the basis of their boiling points, their design had four interlinked fractional distillation columns working at cryogenic temperatures. The system was capable of separating a mixture of isotopes into different high purity streams of H₂, D₂, T₂, HD, and HT. [15] Since then the method is being improvised to increase the efficiency and reduce the cost by several research groups. For instance, Enoeda *et al* prepared a distillation system with a column, gas chromatographs, and He refrigerator which could be used in three different modes. Yamanishi and coworkers worked on the simulations of Enoeda within multiple distillation columns and modified the system by introducing a feedback stream. These distillation assemblies with few modifications are still used heavily because of high separation factor, large flow rate, and purity of isotopes.[16] Despite several studies, the high energy input requirements to maintain the temperature can't be ignored and the startup/shutdown procedures are quite critical in these large-scale set-ups.

3.2.3.2 Non-cryogenic methods

A difference in the affinity for different hydrogen isotopes towards the surface of an adsorbent may be used to separate hydrogen isotope as well. Since the isotopes of hydrogen differ in mass, they travel at different speeds through the material. Choice of the active materials relies on the interaction with hydrogen such as hydride forming ability. Palladium is extensively used

due to its isotopic effect and to capture large amounts of hydrogen. Due to the cost associated with the noble metal, researchers are looking into alternative materials.[17]

Electrolysis can be another way to separate the isotopes and it is based on production of hydrogen and deuterium atoms on the electrode followed by the exchange of atoms between solution and electrode. Finally, the separated atoms are used to produce molecular gas and stored. [18]

3.3 The solution

3.3.1 Pressure swing adsorption for separating isotopes:

A general introduction on PSA and its principles on separating gas mixture is provided in chapter 1 (Section 3). The main emphasis here is on separation of lighter gas molecules such as H₂, D₂, T₂, and He by PSA.

While most isotopic separations currently rely on differences in boiling point, diffusivity, or mass, there has been growing interest in developing adsorption-based technologies for isotope recovery, especially for molecular hydrogen/deuterium. Adsorption-based separations would utilize Pressure-Swing Adsorption (PSA) or similar separations such as vacuum- or temperature-swing adsorption.[19] PSA processes work through a series of beds, each containing a sorbent selective for the gas to be selected. Different beds do not necessarily need to have the same sorbent, and recent experiments have shown great success using two-bed separations with different sorbents in each bed.[20] In PSA, one bed is pressurized with the mixture gas so that material may separate it; the purified off-gas is collected and stored or passed through another bed for further separation. The original bed is depressurized to collect the gas trapped by the material, and that gas is either collected or passed on to subsequent beds for further purification. The materials separate the gas mixture by either sieving, selectively adsorbing one of the gas components to the

surface of the material, or a combination of the two. There are several issues to be addressed to develop a practical separation process. Firstly, deuterium is currently recovered from the electrolysis of D₂O, not as deuterium gas. However, since hydrogen gas is produced in large quantities by the petroleum industry through steam reforming and similar processes, it is not difficult to imagine adding a step to an existing hydrogen production facility where some of the deuterium is recovered as a valuable co-product via a relatively low cost means of gas phase isotope separation. We also recognize that deuterium would be present initially as HD molecules, not D₂. A realistic process would require enrichment of HD, an isotope-exchange process (such as occurs over a Pd catalyst), and subsequent enrichment of D₂. While developing a practical process is beyond the scope of this project, the first step towards such a process is the identification of deuterium-selective adsorbents capable of driving it efficiently.

Practical adsorbents require good adsorption behavior for three key parameters: adsorption equilibria, kinetics, and heats of adsorption.[21] Materials with favorable adsorption equilibria for separation have high selectivities for one of the mixture gases to be separated. Sufficiently fast adsorption and desorption kinetics are required for a process to be practical (large kinetic differences between gases can also be used as a basis for separations). Finally, heats of adsorption need to be appropriate to minimize energy consumption during desorption cycles. Other parameters that must be considered include the capacity of a sorbent and cost.

The well-known and commercially important PSA process to separate atmospheric O₂ from N₂ illustrates the principles behind adsorbent selection.[22] N₂ and O₂ are similar in many respects including their kinetic diameters (3.64 vs. 3.8 Å), boiling points (77 vs. 87 K), polarizability (1.74 vs. 1.58 Å³), and molecular weights (28 vs. 32 amu).[19] Nevertheless, sorbents with high local electric fields, as provided by Li⁺ and Ca²⁺, effectively separate these gases based on their differing

quadrupole moments. Similar gases that differ in strength or order of their highest multipole moment can be separated by adsorbents with local electric fields. Temperature swing sorption is now the preferred technique for O₂/N₂ separations at small to medium scales (≈250 tons O₂/day or less).[23]

3.3.2 Quantum Sieving

Given the light mass of hydrogen isotopes, the adsorption often exhibits strong quantum effects compared to heavy adsorbing gases such as methane, N₂, Kr, etc. Much of the total current work on adsorbents is relevant to hydrogen/deuterium separations and utilizes an effect known as quantum sieving.[24] This effect, first noted in 1995 by Beenakker *et al.*,[25] only becomes significant when gas particles are confined and temperatures and masses are sufficiently low that adsorption may no longer be treated classically. As the pore diameter, d , approaches the size of the hard core of the adsorbent, σ , the transverse motion of the adsorbent is sufficiently restricted, and quantization becomes important. Specifically, as the difference, $d-\sigma$, approaches the order of the de Broglie wavelength ($\lambda=h/p$) of the adsorbent, its wave-like behavior becomes far more pronounced and the classical treatment will break down. Therefore, quantum effects become most pronounced when pore (or pocket) diameters are comparable to the size of the gas particles, gas particles are of low mass, and adsorption temperatures are low. The wavelength of particles is determined as the thermal de Broglie wavelength: $\lambda=h/(2\pi mkT)^{1/2}$. [26] The inverse mass-dependence leads to large differences between hydrogen and deuterium, and may serve as a basis to separate the gases. This effect is smaller for heavier isotopes, but still important to properly model isotope-dependent processes.

One way to include quantum effects is through the use of path integral GCMC (PI-GCMC).[27] The path integral formalism follows the ideas of Feynman that connect a quantum system to a system of classical ring polymers. Most of the theoretical studies on hydrogen isotope adsorption/separation into SWCNTs employed the PI-GCMC approach. Garboglio studied quantum sieving in organic frameworks using PI-GCMC,[28] and showed a trend that the D_2/H_2 selectivity was about half that of T_2/H_2 for all temperatures studied. Also, quantum sieving occurs not only in SWCNTs, but also in slit pores and organic frameworks. The selectivity in frameworks showed a nearly exponential decay with increasing temperature, with the selectivities being less than 2 at 40 K, nearly 1 at 90 K, and 1 at 200 K. The selectivities in the organic frameworks depended less on system pressure than the results for SWCNTs of Challa *et al.*, and the selectivities for SWCNTs were orders of magnitude (tens to hundreds) less than the previously published work.[29, 30]

The use of PI-GCMC is very tedious and slow, but Feynman and Hibbs, using the same path integral formulation, found a correction for quantum effects using classical potentials, which allows a significant reduction in computation time.[31] By approximating the quantum mechanical particle as a Gaussian wave packet of width $w=\beta\hbar^2$, the Feynman-Hibbs potential can be expressed as $V_{FH}(r)=(6\mu/\pi w)^{3/2} \int du V(r+u)\exp(-6\mu^2/w)$, where μ is the reduced mass. This form is clearly not useful for efficient GCMC implementations, but if only quadratic terms in u are kept, one arrives at the form $V_{FH}(r)=V(r) + (w/24\mu) \nabla^2 V(r)$. [30] This is the most common form used in molecular simulation of quantum sieving. Typically, a Lennard-Jones potential is used in this formulation, but it can be replaced with any radial potential. The Feynman-Hibbs correction has been taken out to the higher quartic order in the integration variable u , which adds an extra term to the quadratic form that involves even higher derivatives. Kumar and Bhatia showed that the quartic potential

significantly reduces the percent error of the approximation in a practical application and that the percent error increases with decreasing temperature.[32] Kaneko *et al* demonstrated that a Feynman-Hibbs-corrected potential produces results comparable to those of a full PI-GCMC approach for quantum sieving. It should be noted that the Feynman-Hibbs-corrected potential is only as good as the underlying potential it is correcting, i.e., a poorly-described system will still be poorly-described even with the corrected potential. Fu and Sun demonstrated that when their derived force field was corrected with a quartic Feynman-Hibbs correction, the simulated adsorption results agreed much better with experiment.[33]

Another way to look at the de Broglie wavelength is to consider it as ‘quantum mechanical swelling.’ Kumar *et al* studied hydrogen adsorption into the zeolite with international zeolite association (IZA) code RHO with a standard Lennard-Jones potential and a quantum corrected formulation;[32] they showed that the original Lennard-Jones potential had a deeper well than the corrected potential. The change in the potential indicated an increase in the effective size of the potential parameters for hydrogen, dubbed ‘quantum mechanical swelling.’ This swelling is best understood as a delocalization of the electron cloud for the light gas for which an identical expression as the thermal wavelength can be derived from the Heisenberg uncertainty principle.[34, 35] Both delocalization and quantum mechanical swelling describe the same phenomenon, and can be used to show why heavier isotopes diffuse faster. Liu *et al* put the same concept to further use by creating the new idea of a ‘quantum effective pore size.’[36] The quantum mechanical swelling of the potential parameters for the material-gas interaction can be used to calculate an effective pore size for the material. They were able to show that the selectivity observed in hydrogen isotopes correlates with the quantum effective pore size, and that materials with smaller quantum effective pores were better for selective adsorption.

3.4 Earlier work to separate H₂/D₂ by porous materials

Single Walled Carbon Nanotubes (SWCNTs) were one of the first adsorbents to be used to separate hydrogen and its isotopes. In principle, the growth of SWCNTs can be controlled for desired pore diameters in the nanometer and sub-nanometer range and they are nearly perfect cylindrical system. Owing to early difficulties in uniform sample preparation and the complexity of measuring D₂/H₂ gas sorption at 20 K, quantum sieving in nanotubes was initially studied computationally and remains the most developed part of this field. Wang et al. performed a simulation of quantum sieving in SWCNTs at 20 K.[37, 38] They found a high selectivity for SWCNTs of diameters below 7 Å, and they showed that the interstitial channels in bundles of SWCNTs tend are smaller than the diameter of the tubes and could also be used to perform the separation. They showed that the heavier isotopes will adsorb at lower pressures in the SWCNTs and interstices, and that H₂ could effectively be excluded from adsorption via pressure control. Challa *et al* later extended the work of Wang to include temperature, pore size, and pressure; their results showed that quantum sieving behaves like all other adsorption processes with selectivities being very dependent on temperature and pressure.[29, 30] They computed an enormous selectivity of T₂ over H₂ at 20 K: 10⁵ in (3,6) and 10⁴ in the larger (10,10) SWCNTs. For D₂/H₂, they computed selectivities about a factor of 20 less than that of T₂/H₂, and the (6,6) SWCNT showed the highest selectivity. Johnson *et al* performed several theoretical studies, which showed that IAST provides good agreement at low pressures, but at high pressures PI-GCMC simulation exhibit a plateau in selectivity, whereas IAST simulations does not.[30] The typical simulated and measured mixture had been chosen as 50/50 for experimental simplicity, but Johnson *et al* showed that the selectivities greatly depend on the composition of gas mixture and that simulation and

experiment needs to be done on a mixture more akin to the real mixture in relevant applications. Some groups have studied D₂/H₂ selectivity as a function of nanotube arrangement and have found that tightly packed nanotubes performed better than loosely arranged nanotubes through a combination of beneficial effects.[39, 40] Tanaka *et al* also compared slit pores with cylindrical pores, predicting that cylindrical pores were better at quantum sieving. At 77 K, an optimal pore diameter of 6.23 Å produces a D₂/H₂ selectivity of 9.9.[41, 42] Although very large selectivities have been observed around 20 K, such low temperatures would be impractical for separations from the perspective of energy consumption and equipment complexity.[43-45] Experimental studies in SWCNTs and other materials are typically conducted at 77 K due to the simplicity of liquid nitrogen cooling. SWCNTs are also difficult to fabricate with uniform pore diameters and lengths corresponding with those used in theoretical predictions.

Current PSA adsorbents for most separations are almost invariably zeolites or activated carbons due to their low cost per volume, high surface area, and selectivity.[46, 47] Zeolites have been more thoroughly measured than SWCNTs. Zhou *et al* surveyed the zeolite D₂/H₂ selectivity results in their 2012 review and can be summarized as follows:[24, 48] Stephanie-Victoire *et al* measured 1.16 on NaA (a sodium substituted version of aluminosilicate zeolite A, IZA code: LTA),[48] Kotoh *et al* measured 1.207 on zeolite 5A (a variant of LTA with an effective window diameter of 5 Å) due to thermal diffusion,[49] and Chu *et al* found a range of 1.02-1.15 in various molecular sieves.[50] Kotoh *et al* studied the zeolites 4A and 5A at both 77 K and 87 K as a function of pressure.[51] For 4A and over a range of 10⁻¹ to 10⁵ Pa, selectivities ranged from 4.5 to 2.5 at 77 K and 3.3 to 2.2 at 87 K. In 5A, the values ranged from 3.4 to 1.8 at 77 K and 2.6 to 1.8 at 87 K. Kotoh *et al* also measured diffusivities via breakthrough, and showed that mixtures with higher concentrations of D₂ had longer breakthrough times.[52] In the zeolite 3A, Kotoh *et*

al measured a selectivity of 2.24 at 160 K, which is far larger than one would expect for a material at that temperature, indicating more interesting underlying physics.[47] Kaneko *et al* compared several molecular sieves including activated carbon fibers, zeolites, and SWCNTs. Some of the zeolites outperformed all of the other materials, with the SWCNTs being better than the activated carbon fibers and about half of the measured zeolites.[53] Experimental results for D₂/H₂ selectivity in four different SWCNTs were more modest (1.5-4) than the simulated results (1-14), yet the results showed a slight dependence on pressure and a greater dependence on temperature.[40]

Materials other than zeolites, such as metal-organic frameworks (MOFs), covalent organic frameworks (COFs), and zeolitic imidazolate frameworks (ZIFs) have found many uses in adsorption applications. These materials are crystalline and porous, exhibiting long range ordering in the internal structure. Their internal porosity creates a surface area far greater than any bulk material, especially for MOFs, where the internal surface area is enhanced by orders of magnitude. With appropriate ligands and metal atoms/clusters, design of MOFs with specific pore geometries is often possible,[54] as exemplified by Yaghi's famous IRMOF series.[55] The ability to design a MOF with the choice of metal cluster and ligand was used by Snurr and co-workers to create over 137,000 hypothetical MOFs as part of a study to determine which MOF topologies would work best in adsorption-based separations of Kr and Xe.[56] A vast majority of adsorption studies with MOFs and hydrogen has focused on hydrogen storage, but many of those results can also be used to enhance deuterium separation. FitzGerald *et al* have studied the adsorption H₂ and D₂ into the Fe, Co, and Ni form of MOF-74 in temperatures ranging from 77 to 120 K.[57] Their adsorption results indicate that D₂ is preferentially adsorbed over H₂ at temperatures as high as 120 K. The HOA for D₂ is between 1 to 2 kJ/mol higher than that of H₂, up to a certain quantity

of adsorbed molecules, upon which the HOA curves fall off, presumably from saturation of the metal site.

3.5 VSB-5 - Structure and applications

VSB-5 (Versailles-Santa-Barbara) was first reported in 2003 by Guillou and coworkers as a magnetic nanoporous hydrogenation catalyst. VSB-5 is a nickel (II) phosphate ($\text{Ni}_{20}[(\text{OH})_{12}(\text{H}_2\text{O})_6][(\text{HPO}_4)_8(\text{PO}_4)_4 \cdot 12\text{H}_2\text{O}]$) (Figure 3.1) with one dimensional pores running in the [001] direction and are bordered by 24 NiO_6 octahedra which are connected by edges, corners, and by sharing faces. It has large pores (~ 10 Å) compared to other adsorbents such as zeolites and metal organic frameworks. Pattern indexing performed in 2003 using DICVOL91 provided a hexagonal unit cell with $a = 18.209$ Å, $c = 6.3898$ Å with a volume of 1834.8 Å³. X-ray thermodiffraction shows that the structure persists around 723 K before collapsing to give an amorphous phase. It also recrystallizes to form $\text{Ni}_3(\text{PO}_4)_2$ at much higher temperatures.[58, 59] As far as porous nature of the material is concerned, it has monodisperse pores and the specific surface area is ~ 500 m²/g. One should always keep in mind the density of VSB-5 (~ 2.6 g/cc) while comparing this specific surface area with zeolites or other porous materials. So overall this material offers high number of unsaturated Ni sites with additional space in the framework for gas adsorption. The Ni sites have great affinity for water molecules and so prior gas measurement studies, a thorough activation is required which is described later in the text.

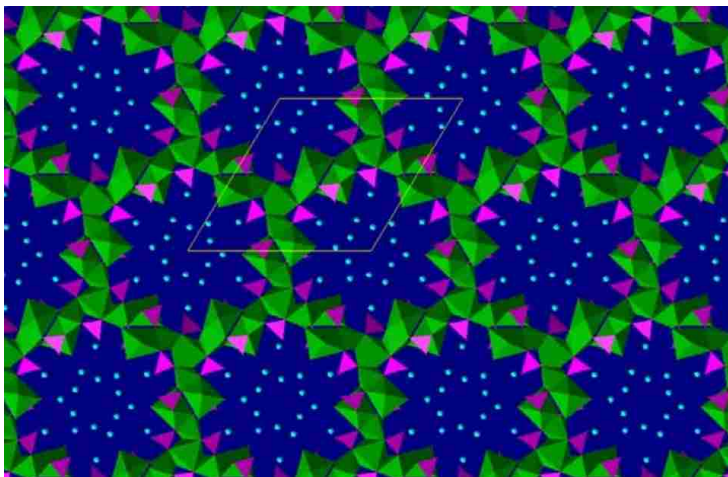


Figure 3.1: VSB-5 viewed down the *c* axis with octahedral nickel represented in green and tetrahedral phosphorous represented in purple. Disorder is omitted for clarity.[58]

This material has been used in hydrogenation for the conversion of 2-methyl-3-butyn-2-ol with high selectivity (>99%) for the formation of acetone and acetylene. VSB-5 was also used for epoxidation of cyclic olefins (cyclohexanediol and cyclooctene) with hydrogen peroxide where its shape-selective nature was observed. Due to its robust nature, it was used several times without any loss in structure, nickel species, or any other activity concerning the catalytic nature of VSB-5. Due to the strong magnetic moment provided by the Ni sites, it was used to study hydrogen adsorption by Forster and coworkers. They observed that the unsaturated Ni sites have strong interaction with hydrogen at several loadings.

3.6 Earlier work on VSB-5 and hydrogen adsorption

The first study on hydrogen interaction with VSB-5 was performed in 2003 by Forster et al with BET, TPD and INS. From the INS measurements authors confirmed the presence of unsaturated Ni²⁺ sites which actively participate in hydrogen adsorption. Broadening of a peak at 1.5 meV at higher loading helps in explaining enhancement of hydrogen adsorption at Ni sites by

removal of water molecules bonded at the Ni sites. This energy is quite lower than the rotational tunneling energy for physisorbed H₂ in other porous materials (CoNaA) and exhibits stronger interaction. Determination of heat of adsorption to investigate the D₂/H₂ separation was not performed at that time and herein we provide the insight behind the thermodynamics of D₂/H₂ separation.

3.7 Experimental

3.7.1 Materials and Methods

Out of the possible ways to synthesize VSB-5, we used the hydrothermal diaminopropane based synthesis where 6.0 g of NiCl₂.6H₂O was dissolved in 60 ml of deionized water. H₃PO₄ (85%), 6.2 g, was added dropwise with constant stirring followed by slower addition of 1,3-diaminopropane. Addition of diaminopropane formed temporary greenish-white precipitate, which dissolved eventually to give a final dark blue-purple colored solution with pH close to 9. The solution was transferred to a Parr autoclave and heated to 180 °C for five days to get green colored material which was washed with deionized water and activated thoroughly, as explained later in the text. Gas adsorption measurements were performed with our Helium fitted Micromeritics ASAP2020 the functioning of which is already explained in Chapter 1.

3.7.2 Adsorption simulation

The unit cell of the starting structure of VSB-5 has 32 H, 66 O, 12 P, and 20 Ni (with 6 H₂O molecules). The lattice constants are $a=b=18.209 \text{ \AA}$, $c= 6.3898 \text{ \AA}$, $\alpha=\beta=90^\circ$, $\gamma=120^\circ$. The initial structure was relaxed by DFT calculations using the Vienna *Ab initio* Simulation Package (VASP). The spin-polarized calculations used the Projector Augmented Wave (PAW) method to

describe the effects of core electrons, and the optB86b-vdW functional with built-in dispersion corrections was applied.[60-65] The energy cutoff for the plane-waves was 800 eV, the energy tolerance for electronic structure calculation is 10^{-8} eV, and the energy tolerance for structural optimization is 10^{-7} eV. A Hubbard +U term of 6.4 eV⁶ was applied to Ni to describe the localized 3d orbitals. All calculations were performed on a 1×1×3 Monkhorst-Pack mesh. The DFT optimized structure was ‘activated’ for adsorption simulations by manually removing the Ni coordinated water molecules. The surface area of VSB-5 was computed using the ‘rolling an atom over the surface’ Monte Carlo technique. The TraPPE forcefield for N₂ was utilized, and the spherical test distance was set to σ for each framework atom.[66] The surface area for no waters removed is 367.37 m²/g, for one water removed is 381.30 m²/g, and for all 6 waters removed is 457.09 m²/g.

Gas adsorption was simulated with Grand Canonical Monte Carlo (GCMC) with the RASPA 2.0 package.[67] GCMC fixes the system temperature, system volume, and chemical potential of the adsorbed species. A 2x2x4 super cell of fully activated VSB-5 was used for the simulations. The chemical potential is determined using the Peng-Robinson [68] equation of state from the desired system pressure using the critical parameters (Table 1) as found in the NIST Webbook.[69] A total of 31 pressure points between 0.001-800 mmHg were used to simulate the isotherms. The framework atoms are fixed at their DFT optimized positions and the adsorbed particles are randomly translated, rotated, inserted and deleted with equal weight to allow the number of particles to fluctuate. Each simulation employed 100,000 equilibration cycles and 500,000 production cycles. A cycle here consisted of N moves per cycle, where N is the number of gas particles adsorbed into the simulation volume and must be ≥ 20 . The accessible pore volume percentage was taken as the average Widom insertion parameter from 500,000 298 K He insertion

trials: $\sigma = 2.64 \text{ \AA}$, $\epsilon = 10.9 \text{ K}$. All simulated isotherms are excess corrected using the volumetric method.[70] Heats of adsorption were simulated with fluctuation theory and corrected for the residual enthalpy as computed by the equation of state.

	Critical Temperature T_c (K)	Critical Pressure P_c (MPa)	Critical Density D_c (mol/L)	Acentric Factor ω
H ₂	33.145	1.2964	15.508	-0.219
D ₂	38.34	1.6653	17.327	-0.175

Table 3.1: Critical parameters for H₂ and D₂.

The adsorbate/framework interactions were simulated with electrostatics and a quadratic Feynman-Hibbs corrected 12-6 Lennard-Jones (LJ) potential with a cutoff of 12 \AA . The Lorentz-Berthelot mixing rules were used to obtain the pairwise LJ parameters. The atomic LJ parameters for the framework come from the Drieding forcefield if possible, and the Universal Forcefield if not. The partial atomic charges on the framework atoms were determined by the EQeq method with the Ni charges centered around a value of +2 and all others centered at 0. Two different water models were evaluated: the Darkrim-Levesque (DL) and the Belof-Stern-Space-Polar (BSSP), see Table 2. The BSSP model was used with all polarization effects turned off, and with the framework able to polarize the adsorbed guest species.

Model	Atomic Site	r (Å)	ϵ (K)	σ (Å)	q (e-)	α (Å ³)
	EL	0.37050	0.00000	0.00000	0.46640	0.00000
DL	COM	0.00000	36.70000	2.95800	-0.93280	0.00000
	EL	-0.37050	0.00000	0.00000	0.46640	0.00000
	EL	-0.37100	0.00000	0.00000	0.37320	0.00044
	LJ	-0.32900	2.16726	2.37031	0.00000	0.00000
BSSP	COM	0.00000	12.76532	3.15528	-0.74640	0.69380
	LJ	0.32900	2.16760	2.37031	0.00000	0.00000
	EL	0.37100	0.00000	0.00000	0.37320	0.00044

Table 3.2: Force field parameters for H₂. D₂ parameters are the same. COM represents the center of mass site for the molecule, EL represents an additional electrostatic site to model the quadrupole, LJ represents an additional off-center Lennard-Jones dispersion site.

3.8 Results and Discussion

3.8.1 Need of activation

Due to the high affinity of water for Ni sites, the first step in utilizing VSB-5 is to remove all the water molecules and expose Ni sites for gas adsorption. Based on the thermogravimetric data presented in 2003 paper, where the structure is lost above 723 K and an appreciable mass loss around 400 K, between 473-673 K and 723 K is observed, we activated the material 573 K

overnight and a lower specific surface area was measured. Also, the material went from being green, to a yellow center surrounded a ring of ashy material. The broad descent was initially thought to be gradual release of water, however, we believe the broad descent in the TGA and low SSA after initial activation is due to the destruction of the material by either: too rapid removal of the water molecules and subsequent steaming of the framework, or the removal of the Ni-coordinated waters destabilizing and eventually destroying the coordination network. Because of this destruction of the framework, we evaluated the activation of a fresh sample at several temperatures to determine the appropriate activation conditions before going for D₂/H₂ separation. A good activation on VSB-5 is needed to have the unsaturated open Ni sites for gas adsorption as mentioned earlier. The SSA initially increases with temperature implying the removal of strongly bound water at the Ni sites, and following the TGA data there appears to be a maximum around 563-573 K. By 583 K, the framework is lost due to the collapse of the long one-dimensional tunnels, and visually all the green and yellow coloration of the sample is lost resulting in just an ashy, grey powder. The other parameter determining a good activation is the ramp rate of activation. We have observed that if the ramp rate of activation is higher (≥ 5 C/min), the material seems to lose its crystallinity, because of the strongly bound water molecules are removed all at once likely steaming the framework. Due to this sensitivity, the recommended activation of VSB-5 should have a slow ramping to the target temperature (≤ 0.5 C/min), holding it at intermediate temperatures of 373 K and 473 K for at least two hours respectively and finally holding the temperature at 563 K for 18 hours under 10^{-6} mbar vacuum. The final 77 K N₂ adsorption-desorption isotherm of activated VSB-5 shows a type I behavior with little hysteresis, which is anticipated for microporous materials and provides a BET SSA of 420 m²/g. As the surface area is slightly lower than the original report (500 m²/g), the surface area was simulated using the rolling

an atom over the surface Monte Carlo technique, which predicts a BET SSA of 460 m²/g of ideal VSB-5 with all the coordinated water molecules removed. The minor discrepancy between our measurement and the predicted ideal may result from either a small fraction of pore blockage or a minor sample mass error and should have a negligible influence on heat of adsorption determination. Powder X-ray diffraction pattern (Figure 3.2) was also collected to confirm the correct phase of the material.

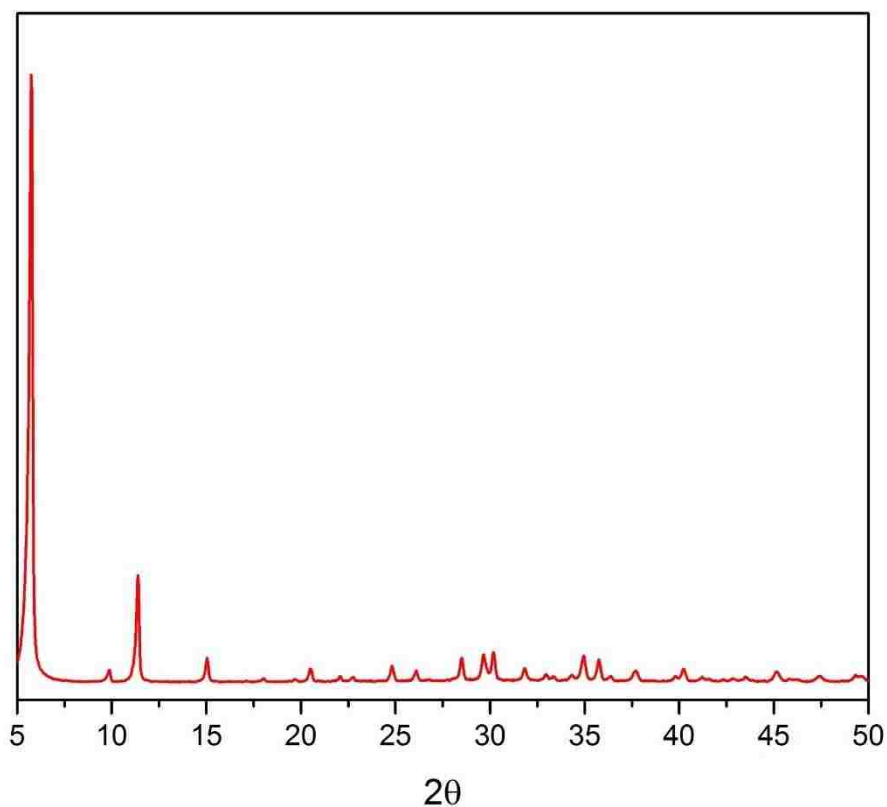


Figure 3.2 : Measured powder X-ray diffraction data for activated VSB-5.

3.8.2 Need of colder adsorption isotherms

Following the determination of proper activation conditions confirmed by BET SSA, the next step in assessing VSB-5 for H₂ storage applications was to proceed with the customary adsorption isotherms at liquid N₂ (77 K) or Ar (87 K) temperatures, so preliminary H₂ adsorption isotherms were measured starting at 80 K and going up in 10 K increments, see Figure 3.3 (left). It should be noted that in between each isotherm, the sample was reactivated at 100 C under high vacuum for an hour, and then allowed to equilibrate to the target temperature for an hour.

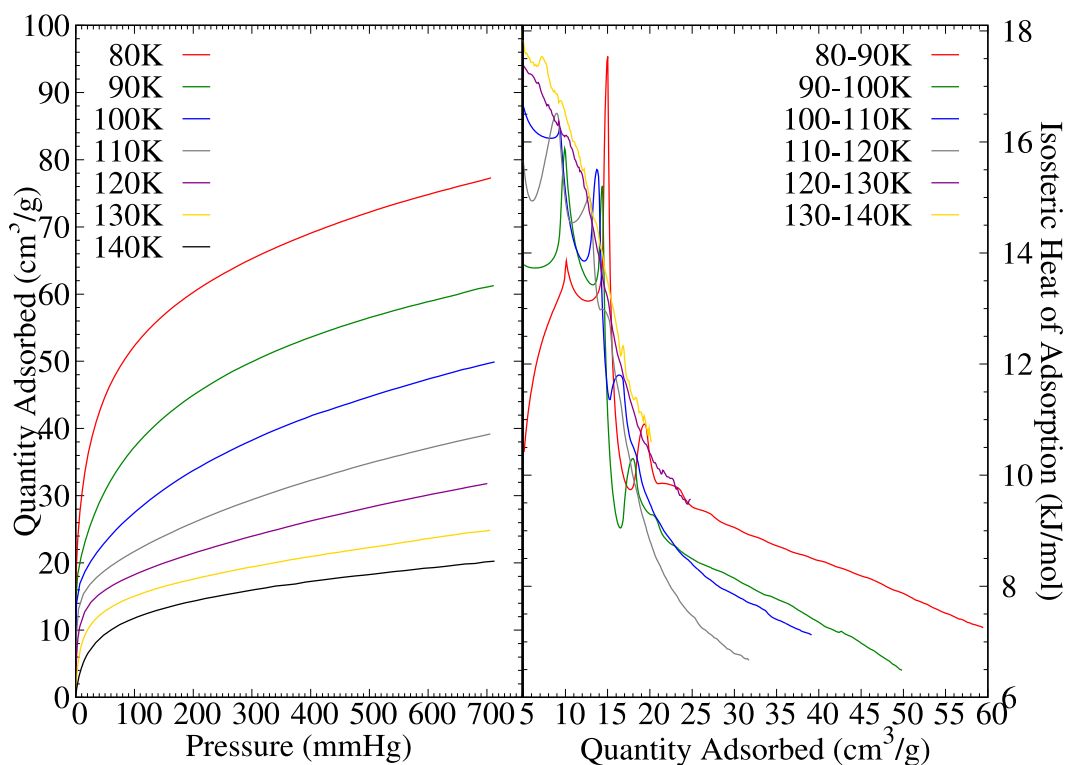


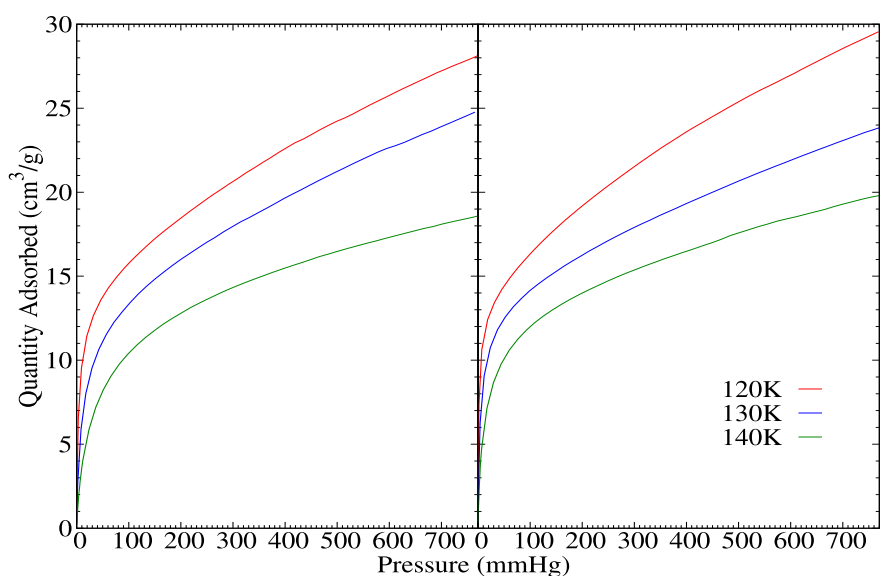
Figure 3.3: Measured temperature dependence of H₂@VSB-5 adsorption: isotherms every 10 K between 80-140 K (left), and the isosteric heats of adsorption obtained from the Clausius-Clapeyron equation for each pair of isotherms in separated by 10 K (right).

The reason behind measuring the adsorption isotherm at cryogenic temperatures is to demonstrate a high storage capacity of the material because there are typically only weak van der Waals interaction between H₂ and the adsorbent. At colder temperatures, the adsorption isotherm is nearly vertical before the saturation point, and while this accurately depicts the asymptotic storage capacity of the material, it is problematic for other reasons. First when the adsorption is that steep, the adsorption kinetics and the accuracy of any individual isotherm point before the saturation pressure is questionable. Most adsorption instrumentation operates by looking for changes in pressure below a certain threshold. Kinetics will be limited at very low temperature in most micro-nanoporous materials, and a low change in pressure over a finite time may not indicate that a steady state of adsorption has been achieved and all the gas possible has been adsorbed for that pressure and temperature. This is of grave importance when analyzing different isotopes of the same gases like H₂ and D₂ where their differential adsorption will be governed by diffusion and subtle quantum effects.

Along with that, the determined pressures in the nearly vertical regime are less than the expected error bars; these small and erroneous values lead to meaningless values for the initial heat of adsorption when determined by Clausius-Clapeyron equation, see Figure 3.3 (right). This provides no insight into the interaction of the adsorbate and adsorbent. For H₂@VSB-5 adsorption, it was not until 120 K that a smooth initial HOA without an abrupt spike at ~10 cm³/g was observed. Lastly, the slope of the Henry's law region, where quantity adsorbed is a linear function of the pressure, is nearly vertical. This slope provides the Henry's law constant (K_H, to understand adsorption/desorption selectivity and kinetics) is too steep to provide any information about the adsorbate-adsorbent interactions. Particularly, the nearly vertical Henry's law slope gives

meaningless selectivities, since its mathematical evaluation involves a nearly infinite numerator and/or denominator.

By 120 K, the Henry's law region of the H₂ isotherm exhibited a non-infinite slope, so H₂ and D₂ adsorption measurements were taken on a fresh sample of VBS-5 using the activation guidelines outlined previously in 5 K increments from 120 K until 150 K for reason that will be discussed later. The isotherms in Figure 3.4 are all type 1 with minimal desorption hysteresis.



VSB-5 is a nanoporous material. A single inflection point around 10-20 torr shows there is one strong adsorption site in this material, the unsaturated Ni sites. Following the inflection point, the isotherms all exhibited a slightly upwards slope. This indicates that although the primary adsorption site has been saturated, VSB-5 has yet to achieve its asymptotic adsorption capacity, and that would require over-pressurization beyond the capabilities of our instrumentation. The additional sites correspond to fluid-like adsorption to the remaining internal surface area of the material or from additional, multi-layer adsorption. Much of H₂ adsorption studies in the literature

focus on hydrogen storage since United States Department of Energy has set a 4.5 wt % H₂ uptake as the target for fuel storage purposes. VSB-5 exhibits a 0.251 wt % H₂ uptake at 1 atm, 120 K, and a 0.166 wt% H₂ uptake at 1 atm, 140 K, both far below the target value. This low wt % H₂ uptake is expected for a metal containing coordination polymer or a MOF. In these kinds of materials, the coordinatively unsaturated metal sites provide a stronger interaction site for the H₂ at the cost of introducing heavier atoms to the material. Frost *et al* and Bae *et al* found through grand canonical Monte Carlo simulations that H₂-MOF interactions at ambient conditions require a high heat of adsorption (> 20 kJ/mol) to achieve at least 6 wt% H₂ uptake. This deficiency of VSB-5 is not a concern, as meeting the target wt% uptake was not the goal of this study.

The simulated isotherms and the heats of adsorption (explained next) for H₂ and D₂ by DL model (Figure 3.5) and BSSP model (Figure 3.6) are provided below. A good agreement between the two models can be observed.

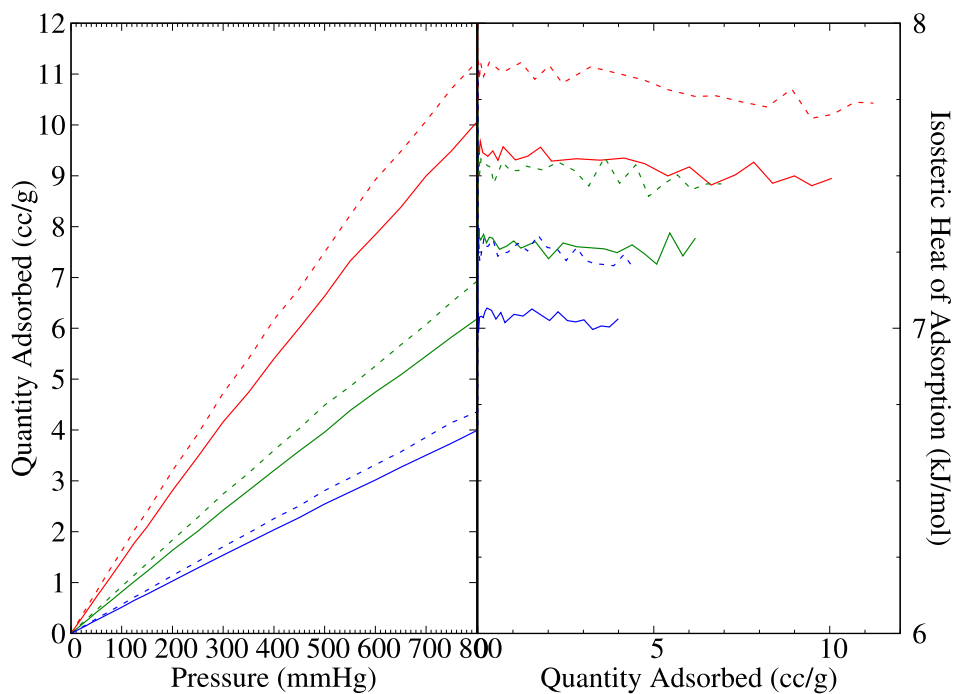


Figure 3.5: Simulated H₂ (solid) and D₂ (dashed) adsorption isotherms (left) and isosteric heats of adsorption (right) using the DL H₂ model at 120 K (red), 130 K (green), and 140 K (blue).

	120 K	130 K	140 K
H ₂	19.57	19.62	19.62
D ₂	20.74	20.80	20.77
dQ _{st}	1.17	1.19	1.15

Table 3.3: initial heats of adsorption simulated for a system pressure of 0.1 mmHg using the BSSP H₂ model with polarization.

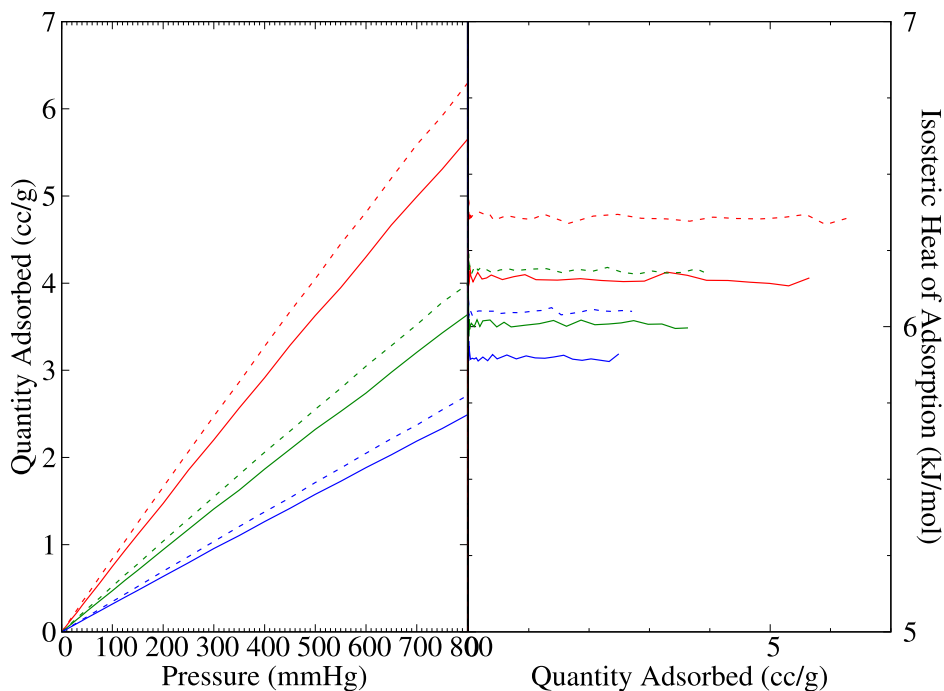


Figure 3.6: Simulated H₂ (solid) and D₂ (dashed) adsorption isotherms (left) and isosteric heats of adsorption (right) using the BSSP H₂ model without polarization at 120 K (red), 130 K (green), and 140 K (blue).

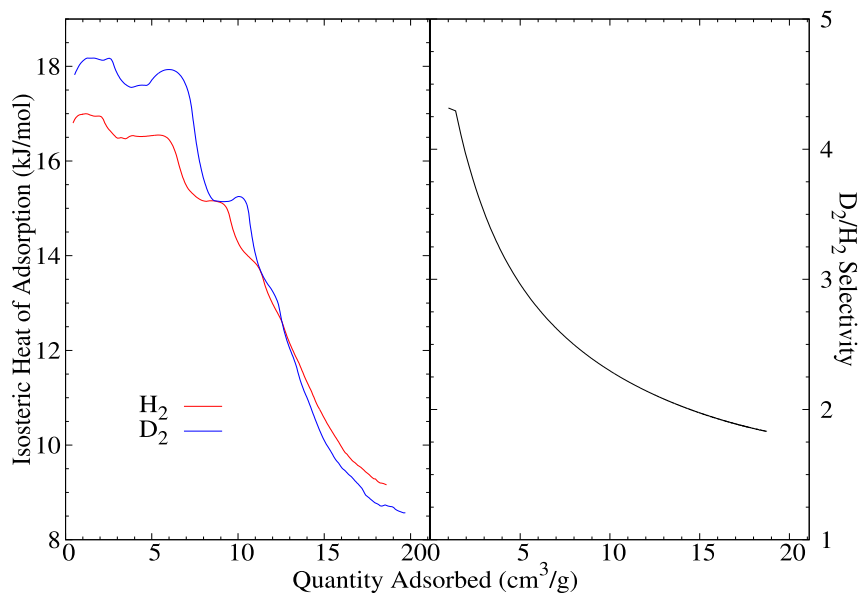
3.8.3 Heat of adsorption measurement

The aforementioned isosteric heat of adsorption (HOA) is the primary metric to describe the strength of interaction between an adsorbed gas and the solid surface, and it can be extracted using the Clausius-Clapeyron equation with a minimum of two isotherms of varying temperature. All H₂ and D₂ isotherms used for HOA determination were measured on the same sample to eliminate run-to-run variation arising from issues such as sample mass errors. We also found it necessary to carry out a brief 373 K reactivation of the sample between each measurement to ensure gas from the previous measurement diffused out of the pores and to remove trace gas which may otherwise build up in the pores over time. Figure 3.7 displays the HOA measured for H₂ and

D₂ using the adsorption isotherms measured at 120, 130, and 140 K as shown in Figure 3.4. The HOAs for H₂ and D₂ exhibit the same shape and thus describe an identical adsorption process: the Ni sites are saturated followed by filling of micropores and small interstices. The initial heats of adsorption are around 16 kJ/mol for H₂ and 18 kJ/mol for D₂, and saturate at an adsorption around 7 cc/g. The strength of this interaction between the coordinatively unsaturated nickel site and a single gas molecule is beyond a typical van der Waals physisorption value of 4-7 kJ/mol and is more a direct chemisorption via some form of bonding (as a ligand, covalent hydride formation, etc.) occurring between the hydrogen and Ni. Next there is a plateau down 2-3 kJ/mol that persists for another 2-3 cc/g of adsorbed gas. This behavior is often indicative of multiple adsorption sites in the material. Given the shape of the isotherms and the atomic structure of VSB-5, we believe this plateau doesn't correspond to a unique secondary adsorption site, but rather multiple gas molecules trying to adsorb onto the same Ni site because of the very favorable interactions and minimal gas-gas repulsion. Following that plateau, the HOA monotonically decreases as a function of gas loaded indicating the fluid like adsorption to the remaining internal surface area of the material. An initial heat of adsorption greater than 15 kJ/mol is momentous, as to the best of our knowledge this is the second material to surpass that United States Department of Energy fuel storage goal; although we recognize that the overall uptake in the material is likely to be too low for this compound to be important for mobile H₂ storage applications.

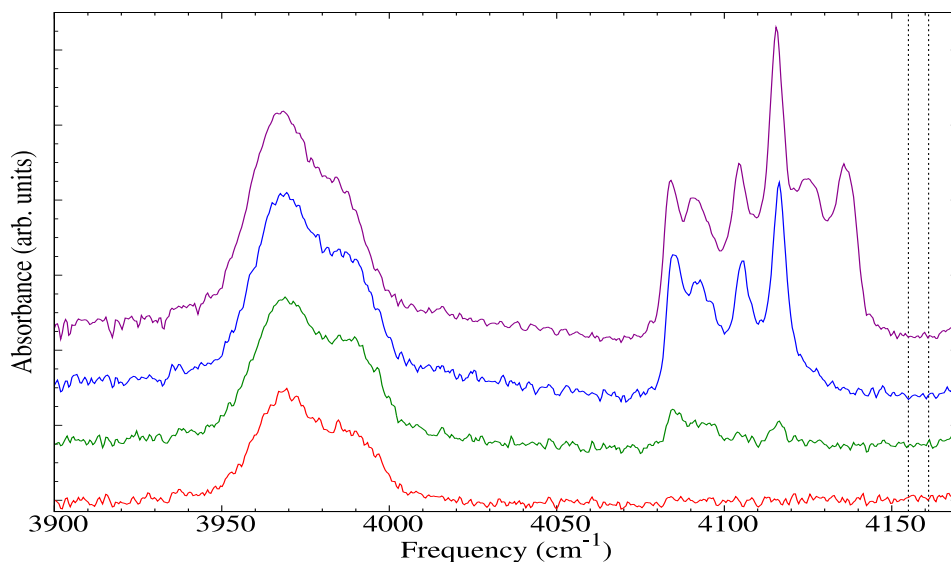
The initial HOAs differs by nearly 1.5 kJ/mol between H₂ and D₂, yet at higher loadings the HOAs converge to a nearly similar value. This trend was verified by Prof. FitzGerald group at Oberlin college on their custom built cryostat using a sample that we provided. Initial HOA values of 16.8 and 18.4 kJ/mol were obtained for H₂ and D₂ respectively. These are consistent within experimental error to our earlier values. As H₂ and D₂ are identical electronically and differ only

by mass, this difference in HOA must come from quantum effects. These quantum effects can be simply explained as the heavier isotopes bind in the same electronic potential energy well, but have lower zero-potential vibrational energies. The lower zero-potential vibrational energy causes the heavier isotope to sit lower in that potential well and therefore give the heavier isotopes a slightly preferable binding energy. The difference in binding energy arising from the zero-point vibrational energies is lost quickly with increased temperature as other free energy components begin to dominate causing the measured H₂ and D₂ HOAs to become the same. This has been observed in SWCNTs, and is the basis of the interest in those materials for D₂/H₂ separation. In SWCNTs the hydrogen binds purely through weak van der Waals dispersion interactions, and the quantum effects are often no longer observed by 77 K. The quantum effects are still very important at the unsaturated metal centers persisting to upwards of 140 K, one of the highest temperatures reported for having a difference in the H₂ and D₂ HOAs. Since the HOAs converge to a nearly identical value after the Ni sites saturate, we know the quantum effects must arise from the strong bonding-like Ni-hydrogen interaction. The confined ~11 Å pores of VSB-5 likely also contribute to the quantum effects in the same way do in SWCNTs, however much like in SWCNTs they are mitigated by the higher temperatures measured here.

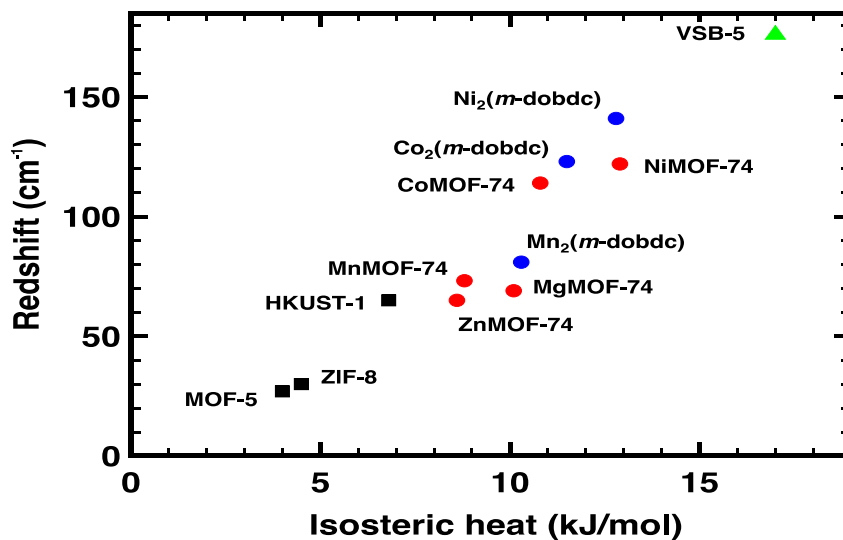


The diffuse reflectance IR spectra (Figure 3.8) of adsorbed H₂ measured in FitzGerald *et al* study shows a growing in of additional features in the Q-band region with increased H₂ uptake. These features arise from the vibrational motion of adsorbed H₂, and are red shifted from the IR inactive frequency of free H₂. It has been demonstrated that a large red shift is correlated to large adsorption enthalpies.[71] They have noted a consistent redshift in the frequency of the H₂ vibrational mode relative to its gas phase value (4161 cm⁻¹). The magnitude of the shift shows a linear correlation with the strength of the sorbent – H₂ interaction. Although the H₂ vibration is not IR active, interactions with the framework induce a dipole moment such that the transition can now be measured with IR spectroscopy. Figure 3.8 presents IR absorption spectra obtained using a customized diffuse reflectance apparatus. The spectra are referenced to degassed VSB-5 and show the vibrational modes of the adsorbed H₂. At the lowest concentration only a broad doublet is observed with features at 3970 and 3986 cm⁻¹. We believe these to be the highly perturbed Q(1) and Q(0) modes respectively. At higher concentrations, additional features appear in the region of 4080 to 4140 cm⁻¹. These are indicative of H₂ adsorbed at weaker secondary sites.[71] At low

concentration H₂ first adsorbs in the most strongly binding (primary) site and once this is saturated it starts to occupy secondary sites. The primary site H₂ modes are shifted by roughly 180 cm⁻¹ relative to the corresponding gas phase values representing the largest reported redshift for a porous material.



When the red shift observed here is compared to the red shift in other MOF materials (Fig. 3.9), it can easily be seen that the red-shift in VSB-5 is of the largest observed to date, which corroborates the very high HOA. Figure 3.9 shows the measured vibrational redshift as a function of HOA for a series of MOF materials. There is a strong correlation between the two, and as can be seen our measured HOA value for VSB-5 is perfectly in line with the overall trend.



To our knowledge, VSB-5 is the second nanoporous framework demonstrated to bind hydrogen with a HOA above 15 kJ/mol. The first example is found in a 2017 paper describing a Cu(I)-based MOF with a 32 kJ/mol HOA attributed to H₂ sorption on the Cu(I) site.[72] Besides the high HOA for H₂, Cu-I-MFU-4l has an initial preference for H₂ at under coordinated Cu-sites which then favour D₂ at temperatures higher than 90 K. This thermodynamically controlled isotopic exchange at higher temperatures allows for separation at lower concentrations in the gas phase.

The most widely used metal cluster in MOF synthesis containing a coordinatively unsaturated metal site is the Cu-paddlewheel. HKUST-1 (CuTMA, CuBTC) is one of the first MOFs to be synthesized and remains one of the most studied, both theoretically and experimentally. In previous work, we have already focused on studying HKUST-1's ability to separate Kr and Xe. In the course of those studies, we also measured HKUST-1's adsorption isotherms for H₂ around liquid nitrogen temperatures (57-77 K). The experimental HOA extracted from those isotherms has an initial value of about 6.7 kJ/mol and decreases after 5 mmol/g adsorbs,

similar to what we observed in the MOF-74 family and the Ni-phosphate material. 5 mmol/g, stoichiometrically, corresponds to the point when both small pockets and all Cu(II) sites are saturated (at 0.83 mmol/g, the metal sites should be saturated). This likely indicates a cooperative effect between the small cage of HKUST-1 and the unsaturated metal sites. In that work, the HOA of HKUST-1 was simulated using two different common H₂ models that only include electrostatics and quantum- (i.e., Feynman-Hibbs) corrected dispersion. Both models dramatically underpredict the experimental observations. In contrast, those parameters worked well describing H₂ adsorption into MOF-5 (IRMOF-1), which has no open metal sites. The failure of both models indicates that there are more complex effects at play than described by the simplest physisorption model, further proving that there is a bonding-like chemisorption with relevant quantum effects occurring in materials with coordinatively unsaturated metal sites that is not captured by traditional classical adsorption force fields. The lack of a good force field to describe hydrogen chemisorption to coordinatively unsaturated metal sites in the literature is why adsorption was not simulated in this work.

The difference in the H₂ and D₂ HOA indicate that VSB-5 will be selective for D₂. Using the slopes of the Henry's law region can only supply a coarse estimate for the initial selectivity, and it is better to use either Ideal (IAST) or Real adsorbed solution theory (RAST). IAST combines experimental isotherms for different gases measured at the same temperature to estimate the selectivity of the material for a binary gas mixture of any composition across a range of loadings. The initial measured selectivity at 140 K for VSB-5 is in excess of 4 using both Henry's law slopes and IAST (IAST curve in Figure 3.7 (right)). This is again one of the highest measured values reported, and we believe it may be the highest measured selectivity at this temperature. The selectivity for D₂ is highest at the initial loadings and falls smoothly for higher loadings

presumably because saturation of the coordinately unsaturated metal site with adsorbed hydrogen isotopes. This implies that the selectivity, much like the difference in heat of adsorption, arises from the strong quantum effects that occur when the hydrogen chemisorbs to the coordinately unsaturated metal site, which goes away as the metal site saturates. A selectivity of 1 indicates that the material sees the two gases identically, and that a selectivity >1 persists out to the highest loading available with IAST shows that the narrow pores are contribute to this material being one of the best identified for separating hydrogen isotope gas mixtures. The selectivity results from IAST and from an isothermal fit shows an initial selectivity for $D_2 > 1$ at temperatures up to 150 K, however the values are much closer to 1 indicating a thermal mitigation of the pronounced quantum effects. For zeolites, selectivity as high as 4.5 is measured at 77 K and 10^{-1} Pa. For the leading MOFs, FitzGerald *et al* have studied the adsorption H_2 and D_2 into the Fe, Co, and Ni forms of MOF-74 in the temperatures ranging from 77 to 120 K, with Ni-MOF-74 having the highest D_2/H_2 selectivity at 77 K. Their adsorption results indicate that D_2 is preferentially adsorbed over H_2 at temperatures as high as 120 K for the same reasons as in VSB-5.

3.9 Conclusions

In conclusion, VSB-5 is shown here to have one of the highest measured initial heat of adsorption, >16 kJ/mol, of any material to the best of our knowledge. However, many other previously examined materials are likely to have comparable HOAs, if their adsorption were to be re-evaluated at several temperatures with careful attention paid to the slope of the Henry's law region of the isotherm. D_2 maintained a > 1.5 kJ/mol greater initial heat of adsorption than H_2 , which resulted in what we believe to be the highest measured initial D_2/H_2 selectivities at a temperature > 120 K. The reason for this high selectivity is that there are still very pronounced

quantum effects in the strong chemisorption between the coordinatively unsaturated Ni site and the hydrogen isotope that have yet to be washed out by other free energies contributions even by 140 K. VSB-5, while not a candidate for H₂ fuel storage, is the leading candidate material for lower energy cost PSA separations of D₂/H₂ gas mixtures.

3.10 References

1. Satyapal, S. *Hydrogen: A clean, flexible energy carrier*. 2017 [cited 2018; Available from: <https://energy.gov/eere/articles/hydrogen-clean-flexible-energy-carrier>.
2. Sharma, S. and S.K. Ghoshal, *Hydrogen the future transportation fuel: From production to applications*. Renewable and Sustainable Energy Reviews, 2015. **43**(Supplement C): p. 1151-1158.
3. Ramachandran, R. and R.K. Menon, *An overview of industrial uses of hydrogen*. International Journal of Hydrogen Energy, 1998. **23**(7): p. 593-598.
4. Schlapbach, L. and A. Züttel, *Hydrogen-storage materials for mobile applications*, in *Materials for Sustainable Energy*. 2012, Co-Published with Macmillan Publishers Ltd, UK. p. 265-270.
5. Center, A.F.D. *Fuel Cell Electric Vehicle*. [cited 2018; Available from: https://www.afdc.energy.gov/vehicles/fuel_cell.html.
6. Office, F.C.T. *Technology Validation*. [cited 2018; Available from: <https://energy.gov/eere/fuelcells/technology-validation>.
7. Keppler, F., et al., *Methoxyl groups of plant pectin as a precursor of atmospheric methane: evidence from deuterium labelling studies*. New Phytologist, 2008. **178**(4): p. 808-814.
8. Wolfsberg, M., et al., *Isotope Effects*. 1 ed. 2009: Springer Netherlands. 466.
9. Bier, D.M., et al., *In-vivo Measurement of Glucose and Alanine Metabolism with Stable Isotopic Tracers*. Diabetes, 1977. **26**(11): p. 1005-1015.
10. Sun, X., et al., *Nano-graphene oxide for cellular imaging and drug delivery*. Nano Research, 2008. **1**(3): p. 203-212.
11. Audi, G. and A. Wapstra, *The 1993 atomic mass evaluation:(I) Atomic mass table*. Nuclear Physics A, 1993. **565**(1): p. 1-65.
12. Vargaftik, N.B., *Handbook of physical properties of liquids and gases - pure substances and mixtures. Second edition*. 1975, United States: Hemisphere Publishing Corporation, New York, NY.

13. Lässer, R., *Properties of tritium and ^3He in metals*. Journal of the Less Common Metals, 1987. **131**(1): p. 263-273.
14. Hammel, E.F., *Some Calculated Properties of Tritium*. The Journal of Chemical Physics, 1950. **18**(2): p. 228-229.
15. Bartlit, J.R., et al., *Hydrogen isotope distillation for fusion power reactors*. Cryogenics, 1979. **19**(5): p. 275-279.
16. Yamanishi, T., et al., *Experimental Study for Separation Characteristics of Cryogenic Distillation Columns with An H-D-T System*. Fusion Technology, 1991. **20**(4P1): p. 419-424.
17. Lässer, R. and K.H. Klatt, *Solubility of hydrogen isotopes in palladium*. Physical Review B, 1983. **28**(2): p. 748-758.
18. Hammerli, M., W.H. Stevens, and J.P. Butler, *Combined Electrolysis Catalytic Exchange (CECE) Process for Hydrogen Isotope Separation*, in *Separation of Hydrogen Isotopes*. 1978, AMERICAN CHEMICAL SOCIETY. p. 110-125.
19. Li, J.-R., R.J. Kuppler, and H.-C. Zhou, *Selective gas adsorption and separation in metal-organic frameworks*. Chemical Society Reviews, 2009. **38**(5): p. 1477-1504.
20. Banerjee, D., et al., *Potential of Metal–Organic Frameworks for Separation of Xenon and Krypton*. Accounts of Chemical Research, 2015. **48**(2): p. 211-219.
21. Sircar, S., *Basic Research Needs for Design of Adsorptive Gas Separation Processes*. Industrial & Engineering Chemistry Research, 2006. **45**(16): p. 5435-5448.
22. Nandi, S.P. and P.L. Walker, *Separation of Oxygen and Nitrogen Using 5A Zeolite and Carbon Molecular Sieves*. Separation Science, 1976. **11**(5): p. 441-453.
23. Yang, R.T., *Adsorbents: Applications and Fundamentals*. 2003, Hoboken: Wiley.
24. Cai, J., Y. Xing, and X. Zhao, *Quantum sieving: feasibility and challenges for the separation of hydrogen isotopes in nanoporous materials*. RSC Advances, 2012. **2**(23): p. 8579-8586.

25. Beenakker, J.J.M., V.D. Borman, and S.Y. Krylov, *Molecular transport in subnanometer pores: zero-point energy, reduced dimensionality and quantum sieving*. Chemical Physics Letters, 1995. **232**(4): p. 379-382.
26. Zijun, Y., *General thermal wavelength and its applications*. European Journal of Physics, 2000. **21**(6): p. 625.
27. Barker, J.A., *A quantum-statistical Monte Carlo method; path integrals with boundary conditions*. The Journal of Chemical Physics, 1979. **70**(6): p. 2914-2918.
28. Garberoglio, G., M.M. DeKlavon, and J.K. Johnson, *Quantum Sieving in Single-Walled Carbon Nanotubes: Effect of Interaction Potential and Rotational–Translational Coupling*. The Journal of Physical Chemistry B, 2006. **110**(4): p. 1733-1741.
29. Kagita, H., et al., *Quantum Molecular Sieving Effects of H₂ and D₂ on Bundled and Nonbundled Single-Walled Carbon Nanotubes*. The Journal of Physical Chemistry C, 2012. **116**(39): p. 20918-20922.
30. Challa, S.R., D.S. Sholl, and J.K. Johnson, *Adsorption and separation of hydrogen isotopes in carbon nanotubes: Multicomponent grand canonical Monte Carlo simulations*. The Journal of Chemical Physics, 2002. **116**(2): p. 814-824.
31. Feynman, R., *Quantum Mechanical Path Integrals*. 1965: Dover Publications.
32. Kumar, A.V.A. and S.K. Bhatia, *Quantum Effect Induced Reverse Kinetic Molecular Sieving in Microporous Materials*. Physical Review Letters, 2005. **95**(24): p. 245901.
33. Fu, J. and H. Sun, *An Ab Initio Force Field for Predicting Hydrogen Storage in IRMOF Materials*. The Journal of Physical Chemistry C, 2009. **113**(52): p. 21815-21824.
34. Kowalczyk, P., et al., *Thermodynamics of Hydrogen Adsorption in Slit-like Carbon Nanopores at 77 K. Classical versus Path-Integral Monte Carlo Simulations*. Langmuir, 2007. **23**(7): p. 3666-3672.
35. K Binder, D.H., *Monte Carlo Simulations in Statistical Physics*. 2002, Berlin: Springer.

36. D Liu, W.W., J Mi, C Zhong, Q Yang, D Wu, *Quantum Sieving in Metal Organic Frameworks*. Industrial & Engineering Chemistry Research, 2012. **51**.
37. Cessford, N.F., N.A. Seaton, and T. Düren, *Evaluation of Ideal Adsorbed Solution Theory as a Tool for the Design of Metal–Organic Framework Materials*. Industrial & Engineering Chemistry Research, 2012. **51**(13): p. 4911-4921.
38. Wang, Q., et al., *Quantum Sieving in Carbon Nanotubes and Zeolites*. Physical Review Letters, 1999. **82**(5): p. 956-959.
39. Kagita, H.O., T.; Fujimori, T.; Tanaka, H.; Hata, K.; Taira, S.; Kanoh, H.; Minami, D.; Hattori, Y.; Itoh, T.; Masu, H.; Endo, M.; Kaneko, K., *Quantum Molecular Sieving Effects of H₂ and D₂ on Bundled and Nonbundled Single-Walled Carbon Nanotubes*. J Phys Chem C, 2012. **116**.
40. Daisuke, N., et al., *Selective D₂ adsorption enhanced by the quantum sieving effect on entangled single-wall carbon nanotubes*. Journal of Physics: Condensed Matter, 2010. **22**(33): p. 334207.
41. Tanaka, H. and M.T. Miyahara, *Hydrogen Isotope Separation in Carbon Nanopores*. JOURNAL OF CHEMICAL ENGINEERING OF JAPAN, 2011. **44**(5): p. 355-363.
42. Gotzias, A. and T. Steriotis, *D₂/H₂ quantum sieving in microporous carbons: a theoretical study on the effects of pore size and pressure*. Molecular Physics, 2012. **110**(11-12): p. 1179-1187.
43. Alekseev, I.A., et al., *Heavy water detritiation by combined electrolysis catalytic exchange at the experimental industrial plant*. Fusion Engineering and Design, 2003. **69**(1): p. 33-37.
44. Kowalczyk, P.G., P. A.; Terzyk, A. P. , *Cryogenic Separation of Hydrogen Isotopes in Single-Walled Carbon and Boron-Nitride Nanotubes: Insight into the Mechanism of Equilibrium Quantum Sieving in Quasi-One-Dimensional Pores*.
45. Richter, F.M., et al., *Isotopic fractionation of the major elements of molten basalt by chemical and thermal diffusion*. Geochimica et Cosmochimica Acta, 2009. **73**(14): p. 4250-4263.
46. Breck, W.D., *Zeolite Molecular Sieves*. 1974, New York: Wiley.

47. Kotoh, K., S. Takashima, and Y. Nakamura, *Molecular-sieving effect of zeolite 3A on adsorption of H₂, HD and D₂*. Fusion Engineering and Design, 2009. **84**(7): p. 1108-1112.
48. Stephanie-Victoire, F.G., A.-M.; Lara, E. C., *Adsorption and Coadsorption of Molecular Hydrogen Isotopes in Zeolites. 1. Isotherms of H₂, HD, and D₂ in NaA by Thermomicrogravimetry*. Langmuir, 1998. **14**.
49. Kotoh, K., T. Nishikawa, and Y. Kashio, *Multi-component Adsorption Characteristics of Hydrogen Isotopes on Synthetic Zeolite 5A-type at 77.4K*. Journal of Nuclear Science and Technology, 2002. **39**(4): p. 435-441.
50. Chu, X.-Z., et al., *Adsorption of Hydrogen Isotopes on Micro- and Mesoporous Adsorbents with Orderly Structure*. The Journal of Physical Chemistry B, 2006. **110**(45): p. 22596-22600.
51. Kotoh, K., et al., *Multi-component behaviors of hydrogen isotopes adsorbed on synthetic zeolites 4A and 5A at 77.4K and 87.3K*. Fusion Engineering and Design, 2010. **85**(10): p. 1928-1934.
52. Kotoh, K., et al., *Breakthrough curves of non-trace H₂-D₂ mixture replacement adsorption with SZ-13X packed column at 77.4K*. Fusion Engineering and Design, 2013. **88**(9): p. 2223-2227.
53. Niimure, S.F., T.; Minami, D.; Hattori, Y.; Abrams, L.; Corbin, D.; Hata, K.; Kaneko, K., *Dynamic Quantum Molecular Sieving Separation of D₂ from H₂-D₂ Mixture with Nanoporous Materials*. J Am Phy Soc, 2012. **134**.
54. Han, S.S., W.-Q. Deng, and W.A. Goddard, *Improved Designs of Metal-Organic Frameworks for Hydrogen Storage*. Angewandte Chemie International Edition, 2007. **46**(33): p. 6289-6292.
55. Li, H., et al., *Design and synthesis of an exceptionally stable and highly porous metal-organic framework*. Nature, 1999. **402**: p. 276.
56. Sikora, B.J., et al., *Thermodynamic analysis of Xe/Kr selectivity in over 137 000 hypothetical metal-organic frameworks*. Chemical Science, 2012. **3**(7): p. 2217-2223.
57. FitzGerald, S.A.P., C. J.; Rowsell, J. L. C.; Bloch, E. D.; Mason, J. A., *Highly Selective Quantum Sieving of D₂ from H₂ by a Metal-Organic Framework As Determined by Gas Manometry and Infrared Spectroscopy*. J Am Phy Soc, 2013. **135**.

58. Guillou, N., et al., *Nickel(II) Phosphate VSB-5: A Magnetic Nanoporous Hydrogenation Catalyst with 24-Ring Tunnels*. *Angewandte Chemie International Edition*, 2001. **40**(15): p. 2831-2834.
59. Jhung, S.H., et al., *Template-Free Synthesis of the Nanoporous Nickel Phosphate VSB-5 under Microwave Irradiation*. *Chemistry of Materials*, 2004. **16**(8): p. 1394-1396.
60. Kresse, G. and J. Hafner, *Ab initio molecular dynamics for liquid metals*. *Physical Review B*, 1993. **47**(1): p. 558.
61. Kresse, G. and J. Hafner, *Ab initio molecular-dynamics simulation of the liquid-metal–amorphous-semiconductor transition in germanium*. *Physical Review B*, 1994. **49**(20): p. 14251.
62. Kresse, G. and J. Furthmüller, *Efficiency of ab-initio total energy calculations for metals and semiconductors using a plane-wave basis set*. *Computational materials science*, 1996. **6**(1): p. 15-50.
63. Kresse, G. and J. Furthmüller, *Efficient iterative schemes for ab initio total-energy calculations using a plane-wave basis set*. *Physical review B*, 1996. **54**(16): p. 11169.
64. Blöchl, P.E., *Projector augmented-wave method*. *Physical review B*, 1994. **50**(24): p. 17953.
65. Kresse, G. and D. Joubert, *From ultrasoft pseudopotentials to the projector augmented-wave method*. *Physical Review B*, 1999. **59**(3): p. 1758.
66. Siepmann, J. *Transferable Potentials for Phase Equilibria*. [cited 2018; Available from: <http://chem-siepmann.oit.umn.edu/siepmann/trappe/index.html>].
67. Dubbeldam, D., et al., *RASPA: molecular simulation software for adsorption and diffusion in flexible nanoporous materials*. *Molecular Simulation*, 2016. **42**(2): p. 81-101.
68. Peng, D.-Y. and D.B. Robinson, *A new two-constant equation of state*. *Industrial & Engineering Chemistry Fundamentals*, 1976. **15**(1): p. 59-64.
69. Mallard, P.J.L.a.W.G., *NIST Chemistry WebBook, NIST Standard Reference Database Number 69*.
70. Widom, B., *Some topics in the theory of fluids*. *The Journal of Chemical Physics*, 1963. **39**(11): p. 2808-2812.

71. FitzGerald, S.A., et al., *Metal-Specific Interactions of H₂ Adsorbed within Isostructural Metal–Organic Frameworks*. Journal of the American Chemical Society, 2011. **133**(50): p. 20310-20318.
72. Weinrauch, I., et al., *Capture of heavy hydrogen isotopes in a metal-organic framework with active Cu(I) sites*. Nature Communications, 2017. **8**: p. 14496.

Note:

The work compiled in this chapter is a joint effort with Dr. Stephen FitzGerald's group at Oberlin University. From UNLV, Amit Sharma synthesized all the necessary batches of VSB-5 needed for this project. He performed a minor project to investigate the proper activation conditions for VSB-5 which were required for the remainder of the studies. He also measured the necessary H₂-D₂ gas adsorption isotherms and the corresponding heats of adsorption which were then used by Dr. Keith V Lawler for the calculations of selectivity using the principles of IAST as explained in the text. All the necessary simulations for this study were performed by Dr. Lawler. Dr. Stephen FitzGerald's group checked the heats of adsorption data by measuring the adsorption isotherms on their system on the batch provided by Dr. Forster's group. Besides, they also measured the diffuse reflectance IR spectra on VSB-5 and also provided the IR red shift as a function of initial isosteric heats of adsorption for various MOFs to compare VSB-5's performance.

Chapter 4: Using Inelastic Neutron Scattering to Probe Weak and Strong Hydrogen

Binding in Graphene and VSB-5

Index

- 4.1 Abstract
- 4.2 Introduction to neutron scattering
 - 4.2.1 Neutron Sources
 - 4.2.2 Beamline 16-B: VISION
 - 4.2.3 Inelastic Neutron Scattering (INS)
 - 4.2.3.1 Why INS
 - 4.2.3.2 The Scattering Law
 - 4.2.3.3 How to Model INS
- 4.3 Rotation of the dihydrogen molecule
 - 4.3.1 ortho ($o\text{-H}_2$) and para-hydrogen ($p\text{-H}_2$)
 - 4.3.2 An outline of the INS spectrum of dihydrogen
 - 4.3.3 The INS of dihydrogen in an anisotropic potential
- 4.4 Motivation
- 4.5 Earlier work on carbonaceous materials and dihydrogen interactions
- 4.6 Materials and Methods
- 4.7 Characterization
- 4.8 Results and discussion of para-hydrogen loadings on graphene
- 4.9 Results and discussion of para-hydrogen loadings on VSB-5
 - 4.9.1 Kubas Complex
 - 4.9.2 para-hydrogen loadings on VSB-5
- 4.10 References

4.1 Abstract

We examine the adsorption of dihydrogen on layers of graphene and into the nanoporous nickel phosphate VSB-5. On the basis of gas sorption analysis we have already established that VSB-5 exhibits one of the highest measured heat of adsorption for dihydrogen as discussed in chapter 2. Inelastic Neutron Scattering (INS) measured the shift in the rotational line of dihydrogen for VSB-5 and indicates a strong interaction with the available unsaturated Ni²⁺ sites. This strong interaction of dihydrogen with metal sites is related to a series of metal-dihydrogen complexes referred to as Kubas complexes. Similar adsorption studies are performed on graphene as well to compare the behavior of dihydrogen on a weakly interacting surface.

4.2 Introduction to neutron scattering [1]

Neutron scattering can be used to study the positions (structure) and motions (dynamics) of atoms in condensed matter. The neutron has no charge, a mass slightly larger than proton, and a spin of one-half. A summary of physical properties is provided in the table below. Due to high penetrating capability compared with photons and electrons, it travels relatively long distances through most materials without being scattered or absorbed. It has a half-life of ~ 900 seconds and decays into a proton, an electron, and an antineutrino. Its interactions with matter are confined to the short-range nuclear and magnetic interactions and since the interaction probability is small, neutrons penetrate well through matter making it a unique probe to investigate bulk condensed matter. In addition to being scattered by the nuclei, they also interact with the unpaired electrons through the spin of the neutron.

The neutron displays both wave and particle properties. With energy distributions in equilibrium to room temperature, both properties are significant and whether we treat the neutron

as wave or particle depends on the phenomenon observed. In incoherent inelastic neutron scattering, (the case that we will be referring in this work), the particle description is the more important and useful of the two. However, the spherical wave nature of the scattered neutron cannot be neglected. The wave properties of neutron are revealed by interference/diffraction or by observing the way in which a beam of neutrons propagates and spreads. The de Broglie wavelength of a thermalized neutron is comparable to interatomic and intermolecular distances and its energy is comparable to molecular vibrational energies. Due to these reasons, neutron scattering experiments can yield structural and dynamic information on the scattering system simultaneously.

Property	Value
m_n /kg	1.674×10^{-27}
m_n /u	1.008
$m_n c^2$ /MeV	939.565
Spin, I	$\frac{1}{2}$
Charge number, z	0
Mean life /s	889.1

Table 4.1: A brief overview on the physical properties of a neutron.

4.2.1 Neutron sources

Since the early days of neutron scattering, there has been an increasing demand for higher neutron fluxes. Neutron sources are based on various processes that liberate excess neutrons from

neutron-rich nuclei such as Be, W, U, Pb or Hg. Presently for neutron scattering purposes, two types of sources are established.

(i) Continuous reactors:

To explain the continuous reactors for neutron production, consider a nuclear fission reaction where the heavy nuclides (U-233, U-235, Pu-239) undergo fission reaction to produce lighter nuclei upon interacting with energetic neutrons. Each fission reaction generates enormous amounts of energy (200 MeV) released as gamma rays and kinetic energy in fission fragments (fission isotopes, neutrons). Most of the particles are shielded and slowed down by different moderators (D₂O, H₂O) to give a filtered neutron beam to be used in beam tubes for scattering studies. Neutrons generated from fission can either slow down to epithermal and then thermal energies or may be absorbed by radiative capture, or might escape the system. The slowing down process is maintained through collisions with low Z elements and the neutron leakage is minimized by having a low Z blanket surrounding the core. For these reactors, the intensity at the sample and the detector is shown below.

One example of continuous reactors is High Fluxed Isotope Reactor (HFIR) at Oak Ridge National Laboratory (ORNL) in Tennessee, USA. HFIR was constructed in 1960s for the production of transuranic isotopes and since then it has grown to include materials irradiation, neutron activation, and neutron scattering. HFIR is a beryllium-reflected, light water cooled and flux type reactor that uses U-235 (highly enriched) fuel with an operating power of ~ 85 MW.

(ii) Spallation neutron sources

Spallation is the process of releasing neutrons from target element by bombardment with energetic protons. Based on the energy of proton and the target material, the spallation process

emits fewer neutrons/proton when compared with continuous reactors. Unlike continuous reactors, these neutrons are released in short pulses and the neutron flux during these pulses is appreciably higher. Since the proton pulses arriving at the target produces neutrons at a specific time, additional information related to the time of the flight can be captured which is not normally available. For many experiment types, this allows all of the neutrons arriving at the sample to be used to interrogate the material rather than having to select a monochromatic slice of the neutrons as is necessary at a reactor. A simplistic way to consider the difference is that reactors allow instruments to use *some* of the neutrons *all* of the time, and spallation sources allow the use of *all* of the neutrons *some* of the time.

Spallation sources have existed since the 70s. Some of the earlier spallation sources are no longer operational like LANSCE and IPNS in the USA, KENS in Japan. The most modern spallation sources are ISIS (UK), SINQ (Switzerland), JPARC (Japan) and the most powerful pulsed neutron source, the Spallation Neutron Source (SNS) at ORNL. SNS began its operation in 2006 and is presently the most powerful accelerator-driven neutron source in the world operating at 1.2 MW.

The front end of the SNS houses the ion source which produces negative hydrogen ions meaning each atom has two electrons instead of one electron and one proton. The negative hydrogen ions are cut into pulses of nanoseconds duration which are then fed into the linear accelerator (Linac) before accelerating the ions to ~ 2.5 MeV. These energetic ions are injected into Linac which is a superposition of superconducting and normal radio-frequency cavities which accelerates the ions (in form of beam) to even higher energies ~ 1 GeV. The beam of ions is focused and steered while accelerated. The cavities are cooled to ~ 2 K by liquid helium. [2]

After the Linac, the hydrogen beam enters the proton accumulating ring. The ring structure bunches and intensifies the ion beam for delivery onto a mercury target. The hydrogen beam pulses from the linac is wrapped into the ring through the carbon foil and that strips the electrons from the negatively charged hydrogen ions to produce the protons that circulate in the ring. More than 1200 turns are accumulated and are then ejected at once, producing a sub microsecond pulse which is delivered to the target. So, intense proton pulses are produced, stored, and extracted at a rate of 60 times a second to bombard the target.[2]

The target is liquid mercury which emits around 30 neutrons for each high energy proton which bombards the mercury target. These neutrons as produced are too energetic for most experiments conducted at the SNS and must be slowed down and turned into low-energy neutrons required for the research. The neutrons are slowed down by passing them through cells filled with water to produce room temperature neutrons or by passing them through containers of liquid dihydrogen at a temperature at 20 K to produce cold neutrons. These moderators are placed above and below the target. The moderated, pulsed neutrons are guided through beam tubes to the various instrument stations. The instruments are unique and a variety of sample environments are available with each instrument providing different environmental conditions, such as high pressures and temperatures needed for research purposes. [2]



Figure 4.1: Layout of Spallation Neutron Source at Oak Ridge National Laboratory in Tennessee, USA.[2]

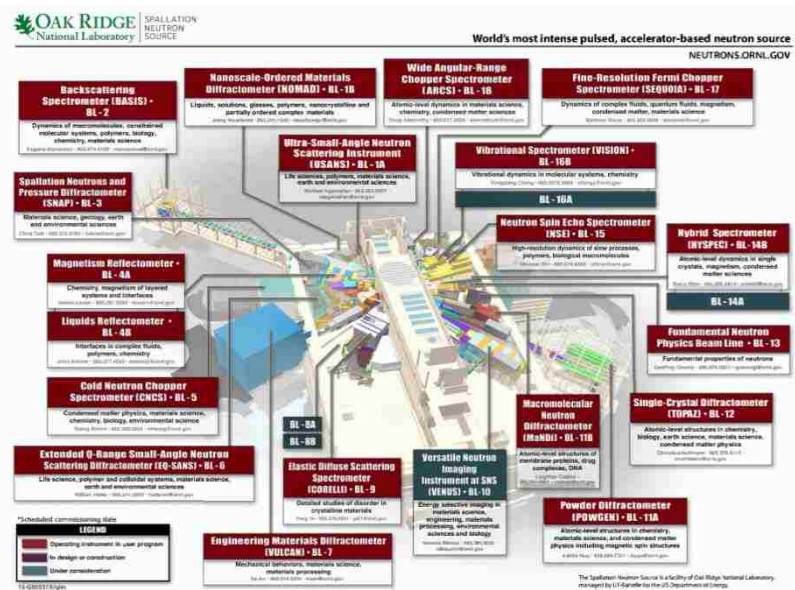


Figure 4.2: Layout of Target building at Spallation Neutron Source at Oak Ridge National Laboratory housing several beamlines.[2]

4.2.2 Beamline 16-B: VISION

The work compiled here was performed at VISION (Beamline – 16B) which is a neutron vibrational spectrometer and here is described briefly. VISION uses neutrons rather than photons as a probe of molecular vibrations. Neutrons provide several advantages over optical spectroscopy such as high sensitivity to hydrogen, ease of computation of vibration spectrum, absence of selection rules, isotopic sensitivity and high neutron penetrability through bulky sample. VISION is the highest resolution broadband INS spectrometer in the world. It is also the world's first high throughput INS instrument. It is designed to study the vibrational dynamics of atoms in molecules and solids; and, by combining a series of diffraction banks, the instrument simultaneously provides structural information. VISION is neutron analogue of an infrared or Raman spectrometer and uses neutrons as a probe for molecular vibrations over a broad energy range (-2 – 1000 meV) while simultaneously recording structural changes using diffraction detectors. The double-focusing crystal arrays focus the neutrons scattered by the sample on a small detector area. Better signal-to-noise ratio and enhanced performance is observed in this inverted geometry instrument by coupling the incident beam of neutrons with two banks of seven analyzer modules which are equipped with curved pyrolytic graphite crystal analyzer arrays that focus on a series of small detectors. The high inelastic count rate is more than two orders of magnitude when compared to similar spectrometers. Two large diffraction detectors with perpendicular scattering angles and backscattering (Q-range 1.3 to 30 \AA^{-1}) offer high resolution. Simultaneous powder diffraction and INS provides a detailed description of sample structure and dynamics in the samples. VISION relies on state-of-art hardware and software to compute vibrational spectra. The simplicity of the neutron-nucleus interaction permits the easy calculation of the neutron vibrational spectrum: mode frequencies and mode intensities. VISION is the first SNS instrument that has computer modeling as integral part

of the data analysis and interpretation of the spectra. Besides, VISION offers various sample environments such as high pressure, *in situ* gas adsorption with custom gas manifold, and low temperatures.[3]



Figure 4.3:VISION instrument : Outside view of the spectrometer chassis, facing upstream (left), real working spectrometer with beam stop (middle), and inside view of the upstream double-focusing crystal array analyzers and corresponding beryllium filter assemblies (right).[3]

As far as the specifications are concerned, the source-to- T_0 chopper distance is 7.6 m and the source to sample distance (the primary flight path) is 16 m. The secondary flight path, or sample-to-detector distance is 0.732 m. With a 45° analyzer Bragg angle, the total analyzer area is close to 0.7 m^2 . To elaborate on the design, the engineer drawing of the instrument is provided.

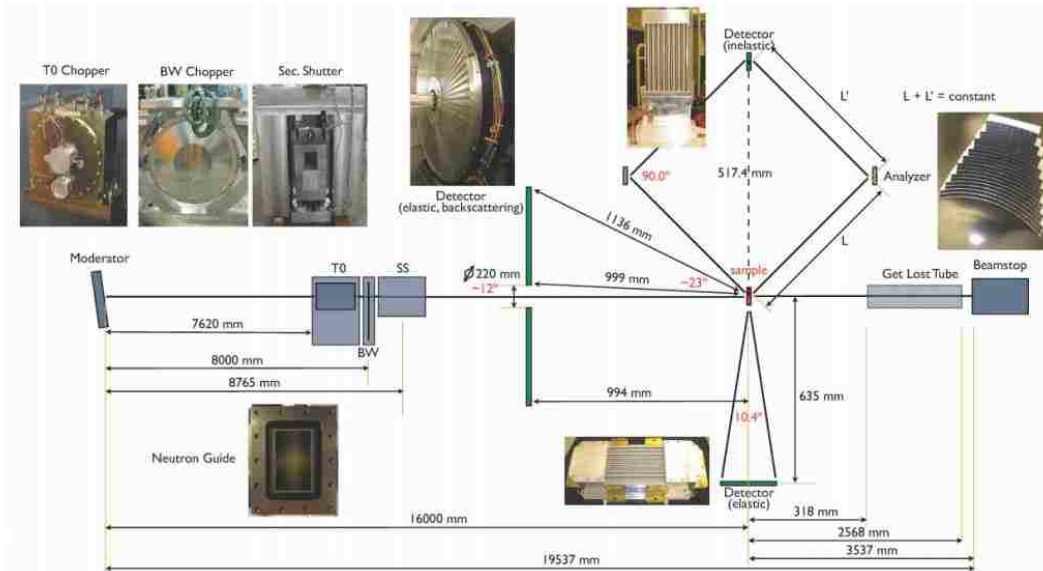


Figure 4.4: Engineer drawing of the VISION Beamline showing the several components of the beamline with their specific orientation and distance from the source. [3]

VISION is an indirect geometry instrument which means that the final energy of the neutron is fixed. The sample is illuminated with white beam of neutrons, the faster neutrons arrive early and the slower ones later. After scattering, the neutrons travel through the secondary spectrometer, set at specific angles and is equipped with curved pyrolytic graphite (PG 002) which selects and focus the neutrons on a series of small detectors and the final energy is selected. The neutrons are diffracted on the analyzers and only those that satisfy the Bragg condition are reflected towards the detectors. After the graphite analyzers, the spectrometer has Beryllium filters, cooled down to 10 K that remove the high order reflections. The final energy of the neutrons selected with this arrangement is ~ 3.5 meV.

The initial energy of the neutrons is calculated using the concepts of time-of-flight. At a pulsed source, each neutron is time stamped at its moment of creation and this makes the time-of-flight technique the method of choice. The aim is to exploit energy dispersion during neutron flight time.

The neutrons with different energies are produced instantly and they have different velocities to travel along the beam tube. This difference in velocities leads to a dispersion of neutrons in the beam tubes when neutrons leave the moderator.

Since the mass of the neutron (m_n , in kg) as are the neutron flight distance (d , in m), for an elastic scattering (diffraction) process the flight time (t , in μs) determines the neutron velocity (v_n) and so its energy (E , cm^{-1}) is:

$$E = \frac{m_n v_n^2}{2} = \frac{m_n}{2} \left(\frac{d}{t} \right)^2 \quad (1)$$

For an inelastic process, the total flight time t_t is given by:

$$t_t = t_i + t_f$$

which is

$$\frac{d_t}{v_t} = \frac{d_i}{v_i} + \frac{d_f}{v_f} \quad (2)$$

$$\frac{d_t}{v_t} = \left(\frac{d_i}{\sqrt{\frac{m_n}{2E_i}}} \right) + \left(\frac{d_f}{\sqrt{\frac{m_n}{2E_f}}} \right) \quad (3)$$

$$t_t = \left(\sqrt{\frac{m_n d_i^2}{2(E_i - E_f)}} \right) + \left(\sqrt{\frac{m_n d_f^2}{2E_f}} \right) \quad (4)$$

where t_t is the sum of the incident (before scattering) t_i and final t_f (after scattering) flight times and so it is necessary to know the distance from the source to the sample d_i , the sample to detector d_f , and either the incident E_i , or final energy E_f as well as the total flight time t_t .

A combination of analyzer and filter define the final energy and a schematic of the instrument is shown in the figure. The dispersion of neutrons is directly proportional to the flight-path and so longer flight-path gives better dispersion which in turn provide a better incident resolution. The resolution features of the final flight path is controlled by the filters and to get a better flux, there should be a good match between initial and final resolution.

Here is a comparison of VISION with Raman/Infra-Red:

VISION	Raman/IR
Measures dynamics of nuclei (direct)	Measures response of electrons (indirect)
Weighted by neutron scattering cross section	Weighted by polarizability or dipole moment
Easy to simulate/calculate	Difficult to simulate/calculate
No selection rules	Selection rules apply
No direct dependence on band gap	Band gap dependent
High penetration (bulk probe)	Low penetration (surface probe)
Easy access to low energy range for librational and translational modes	Energy cutoff is between 200-400 cm ⁻¹ so few modes are invisible
Trajectories in (Q,ω) map	Gamma point

Table 4.2: Brief comparison between the VISION spectrometer with corresponding Raman and IR spectrometers.

4.2.3 Inelastic Neutron Scattering

The neutrons interact with the matter and are primarily scattered. Scattering is the process where the moving particles deviate from their trajectory due to the non-uniformity provided by the medium or matter (scattering nucleus). Scattering can arise due to a single scattering center (random) or by scattering centers placed together to give multiple scattering of neutrons.

Scattering can be elastic, where there is no exchange in energy between the neutron and the scattering nuclei occurs; or inelastic, where an exchange in energy or momentum takes place. The scattered neutron may gain or lose energy. The energy transferred from the neutron excites rotational, vibrational or translational motion of the scatterer.

The scattering of neutrons can be coherent or incoherent. The motions of single atom or molecules such as rotations and vibrations as studied in neutron chemical spectroscopy focuses on the

incoherent scattering which states that the scattered waves from multiple nuclei don't interfere and the position of an atom j , at $t=0$ and $t=t$ are correlated. Since the scattering in incoherent scattering process is same for any scattering angle, it is called as isotropic. On the other hand, coherent scattering is based on interference of scattered waves of a neutron from multiple nuclei. The total number of scatter neutrons is given by scattered intensity which depends on multiple factors such as – magnitude of atomic displacements, the number of scattering atoms in neutron beam and the cross-section of the scatterer. The scattering intensity describes the scattering law and here we will discuss it along with the associated cross-sections.

4.2.3.1 Why INS?

The most established experimental methods for studying the molecular vibrations are the optical techniques of infrared and Raman spectroscopy. A direct comparison with these techniques informs about the advantages INS holds:

INS spectra are readily and accurately modelled:

Measured INS intensities are straightforward related to the atomic displacements of the scattering nuclei, which can often be obtained from simple classical dynamics. Due to absence of selection rules, the electro-opto processes are avoided which makes the modeling easier to perform. Also, modern ab initio methods are used to calculate the band positions and the intensities of complicated systems. Modifications in INS spectrum such as subtraction of a background is also easier. These methods are already established to understand the molecular structure and dynamics making INS a valuable technique.

INS spectra are sensitive to hydrogen atom vibrations

Optical techniques (IR and Raman) are generally more sensitive to vibrations involving the heavier atoms because of the higher number of electrons they contain. The neutron incoherent scattering cross-section of hydrogen is uniquely high, and makes it about ten times more visible than any other atom. This means that INS is a highly quantitative technique in comparison to conventional spectroscopy.

Element	Total neutron scattering cross-section/barn	Total absorption cross-section/barn
¹ H	82.03	0.3326
² H	7.64	.0005
¹⁰ B	3.1	3835.0
¹¹ B	5.77	0.0055
C	5.551	0.0035
O	4.232	0.0001
N	11.1	1.9
Al	1.503	0.231
Au	7.75	98.65
Si	2.167	0.171
Fe	11.62	2.56
Ni	18.5	4.49
Ru	6.6	2.56
Pd	4.48	6.9
Pt	11.71	10.3

Table 4.3: A list of the elements with their respective total neutron scattering cross-section (measured in barn). The higher is the cross-section, the more the element will scatter during the inelastic neutron scattering measurements.[4]

INS spectra are not subject to the rules of optical selection

All vibrations are active in INS and measurable. When scattered, neutrons transfer momentum to the atom and INS measurements are not limited to observation at the Brillouin zone center, as are photon techniques. The measured INS intensities are inter alia, proportional to the concentration of the elements in the sample.

Neutrons are penetrating, photons are not

Neutrons penetrate deeply, into typical samples and pass readily through the walls of containment vessels. INS results are thus naturally weighed to the measurement of bulk properties. Because neutrons are highly penetrating, engineering materials like aluminum and steel can be used for sample containment and for other equipment which may be in the neutron beam, simplifying the design and manufacture of a complex sample environment if desired. In general, neutron scattering measurements can be undertaken at temperatures in the range of 0.05-2000 K, pressures from 10^{-9} to 10^5 bar and magnetic fields up to 7 T. However, the Debye-Waller factor, which enters into the equation via the temperature dependence of the amplitude of vibrations is strongly dependent on the sample temperature and severely suppresses the INS signal, particularly when dealing with hydrogen. This in turn means that most of the INS studies in indirect geometry instruments are performed at temperature of 30 K or lower.

Wide spectral range

INS spectrometers cover the whole molecular vibrational range of interest. The lower energy range, below 49.5 meV (400 cm^{-1}), is readily accessible. At zero energy transfer (as shown in Figure 5), the scattering is elastic; the sample does not exchange energy with the neutron. If

there are processes like diffusion, i.e. stochastic processes that are non-periodic in nature, a broadening of the signal can be observed. This broadening is a similar effect to a Doppler broadening. The neutron can transfer energy with the sample and this manifests itself as a broadening of the elastic peak. This particular case of inelastic neutron scattering is called quasi-elastic neutron scattering. The energies associated with transitions between quantized rotational levels are usually so small that these transitions fall into the much more intense elastic (QENS) peak. However, for sufficiently low mass rotors such as dihydrogen or methyl groups, they may also appear as sharp features in the low energy region of the spectrum. Vibrations of molecules and solids usually go up to $\sim 4000 \text{ cm}^{-1}$ or 500 meV.

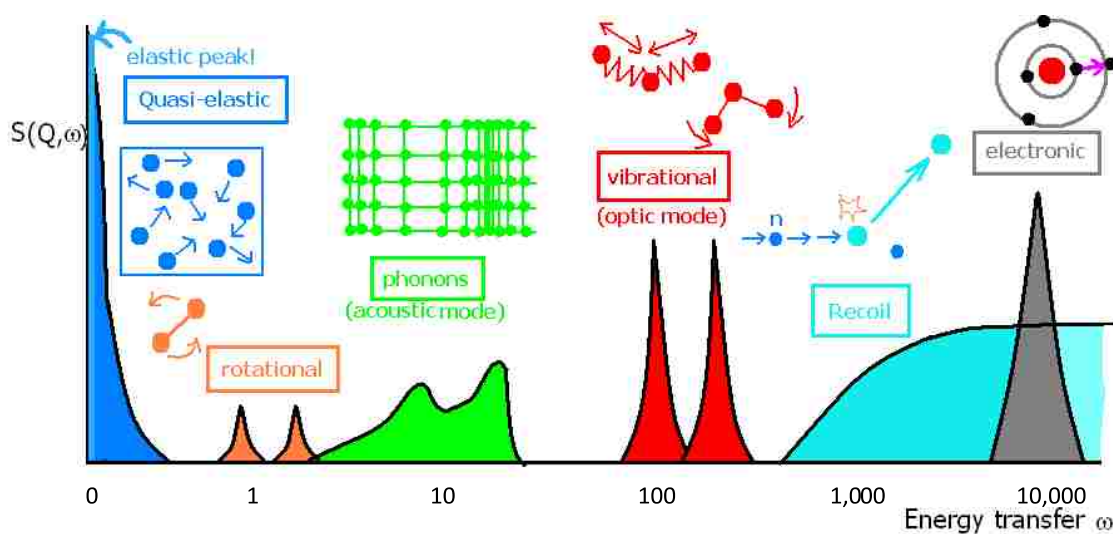


Figure 4.5: Schematic representation of INS showing the different interactions occurring at respective energy transfer.

4.2.3.2 The scattering law

The double differential scattering cross section relates to the scattering law l , $S(\mathbf{Q}, \omega)$:

$$\left(\frac{d^2\sigma}{dE_f d\Omega} \right)_l = \frac{\sigma_l k_f}{4\pi k_i} S(\mathbf{Q}, \omega) \quad (5)$$

In the case of vibrations. For a given atom j in a vibrational mode ν , with the vibrational frequency ω_ν involving an amplitude of vibration $U_{\nu j}$, the spectral intensity is: at 0K

$$S(Q, \omega_\nu)_j^n \propto \frac{\sigma_j (Q \cdot U_{\nu j})^{2n}}{n!} \times \exp\left(-\left(Q \cdot \sum_\nu U_{\nu j}\right)^2\right) \quad (6)$$

where Q is the momentum transfer, σ_j is the cross-section of atom j and n is the order of the final state of the mode excited by the neutron.

If we include thermal population and detailed balance in the equation:

$$S(Q, \omega_\nu)_j^n \propto \frac{\sigma_j \left((Q \cdot U_{\nu j})^2 \left(\frac{\coth\left(\frac{\hbar\omega_\nu}{T}\right) + 1}{2 \times \coth\left(\frac{\hbar\omega_\nu}{T}\right)} \right) \right)^n}{n!} \times \exp\left(-\left(Q \cdot \sum_\nu U_{\nu j}\right)^2\right) \quad (7)$$

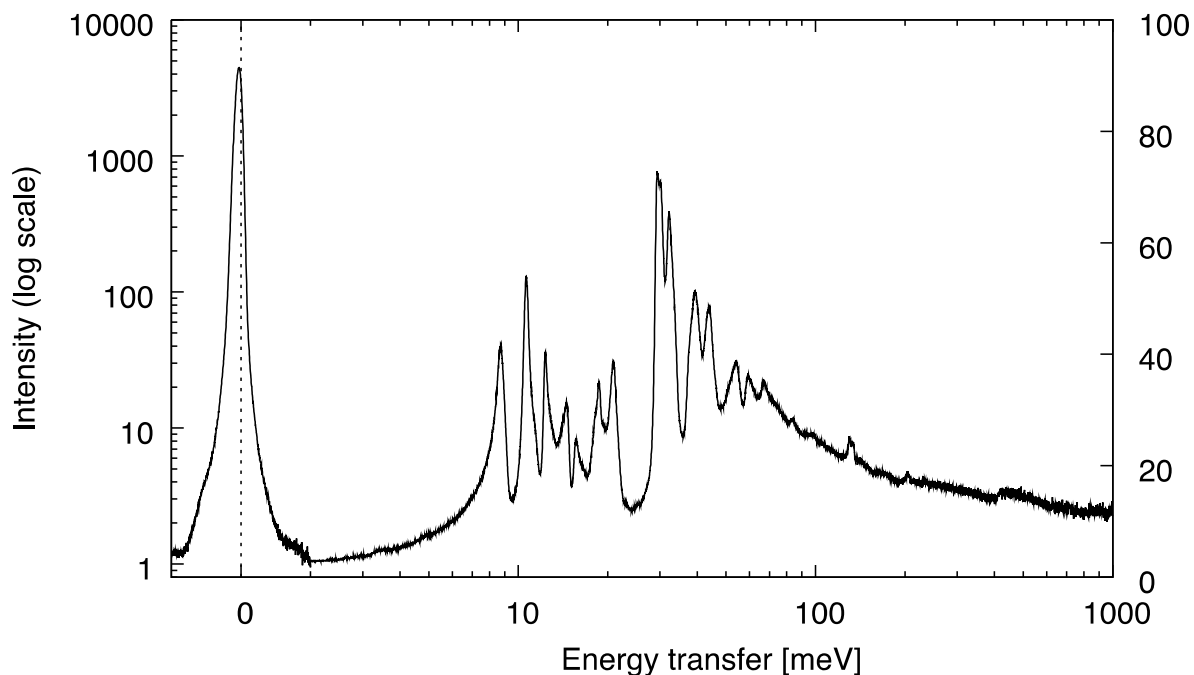


Figure 4.6: The inelastic neutron scattering of a solid, ammonia containing material as function of energy. The energy axis is linear between -1,1 meV range (the QENS signal of ammonia) and logarithmic from 1 meV to 1000 meV where the INS data is. Note that the left axis corresponding to the QENS signal is logarithmic (goes up to 10,000) and the INS data vertical scale is up to 100. The QENS signal is two orders of magnitude higher.

The strength such transitions is governed by atomic displacement which occur in the vibration and transfer of momentum by the neutron. The shift in the atomic positions is determined by the various intramolecular forces and the molecular structure which leads to variation in intensities for the transitions. The intensity of the peak is calculated from the peak height or the area under that peak. Also, a similarity with the Beer-Lambert law in optical absorption can be made as the number of scattered neutrons from the beam is constant for a given element for a fixed or constant mass.

It is easy to compare experimental data with any type of dynamic calculation; nowadays the most common methods are density functional theory-based calculations. The neutron

interaction with a nucleus is a kinematic collision; this is why the interpretation of vibrational scattering from atoms and molecules does not have selection rules and is directly proportional to the amplitude of the atomic displacement.

If we have a solid the amplitude of motion can be approximated, for interpretation purposes, as:

$$\langle U_{\omega_j} \rangle^2 = \frac{\hbar}{2\mu\omega} \times \coth\left(\frac{\hbar\omega}{T}\right) g_j(\omega) \quad (8)$$

Where the U_{ω_j} is the amplitude of motion for atom j at frequency ω and is the phonon density of states (PDoS) of atom j .

The scattering law, now simplifies to, for the first order into:

$$S(Q, \omega)_j \propto \frac{\sigma_j Q^{2n}}{n!} \frac{\hbar}{2\mu\omega} \times \left(\frac{\coth\left(\frac{\hbar\omega}{T}\right) + 1}{2} \right) g_j(\omega) \\ \times \exp\left(-Q^2 \int \frac{\hbar}{2\mu\omega} \times \coth\left(\frac{\hbar\omega}{T}\right) g_j(\omega) d\omega\right) \quad (9)$$

In this interpretation, it can be seen that it is possible to extract a neutron weighted PDoS from an INS spectrum.

4.2.3.3 How to model INS

The modeling of INS spectra from the experimental data is based on the atom positions which is considered to be the primary assumption.

As expected, the atoms undergo various motions such as vibrations, near their equilibrium position and the vibrational motion is studied by the phonon such that all atoms will oscillate at one frequency. This is also known as the normal mode and they can be calculated by various programs such as VASP, CASTEP, QUANTUM ESPRESSO etc.[5-7] The INS spectra can be calculated using the aClimax software from the calculated frequencies and eigenvectors.[8]

4.3 Rotations of the dihydrogen molecule [1]

At low temperatures, in the solid state, small molecules are able to locate enough space in their local lattice to rotate. The free or unrestricted rotations are clearly observed in an INS spectrum as the effects of molecular recoil are seen as broad wing on the high energy side of a vibrational or rotational transition.

The first rotational transition for dihydrogen occurs at 14.7 meV (118 cm⁻¹). The transition occurs at a higher energy than other rotational transitions as a consequence of the low mass of the H₂ molecule and its short bond (0.746 Å), which gives it a high rotational constant, $B_{\text{rot}}^{\text{HH}} = 7.35$ meV (59.3 cm⁻¹). $B_{\text{rot}}^{\text{HH}}$ refers the molecule to its ground vibrational state. Direct excitation of the rotational spectrum of dihydrogen will therefore produce transitions that intrude into the lower vibrational region. The only intramolecular vibrational of dihydrogen has its harmonic fundamental near 545 meV (4400 cm⁻¹).

The rotational energy of the molecule in free space is

$$E_{JM} = E_J = J(J + 1) \frac{\hbar^2}{2I} = J(J + 1)B_{\text{rot}}$$

(10)

Where I is the moment of inertia of the molecule is given as:

$$I = 2 \left(\frac{r}{2} \right)^2 m \text{ and for dihydrogen, } I_{HH} = \mu r_{HH}^2 \quad (11)$$

The rotational constant B_{rot} is:

$$B_{\text{rot}} = \frac{\hbar^2}{2I} \text{ and for dihydrogen } B_{\text{rot}}^{\text{HH}} = \frac{\hbar^2}{2I_{HH}} 7.35 \text{ meV} \quad (12)$$

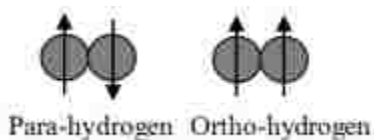
In principle, INS spectroscopy is useful to observe all the rotational transitions of dihydrogen however, some transitions are rather weak since they depend on the coherent neutron scattering cross section of hydrogen (1.76 barn) and these transitions are too weak to be observed in its INS spectrum.

A fortunate consequence of the weakness of these transitions is uniquely beneficial for INS spectroscopy, elastic scattering from ground state parahydrogen (p-H₂) is effectively suppressed. We represent the transition as $J_{0 \rightarrow 0}$. Elastic scattering is observed when no exchange of energy occurs, usually the transition is thus restricted to a single manifold and the cross-section is low. Spin-flip transitions, between the manifolds (i.e. parahydrogen to orthohydrogen (o-H₂)), are controlled by the incoherent cross section of hydrogen, 80.3 barn, and are enabled by spin exchange with neutron, $I_n = 1/2$.

The reason for the strength of the $J_{0 \rightarrow 1}$ feature in the INS spectrum of dihydrogen is its access to the incoherent scattering cross section. The strong features of the dihydrogen INS spectrum are, therefore, the $J_{0 \rightarrow 1}, J_{0 \rightarrow 3}$ etc and the $J_{1 \rightarrow 2}, J_{1 \rightarrow 4}$ etc transitions. In order to take advantage of this, the experiments are usually performed using parahydrogen that is prepared separately, using a special equipment at the VISION beamline, we usually have only $J=0$ as the initial state. A full treatment of the INS spectrum of dihydrogen might take as its starting point of the Young-Koppel model which has seen some recent refinement. [9]

4.3.1 Ortho and para hydrogen

Ortho and para-hydrogen are the two molecular species for dihydrogen due to the quantum restrictions on the symmetry of rotational wavefunction. The dihydrogen nucleus has half-integer spin and is a fermion. The quantum mechanical description meets the Fermi statistics rules. This leads to the occupation of certain states only and also puts a symmetry requirement on molecular wavefunction. Identical nuclei are indistinguishable; their exchange can change the sign of the total wavefunction.



The antisymmetric wavefunction is described by the even values of J and it must be paired with the symmetric spin wavefunctions. So this gives us the only allowed rotational states of antiparallel or spin paired dihydrogen as $J = 0, 2, 4$ and so on. This is called as **para-hydrogen**. For each acceptable J , a total of $2J+1$ spin states can be observed and the only allowed spin state for the ground state of para-hydrogen is given by $J = 0$.

Likewise, the symmetric wavefunction is described by the odd values of J and it must be paired with the antisymmetric spin wavefunctions. So, this gives us the only allowed rotational states of parallel or unpaired dihydrogen as $J = 1, 3, 5$ and so on. This is called as **ortho-hydrogen**. For each acceptable J , a total of $2J+1$ spin states can be observed.

In natural state, the ortho and para-hydrogen species are spin trapped as the transitions between the spin-paired and unpaired are negligible. In the natural state, dihydrogen is seen as a mixture of these two stable species, where there is little exchange between the two populations. However there is a slight difference in the physical properties of two states. The ground state rotational energy of dihydrogen, zero, is the minimum rotational energy for para-hydrogen molecules. On the other hand, the minimum energy of ortho-hydrogen molecules is $2B_{\text{rot}}$. In states are significantly occupied and in proportion to their degeneracies, namely 1 and 3. Dihydrogen in gaseous state is so a mixture of 25% para-hydrogen and 75% ortho-hydrogen.

Liquid dihydrogen below its boiling point converts to para-hydrogen and this process is expedited by a suitable catalyst. When the liquid is brought into contact with a paramagnetic catalyst the conversion is achieved at a faster rate and time constant going into seconds. A simple approach to obtain milliliters of liquid para-hydrogen is by using nickel as a catalyst during the liquification process of dihydrogen. The conversion container should have a slight temperature gradient such that the convection will remove the present para-hydrogen from the catalyst leaving the catalyst exposed to other ortho-molecules. Equilibrium can be achieved at the boiling point of dihydrogen however it may take few hours. There is such a para-hydrogen converter installed in the VISION cave that generates almost pure parahydrogen required by the researchers for their experimental needs.

4.3.2 An outline of the INS spectrum of dihydrogen

An INS spectrum of solid dihydrogen at 5 K obtained with the VISION instrument is shown in Figure 7. It consists of a sharp, intense transition centered at 14.7 meV (118 cm^{-1}); to higher energies there is a strong broad shoulder with some weak overlaying features. The shoulder, centered at $\sim 37.2 \text{ meV}$ (300 cm^{-1}), is overall smooth. But for energies below the rotational transition, a sharp feature is observed. Intensity here is due to the displacement of rotational transitions by the translational recoil of the dihydrogen molecule.

When the solid dihydrogen is heated, the recoil effects become more prominent. Close to the melting point (around 15 K) the transition line diminishes to an edge. In liquid, the recoil occurs below the rotational transition and the edge continues to disappear.

The interaction potential provided by the surface/sites/etc controls the formation of spectra. Stronger and weak interactions with the interaction potential can be observed due to this effect. The effect of recoil on the spectrum decreases when the hinderance to translations is increases and this leads to an increase in the relative strength of the relative strength of the rotational line, when compared with the shoulder. When different molecules are under varying isotropic potential field, there could be a noticeable change in the rotational transitions. For instance, it might get broadened or shifted. So, when the interacting potential is stronger, the M degeneracy is lifted under the influence of strong anisotropy and could lead to huge changes in the transitions. And for weaker anisotropy we can also observe some broadening in the transitions.

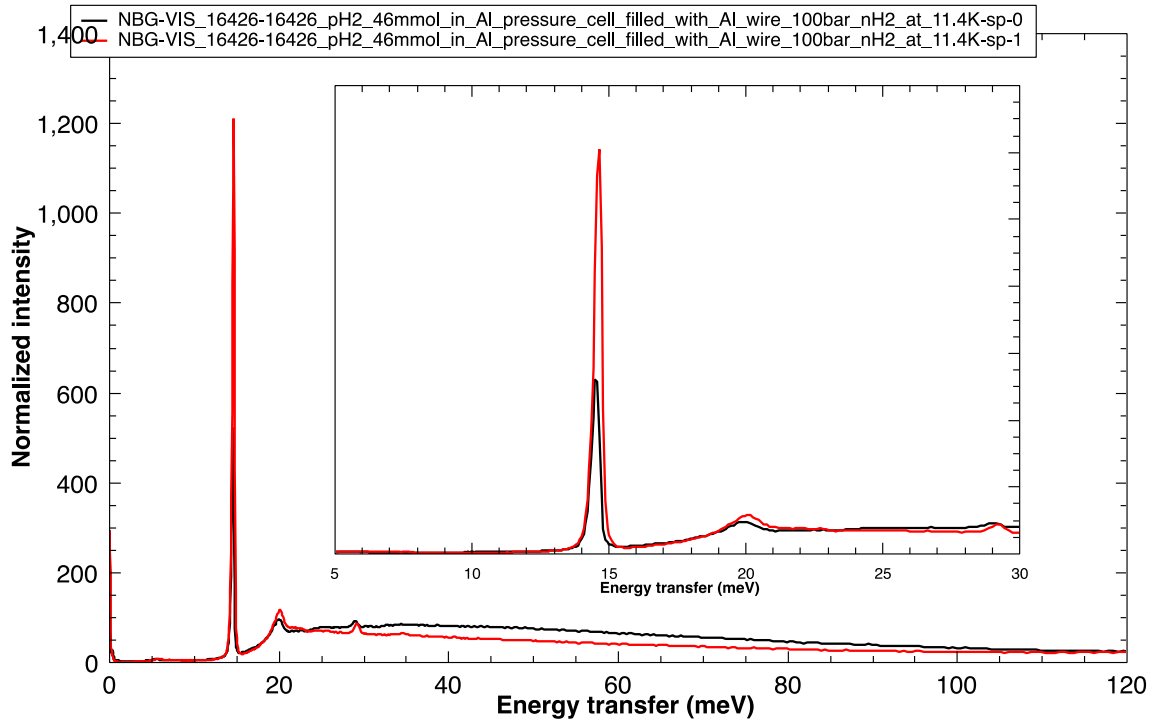


Figure 4.7: INS Spectra of solid parahydrogen at 5K as measured in VISION) The insert in the figure shows a zoomed-in area The red trace is the forward scattering bank and the black trace is the back-scattering bank. The rotational line of dihydrogen is the main peak at 14.7 meV (118 cm^{-1}). The peak around 20 meV corresponds to the translational vibration of the center of mass (CoM) of the parahydrogen molecule. The higher rotational transitions are affected by the recoil of the dihydrogen molecule

4.3.3 The INS spectrum of dihydrogen in an anisotropic potential

When dihydrogen is adsorbed on a surface, where x - and y - axes are defined in the plane of the surface, the unique direction of the anisotropic potential is taken on the z -axis. Now the rotational states probing the near surfaces will be perturbed when the out of plane forces along z , securing the dihydrogen to the surface increase in strength. So, the total energy of the system in polar coordinates by separation can be given as:

$$V(z, \theta, \phi) = V_0 + f_{ads}(z - z_0)^2 + V(\theta, \phi) \quad (13)$$

where the minimum isotropic potential is V_0 and relies on the distance of the molecule to the surface, z . The potential that governs the rotation of the molecule is given as considering only the orientational terms:

$$V(\theta, \phi) = \left[a + \frac{b}{2} \cos 2\phi \right] \sin 2\theta \quad (14)$$

where the polar angle, the angle between the H-H bond and the surface normal z , is given by θ and the azimuthal angle is ϕ . The relative weights of the potential is given by a and b and 2ϕ is the symmetry of the field matches the C_2 molecular symmetry. The Schrodinger equation for the system is given by the system by treating the orientational potential as a perturbation and expanding it in spherical harmonics and the resulting matrix can be diagonalized for determination of energy states of the perturbed rotor. When $a < 0$, then the potential $V(\theta, \phi)$ is most attractive when the dihydrogen molecule is parallel to the surface as shown in the figure and if $a > 0$ the molecule tends to align perpendicular to the surface.

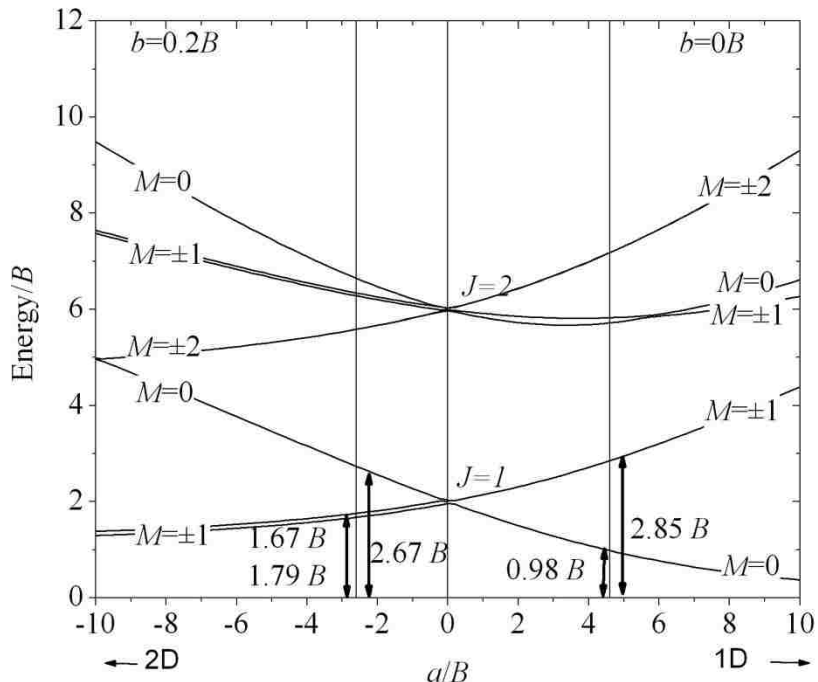


Figure 4.8 depicts the range of a/B and how the potential changes accordingly. The values of ' a ' determines the alignment of the dihydrogen molecule with the surface.

4.4 Motivation:

The importance of physical storage of dihydrogen (H_2) is introduced in chapter 2 and here we present the usage of one of the simplest, yet important, surface for dihydrogen interactions – graphene. Being discovered in 2004 by Dr. A. Geim and Dr. K. Novoselov as a layer with atomic thickness, graphene continues to provide striking surface chemistry due to its large specific surface area and exceptional chemical, electrical, mechanical and thermal properties.[10] The atomic thick graphene layer exists as a hexagonal lattice of carbon bonded in sp^2 hybridization with a bond length of 1.42 \AA . When this allotrope of carbon is stacked, it gives rise to graphite, where the interplanar spacing is 3.35 \AA . Now graphene, the new rising star of the carbon family has established its position with its remarkable properties as displayed in the table later and so some understanding of the interaction of dihydrogen with graphene is therefore of interest, not only in

the context of use of carbonaceous materials for dihydrogen storage, but also from the standpoint of fundamental surface science. To explain its use in the fundamental surface science, remember that the interaction of dihydrogen gas with carbon is weak and since the structure of graphene only consists of carbon in hexagonal lattice, it can act as a good model to test the validity of dihydrogen in an anisotropic potential. Here, the graphene isn't processed with other chemical or thermal treatments (such as KOH wash) to enhance the surface area but repetitive washing with water is performed to obtain a continuous and smooth layers of graphene. [11]

Other simple carbonaceous materials such as graphite – the cheapest source of carbon or graphoil [12, 13] – which is flexible graphite with slightly more use as gasket material, aren't interesting to study the dihydrogen – carbon interactions primarily because of two reasons: (a) these materials have significantly low specific surface area, around 20 m²/g which as we can imagine won't be sufficient to adsorb enough quantities of dihydrogen gas because amount of gas adsorbed scales with specific surface area and (b) the accessible surface is highly non-uniform. Since the focus is to study the adsorbate-adsorbent interactions only, any non-uniformity in the surface will lead to different (attractive or repulsive) interactions thereby defeating the purpose to study the fundamental surface science. Although closely related, materials such as graphite oxide, were not selected because the functionalization results the presence of functional groups (carbonyls, hydroxyls, and epoxides) on the graphite oxide surface could provide additional adsorption sites for dihydrogen and provide non-uniform surface. [14, 15]

4.5 Earlier work on carbonaceous materials and dihydrogen interactions

To understand the science of adsorption on graphene, theoretical efforts have been put by researchers.[16-24] In one of the studies, hydrogen cluster formation on graphite was studied

which isn't involve diffusion but preferential sticking on the surface which leads to formation of larger clusters. [19] Another study to understand the adsorption of dihydrogen on graphene surface employed plane-wave based density functional theory calculations and computed the binding energies up to four atoms of hydrogen with different possible configurations. [20] Xia *et al.* applied non-equilibrium thermodynamics methods to explain the adsorption and desorption of molecular hydrogen and pointed out the need for high quality temperature controlled desorption data for quantitative analysis. [25] A density functional theory study on layering in hydrogenated graphene for electronic structure and magnetic properties was also performed and single-layered, bi-layered, and multi-layered graphene was compared with most stable configuration of low hydrogenated graphene. [21] Balog *et al.* demonstrated the opening of bandgap by adsorption of dihydrogen and mentioned the need of more experimental evidence for graphene-based electronic devices. [22] A recent study on perforated graphene demonstrated a joint effort of experimental data and grand canonical Monte Carlo simulations and estimated ~6.5 wt% hydrogen uptake at 77 K. [23] Zhang *et al.* studied the effect of temperature on hydrogenation in graphene by molecular dynamics calculations. Formation of hydrogen pairs and cleavage of C=C bonds as additional C-H interactions were studied. [24] Application of KOH treatment on reduced graphene oxide was mentioned recently with a high specific surface area of ~3400 m²/g. A pore volume of 2.2 cm³/g was reported which holds to improve dihydrogen storage. [26] Rotational and translational motions of immobilized dihydrogen in confined pores in microporous carbon at broad pressures and temperatures range were studied by Inelastic Neutron Scattering (INS) to investigate gas-matrix interactions. [26]

4.6 Materials and Methods:

A modified version of Hummers-Offerman method was used to synthesize graphite oxide, which was then thermally exfoliated to yield graphene.[27] Graphite powder (Company name, 99.99% purity) was stirred overnight at room temperature in a mixture of 250 ml sulfuric acid (Sigma-Aldrich) and 100 ml 50% hydrogen peroxide (Sigma-Aldrich). The suspension was filtered, and the graphite was washed several times with deionized water prior to drying in a vacuum oven at 110 °C. 6.0 g of this graphite powder was added to a mixture of 360 ml sulfuric acid and 40 ml 85% phosphoric acid (Amersco) to get a black colored suspension. 18 g potassium permanganate (Sigma-Aldrich) was added slowly with continuous stirring to avoid overheating. The reaction was then heated to 50 °C and stirred for 12 hours. An additional 9 g potassium permanganate was added and the mixture was stirred for another 24 hours. The reaction was cooled to room temperature and slowly poured onto 0.5 L ice with constant stirring. 30% hydrogen peroxide (Sigma-Aldrich) was poured in small increments (~10 ml), resulting in a bright orange-yellow colored solution. This mixture was sonicated for 1 hour and then vigorously washed by centrifugation with deionized water, 5% hydrochloric acid (Fisher Chemicals), and acetone (Fisher Chemicals). The final product was dried in vacuum oven at 50 °C for 12 hours to give 3.9 g of graphite oxide.

This graphite oxide was then thermally exfoliated in small batches in a tube furnace set to 1000 °C under inert atmosphere to get a 1.6 g of black graphene powder.

To study the interactions of dihydrogen on graphene, a clean, homogeneous and smooth graphene surface is required. There are different synthesis options being investigated by researchers as mentioned in introduction such as KOH treatment, chemical exfoliation, chemical

decoration etc. The scotch-tape method used by Geim and Novoselov for discovery of graphene isn't preferred here due to the need of large amounts for inelastic neutron studies and other characterization. One of the good characteristic for any adsorbent is to have a better surface area and the KOH treatment of graphene has proven to enhance the surface area of graphene significantly. However, KOH treatment also leads to big and random 'holes' on the surface which doesn't end up on giving a homogeneous surface. These random inconsistencies aren't desirable to study the weak dihydrogen interaction and so we focused on the Hummers-Offerman method for bulk synthesis. To describe it briefly, this synthesis method uses sulfuric acid and potassium permanganate solutions for oxidation purposes to give graphite oxide gel. This gel after drying is exfoliated (chemically or thermally) to yield graphene.

Instead of using the Hummers-Offerman method as described in various research articles, we worked by adding a few steps to get a better surface for the dihydrogen studies. Firstly, we pre-treated the graphite (99.99% pure) with concentrated sulfuric acid and 50% hydrogenperoxide solution to clean the graphite surface by removing all the impurities which might be present. A small amount of impurity will lead to a lower yield of graphite oxide and hence graphene. Also, the impurities which are still present in graphite oxide might lead to an improper exfoliation as well. Impurities such as Fe, Mn, K, or other metal present in the graphite batch lead to formation of metal salts which are difficult to remove if trapped. After cleaning the precursor with acidic solution, we washed it excessively with deionized water to remove any sulfuric acid or hydrogen peroxide traces. The water was removed by drying the graphite batch in vacuum oven pre set to 110 C for several hours.

The other difference with Hummers-Offerman method is addition of extra potassium permanganate. When potassium permanganate is added to the graphite-acid gel step of the method,

excessive bubbling is observed indicating the oxidation reaction. Now as per the method, 18 g of potassium permanganate is required to completely oxidize graphite to be later recovered as graphite oxide but we observed oxidation continuing when we kept on adding potassium permanganate beyond 18 g. Before exceeding the required amount, the solution was kept stirred to give ample amount of time for complete reaction. Once the bubbling stopped, potassium permanganate addition was stopped. This extra 9 g of potassium permanganate leads to complete oxidation and higher yield of graphite oxide.

Besides these chemical treatment, we focused on excessive washing of the intermediary graphite oxide as we observed presence of K, Mn, Fe, and Sr in graphite oxide before washing. Excessive washing with deionized water, acetone, and mild hydrochloric acid solution helped in removing the major impurities. Only after confirming the removal of impurities we proceeded for thermal exfoliation to get the graphene. Thermal exfoliation was preferred over chemical exfoliation even though chemical exfoliation sounds consistent because, higher surface area was measured after thermal exfoliation. Chemical exfoliation with LiAlH_4 and other reagents was a bit time consuming and didn't lead to consistent surface area measurements.

So, the method employed to extract graphene was quick, with higher yield, consistent with surface area measurements and a well-dispersed product was obtained.

4.7 Characterization:

Structure determination by Powder X-ray Diffraction (PXRD) was performed on a PANalytical X'Pert X-ray diffractometer in reflection geometry mode with monochromated $\text{Cu K}\alpha_1$ ($\lambda = 1.5425 \text{ \AA}$) and $\text{K}\alpha_2$ ($\lambda = 1.5442 \text{ \AA}$) incident radiation operated at 40 kV and 40 mA. The X-ray diffraction patterns were collected over a 2θ range of 5° to 70° . Fourier Transform Infra-

Red spectroscopy (FTIR) was carried using a JASCO 6100 spectrometer with attenuated total reflectance method. A Gemini VII gas sorption analyzer from Micromeritics was used to measure the BET (Brunauer-Emmet-Teller) surface areas of the samples at 77 K using a liquid nitrogen dewer for temperature control. Prior to the BET surface area measurements, the samples were activated to 150 °C for 24 hours under dynamic vacuum. The BET range for surface area measurement was set from 0.05 P/P₀ to 0.3 P/P₀. Elemental analysis to examine the purity of graphite oxide and graphene was performed by a bench top MiniPal4 Energy-Dispersive X-ray Florescence spectrometer (ED-XRF) with a rhodium target. Inelastic Neutron Scattering (INS) data was measured at beamline-16B (VISION). Approximately 0.7 g of sample was transferred to a cylindrical aluminum sample can to fill the entire volume and sealed using aluminum foil. After measuring the blank, gas was dosed into the can at 35 K using a custom-built gas dosing manifold. Para-hydrogen was prepared at 5 K by liquefying dihydrogen gas using OXISORB[®] catalyst in an in-house converter. The sample was cooled to the base temperature (~5 K) before measuring the inelastic neutron scattering data.

4.8 Results and Discussions of para-hydrogen loadings on graphene

Since the inelastic neutron scattering cross-sectional area of para-hydrogen is significantly larger than ortho-hydrogen, we have used pure para-hydrogen for the experiments.[4] The conversion of normal-hydrogen to para was done in the in-house catalytic converter as explained above. To study the interaction of dihydrogen molecules with the graphene surface, we have measured INS spectrum at increasing coverages of dihydrogen. The coverage of dihydrogen on graphene was as follows: 0.1 ML, 0.25 ML, 0.5 ML, 0.75 ML, 1.0 ML (ML: Monolayer), and a final saturation was observed with 1.83 ML of dihydrogen on graphene surface. The data

presented in the Figure 4.9 is analyzed after subtracting a general background (least square fit to a polynomial order 4) that takes into account the smooth recoil of the dihydrogen rotation signal. Looking superficially at the Figure 4.9, we have energy transfer from 0 to 1000 meV and we observe a broad feature converting to a sharp and narrow feature (the rotational peak) at 14.4 meV when we increase the amount of para-hydrogen in the sample, which corresponds to para \rightarrow ortho transition *i.e.* $J=0$ to $J=1$ rotational transition of the adsorbed molecules. The recoil peaks are observed at higher energy transfer and they correspond to higher order rotational transitions. The first recoil peak corresponds to the scattering from the molecules going a rotational transition from $J=0$ to $J=1$ states. Remember that the intensity of the INS spectrum is directly proportional to the amount of dihydrogen adsorbed on the sample. A zoomed version of the following figure is displayed in figure 4.10.

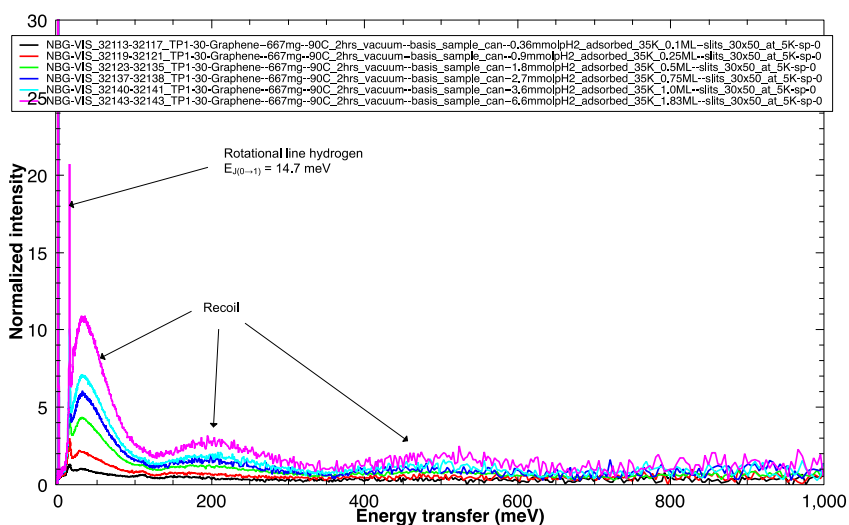


Figure 4.9. The INS spectra of parahydrogen dosed on graphene at 5K as function of loading. The arrows point to the most important features, the rotational line and the recoil features.

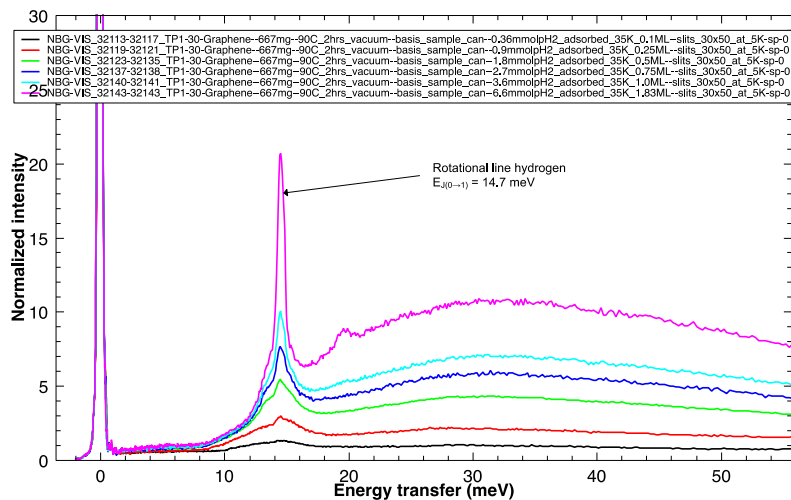


Figure 4.10: Zoomed-in spectra of parahydrogen as function of loading.

The above Figures 4.9 and 4.10 provide information on the nature of how hydrogen gas molecules interact with the surface. Recall that, when H_2 molecules interact with a surface or with a specific binding site, the rotational transition may shift in value, or can split into multiple transitions. As reported numerous times, the splitting is due to the presence of an anisotropic potential field. A downward shift is due to elongation of H-H bond and a consequent decrease in the value of the rotational constant B . In other words experimentally observed shifts in the quantized energy for dihydrogen rotation decreases due to redistribution of the electronic charge density of the adsorbed dihydrogen molecules due to interaction with the surface. An adsorbed H_2 molecule has an induced dipole moment which is responsible for the dihydrogen – surface interaction. So, a distortion or redistribution of the electronic charge would lead to a new proton-proton distance in dihydrogen leading to a new value for the rotational constant. So, the shape of the rotational feature and the shift from the ‘free’ rotation (centered at 14.7 meV) helps to describe the interaction with the surface.[28-34]

In the case of dihydrogen adsorption at the graphene surface considered here, for the low coverage of 0.1 ML, we observe a broad feature spread within 10 – 20 meV. This feature starts to converge at higher loadings and seems to center at ~ 14.3 meV but a precise and reliable peak deconvolution is required to completely understand the spectrum and therefore, deconvolution of rotational line of para-hydrogen for the loadings of 0.1 ML, 0.25 ML, 0.75 ML, and 1.8 ML is performed and shown in the Figure 4.11. Note that the x -axis is the shift from the 14.7 meV in units of μeV . The deconvolution of the experimental signal was performed using the QClimax software. The rotational signal of pure solid para-hydrogen is measured and used as the unperturbed signal. The model uses five Lorentzian functions that are used to minimize using the least square difference between the experiment and the model. The loadings are represented in the Figure and the parameters obtained after fitting are shown in the table below.

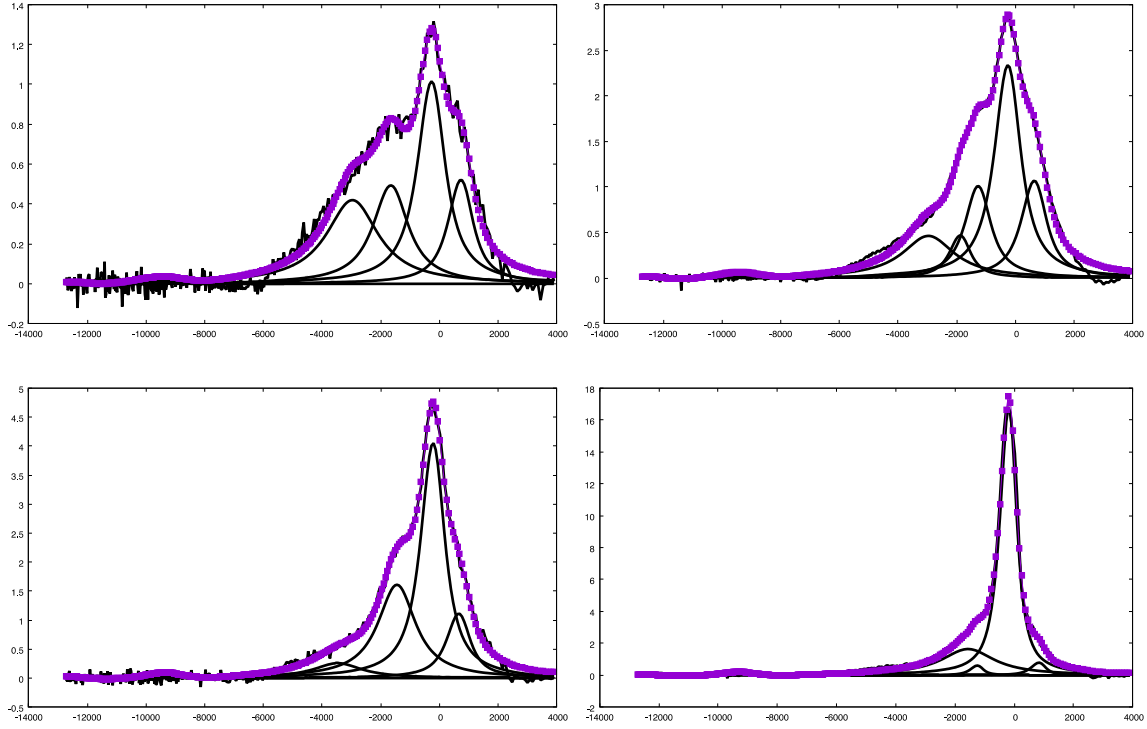


Figure 4.11: Deconvolution of the rotational line of para-hydrogen for the 0.1 ML, 0.25 ML, 0.75 ML and 1.8 ML loadings. Note that the x -axis corresponds to the shift in the shift from the rotational line (14.7 meV) of dihydrogen in μeV .

Loading (ML)	Peak Center (meV)	Peak Area	Peak Area/Total Area	Peak Width (meV)
0.1	11.220 \pm 0.108	0.297 \pm 0.091	0.176 \pm 0.054	0.824 \pm 0.127
	12.700 \pm 0.095	0.465 \pm 0.213	0.275 \pm 0.126	0.702 \pm 0.223
	13.497 \pm 0.101	0.084 \pm 0.132	0.050 \pm 0.078	0.292 \pm 0.335
	14.376 \pm 0.025	0.529 \pm 0.111	0.313 \pm 0.066	0.411 \pm 0.080
	15.342 \pm 0.049	0.317 \pm 0.066	0.187 \pm 0.039	0.430 \pm 0.066
0.25	11.200 \pm 0.100	0.309 \pm 0.000	0.097 \pm 0.000	0.968 \pm 0.000
	12.743 \pm 0.098	0.000 \pm 0.000	0.000 \pm 0.000	0.201 \pm 0.000
	13.165 \pm 0.021	1.115 \pm 0.000	0.350 \pm 0.000	0.738 \pm 0.000
	14.390 \pm 0.005	1.245 \pm 0.000	0.391 \pm 0.000	0.441 \pm 0.000
	15.281 \pm 0.010	0.514 \pm 0.000	0.161 \pm 0.000	0.383 \pm 0.000

0.5	11.200 \pm 0.153	0.316 \pm 0.094	0.077 \pm 0.023	0.963 \pm 0.168
	12.700 \pm 0.007	0.424 \pm 0.174	0.103 \pm 0.042	0.546 \pm 0.166
	13.355 \pm 0.038	0.640 \pm 0.227	0.156 \pm 0.055	0.411 \pm 0.121
	14.411 \pm 0.013	2.143 \pm 0.241	0.521 \pm 0.059	0.396 \pm 0.040
	15.286 \pm 0.052	0.586 \pm 0.134	0.143 \pm 0.033	0.387 \pm 0.063
0.75	11.200 \pm 0.000	0.400 \pm 0.000	0.078 \pm 0.000	1.000 \pm 0.000
	12.745 \pm 0.000	0.000 \pm 0.000	0.000 \pm 0.000	0.119 \pm 0.000
	13.225 \pm 0.000	1.382 \pm 0.000	0.270 \pm 0.000	0.668 \pm 0.000
	14.428 \pm 0.000	2.918 \pm 0.000	0.570 \pm 0.000	0.358 \pm 0.000
	15.366 \pm 0.000	0.420 \pm 0.000	0.082 \pm 0.000	0.271 \pm 0.000
1.0	11.200 \pm 0.196	0.432 \pm 0.242	0.056 \pm 0.031	1.000 \pm 0.180
	13.097 \pm 0.000	0.010 \pm 2.166	0.000 \pm 0.280	0.870 \pm 0.000
	13.231 \pm 0.150	1.412 \pm 2.407	0.183 \pm 0.312	0.590 \pm 0.265
	14.439 \pm 0.004	5.613 \pm 0.140	0.726 \pm 0.018	0.213 \pm 0.007
	15.455 \pm 0.041	0.269 \pm 0.067	0.035 \pm 0.009	0.188 \pm 0.077
1.8	11.200 \pm 0.000	10.432 \pm 0.000	0.126 \pm 0.000	1.000 \pm 0.000
	12.859 \pm 0.000	6.900 \pm 0.000	0.084 \pm 0.000	1.000 \pm 0.000
	14.300 \pm 0.000	9.332 \pm 0.000	0.113 \pm 0.000	1.000 \pm 0.000
	14.423 \pm 0.000	55.836 \pm 0.000	0.677 \pm 0.000	0.003 \pm 0.000
	14.489 \pm 0.000	0.000 \pm 0.000	0.000 \pm 0.000	0.021 \pm 0.000

Table 4.4: Rotational peak shape parameters (shape, area, width) for all the para-hydrogen loadings on graphene. Data in the table is used to generate the figure 11. “ML” for loading represents the fraction of a full monolayer of adsorbed H₂.

Now, with the spectra broken into individual peaks, we can address the important features. Starting with the lowest coverage of 0.1 ML there two important features needs to be addressed. First, the decrement (shift) in the rotational peak is indicative of interaction of dihydrogen with the graphene surface, possibly at the ring. This interaction is quite strong due to the broad feature and the shift of the rotational peak. Remember that a sharp peak at 14.7 meV is indicative of free and unhindered dihydrogen molecules with J=0 to J=1 transition. For this first dose of para-hydrogen, the entire surface of graphene is available and hence this feature should be associated with the

most favorable site for hydrogen binding. This broad feature in the spectra (spread between 10 – 20 meV) is visible for 0.25 ML coverage as well indicating that hydrogen molecules are easily able to find other sites on graphene surface. As the dose is increased and when we saturate the surface with 1.83 ML of para-hydrogen, the other feature to note is that the broad spread gets quite sharp at higher coverages (greater than one monolayer) which informs that now H₂ molecules are weakly interacting with the graphene surface and so are behaving almost as a free rotor. The final dose of para-hydrogen now encounters a layer of para-hydrogen already adsorbed on the surface and so it doesn't interact directly with the surface. Note that now the sharp peak is now centered at ~ 14.42 meV and so there is a positive shift (compared to the first dose of 0.1 ML) in this peak at higher coverage. This positive shift at higher coverages is indicative of the weak interaction between the para-hydrogen and graphene and any other additional dose will lead to further positive shift away from 14.3 meV.

Looking closely at the shape of rotational peak for 0.1 ML, we can see a shoulder at 14.3 meV and one shoulder at around 14.5 meV. These shoulders, as mentioned before, are indicative of interactions of dihydrogen close to one another and we can observe that graphene offers three close binding sites for dihydrogen molecules.

So, the INS spectrum, deconvolution of the peaks and the associated table help in determining the effect of coverage on the broadening and hence the interaction of the dihydrogen molecules with the surface of graphene. Again, from the figure below, it can be concluded that the peak center of the main rotational line gets closer to a definite value as the coverage on the graphene increases. This is due to the fact that as one monolayer of dihydrogen is adsorbed on the surface, the second layer doesn't 'see' the surface and hence is weakly interacting. This accounts for a much higher mobility (partial mobility or liquid-like mobility) of the hydrogen gas molecules.

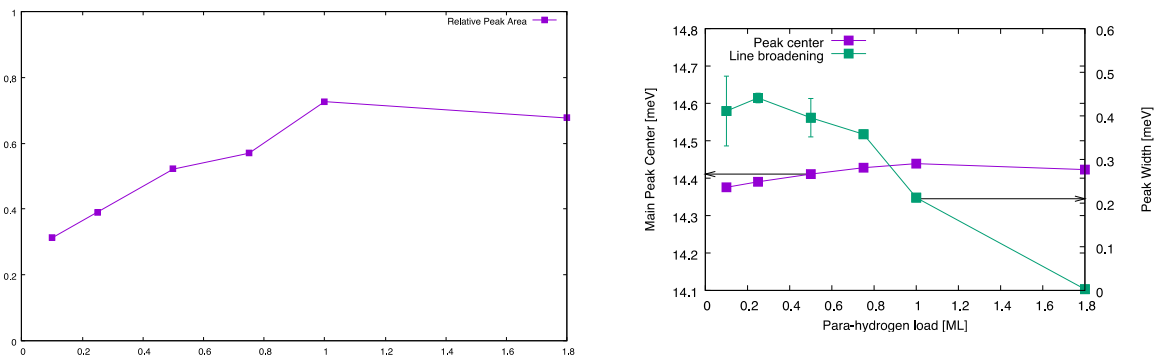


Figure 4.12: Relative peak area (Area of main peak/total peak area) for all coverages.

Figure 4.12 displays the position of the main peak ~ 14.3 meV, (the fourth peak from the tabular values) as a function of para-hydrogen loading (on the left axis) and the corresponding peak broadening (on the right axis). The peak center drifts as the coverage increases which is attributed towards the weak interaction of dihydrogen with the saturated surface of graphene. After the completion of first monolayer, it stays constant (as expected) because now the attractive interaction between the para-hydrogen has saturated the graphene surface and dosage of the gas cannot be adsorbed to the surface directly Adsorption onto the monolayer covering the surface is expected to be similar to the interactions already well-studied in solid hydrogen. The peak broadening as expected converges, in this case from a spread of ~ 0.4 meV to 0.003 meV.

To conclude, dihydrogen adsorbs to the most energetically favorable sites at lower coverages. The areas of the lower energy peak as presented (below 14.3 meV) are around twice the areas of the peak above 14.4 meV. This agrees with the model presented above [**The INS spectrum of dihydrogen in an anisotropic potential**] and corresponds to a 2D rotor with a rotational barrier of around 4 meV. The broadening of the unperturbed rotational line is negligible

above 1 ML. This can be interpreted as: there is another site where the hydrogen molecule can adsorb. Above 1ML the dihydrogen molecule does not see the surface anymore and it has almost no broadening and behaves 'freely'.

Now let us consider interaction of para-hydrogen with a strong interacting surface or potential as provided by VSB-5:

4.9 Results and discussions of para-hydrogen loadings on VSB-5

4.9.1 Kubas Complex

In 1984 Kubas reported for the first time the presence of dihydrogen complexes in $W(CO)_2(PCy_3)_2(H_2)$. As explained by Kubas, a dihydrogen molecule can interact with a transition metal complex without breaking the H-H bond. The interaction is observed as a coordination complex with H_2 acting as a ligand. More information on the transition-metal complexes or the Kubas complexes is provided in a recent review by Kubas. A Kubas complex has the following features: (a) There is a three center interaction from the hydrogen's σ orbital to an empty metal d-orbital, (b) A π back donation from the occupied metal d-orbital to σ^* antibonding H_2 orbital, (c) A short H-H bond lengthening but not leading to bond cleavage and (d) A low metal co-ordination T-shaped structure.

While working on the $W(CO)_2(PCy_3)_2(H_2)$ complex, Kubas observed the H-H bond length increased to 0.84 Å from the free H_2 value of 0.74 Å. Prior to Kubas' discovery, the formation of dihydrogen was considered as an intermediate only before forming the dihydride. As per Kubas, there needs to be a balance between the σ -donation and the back donation for coordination of H_2 on the metal site. The orientation of H_2 towards the metal is governed by the π back donation and

the extent to of this donation leads to formation of hydrides. This in turn leads to a continuum of H-H bond lengths from 0.74 Å (free) to as long as 1.6 Å although Kubas considered complexes with bond length < 0.9 Å to be true and the others as elongated H- bonds. The interaction between the metal site and the H₂ can always be controlled by σ donation and π back donation by placing different ligands in different geometry on various transition metals.[35-39]

A downward shift in the H-H stretching frequency (usually monitored by Raman spectroscopy) is an indication of Kubas interactions and a more definitive response is provided by inelastic neutron scattering by observing the hydrogen molecules' rotational transitions. The INS measurements describe the potential barrier to the rotation of hydrogen molecules. The barrier is present due to the particular orientation of hydrogen molecules at a specific site which aligns with d-orbitals of metal for π back donation and so leading to a stronger interaction. Several research groups have worked on this problem to locate the site for hydrogen gas molecules with transition metal complexes (Zeolites, MOFs, metal phosphates, etc) by a combined effect of neutron diffraction, heat of adsorption measurement, and INS. The exceptionally high heat of adsorption for dihydrogen measured on VSB-5 in our recent work[40] combined with the INS measurements (explained shortly), we can, with absolute certainty describe this as a typical case of Kubas complex.

4.9.2 para-hydrogen loadings on VSB-5

Figure 4.13 displays the para-hydrogen loadings on VSB-5 where we dosed 0.5 p-H₂ per Ni₂₀ as a function of increasing temperature. For each temperature, 2 hours of data collection were given before measuring for the next temperature. As can be seen, the measurements started at 5 K and temperature was increased to reach a final temperature of 140 K. Figure 4.14 is the magnified

version and focuses on the bound spectrum where we observe the rotational features of the para-hydrogen.

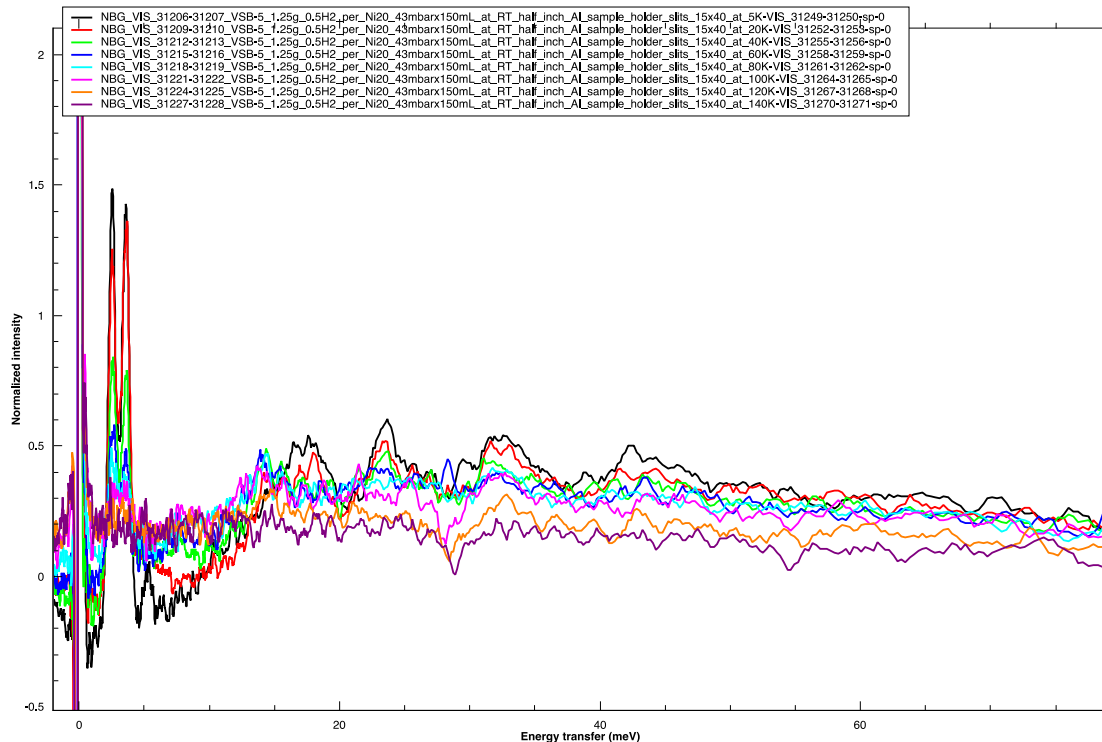


Figure 4.13: para-hydrogen loadings on VSB-5 as a function of increasing temperature.

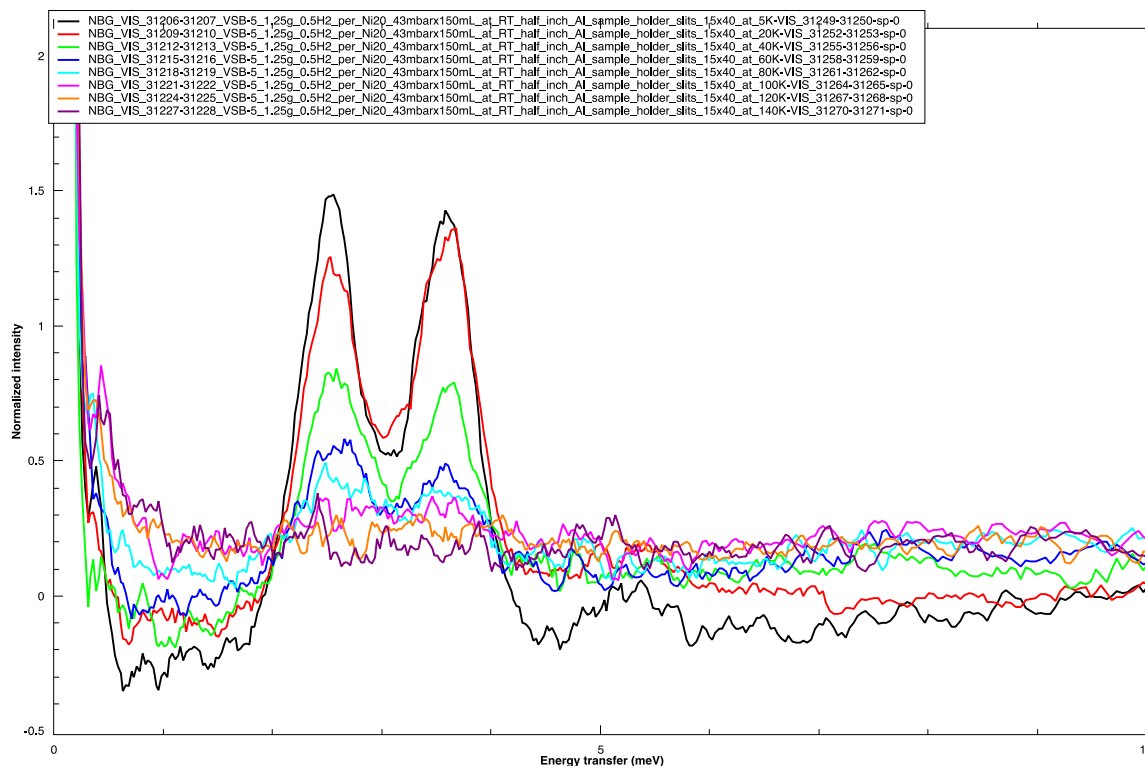


Figure 4.14: magnified bound spectrum of para-hydrogen loadings on VSB-5 as a function of increasing temperature.

From the above figure it can be seen that the rotational line of dihydrogen appears as two distinctive peaks centered at 2.5 meV and 3.6 meV respectively. This is an extremely low value for the rotational line and indicates a strong interaction with the material. The strong interaction can also be represented as Kubas interaction because in VSB-5 after the removal of water molecules, the metal sites (Ni^{2+}) are unsaturated Lewis acid sites and so can attract the hydrogen gas easily. Our strong and detailed study on the activation as discussed in chapter 3 confirms complete removal of the trapped water molecules from the material. Secondly, we have measured one of the highest heat of adsorption for dihydrogen on VSB-5 (16 kJ/mol) which confirms that Ni^{2+} sites are the primary site for dihydrogen adsorption and interactions. Therefore, due to the

high affinity towards the available metal sites, there is a huge shift in the rotational line for hydrogen and the gas isn't considered as 'free' at all.

The other important feature about the doublet to notice is that, these remain observable at 80 K before disappearing to give a broad spread in that energy range. Remember that dihydrogen boils at 20 K and for any temperatures above 20 K will make adsorption of dihydrogen difficult. The presence of rotational features through 80 K signifies the strong interaction between the gas and the material. When the temperature is sufficiently high that only a small fraction of the dihydrogen remains bound, we lose the rotational features. This signifies that the gas molecules are now acting free and are not interacting with the material that strongly. The third important point to note here is para to ortho-hydrogen conversion by the presence of a strong magnetic moment of Ni. Previously we mentioned that in the absence of a catalyst, in normal dihydrogen, there is an equilibrium between the two spin states of dihydrogen. But a magnetic moment of 2.8 BM provided by Ni²⁺ sites is strong to cause the ortho – para conversion as discussed in earlier section.

4.10 Conclusions

Utilizing inelastic neutron scattering with in-situ para-hydrogen (p-H₂) dosed graphene we have observed that a barrier to rotation of dihydrogen happens at low coverage (0.1 ML). The observed dynamics suggests that the initial dihydrogen adsorbed (0.1 ML) on the surface is random and not a particular ring is favored. However, this initial adsorption is energetically favorable which leads to a shift in the rotational line of dihydrogen. Besides the shift in the rotational line, a broad feature is seen which is again indicative of a stronger interaction between dihydrogen and graphene

surface. The next loadings of the gas brings a rise in a shoulder ~ 14.5 meV which suggests that initial loadings lead to a small charge redistribution which causes more dihydrogen to be adsorbed at or near those sites. Increasing the surface loadings to 1.83 ML leads to appearance of the rotational line of dihydrogen as now the gas is acting freely due to the weak interaction with the surface. A well covered graphene surface doesn't allow the 1.83 ML molecules to interact with the surface giving the signature dihydrogen rotational feature. Overall, this is well suited system to study the interaction of dihydrogen in an anisotropic potential provided by the graphene surface. Our next work is focused on studying the quasielastic scattering to observe the diffusion of dihydrogen at lower temperatures.

A hand-in-hand comparison with a strong interacting surface provided by VSB-5 is also studied and it can be seen that how the rotational feature of dihydrogen shifts from 14.7 meV to 2-4 meV. This drastic shift is indicative of much strong interaction of hydrogen with the primary site of adsorption – Ni^{2+} and represents a classic case of Kubas complex where the interaction between dihydrogen and metal is too strong to possibly form metal dihydride. Also, presence of a transitional metal provides a strong magnetic moment which leads to ortho-para conversion again indicative of strong binding of dihydrogen in activated VSB-5.

4.11 References

1. PCH Mitchell, S.P., AJ Ramirez-Cuesta, J Tomkinson, *Surface Chemistry and Catalysis*, in *Vibrational Spectroscopy with Neutrons*. 2012, WORLD SCIENTIFIC. p. 285-366.
2. *Spallation Neutron Source*. [cited 2018; Available from: <https://neutrons.ornl.gov/sns>.
3. *Vibrational Spectrometer*. [cited 2018; Available from: <https://neutrons.ornl.gov/vision>.
4. Munter, A. *Neutron Scattering Lengths and Cross Section*. 1999 [cited 2018; Available from: <https://www.ncnr.nist.gov/resources/n-lengths/list.html>.
5. Clark, S.J., et al., *First principles methods using CASTEP*. *Zeitschrift für Kristallographie-Crystalline Materials*, 2005. **220**(5/6): p. 567-570.
6. Kresse, G. and J. Hafner, *Ab initio molecular dynamics for liquid metals*. *Physical Review B*, 1993. **47**(1): p. 558.
7. Giannozzi, P., et al., *QUANTUM ESPRESSO: a modular and open-source software project for quantum simulations of materials*. *Journal of physics: Condensed matter*, 2009. **21**(39): p. 395502.
8. Ramirez-Cuesta, A., *aCLIMAX 4.0. 1, The new version of the software for analyzing and interpreting INS spectra*. *Computer Physics Communications*, 2004. **157**(3): p. 226-238.
9. Young, J.A. and J.U. Koppel, *Slow neutron scattering by molecular hydrogen and deuterium*. *Physical Review*, 1964. **135**(3A): p. A603.
10. Geim, A.K. and K.S. Novoselov, *The rise of graphene*. *Nature materials*, 2007. **6**(3): p. 183-191.
11. Wang, J. and S. Kaskel, *KOH activation of carbon-based materials for energy storage*. *Journal of Materials Chemistry*, 2012. **22**(45): p. 23710-23725.

12. Harris, A. and A. Berlinsky, *Mean field theory of the orientational properties of ($J= 1$) hydrogen molecules on the surface of Grafoil*. Canadian Journal of Physics, 1979. **57**(11): p. 1852-1869.
13. Howe, J.P., *Properties of graphite*. Journal of the American Ceramic Society, 1952. **35**(11): p. 275-283.
14. Stankovich, S., et al., *Synthesis of graphene-based nanosheets via chemical reduction of exfoliated graphite oxide*. Carbon, 2007. **45**(7): p. 1558-1565.
15. Schniepp, H.C., et al., *Functionalized Single Graphene Sheets Derived from Splitting Graphite Oxide*. The Journal of Physical Chemistry B, 2006. **110**(17): p. 8535-8539.
16. Patchkovskii, S., et al., *Graphene nanostructures as tunable storage media for molecular hydrogen*. Proceedings of the National Academy of Sciences of the United States of America, 2005. **102**(30): p. 10439-10444.
17. Henwood, D. and J.D. Carey, *Ab initio investigation of molecular hydrogen physisorption on graphene and carbon nanotubes*. Physical Review B, 2007. **75**(24): p. 245413.
18. Cavallari, C., et al. *Hydrogen on graphene investigated by inelastic neutron scattering*. in *Journal of Physics: Conference Series*. 2014. IOP Publishing.
19. Hornekær, L., et al., *Clustering of chemisorbed H (D) atoms on the graphite (0001) surface due to preferential sticking*. Physical review letters, 2006. **97**(18): p. 186102.
20. Casolo, S., et al., *Understanding adsorption of hydrogen atoms on graphene*. The Journal of chemical physics, 2009. **130**(5): p. 054704.
21. Boukhvalov, D., M. Katsnelson, and A. Lichtenstein, *Hydrogen on graphene: Electronic structure, total energy, structural distortions and magnetism from first-principles calculations*. Physical Review B, 2008. **77**(3): p. 035427.

22. Balog, R., et al., *Bandgap opening in graphene induced by patterned hydrogen adsorption*. Nature materials, 2010. **9**(4): p. 315-319.
23. Baburin, I.A., et al., *Hydrogen adsorption by perforated graphene*. International journal of hydrogen energy, 2015. **40**(20): p. 6594-6599.
24. Zhang, J., et al., *Chemisorption of hydrogen on graphene: insights from atomistic simulations*. Journal of Physics: Condensed Matter, 2017. **29**(19): p. 195001.
25. Xia, Y., et al., *Adsorption and desorption of hydrogen on graphene with dimer conversion*. Surface Science, 2013. **617**: p. 131-135.
26. Klechikov, A., et al., *Hydrogen storage in high surface area graphene scaffolds*. Chemical Communications, 2015. **51**(83): p. 15280-15283.
27. Hummers Jr, W.S. and R.E. Offeman, *Preparation of graphitic oxide*. Journal of the American Chemical Society, 1958. **80**(6): p. 1339-1339.
28. Georgiev, P., et al., *Hydrogen site occupancies in single-walled carbon nanotubes studied by inelastic neutron scattering*. Journal of Physics: Condensed Matter, 2004. **16**(8): p. L73.
29. Georgiev, P., et al., *In situ inelastic neutron scattering studies of the rotational and translational dynamics of molecular hydrogen adsorbed in single-wall carbon nanotubes (SWNTs)*. Carbon, 2005. **43**(5): p. 895-906.
30. Georgiev, P., et al., *Experimental Q-dependence of the rotational J= 0-to-1 transition of molecular hydrogen adsorbed in single-wall carbon nanotube bundles*. Chemical Physics, 2006. **328**(1): p. 318-323.

31. Georgiev, P., et al., *The rotational and translational dynamics of molecular hydrogen physisorbed in activated carbon: a direct probe of microporosity and hydrogen storage performance*. Carbon, 2006. **44**(13): p. 2724-2738.
32. Ramirez-Cuesta, A., et al., *Dihydrogen in cation-substituted zeolites X—an inelastic neutron scattering study*. Journal of Materials Chemistry, 2007. **17**(24): p. 2533-2539.
33. Bahadur, J., et al., *Properties of immobile hydrogen confined in microporous carbon*. Carbon, 2017. **117**: p. 383-392.
34. Yang, S., A.J. Ramirez-Cuesta, and M. Schröder, *Inelastic neutron scattering study of binding of para-hydrogen in an ultra-microporous metal–organic framework*. Chemical Physics, 2014. **428**: p. 111-116.
35. Kubas, G.J., *Metal–dihydrogen and σ -bond coordination: the consummate extension of the Dewar–Chatt–Duncanson model for metal–olefin π bonding*. Journal of Organometallic Chemistry, 2001. **635**(1): p. 37-68.
36. Kubas, G.J., *Hydrogen activation on organometallic complexes and H₂ production, utilization, and storage for future energy*. Journal of Organometallic Chemistry, 2009. **694**(17): p. 2648-2653.
37. Geiger, W.E. and N.G. Connelly, *The electron-transfer reactions of polynuclear organotransition metal complexes*. Advances in organometallic chemistry, 1985. **24**: p. 87-130.
38. Kubas, G.J., *Fundamentals of H₂ binding and reactivity on transition metals underlying hydrogenase function and H₂ production and storage*. Chemical reviews, 2007. **107**(10): p. 4152-4205.

39. Kubas, G.J., *Molecular hydrogen complexes: coordination of a sigma bond to transition metals*. Accounts of Chemical Research, 1988. **21**(3): p. 120-128.
40. Sharma, A., et al., *Hydrogen Uptake on Coordinatively Unsaturated Metal Sites in VSB-5: Strong Binding Affinity Leading to High-Temperature D₂/H₂ Selectivity*. Langmuir, 2017. **33**(51): p. 14586-14591.

Note:

The work compiled for this chapter is a joint effort with VISION BeamLine (BL-16B), Spallation Neutron Source, Oak Ridge National Laboratory (ORNL). Amit Sharma synthesized the necessary materials – graphene and VSB-5 at ORNL under the guidance of VISION team. All the characterization needed for this chapter were performed by Amit at ORNL. All the calculations such as deconvolution of the rotational features for para-hydrogen loadings on graphene, were performed by VISION team.

Chapter 5 – Three times higher and reversible ammonia adsorption in acid modified

HKUST-1

Index

- 5.1 Abstract
- 5.2 Motivation
- 5.3 Ammonia: A brief introduction
- 5.4 Ammonia capture
 - 5.4.1 Present storage techniques
 - 5.4.2 Problems with the present storage techniques
- 5.5 Solution
 - 5.5.1 Porous materials for ammonia capture
 - 5.5.2 MOFs for ammonia capture
 - 5.5.3 Brønsted acidity for enhanced ammonia capture
- 5.6 MOF investigated: HKUST-1
 - 5.6.1 Structure
 - 5.6.2 Earlier work on HKUST-1 and ammonia capture
- 5.7 Experimental
 - 5.7.1 Synthesis of HKUST-1 and acidic HKUST-1
 - 5.7.2 Characterization of synthesized MOFs
- 5.8 Results and Discussions
 - 5.8.1 Structure integrity and presence of sulfate in the framework
 - 5.8.2 Binding of sulfate in the framework
 - 5.8.3 Ammonia adsorption captured
 - 5.8.4 Reversible adsorption of ammonia in acidic HKUST-1
- 5.9 Conclusions
- 5.10 References

5.1 Abstract

We have functionalized HKUST-1 [$\text{Cu}_3(1,3,5\text{-benzenetricarboxylate}_2)$] to contain bound sulfuric acid tethered to the framework through terminal oxygen coordination to the accessible Cu(II) sites. The structure remains largely intact through functionalization as confirmed by powder X-ray diffraction. Bound sulfuric acid is confirmed through Inelastic Neutron Scattering (INS) and Fourier Infra-Red Spectroscopy. Acid-modified HKUST-1 shows NH_3 sorption is enhanced by up to 3x uptake compared with unmodified HKUST-1. Significantly, the uptake becomes reversible after heating at 50 °C under vacuum.

A series of DFT simulations reveals that the primary adsorption occurs on the sulfuric acid sites rather than the Cu(II) sites, where primary adsorption occurs in the unmodified material. The adsorption of ammonia at the acid OH site leads to an elongation of O-H-N bond rather than a full transfer of H^+ to the ammonia molecule, explaining the observed reversibility of the adsorption. Simulated INS spectra from the DFT structures closely match experimental INS spectra measured for *in situ* NH_3 loading.

5.2 Motivation

5.2.1 Need to store ammonia:

Due to its variety of applications, the global production of ammonia is increasing to meet the demands. In 2004, a global production of ~100 million tons was reported which shot up to ~180 million tons in ten years. Looking at the continuous usage, it is expected to increase at a faster rate in the near future.[1] Ammonia can enter the human body either by inhalation, swallowing or through skin cuts. Since it readily dissolves in water, it forms ammonium hydroxide which is corrosive and caustic. High concentrations of ammonia leads to immediate burning of

eyes, nose and the respiratory tract. Exposure to high levels may cause blindness, lung damage or death. Even a low dosage of ammonia can lead to nasal and throat irritation with coughing. Ammonia, though not itself flammable, can be explosive upon forming 15-25% ammonia:air mixtures. The U.S. Occupational Safety and Health Administration (OSHA) has set the permissible exposure limit to 50 ppmv. The immediately dangerous to life and health concentration is 300 ppmv with an odor threshold being 5 ppmv before causing any potential danger to olfactory system. Also, United States Emergency Planning and Community Right-to-Know Act have classified ammonia as “extremely hazardous substance”. [2, 3] Considering the value of the gas, its toxicity, and environmental damage which release of the gas can cause, there is always a need to better store and recycle ammonia.

5.3 Ammonia: A brief introduction

5.3.1 What is ammonia

Ammonia (NH_3), one of the widely produced chemicals, is the simplest pnictogen hydride and occurs as a colorless gas with a strong pungent smell. It readily dissolves in water and in its purest form is known as anhydrous ammonia. A few physical properties are highlighted in the table 1. Ammonia has a trigonal pyramidal shape which makes it polar with a dipole moment. [4]

Property	Value
Molar mass	17.031 g/mol
Density	0.769 kg/cc at STP
Boiling point	239.81 K
Melting point	195.42 K
Triple point	195.4 K at 6.060 kPa
Vapor pressure	857.3 kPa
Refractive index	1.3327
Appearance	Colorless gas with strong pungent smell

Table 5.1: Physical properties of ammonia [4]

5.3.2 Where is ammonia

Ammonia is an important part of the ecosystem where it acts as a building block for various proteins and other nitrogen-based compounds. It is found in soil where it helps in balancing the nitrogen content of atmosphere in nitrogen cycle. Naturally, it is produced upon decaying or decomposition of vegetative matter such as plants and animals. Certain organisms have the capability to intake atmospheric nitrogen to synthesize ammonia by the process of nitrogen fixation. Various salts of ammonia are present in fertile soil, seawater and trace amount is observed in rain water as well.

Commercially, ammonia is produced by following the Haber-Bosch process[5] (early 20th century) where hydrogen reacts with nitrogen to form anhydrous ammonia. Natural gases (eg. methane) are used as a precursor to provide hydrogen in the first step. This exothermic and

reversible reaction requires high temperature and pressure conditions (~250 bar, ~500 °C) to achieve a 15% conversion to ammonia in each pass. To achieve a higher conversion, the entire process is carried out multiple times to get an overall conversion close to 97%. Due to this overall high efficiency of conversion (~97%), it is still used worldwide to produce ammonia for its variety of applications. Ammonia is used primarily in agriculture industry (fertilizer), chemical industry (precursor of numerous chemicals), pharmaceuticals, refrigeration, rubber industry, paper and pulp industry, detergent, food and beverage industry, and also as a rocket fuel. [6-9]

5.4 Ammonia Capture

5.4.1 Present storage techniques

Environmental concerns and the toxicity associated with ammonia represent the primary reasons for capturing ammonia in situations when release may occur either into water or gas streams. For waste water treatment, the contaminated water is either stripped with air or a high flow steam is used. Here the waste is first treated with a strong basic solution to dissociate ammonia and to reduce cost, limestone can be used however that requires additional time and more sophisticated equipment. After stirring at appropriate pH, the ammonia may be recovered as sulfates, phosphates, carbonates or similar ionic salts which may be recovered by filtration. [10, 11]

To determine the concentration of ammonia in air, several methods are used. The impinger method (a) pushes the gas stream to be analyzed through, a small diameter opening. The constant air flow passes onto impingers containing strong acidic solutions which react with and retain ammonia. The chemiluminescence method (b), heats the gas stream in order to convert ammonia to NO as this conversion may be monitored by chemiluminescence. Finally, the photoacoustic gas

analyzer method (c) where ammonia is measured for correction in temperature and interference with water and carbon dioxide. [12]

A common commercial ammonia capture technology is referred to as wet scrubbing, where a strong acidic solution (typically sulfuric acid) captures ammonia as ammonium sulfate which may be recovered. Here a tower or the reactor is filled with acidic solution and the air is fed into the reactor vertically or horizontally. Ammonia captured by this method may then be used in the agriculture industry as fertilizers. The amount and concentration of the salts can always be changed as per need. [13]

5.4.2 Problems with the present technology:

With the wet scrubbing technology, the capture efficiency is governed by various parameters such as gas flow rate, water content, gas composition, optimum temperature and pressure and other special requirements such as height of column etc. A small fluctuation in any of these variables might significantly affect the capture process. Additionally, the cost of setting up, operating, and supplying large capital equipment of this nature is considerable and inappropriate for smaller-scale processes. Also, the long-term damage to the column due to usage of harsh chemicals (sulfuric acid, sodium hydroxide) also increases the operating cost of the set up.

5.5 Solution

5.5.1 Porous materials for ammonia capture

In the past few decades, research in the field of porous materials has seen the boom in the discovery of various adsorbents such as zeolites, metal organic frameworks, activated carbon,

silica, alumina, porous organic cages, and other systems able to store and separate different molecules based on the interactions between them as explained in previous chapters. With dry scrubbers based on porous adsorbents, significant advantages are possible. First, the high surface to volume ratio provide more sites for the gas molecules in volumetric terms leading to more efficient storage. Some MOFs have enormous surface areas ($>7000 \text{ m}^2/\text{g}$) with a long-range order in the framework. High crystallinity and ease in modification in these materials such as ion exchange in zeolites, sheet perforation in graphene, post synthesis modification in metal organic frameworks, surface decoration in organic polymers, make these materials interesting for gas adsorption studies. There are also numerous secondary sites for gas molecules to interact after saturation of primary sites such as embedded nanoparticles, cages, long channels, and also possibility of introducing foreign molecules without disturbing the structure.[14-21] While these sorbents may be pressed into pellets of varying shapes, the possibility of embedding these materials in mixed membrane polymers provide more options to enhance the surface interactions with the gas molecules. Following the properties and the advantages, efforts have been made to use these materials for gas storage and separation studies and the robustness of these materials help to capture the toxic gases such as ammonia.

Applications exist for two categories of ammonia capture; irreversible and reversible.[22] The application of materials suiting the first category will be seen in gas masks where two major criteria need to be considered.

Firstly, the material should capture ammonia effectively across a wide range of atmospheric concentrations. Secondly, the presence of water or humid conditions should not affect the capture of ammonia by the adsorbent.

A good sorbent for reversible capture, should be able to store and transport ammonia when needed. Adsorbents fulfilling these criteria will work at higher pressure ranges, show long-term stability under harsh conditions and demonstrate high cycling performance.

Earlier work on ammonia capture by these materials has seen the application of the simplest adsorbents - carbonaceous material. These materials have proven to be useful in numerous gas adsorption studies and are attractive here because they do not adsorb significant water. Research on ammonia capture by these have shown that since the average pore size of activated carbon ranges between 10-20 Å (significantly larger than an ammonia molecule), the interaction between the ammonia and carbon isn't strong enough to effectively adsorb ammonia around room temperature.[23-26] Even though there is a possibility of modification in the structure by addition of halogens, nitrogen, redox reagents, the interaction has not yet been amplified enough to capture large amounts of ammonia at relevant conditions. Also, the possibility of having the same orientation of porous sheets in other carbon based material -graphene, is rare as it is a random arrangement obtained by thermal or chemical exfoliation. Besides, the low surface area of few materials (such as grafoil, graphite etc) limits the amount of ammonia which these materials can intake. The possibility to modify the surface chemistry here is by introducing mixed structures such as graphene oxide embedded metal organic frameworks.

Zeolites represent a promising class of sorbents for ammonia capture but they require pre-treatment before the application because of their hydrophilic nature. The water molecules which are weakly bound in the framework, can be removed by activating the material under vacuum. Without a proper activation, water molecule will block the adsorption sites leading to a poor overall interaction. Helminen *et al* measured adsorption isotherms for ammonia on Zeolite 13X, 4A, silica

gel, and alumina between 298 and 393 K and observed that ammonia adsorbed strongly on 13X and 4A. They concluded that the interaction favors adsorption only and the regeneration is difficult. For lower concentration of ammonia, zeolites again performed better than silica gel and alumina.[25, 27]

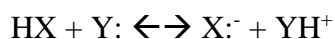
5.5.2 MOFs for ammonia capture

Recently, metal organic frameworks have attracted wide attention in field of gas separation and storage due to the ease in tailoring their surface chemistry and tuning the pore size to enhance the adsorbate-adsorbent interactions. For ammonia capture, numerous MOFs have been studied for this specific application. Yaghi and coworkers studied the ammonia adsorption on M-MOF-74 (M = Mg, Co, Ni, Zn) under dry and humid conditions and reported that MOFs have higher adsorption capacities when compared to zeolites with Mg-MOF-74 and Co-MOF-74 reporting the highest capacities.[28] More recently, a study on various analogues of MOF-74 was performed by DeCoste *et al* where they reported Cu-MOF-74 as the best material overall for ammonia capture. [29] Britt and coworkers examined MOF-5, MOF-177, MOF-74, MOF-199, IRMOF-3, and IRMOF-62 to study ammonia adsorption with kinetic breakthrough measurements and reported higher adsorptive capacities compared to activated carbon. [30] MIL-100 was used by Petit *et al* to study ammonia adsorption, specifically examining the interaction between ammonia and accessible Fe²⁺. [31] UiO-66 is yet another interesting system and was studied by Jasuja *et al*. [32] Humbeck *et al* studied various dense porous organic polymers to find a material useful for ammonia capture. [33] A computational study to screen the potential functional groups for higher ammonia adsorption was performed by Snurr *et al* where they worked with 21 functional groups

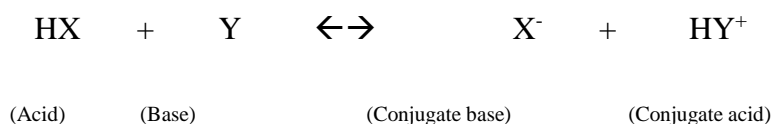
such as halogens, acidic groups, carboxylates, amines, and hydroxyls. Again, the basis of this study was to find the functional group which can increase the interaction with ammonia. For dry conditions, they reported Cu analogue as the best candidate and for humid conditions, both Cu and Ag silver analogue adsorb better.[34]

5.5.3 Brønsted acidity for enhanced ammonia adsorption

A brief overview on Brønsted and Lewis acidity is provided here. Among the various classification of acids and bases, Lewis theory and Brønsted theory are widely accepted. The Lewis theory is based on the electronic structure and involves the transfer of electron pairs and so a Lewis base (donate) is the species which will donate the electron pair to a Lewis acid (acceptor). In other words, Lewis bases have electron pair(s) in their filled orbitals which form Lewis adduct by forming a dative bond. Here is a simplest representation of a Lewis acid-base equilibrium where the base, Y, containing the lone pair of electrons (:) donates to the acid X to give X⁻ as the conjugate base:



Brønsted-Lowry theory on the other hand deals with transfer of proton (H⁺) rather than electron pairs. Here the acids are defined as proton donors and bases are the proton acceptors. A compound acting as both Brønsted acid-base is referred as amphoteric. [35]Simply put,



The measure of the strength of Brønsted acid is given by acid-base dissociation constant equilibrium constant (K_a) for the respective acids which is given as[36]:

$$K_a = \frac{[H_3O^+][X^-]}{[HX]}$$

For stronger acids, K_a is relatively large for instance HCl has K_a close to 1000. For weaker acids, K_a is smaller as for acetic acid K_a is 1.8×10^{-5} . Water has much smaller K_a value (1.8×10^{-16}) and is so considered a weak Brønsted acid. Like K_a , K_b reflects the strength of the conjugate base. When K_a is multiplied to K_b we get:

$$\frac{[H_3O^+][X^-]}{[HX]} * \frac{[HX][OH^-]}{[X^-]}$$

which gives $[H_3O^+][OH^-]$ known as K_w with a value of 1×10^{-14} . This is obtained by substituting K_a for K_b or vice versa in above equation. Since the product, K_w , is a small number, either the acid or its conjugate base can be strong. So, if one is strong, the conjugate must be weak. So, stronger acids have weak conjugate bases. Another important quantity to remember is pK_a (similar to pH or pOH) which is:

$$pK_a = -\log K_a$$

A list of few acids, their conjugate base with their respective dissociation strength is provided here and the table has stronger acids in the upper-left corner with stronger bases in the bottom-right corner.

<i>Compound</i>	K_a	pK_a	<i>Conjugate Base</i>	K_b	pK_b
HI	3×10^9	-9.5	I ⁻	3×10^{-24}	23.5
HCl	1×10^6	-6	Cl ⁻	1×10^{-20}	20
H ₂ SO ₄	1×10^3	-3	HSO ₄ ⁻	1×10^{-17}	17
H ₃ O ⁺	55	-1.7	H ₂ O	1.8×10^{-16}	15.7
HNO ₃	28	-1.4	NO ₃ ⁻	3.6×10^{-16}	15.4
H ₃ PO ₄	7.1×10^{-3}	2.1	H ₂ PO ₄ ⁻	1.4×10^{-12}	11.9
CH ₃ CO ₂ H	1.8×10^{-5}	4.7	CH ₃ CO ₂ ⁻	5.6×10^{-10}	9.3
H ₂ S	1.0×10^{-7}	7.0	HS ⁻	1×10^{-7}	7.0
H ₂ O	1.8×10^{-16}	15.7	OH ⁻	55	-1.7
CH ₃ OH	1×10^{-18}	18	CH ₃ O ⁻	1×10^4	-4
HCCH	1×10^{-25}	25	HCC ⁻	1×10^{11}	-11
NH ₃	1×10^{-33}	33	NH ₂ ⁻	1×10^{19}	-19
H ₂	1×10^{-35}	35	H ⁻	1×10^{21}	-21
CH ₂ =CH ₂	1×10^{-44}	44	CH ₂ =CH ⁻	1×10^{30}	-30
CH ₄	1×10^{-49}	49	CH ₃ ⁻	1×10^{35}	-3

Table 5.2: List of few acids with their respective conjugate base. [37]

There are a few factors which affect the Brønsted acidic character such as:

(a) Electronegativity:

When the atoms attached to the proton becomes more electronegative, the bonding pair of electrons becomes more strongly attracted to atom, and less to the proton. If the bond becomes more polarized away from the proton, it seems likely that the proton will more easily ionize. The molecule containing this bond will be a stronger Brønsted acid. It will not hold onto the proton as tightly. It will have a lower pK_a . In addition, we should think about what happens after the proton has ionized. In most cases, a neutral (uncharged) Brønsted acid will give rise to an anionic conjugate base. Proton transfer is generally reversible, so it could always go back where it came from, unless something stabilizes the anion that forms. However, if an atom has a higher nuclear core charge, it will be more stable as an anion than would other atoms. That means a compound with a hydrogen attached to that atom will give up a proton more easily.

(b) Charge on the proton donor:

When a proton is given up, the proton will have a 1^+ charge, and the atom releasing the proton will become 1^- . Consequently, if the atom attached to the proton already has a negative charge, it is less likely to give up the proton – as losing an additional proton results in a charge of 2^- . Conversely, if the same kind of atom had a positive charge, loss of a proton would be more favorable as it would lower the charge.

(c) Polarizability:

A polarizable atom is generally a large atom that can distribute charge easily over a greater volume, because the charge is less concentrated than it would be in a smaller atom. The distribution of charge is stabilizing. When comparing anionic atoms from the same column of the periodic table, the polarizability of the atom (related to its size) can be used to explain different anion stabilities.

The reason polarizability dominates comparisons within a column, but not within a row, is due to the relatively large change in size of atoms from one row to the next. As electrons occupy an additional energy level, the size of the atom increases greatly. Atoms also change size as we move across a row of the periodic table, getting a little smaller as the nuclear charge increases. However, this change is not as dramatic as the change in size from one row to the next.

Utilization of introduction of Brønsted acidity in acidic HKUST-1 for higher ammonia adsorption is explained in the Results and Discussion section.

Brønsted acidity in the MOFs can be introduced by one of the following three ways (Figure 5.1) as suggested by Yaghi *et al* in their review in 2015[22]:

(a) Encapsulation of Brønsted acid molecules in the pores/cage/cavities of MOFs:

Brønsted acid molecules can be encapsulated in the pores by two mechanisms. In the first, the acid molecules are introduced by diffusion using solvent exchange methods. Alternatively, acid may be introduced during the synthesis of MOF itself- where the acid molecules will interact with the framework by weak intermolecular forces. The size of the interior and the acid molecules are important criteria while encapsulation.

(b) Ligation of acid molecules at the metal sites:

Ligands such as water, oxalic acid, alcohol, hydroxyl, inorganic acids exhibit their proton donor characteristic when bonded at the metal sites. This post-synthesis modification technique has been proven quite useful to introduce Brønsted acidic character in numerous systems. Control over the choice of ligands to monitor the polarization power or other factors governing the proton donation, makes ligation an interesting and easy approach.

Also, substitution of carboxyl groups in MOFs by simple techniques (such as slow sulfation for sulfuric acid introduction), is another way for introduction.

(c) Covalent binding of acid molecules with organic linkers:

The variety of functional groups in the organic linkers provide another host site for introducing acidity. The well-defined organic functionalities in MOFs offer structural advantage when introducing Brønsted acid molecules unlike other porous materials. The various acidic functionalities dangling in the framework provide intrinsic Brønsted acidic character which can further be enhanced by post synthesis modification by either protonation or organic substitution reaction.

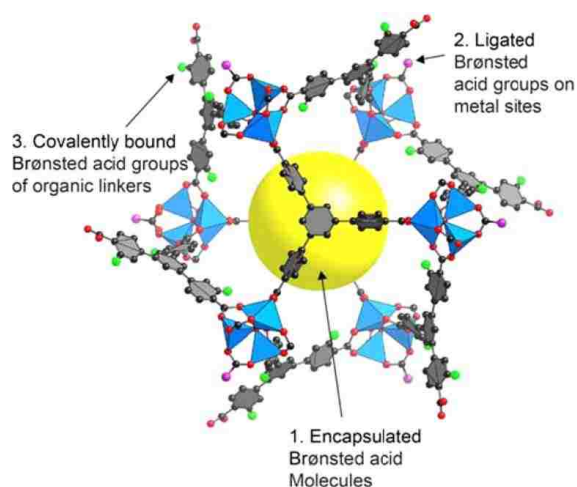


Figure 5.1: Depicting the various ways of introducing Brønsted acidic molecules in the porous framework of MOF. (used from reference 22)

Despite the well-studied ways of adding the Brønsted acidic character, this field is only starting to emerge due to the difficulties associated: the MOFs need to withstand the introduction

of strong acidic molecules in the framework as the acid might interact vigorously and cause a collapse in the crystalline nature of material. If the acidic sites are distributed non-homogenously in the framework, characterization becomes far more challenging. However due to the chemical robustness of various MOFs, researchers are pursuing this field and the applications such as – proton conduction, catalysis, and ammonia capture.

5.6 MOF under investigation

5.6.1 HKUST-1 Structure

HKUST-1 represents one of the first porous MOFs to be studied and remains one of the most extensively frameworks. The structure contains binuclear Cu (II) paddlewheels connected by the carboxylate groups from 1,3,5-benzene-tricarboxylate ligands to give a porous and crystalline material suitable for gas adsorption studies (Figure 5.2). Axial water molecule present on each Cu atom can be removed by heating, providing accessible coordinatively unsaturated Cu(II) sites directed into the pores. The degree of dehydration is well-known to dramatically influence adsorption for a range of gases.[38, 39]

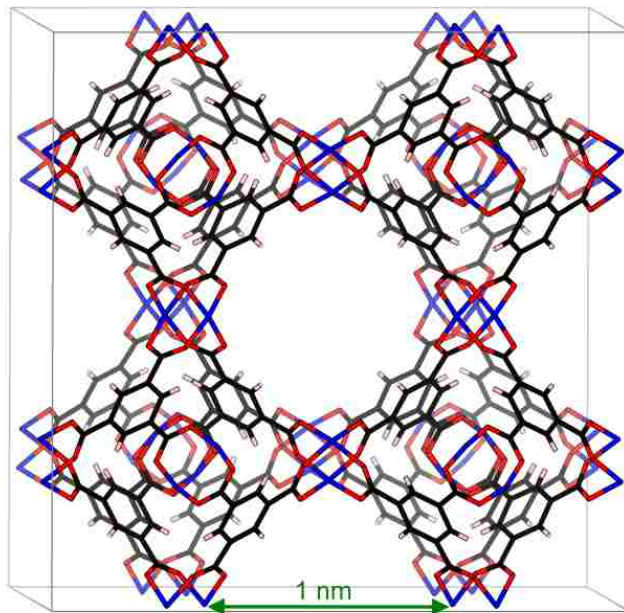


Figure 5.2: Unit cell of HKUST-1 where the Cu-Cu paddlewheels are shown in blue-red and the ring of the ligand (benzene tricarboxylic acid) is shown in black.

5.6.2 Earlier work on HKUST-1 and ammonia capture:

For NH_3 capture, HKUST-1 has been studied by multiple teams. The first studies demonstrated that, not surprisingly, the Cu(II) site acts as the primary site for loading with NH_3 chemisorbed with measured uptakes up to 1 - 1.5 molecule of NH_3 per Cu site per unit cell or in other terms, 3 - 4.5 molecules of NH_3 per formula unit.[39-42] The chemisorption of ammonia on the copper site also brings a permanent change in the color of HKUST-1 from dark indigo to light indigo. In the presence of water, NH_3 uptake leads to the formation of intermediate species - $\text{Cu}(\text{OH})_2$ and $(\text{NH}_4)_3(\text{BTC})$ before the diamine (II) complex - $[\text{Cu}(\text{NH}_3)_4]^{2+}$ forms. [43-46] The stability of Cu-Cu dimer was studied by Gubbins *et al* [47], finding that there is a partial collapse of the structure upon ammonia loading. Ammonia adsorption both under anhydrous and wet conditions appears irreversible. Heating NH_3 -HKUST-1 under flowing inert gas fails to desorb the

NH₃. NH₃ adsorbed on secondary sites is removable by gentle heating, but these sites do not bind with more affinity than seen in typical nanoporous materials.

In this work, we show that we are able to load appreciable H₂SO₄ into the HKUST-1 framework without significant loss in crystallinity. We also show that the H₂SO₄ coordinates to the Cu(II) sites in the framework. When exposed to NH₃, we observe a significant increase in uptake compared to unmodified HKUST-1. The presence of the coordinated H₂SO₄ leads to $\approx 3x$ improvements in overall NH₃ uptake and a high degree of reversibility. The mechanism for primary adsorption is a strong hydrogen bond between one of the acidic protons on the H₂SO₄, although the interaction falls short of complete transfer. We characterize the uptake primarily through a series of inelastic neutron scattering spectra interpreted with simulated spectra based on an extensive DFT investigation.

5.7 Experimental

5.7.1 Synthesis of HKUST-1 and acidic HKUST-1

HKUST-1 was synthesized following Rowsell *et al.* [48] 5.0 g of copper(II)nitrate trihydrate (Sigma-Aldrich) was dissolved in 40 ml of deionized water and 2.5 g of benzene-1,3,5-tricarboxylic acid (Sigma-Aldrich) was dissolved in 40 ml of N,N-dimethylformamide (Sigma-Aldrich). After mixing these two solutions, 40 ml of ethanol (Fisher Scientific) was added and the final solution was stirred in a 250 ml glass jar for 15 minutes. The capped glass jar was heated to 85°C in a water bath for 24 hours to obtain dark blue (violet) colored material at the bottom of the jar. The product was washed several times with ethanol and filtered. The excess solvent was removed by keeping the product under high vacuum (10^{-6} mbar) at elevated temperature.

Acidic HKUST-1 was prepared by dissolving anhydrous sulfuric acid (Sigma-Aldrich) in acetone (Fisher Chemicals) in a glass tube. This solution was immediately poured in a Schlenk flask containing HKUST-1 suspended in 5 ml of acetone. Excess solvent was removed after vigorous mixing by using high vacuum (10^{-6} mbar). The material was collected in a glove box and taken for further characterization to observe the integrity of the structure and presence of sulfuric acid.

5.7.2 Characterization techniques

Powder X-ray diffraction (PXRD) patterns were measured on a PANalytical X'Pert X-ray diffractometer in reflection geometry mode with monochromated Cu $K\alpha_1$ ($\lambda = 0.15425$ nm) and $K\alpha_2$ ($\lambda = 0.15442$ nm) incident radiation operated at 40 kV and 40 mA. The X-ray diffraction patterns were collected over a 2θ range of 5° to 70° to determine the integrity of the HKUST-1 structure upon introduction of sulfuric acid.

Fourier transform infrared spectroscopy (FTIR) was carried using a JASCO 6100 spectrometer with attenuated total reflectance method.

Surface areas were measured using a Gemini VII from Micromeritics where the BET (Brunauer-Emmet-Teller) surface areas of the samples were measured at 77 K using liquid nitrogen. Prior to the BET surface area measurements, the samples were activated to 100°C for 24 hours under dynamic vacuum. The BET range for surface area measurement was set from 0.05 P/P_0 to 0.3 P/P_0 .

The quantity of SO_4^{2-} in the acidic MOF was determined by gravimetric analysis where SO_4^{2-} was precipitated as BaSO_4 . The first step in determination of the sulfate concentration in

acidic HKUST-1 was dissolved in diluted hydrochloric acid and then the trimesic acid was precipitated out using magnesium chloride. To expedite the precipitation (gelation) of trimesic acid, a rotary evaporator (IKA RV 10) was used. To the clear and transparent supernatant collected, a saturated solution of BaCl_2 was added to determine the SO_4^{2-} concentration.

Inelastic Neutron Scattering (INS) data was measured at beamline-16B (VISION), Spallation Neutron Source (SNS) located at Oak Ridge National Laboratory in Oak Ridge, Tennessee. Approximately 2 g of sample was transferred to an aluminum conflat sample holder and sealed using copper gasket in a glove box to maintain the dry environment for the sample. After measuring the blank, ammonia was dosed into the can at room temperature using a custom-built gas dosing manifold of known volume. Ammonia was dosed while the can was continuously shaken in order to facilitate homogenous adsorption of ammonia throughout the sample. The sample can was then heated in a furnace at 80 °C for 15 minutes to further aid equilibration of the ammonia evenly throughout the sample. Despite these measures, a saturated layer with condensed ammonia (purple colored) was seen at the top and a bottom layer lower in adsorbed ammonia (indigo/blue colored) was observed. The sample was cooled to the base temperature (~5 K) before measuring the inelastic neutron scattering data.

DFT calculations of the adsorption energies were performed using the Vienna *Ab initio* Simulation Package (VASP). The calculations used the Projector Augmented Wave (PAW) method to describe the effects of core electrons, and the Perdew-Burke-Ernzerhof (PBE) implementation of the Generalized Gradient Approximation (GGA) for the exchange-correlation functional. The energy cutoff for the plane-waves is 500 eV, the energy tolerance for electronic structure calculation is 10^{-4} eV, and the energy tolerance for structural optimization is

10^{-3} eV. The optB86b-vdW functional for dispersion corrections was applied. All calculations were performed at Γ -point only given the large lattice constant of HKUST (~ 26.3 Å).[49-53]

5.8 Results and Discussions

5.8.1 Structure integrity and presence of sulfate in the framework

For pure HKUST-1 (Figure 5.3), the collected X-ray diffraction pattern matches the simulated pattern. For the acid-modified samples, peak positions remain virtually unchanged demonstrating that the framework is intact. These changes show that binding of sulfuric acid at the Cu site has a slight effect on the framework which doesn't affect the overall framework integrity and stability. We measured PXRD pattern for acidic HKUST-1 on regular intervals and the material is stable for over a period of six months.

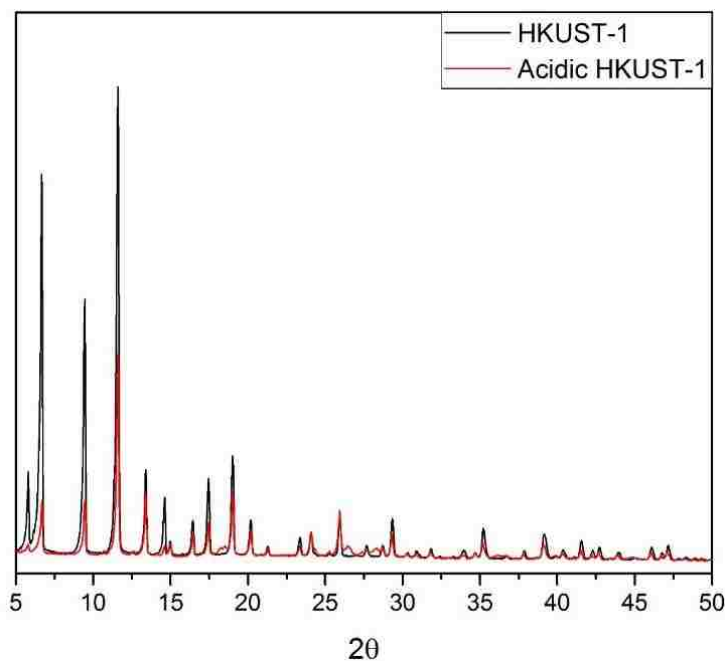


Figure 5.3: PXRD pattern for pure HKUST-1 (black) and acidic HKUST-1 (red) after activation showing that the structure is preserved even after introduction of sulfuric acid in the framework.

Figure 5.4 shows the FTIR spectra measured for the pure and the acidic HKUST-1. The pure and acidic HKUST-1 show C=C stretch from benzene ring at $\sim 1645\text{ cm}^{-1}$ followed by O-H bending vibrational mode in -COOH group around 1440 cm^{-1} , and C-H bending mode $\sim 1380\text{ cm}^{-1}$. C-H bending mode from the benzene ring is observed from $720 - 750\text{ cm}^{-1}$. Acidic HKUST-1 shows the S=O sulfate stretch $\sim 1190\text{ cm}^{-1}$, $\sim 1340\text{ cm}^{-1}$, and $\sim 1000\text{ cm}^{-1}$ and confirms the presence of sulfate moiety in the framework without significant disruption of the HKUST-1 parent structure. BET specific surface area for the pure HKUST-1 at 77 K was measured as $1185\text{ m}^2/\text{g}$. The adsorption isotherm measured is a type I isotherm with micropore volume (t-plot) of $0.44\text{ cm}^3/\text{g}$ and BJH (Barrett-Joyner-Halenda) pore diameter $\sim 20\text{ \AA}$. For acidic HKUST-1, a drop in the BET

surface area was expected because of presence of sulfate moiety in the framework and a BET surface area of 60 m²/g was measured.

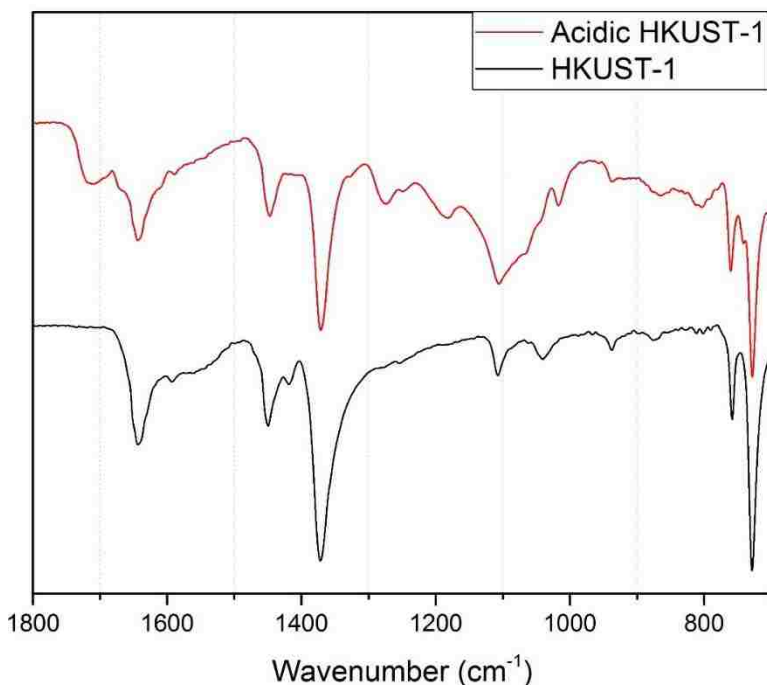


Figure 5.4: FTIR spectra for pure HKUST-1 and acidic HKUST-1 to detect the presence of sulfuric acid and second check for structure integrity.

5.8.2 Binding of sulfate in the framework

After confirming the presence of sulfuric acid and the integrity of the structure, the next step is to assess the location of sulfuric acid with the framework. Given the molecular structure of sulfuric acid, and the Lewis acidity by the Cu site there are few likely configurations with which sulfuric acid will interact with the framework. Consequently, we began by modelling the binding of sulfuric acid in the lattice by DFT calculations with multiple starting geometric configurations. The first possibility is free floatation in the cage or pockets of the framework. The disadvantage of having sulfuric acid in the framework with this free floatation is the randomness in the location

of sulfuric acid. This will lead to inconsistent ammonia adsorption and other results. Also, the binding energy calculated for free floatation is ~ 0.5 kJ/mol which makes this interaction quite weak. The second configuration of sulfuric acid we investigated is bound via one of the -OH groups as shown in figure 5.5 (top). This binding utilizes one -OH group for the binding and leaves only one for interaction with ammonia. Besides this disadvantage, the free -OH group faces inwards (towards the framework) and so the interaction is hindered. The energetics of this interaction were also not very favorable with a binding energy close to that of floatation. The final, most favorable, and the only stable configuration is by binding through one of the two S=O bonds as shown in the figure 5.5 (bottom). This configuration leaves the two -OH groups facing outwards which attract more ammonia inside the cage. Since the two -OH groups are wide apart in the cavity, the first binding of ammonia doesn't affect the binding of second molecule of ammonia. The sulfuric acid which we introduced in the framework post-synthesis, binds to copper with a binding energy of 33.3 kJ/mol and has a Cu-O-S bond with a bond length of 2.4 Å.

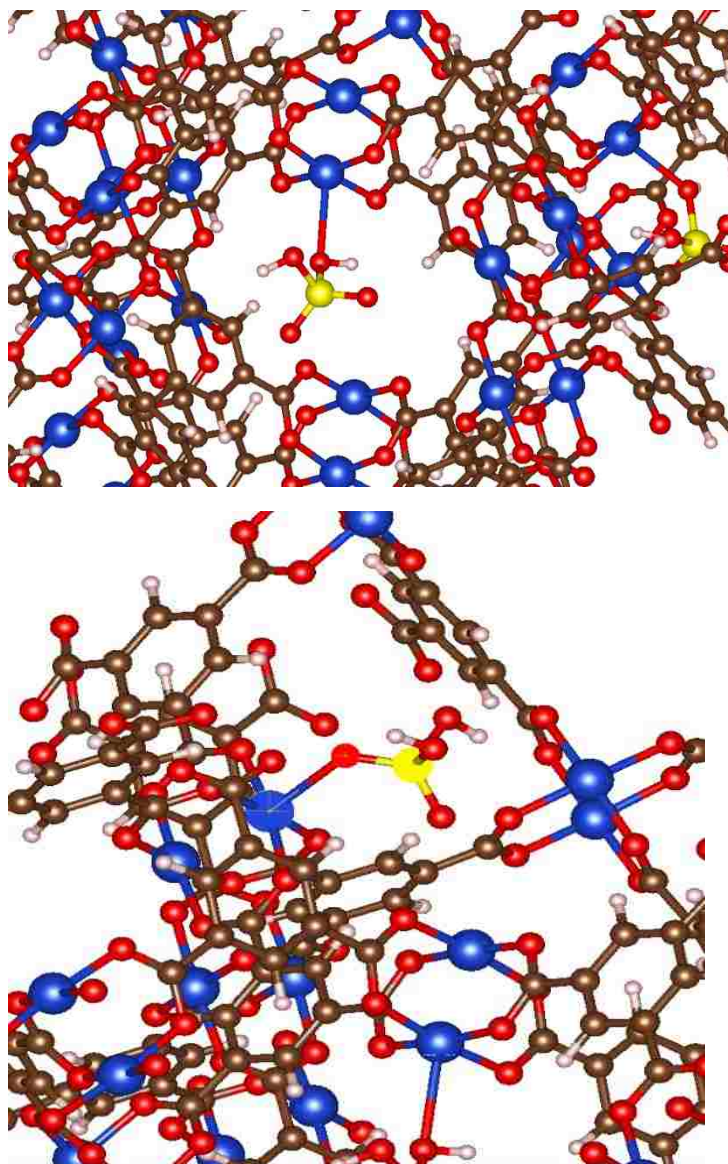


Figure 5.5a (top) An unstable configuration of sulfuric acid in the framework with one -OH group being used for anchoring the molecule and leaving other OH group stereo-hindered for interaction with ammonia. Figure 5.5b (bottom) Most stable and favorable configuration of sulfuric acid binding as it leaves both -OH groups free to exhibit the Brønsted acidic character with a reasonable binding energy of ~ 33 kJ/mol.

5.8.3 Ammonia adsorption compared

As mentioned in the characterization, we employed a vigorous method of gas loading where the sample can was shaken on a vortex mixture while the gas was being dosed in. After dosing the required amount of gas, the sample can was heated gently for ammonia to redistribute evenly. This homogenous distribution of ammonia throughout the structure is better as it doesn't lead to a gradient of adsorbed gas in the material. When ammonia is dosed into the sample can, only the upper layers of the material adsorb ammonia and the distribution isn't uniform as may be easily seen from the Figure 5.6b and 5.6c (Figure 5.6a is the activated sample). Measurements on samples which effectively contain a range of different loadings on different articles are challenging to interpret as most methods of assessing structure assume homogeneity. Once the upper layers saturate, any extra amount of gas dosed will condense on the top layer giving an incorrect indication of saturation. However, when the gas is dosed properly, in this case by using vortex mixture, it is distributed several times before truly saturating the structure. For HKUST-1, it is easier to observe this mechanism as the material changes color upon adsorbing ammonia which is shown in the figure 5.6d.

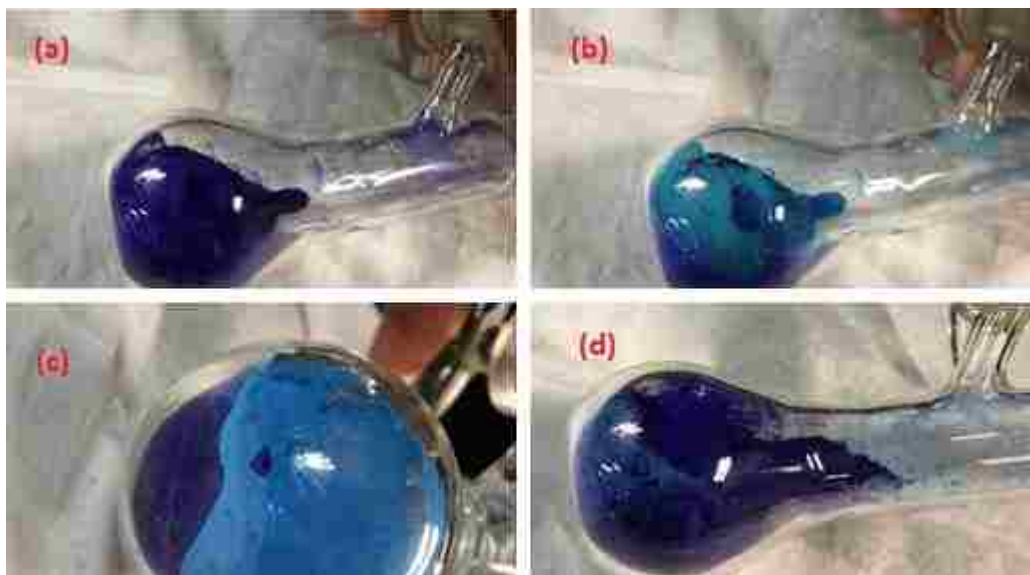


Figure 5.6(a) pure HKUST-1 activated sample before dosing ammonia with its characteristic deep-indigo color. 6b shows the interaction of ammonia with material when ammonia was initially dosed into the Schlenk tube showing uneven adsorption levels. 6c is another view to show clearly, the non-homogeneous distribution of ammonia in the sample with next small dose of ammonia. From 6d, we can see that uniform distribution is achieved after heating the tube gently with mild shaking. This distribution is now ready for next dose of ammonia. Repetition of this method will eventually lead to a true saturation of ammonia.

Experimental observation of ammonia adsorption was studied by neutron vibrational spectroscopy and the INS spectra for pure HKUST-1 and acidic HKUST-1 to study the ammonia adsorption are compared in Figure 5.7a and Figure 5.8a. For unmodified HKUST-1, we observe the increasing amount of ammonia loading starting from 0.5 NH_3 per Cu site before saturating between 1 - 2 NH_3 per Cu site (or 3 - 6 NH_3 per formula unit). The presence of solid ammonia phonons between 70 - 300 cm^{-1} , and specifically at $\sim 75 \text{ cm}^{-1}$, 85 cm^{-1} , and 100 cm^{-1} can be seen for 3 NH_3 per Cu site. The result was also confirmed by measuring FTIR spectra of the sample. INS spectra also show the presence of splitting of libration bands for solid NH_3 between 220 - 270

cm^{-1} which is clearly observed in the saturated HKUST-1. We also noted a significant change in color from dark indigo to a lighter shade after ammonia adsorption as has been previously described. Comparing the ammonia loading with other publications, we observed higher loading of ammonia for the acid-modified compound than was previously reported for pure HKUST-1. Interaction of ammonia in the pure HKUST-1 is depicted in the figure 5.7a (where as reported multiple times), the ammonia chemisorbs at Cu site. The binding energy calculated for Cu-NH₃ interaction is ~ 80 kJ/mol; secondary physisorptive binding in the pores also occurs.

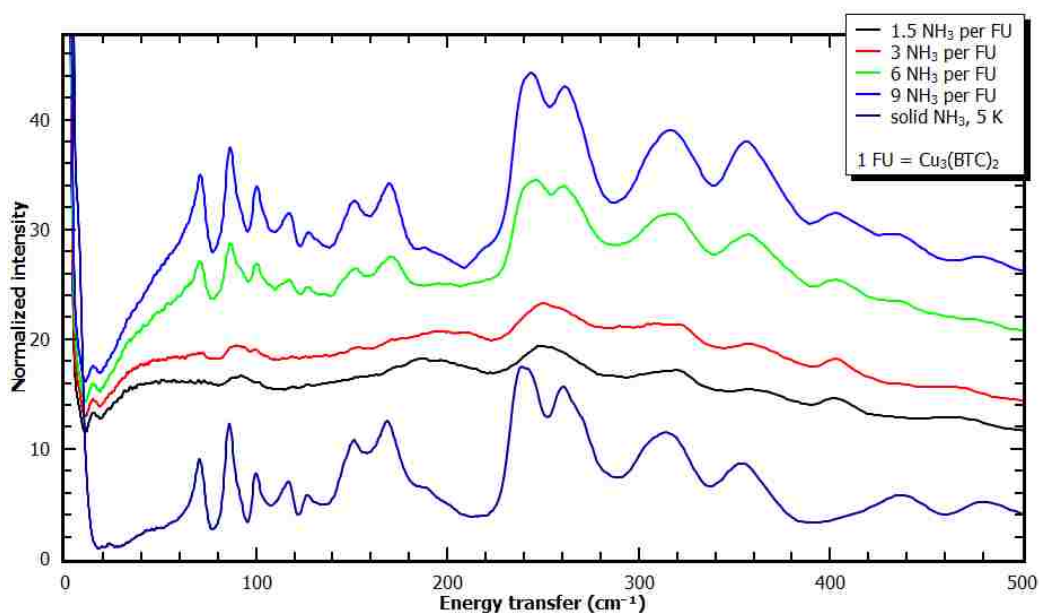


Figure 5.7a: INS spectra for ammonia loadings on pure HKUST-1. It can be observed that the material saturates between 3 and 6 NH₃/ formula unit or 1 and 2 NH₃/Cu site.

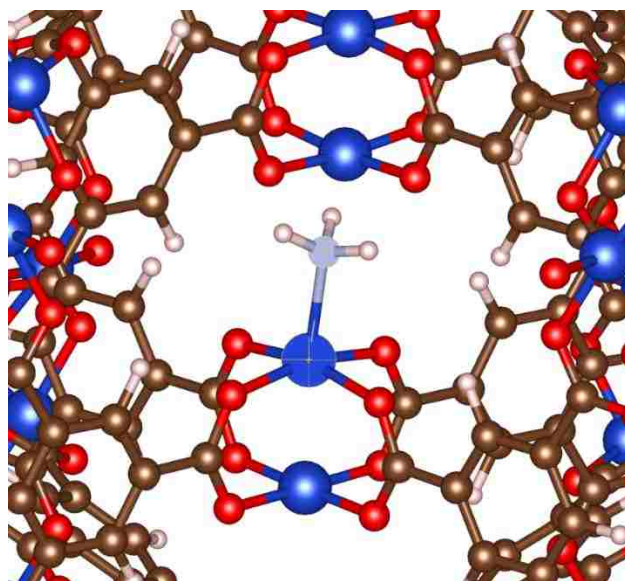


Figure 5.7b: Interaction of NH_3 with pure HKUST-1. Without any acid present, as expected, ammonia first goes and binds strongly with the Cu site.

For acidic HKUST-1, we note a higher amount of ammonia in the material that we attribute to an interaction between the two -OH groups from sulfuric acid which act as Brønsted acid centers for ammonia which acts as both Lewis and Brønsted base. Adsorption of ammonia at the additional sites can be seen $\sim 220 \text{ cm}^{-1}$ and $\sim 280 \text{ cm}^{-1}$. Since ammonia is being adsorbed strongly by the framework, we don't observe peaks associated with solid ammonia ($\sim 75 \text{ cm}^{-1}$, 85 cm^{-1} and 100 cm^{-1}). The splitting of libration band for ammonia which is an indication of presence of condensation of ammonia in the material, is observed for pure HKUST-1, but it doesn't split for acidic HKUST-1 and is another indication of capability of acidic HKUST-1 to adsorb more ammonia. INS spectra for ammonia loadings (Figure 5.8a) shows adsorption of ammonia in the framework before saturating between 3 - 4 NH_3 per Cu site. The amount of ammonia adsorbed in acidic HKUST-1 is three times that sorbed into pure HKUST-1 making it a better candidate for ammonia adsorption.

This higher adsorption of ammonia with acidic HKUST-1 utilizes the concept of Brønsted acid-base interactions, discussed previously. Sulfuric acid is a strong Brønsted acid (proton donor) with a high K_a value (1000; $pK_a = -3$) and can readily donate its proton from the two free -OH groups. The binding of sulfuric acid through a terminal =O allows the two -OH groups to both interact with ammonia molecules. As a Lewis base with a lone pair of electrons, ammonia can easily accept a proton donated by the OH groups of sulfuric acid. This interaction between the lone pair of electrons at ammonia and the donation of proton is not strong enough for a complete transfer, as seen in computer modelling (discussed below). We calculate a binding energy of first molecule of ammonia close to 128 kJ/mol. This energy is sufficient to keep ammonia adsorbed to the OH group and with another OH group available to interact with a second molecule of ammonia. For two ammonia molecules associated with a single H_2SO_4 , we calculate a much weaker interaction that is still consistent with the Brønsted acid-base interactions.

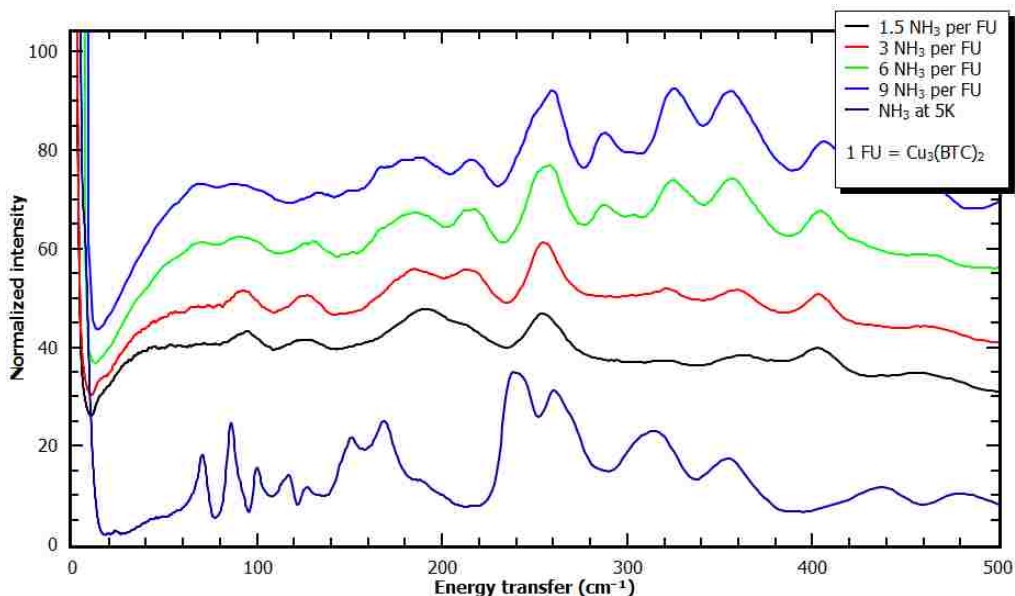


Figure 5.8a: INS spectra describing the ammonia loadings on acidic HKUST-1. It can be observed that the material doesn't saturate even at higher loadings of 3 NH_3 /Cu site or 9 NH_3 / formula unit.

Figure 5.8b shows the interaction of ammonia with the acidic moiety. As anticipated, the ammonia molecules interact with the free -OH group of the acid. The first ammonia molecule binding at one -OH site has the binding energy (from DFT calculations) of 128.9 kJ/mol. Bond distances in the DFT minimized structures provide the following picture of the interaction. The proton is partially transferred to the NH_3 , resulting in an NH_4 species with a significantly longer (~10%) N-H separation than for the other three protons. This partial acceptance or transfer is also corroborated by the elongation of the -O-H bond length from 1.0 Å to 1.6 Å. A longer N-H bond length (1.5 Å) and a shorter -O-H bond length (1.1 Å) is observed when the second ammonia molecule binds to the second -OH site (Figure 5.8c) thereby showing a much weaker proton transfer. The calculated binding energy for the second molecule of ammonia is much weaker (69.5 kJ/mol) compared to the first ammonia binding. During these bindings, there is no trace of formation of ammonium sulfate which would have been observed as a shorter N-H bond length of 0.88 Å as per ICDD database.

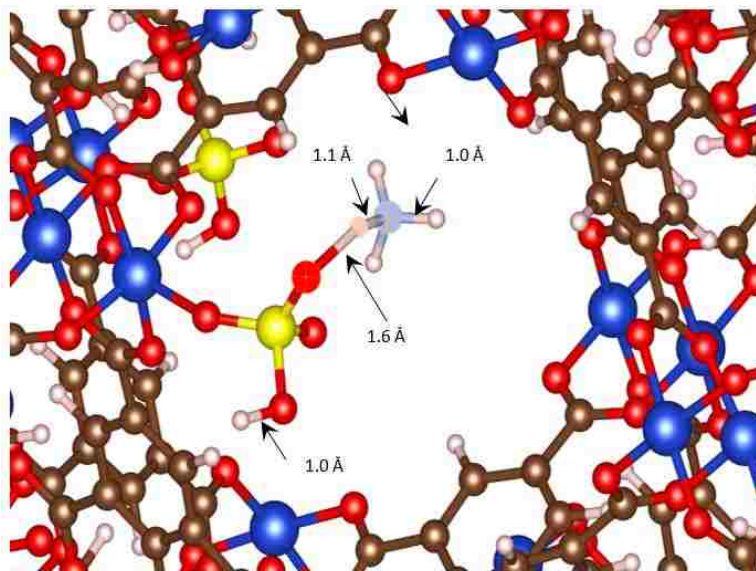


Figure 5.8b: Interaction of first molecule of ammonia with the first acidic site (-OH group)

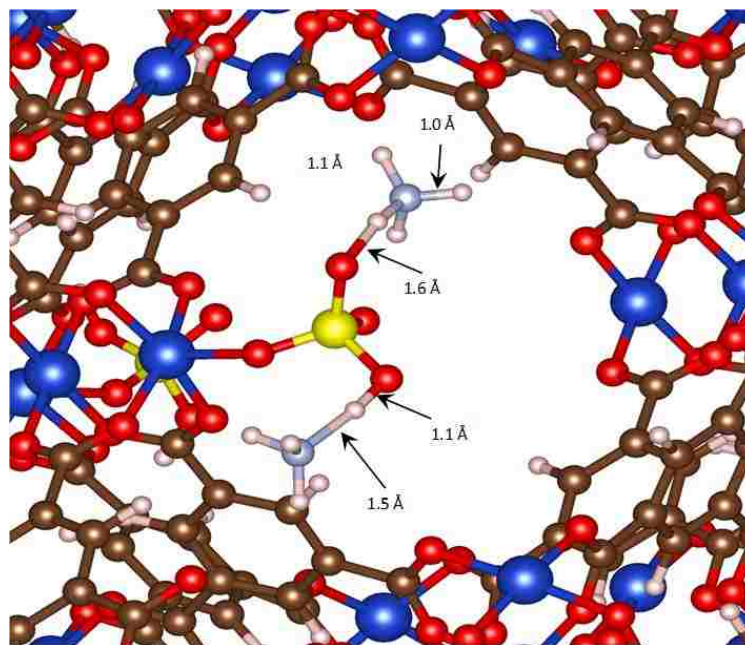


Figure 5.8c: Interaction of second molecule of ammonia with the first acidic site (-OH group)

5.8.4 Recyclability and reversible adsorption

Besides higher adsorption of ammonia in the acidic HKUST-1, we have also observed the reversible nature of binding of the gas. The primary reasoning for a reversible adsorption is explained by DFT calculations where we noticed an incomplete transfer of proton compared with ammonium sulfate. The interaction of ammonia with the copper site in HKUST-1 is well studied and, as mentioned in the introduction, a Cu(II)diamine complex eventually forms in place of the MOF. This binding energy between ammonia and copper site is 77 kJ/mol based on DFT calculations, corresponding to a strong binding between the two species. In acidic HKUST-1, since the transfer of proton is partial, formation of ammonium sulfate (NH_4^+) isn't observed in DFT calculations. N-H bond length in NH_4^+ is 0.88 Å as per ICDD database. This shorter bond length corresponds to a complete transfer of proton and chemisorption. As explained earlier, we observed longer bond lengths thereby confirming a partial transfer.

Besides, as mentioned earlier, the color of HKUST-1 changes from dark indigo to light indigo upon loading of ammonia and can't be reversed because the interaction is too strong. Below, we show the original color of the acidic HKUST-1 (blue) on pumping the ammonia dosed acidic HKUST-1 at 50 °C (Figure 5.9). This change in color of the acidic material is the first indication of removal of ammonia. This also suggests minimal chemisorptive ammonia adsorption at Cu site in acidic material which would lead to a deep indigo color.

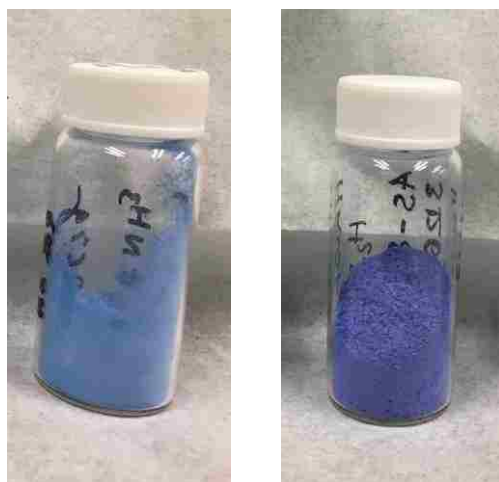


Figure 5.9: Comparison of the final color of the material after pumping the ammonia from the material where the left image shows the acidic material reverting back to original blue color after pumping the gas whereas the pure HKUST-1 on right doesn't show any change in color after pumping indicating chemisorption.

To evaluate the presence of ammonia, the IR spectra (Figure 5.10) for the pumped acidic HKUST-1, was compared and we confirmed complete removal of ammonia. From the Figure below, we can observe the presence of ammonia in saturated acidic HKSUT-1 between 3000 - 3500 cm^{-1} , which are absent in the pumped material. The removal of ammonia is not a rapid process but is a slow process when carried out at 50 C.

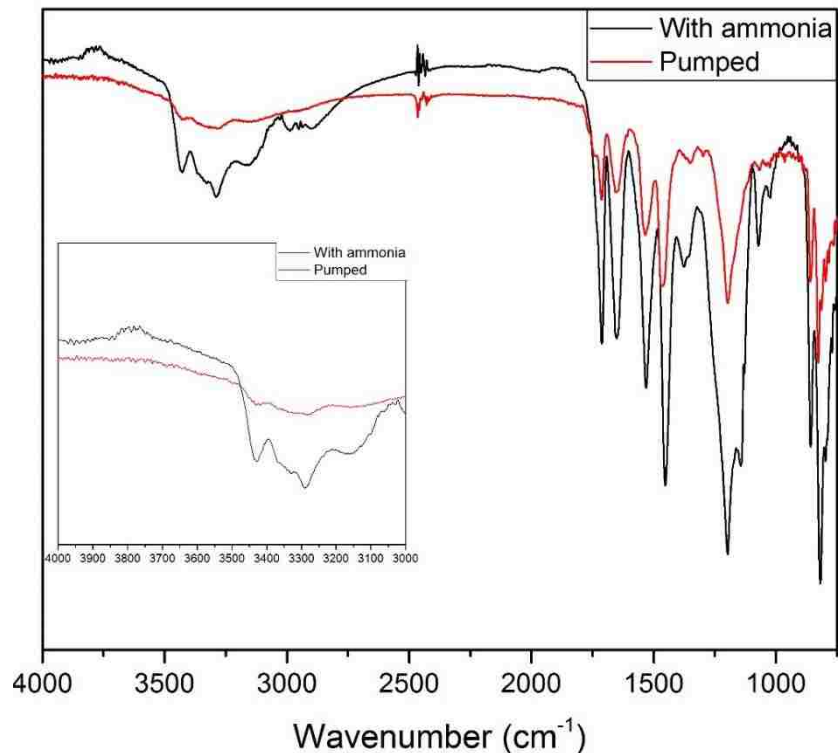


Figure 5.10: FTIR spectra for pumped acidic HKUST-1 showing the removal of gas at 50 C. The inset shows the zoomed range to compare the presence (black) and removal (red) of ammonia in acidic HKUST-1.

Other remarkable feature of the reversible adsorption at sulfuric acid site is a reversible phase transformation as observed in XRD pattern. After saturating the acidic HKUST-1, the XRD pattern of the cubic phase is lost. This is also the case for pure HKUST-1. However, the XRD pattern measured after pumping (Figure 5.11), matches that of acidic HKUST-1 before, thereby implying the integrity of the structure justifying the reversible binding of ammonia. What is remarkable about this phase transformation is the loss from a symmetric phase (cubic) to a different transient phase (presently under our investigation) which, upon vacuum treatment at 50 °C, returns to the diffraction pattern for the cubic phase. Loss in the high symmetry phase upon ammonia loading is expected because the nature of ammonia binding in the pure material (chemisorption;

formation of copper diamine complexes) is already well-established. One possible cause of preserved structure for acidic HKUST-1 is due to partial transfer of proton which doesn't allow for chemisorption of ammonia in the structure. The occupation of significant fractions of the surface by sulfuric acid and formation of sulfuric acid-ammonia complexes leaves little pore volume for additional ammonia adsorption which may prevent the attack on the framework by ammonia for the unmodified form of HKUST-1, instead, when ammonia is dosed in, the gas is adsorbed primarily by the acid-base interactions described previously. In other words, cubic phase modifies to a transitory phase to attract more ammonia molecule due to the Brønsted acid – base interactions. This novel reversibility in ammonia uptake, coupled with dramatically higher adsorbed capacities, makes this form of HKUST-1 attractive as a practical sorbent for removal and recovery of gas phase ammonia.

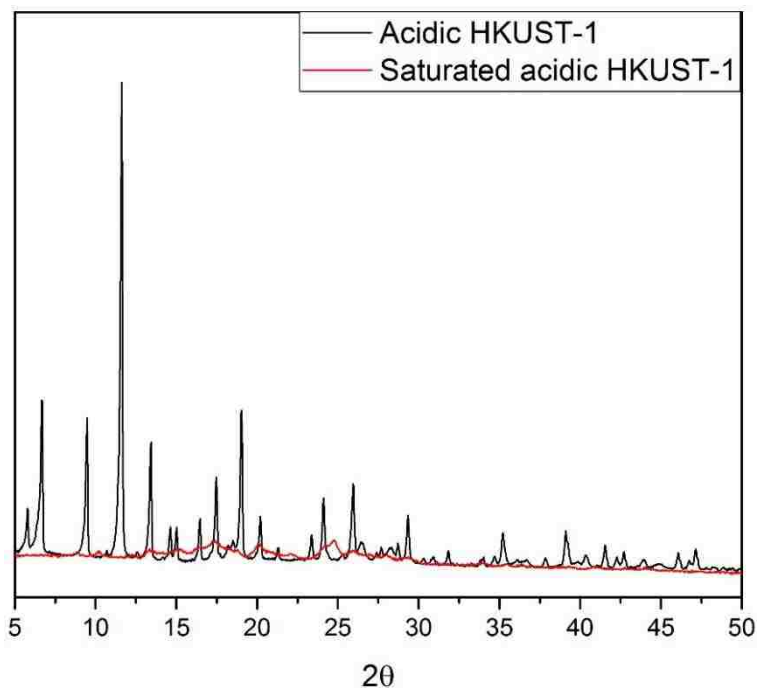


Figure 11a: Complete loss in PXRD pattern in acidic HKUST-1 after saturating the material with ammonia. The new pattern corresponds to a monoclinic phase.

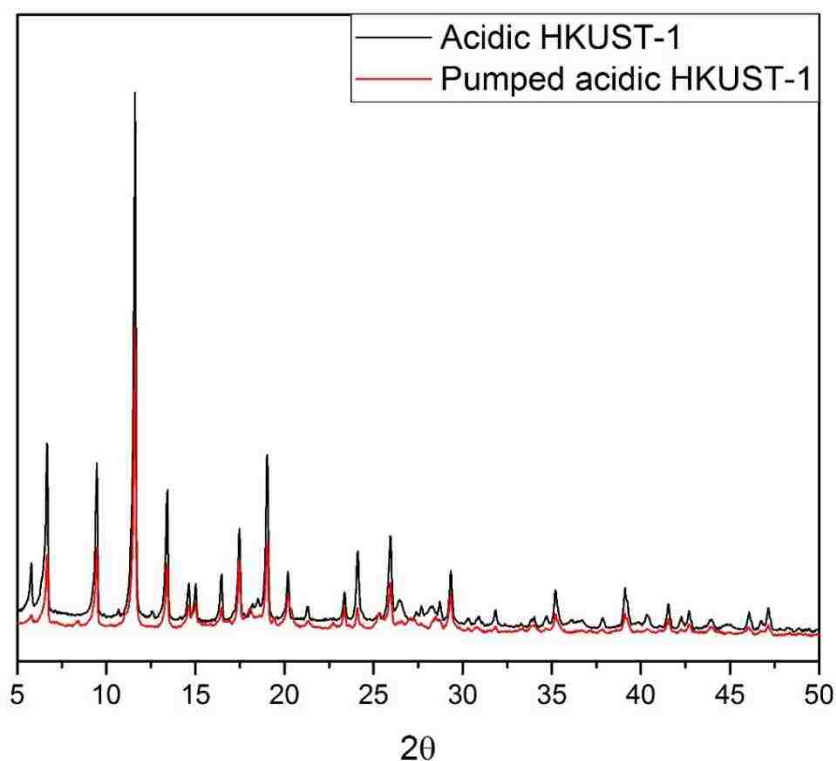


Figure 5.11b : Regeneration of the lost PXRD pattern after pumping the ammonia from the framework.

5.9 Conclusions:

In summary, the post-synthesis modification of HKUST-1 with sulfuric acid created novel binding sites which led to improved, reversible ammonia uptake. A partial transfer of proton observed in DFT calculations from -OH group to NH_3 explains the reversible binding of NH_3 . Ammonia binding for pure HKUST-1, is chemisorbed at the Cu-site with a binding energy of 77 kJ/mol but for acidic HKUST-1, the binding energy calculated for the first molecule of ammonia is 128.9 kJ/mol followed by a weaker interaction. A partial transfer of proton makes the ammonia binding stronger than physisorption but weaker than chemisorption or in simpler terms - reversible. Pumping on the saturated acidic HKUST-1 for few hours breaks the partial transfer of the proton and NH_3 which is adsorbed at sulfate sites, leaves the material and the material is

recycled. The presence of additional sites in the framework improves the framework's total NH_3 uptake, as shown by the comparison between INS spectrum and the DFT calculations.

5.10 References

1. Callaghan, R. *Nitrogen Statistics and Information*. [cited 2018; Available from: <https://minerals.usgs.gov/minerals/pubs/commodity/nitrogen/>].
2. OSHA. *Ammonia Refrigeration*. [cited 2018; Available from: <https://www.osha.gov/SLTC/ammoniarefrigeration/>].
3. *Chemical Emergency Preparedness and Prevention Advisory: Ammonia*. [cited 2018; Available from: <https://www.epa.gov/rmp/chemical-emergency-preparedness-and-prevention-advisory-ammonia>].
4. National Institute of Standards and Technology, U.D.o.C. *Ammonia*. [cited 2018; Available from: <http://webbook.nist.gov/cgi/cbook.cgi?ID=7664-41-7>].
5. Schmidhuber, J. *Haber and Bosch*. Available from: <http://people.idsia.ch/~juergen/haberbosch.html>.
6. Timmer, B., W. Olthuis, and A.v.d. Berg, *Ammonia sensors and their applications—a review*. *Sensors and Actuators B: Chemical*, 2005. **107**(2): p. 666-677.
7. Colonna, P. and S. Gabrielli, *Industrial trigeneration using ammonia–water absorption refrigeration systems (AAR)*. *Applied Thermal Engineering*, 2003. **23**(4): p. 381-396.
8. Weismiller, M., et al., *Characterization of Ammonia Borane (NH₃BH₃) Enhancement to a Paraffin Fueled Hybrid Rocket System*, in *46th AIAA/ASME/SAE/ASEE Joint Propulsion Conference & Exhibit*. 2010, American Institute of Aeronautics and Astronautics.
9. Green, L., *An ammonia energy vector for the hydrogen economy*. *International Journal of Hydrogen Energy*, 1982. **7**(4): p. 355-359.
10. Corporation, T., *Ammonia Recovery Process: Cost Benefits to the Operation of a Typical Wastewater Treatment Plant*. 2007.

11. GMBH, R.P.E. *Ammonia Recovery Plants*. Available from: <http://www.rvtpe.com/ammonia-recovery-plants/?lang=en>.
12. R. W. Melse, N.W.M.O., *AIR SCRUBBING TECHNIQUES FOR AMMONIA AND ODOR REDUCTION AT LIVESTOCK OPERATIONS: REVIEW OF ON-FARM RESEARCH IN THE NETHERLANDS*. American Society of Agricultural Engineers 2005. **48**(6): p. 2303-2313.
13. Byeon, S.-H., B.-K. Lee, and B. Raj Mohan, *Removal of ammonia and particulate matter using a modified turbulent wet scrubbing system*. Separation and Purification Technology, 2012. **98**(Supplement C): p. 221-229.
14. Peralta, D., *Comparison of the Behavior of Metal–Organic Frameworks and Zeolites for Hydrocarbon Separations*. Journal of American Chemical Society, 2011. **134**: p. 8115.
15. Rosi, N.L., et al., *Hydrogen storage in microporous metal-organic frameworks*. Science, 2003. **300**(5622): p. 1127-1129.
16. Demessence, A., et al., *Strong CO₂ binding in a water-stable, triazolate-bridged metal– organic framework functionalized with ethylenediamine*. Journal of the American Chemical Society, 2009. **131**(25): p. 8784-8786.
17. Eddaoudi, M., et al., *Modular chemistry: secondary building units as a basis for the design of highly porous and robust metal– organic carboxylate frameworks*. Accounts of Chemical Research, 2001. **34**(4): p. 319-330.
18. Huang, X.C., et al., *Ligand-Directed Strategy for Zeolite-Type Metal–Organic Frameworks: Zinc (II) Imidazolates with Unusual Zeolitic Topologies*. Angewandte Chemie, 2006. **118**(10): p. 1587-1589.
19. James, S.L., *Metal-organic frameworks*. Chemical Society Reviews, 2003. **32**(5): p. 276-288.
20. Lee, J., et al., *Metal–organic framework materials as catalysts*. Chemical Society Reviews, 2009. **38**(5): p. 1450-1459.
21. Peralta, D., et al., *Comparison of the behavior of metal–organic frameworks and zeolites for hydrocarbon separations*. Journal of the American Chemical Society, 2012. **134**(19): p. 8115-8126.

22. Jiang, J. and O.M. Yaghi, *Brønsted acidity in metal–organic frameworks*. Chemical reviews, 2015. **115**(14): p. 6966-6997.
23. Dubinin, M. and H. Stoeckli, *Homogeneous and heterogeneous micropore structures in carbonaceous adsorbents*. Journal of Colloid and Interface Science, 1980. **75**(1): p. 34-42.
24. Pollard, S., et al., *Low-cost adsorbents for waste and wastewater treatment: a review*. Science of the Total Environment, 1992. **116**(1-2): p. 31-52.
25. Helminen, J., et al., *Adsorption equilibria of ammonia gas on inorganic and organic sorbents at 298.15 K*. Journal of Chemical & Engineering Data, 2001. **46**(2): p. 391-399.
26. Bandosz, T.J., *On the adsorption/oxidation of hydrogen sulfide on activated carbons at ambient temperatures*. Journal of colloid and Interface Science, 2002. **246**(1): p. 1-20.
27. Helminen, J., et al., *Comparison of sorbents and isotherm models for NH₃-gas separation by adsorption*. AIChE journal, 2000. **46**(8): p. 1541-1555.
28. Glover, T.G., et al., *MOF-74 building unit has a direct impact on toxic gas adsorption*. Chemical Engineering Science, 2011. **66**(2): p. 163-170.
29. Katz, M.J., et al., *High volumetric uptake of ammonia using Cu-MOF-74/Cu-CPO-27*. Dalton Transactions, 2016. **45**(10): p. 4150-4153.
30. Britt, D., D. Tranchemontagne, and O.M. Yaghi, *Metal-organic frameworks with high capacity and selectivity for harmful gases*. Proceedings of the National Academy of Sciences, 2008. **105**(33): p. 11623-11627.
31. Petit, C. and T.J. Bandosz, *Synthesis, characterization, and ammonia adsorption properties of mesoporous metal–organic framework (MIL (Fe))–graphite oxide composites: exploring the limits of materials fabrication*. Advanced Functional Materials, 2011. **21**(11): p. 2108-2117.
32. Jasuja, H., et al., *Evaluation of MOFs for air purification and air quality control applications: Ammonia removal from air*. Chemical Engineering Science, 2015. **124**: p. 118-124.
33. Van Humbeck, J.F., et al., *Ammonia capture in porous organic polymers densely functionalized with brønsted acid groups*. Journal of the American Chemical Society, 2014. **136**(6): p. 2432-2440.

34. Kim, K.C., D. Yu, and R.Q. Snurr, *Computational screening of functional groups for ammonia capture in metal–organic frameworks*. *Langmuir*, 2013. **29**(5): p. 1446-1456.
35. P Atkins, L.J., L Layerman, *Chemical Principles*.
36. *Dissociation constant*. Available from: <https://www.britannica.com/science/dissociation-constant>.
37. Bodner. *Chemical Education*. 2004; Available from: <http://chemed.chem.purdue.edu/>.
38. Chui, S.S.-Y., et al., *A chemically functionalizable nanoporous material [Cu₃ (TMA)₂ (H₂O)₃]_n*. *Science*, 1999. **283**(5405): p. 1148-1150.
39. Petit, C., B. Mendoza, and T.J. Bandoz, *Reactive adsorption of ammonia on Cu-based MOF/graphene composites*. *Langmuir*, 2010. **26**(19): p. 15302-15309.
40. Nijem, N., et al., *Ammonia Adsorption and Co-Adsorption with Water in HKUST-1: Spectroscopic Evidence for Cooperative Interactions*. *The Journal of Physical Chemistry C*, 2015. **119**(44): p. 24781-24788.
41. Huang, L., et al., *Reactive adsorption of ammonia and ammonia/water on CuBTC metal-organic framework: A ReaxFF molecular dynamics simulation*. *The Journal of chemical physics*, 2013. **138**(3): p. 034102.
42. Petit, C., S. Wrabetz, and T.J. Bandoz, *Microcalorimetric insight into the analysis of the reactive adsorption of ammonia on Cu-MOF and its composite with graphite oxide*. *Journal of Materials Chemistry*, 2012. **22**(40): p. 21443-21447.
43. Borfecchia, E., et al., *Insights into Adsorption of NH₃ on HKUST-1 Metal–Organic Framework: A Multitechnique Approach*. *The Journal of Physical Chemistry C*, 2012. **116**(37): p. 19839-19850.
44. Huang, L., et al., *Reactive adsorption of ammonia and ammonia/water on CuBTC metal-organic framework: a ReaxFF molecular dynamics simulation*. *J Chem Phys*, 2013. **138**(3): p. 034102.
45. Petit, C., et al., *Toward understanding reactive adsorption of ammonia on Cu-MOF/graphite oxide nanocomposites*. *Langmuir*, 2011. **27**(21): p. 13043-51.
46. Petit, C., B. Mendoza, and T.J. Bandoz, *Reactive adsorption of ammonia on Cu-based MOF/graphene composites*. *Langmuir*, 2010. **26**(19): p. 15302-9.

47. Petit, C., et al., *Toward understanding reactive adsorption of ammonia on Cu-MOF/graphite oxide nanocomposites*. Langmuir, 2011. **27**(21): p. 13043-13051.
48. Rowsell, J.L. and O.M. Yaghi, *Strategies for hydrogen storage in metal-organic frameworks*. Angewandte Chemie International Edition, 2005. **44**(30): p. 4670-4679.
49. Kresse, G. and J. Furthmüller, *Efficient iterative schemes for ab initio total-energy calculations using a plane-wave basis set*. Physical review B, 1996. **54**(16): p. 11169.
50. Blöchl, P.E., *Projector augmented-wave method*. Physical review B, 1994. **50**(24): p. 17953.
51. Kresse, G. and D. Joubert, *From ultrasoft pseudopotentials to the projector augmented-wave method*. Physical Review B, 1999. **59**(3): p. 1758.
52. Perdew, J.P., K. Burke, and M. Ernzerhof, *Generalized gradient approximation made simple*. Physical review letters, 1996. **77**(18): p. 3865.
53. Klimeš, J., D.R. Bowler, and A. Michaelides, *Chemical accuracy for the van der Waals density functional*. Journal of Physics: Condensed Matter, 2009. **22**(2): p. 022201.

Note:

The work compiled for this chapter is a joint effort with VISION BeamLine (BL-16B), Spallation Neutron Source, Oak Ridge National Laboratory (ORNL). Amit Sharma spent more than a year at ORNL where he synthesized the necessary MOFs required for this study under the guidance of VISION team. All the necessary characterization for the samples such as XRD, FTIR, BET, and INS were performed by Amit at ORNL. All DFT calculations were performed by VISION team.

Chapter 6 – Conclusions

In this dissertation we have shown the efficiency of the nanoporous materials dedicated to deal specific gas separation and storage problems. Due to high surface area and energetically favorable sites such as unsaturated metal sites, narrow cavities, channels, embedded nanoparticles these materials offer exceptional surface for gas molecules to interact. Molecular sieving, diffusivity, dispersion, quantum sieving and other thermodynamic effects control the process of gas separation and storage.

In first part of this study we screened all the 229 zeolitic frameworks in their siliceous form by our Grand Canonical Monte Carlo simulations to observe their performance to separate Kr/Xe gas mixture. We observed that how a 9-6 Lennard-Jones potential with a softer repulsion is better to model the fluid-fluid interactions. Our screening shows that presence of a small cage will be selective and adequate to fit a Xe atom followed by a quick saturation indicating a lower utility in practical PSA sorbents. Zeolites working at relevant pressures were found to have zig-zag, elliptical cross-sections and narrow pore systems. For high capacities, CDO, MRE, and PSI calculated a selectivity greater than 10 at all loadings. AFO, ATO, PSI, and ZON can be used to synthesize pure AlPOs and the simulations can be assessed for such systems in Kr/Xe gas separations.

In second part of the work we assess a metal phosphate VSB-5 with unsaturated Ni²⁺ sites providing strong interaction sites for hydrogen gas interactions. A strong magnetic moment, highest measured heat of adsorption (>16 kJ/mol) and highest selectivity (~4) at 140 K range makes this material a strong candidate to study for hydrogen adsorption studies. D₂ measured a higher and consistent heat of adsorption than hydrogen and VSB-5 is selective to D₂ due to the quantum sieving effect observed at temperatures > 120 K.

In third part of this study we work with graphene to test the validity of H₂ interactions in an anisotropic potential. Graphene is one of the most exciting and a simple surface providing weak interactions to model the C-H interactions. Inelastic neutron scattering data measured the shift in the rotational line of dihydrogen upon interaction with smooth graphene surface. At low coverages the most energetically favorable sites dominate the adsorption and the areas of the lower energy peak below 14.3 meV are around twice the areas of the peak above 14.4 meV. This agrees to the anisotropic potential model and the behavior can be described as a 2D rotor. A comparison with a strong site – Ni²⁺ in VSB-5 is also studied where a big shift in the rotational line is observed along with the ortho-para hydrogen conversion due to the strong magnetic moment provided by Ni²⁺.

Finally, we modify one of the well-studied framework of HKUST-1 by introducing Bronsted acidity to increase the amounts of ammonia in the framework. Sulfuric acid tethered framework is stable for a period of more than 6 months and increases the ammonia adsorption by three times. The novel binding sites provided by sulfuric acid as studied by DFT calculations exhibits the -O-H-N bond elongation for ammonia adsorption and corresponds to a weak transfer of proton from -OH to ammonia. The partial transfer of proton leads to a reversible binding of ammonia and a flexibility in framework of HKUST-1 on ammonia adsorption is also observed.

As can be seen, nanoporous materials such as zeolites, metal organic frameworks, carbon based materials, etc provide exciting opportunities in the field of gas adsorption with post-synthesis modifications making the research a lot easier. Due to the striking surface chemistry and reasonable gas capture, focus from cryogenic methods is shifted. Reversible binding, robustness, low cost, environmental friendly are a few characteristics which make this field interesting and a continuous growth to find new material is also seen. Most of the work done so far is considered in preliminary stages but decent efforts by the researchers is pushing the applications close to reality.

Appendix A[1-3]

Introduction to Grand Canonical Monte Carlo (GCMC) Simulations

A partition function is defined to compute the thermodynamic quantities of a system of interest. When the multidimensional integrals are needed to compute the thermodynamics properties, the integration needs to be done numerically. Monte Carlo (MC) methods are the algorithms that integrate the expression by random sampling of all the possible states of system. This random sampling is the first choice however it can lead to false property evaluation because of over-sampling of the regions where the contributions to the values are negligible or where it is impossible for the system to exist. Importance sampling and increasing the number of states sampled can fix this problem. Importance sampling relies on a range of system conditions to sample where the possible probabilities of the properties will be at their peak however, even the sampling can run into difficulties from under and impossible sampling to describe multidimensional integrals that generate points with a probability density exactly proportional to those of the function of interest.

In chemistry, the partition function is sampled with MC and then processed with statistical mechanics to predict the expectation values of relevant thermodynamic properties. The focus is on the evaluation of the Boltzmann distribution and thus the partition function. The Boltzmann distribution is the probability that a system is in certain states at given conditions. Often the configurational portion of the partition function is not of particular interest - just the averages of microscopically determinable quantities $A(r^N)$ are (whose expectation values are defined in the following equation using the partition function):

$$\langle A \rangle = \frac{\int dr^N e^{-\beta U(r^N)} A(r^N)}{\int dr^N e^{-\beta U(r^N)}} = \int dr^N \frac{e^{-\beta U(r^N)}}{Z} A(r^N) \quad (1)$$

This formulation allows us to solve thermodynamic integrals using the efficient sampling scheme described by Metropolis *et al.* Metropolis explained that instead of choosing states at random and determining their Boltzmann factor $e^{-\beta U}$, one could with more efficiency choose configurations with that are connected to other probable nearby states and weigh them evenly. Therefore, the Metropolis algorithm generates sequences of random states that in the end reach a significant probability per the equilibrium distribution of the appropriate statistical ensemble. This is done by solving directly for the thermodynamic average of the observable A. By rewriting it in terms of a summation, this allows us to solve for the average without determining the partition function.

$$\langle A \rangle = \frac{1}{N_samples} \sum_{i=1}^{N_samples} A_i(r^N) \quad (2)$$

Another fundamental part of the Metropolis algorithm is what is known as a Markov chain: a sequence of trials that yields one set of states dependent only on their preceding state. There is a transition probability which connects the Boltzmann probability,

$$\rho(r^N) \equiv \frac{e^{-\beta U(r^N)}}{Z} \quad (3)$$

in the current, M, state through the transition to the next, N, state:

$$\rho_M \pi_{M \rightarrow N} = \rho_N \pi_{N \rightarrow M} \quad (4)$$

Here, π is a dimensionless square matrix that satisfies the condition of microscopic reversibility. Connecting the states M and N are what Metropolis called “trial” moves, which simultaneously move multiple atoms across multiple directions in phase space and relates the energy differences between the final and initial configuration to determine the probability of the transition. The trial move is accepted with the following probability:

$$P_{acc}(r^m \rightarrow r^n) = \min\left(1, \frac{\rho_{boltz}(r^n)}{\rho_{boltz}(r^m)}\right) = \min(1, e^{-\beta \Delta U}) \quad (5)$$

If the determination of the probability from initial M to final N state is found to be less than a randomly generated number between [0,1] then the move becomes rejected outright. If the trial move lowers the energy of the system, then the probability is greater than 1, and the move is always accepted.

The benefits of Monte Carlo simulations are that they can be performed on various statistical ensembles. The simplest type of ensemble is the microcanonical ensemble, which fixes the number of particles in the system, the volume, and the energy of the system. The Boltzmann distribution for this ensemble directly relates to the entropy of the system.

$$\rho = \frac{1}{\Omega}; S = kB \ln \Omega \quad (6)$$

The canonical ensemble builds on this, allowing the energy to fluctuate while holding the volume, temperature and the number of particles fixed. Its partition function is represented as $Q(N,V,T)$, i.e.. the NVT ensemble, and has the Boltzmann probability of a microscopic configuration:

$$\rho_{Boltz} = \frac{V^N}{N! \Lambda^{3N}} e^{-\beta U} \quad (7)$$

where U is the potential energy, V the volume, Λ is the de Broglie's thermal wavelength, β is the Boltzmann distribution, and N is the number of particles. The pre-factor is the connection between the non-interacting ideal and interacting microcanonical states of the system. The free energy associated with the canonical ensemble is the Helmholtz free energy:

$$-\beta A = \ln(Q) \quad (8)$$

The grand canonical ensemble allows the number of particles within the system to fluctuate while it holds the chemical potential μ , volume, and temperature fixed. The number of particles is allowed to fluctuate by equating the chemical potentials for the species of interest with a reservoir of molecules that can be moved into and out of the system. This canonical Boltzmann distribution can be modified in terms of the grand canonical ensemble:

$$P_{Boltz} = \frac{V^N}{N! \Lambda^{3N}} \frac{e^{-\beta(U-\mu N)}}{\Xi_{\mu VT}} \quad (9)$$

The Monte Carlo method, specifically in the grand canonical ensemble, is the leading means for simulating gas adsorption using statistical thermodynamics of the interacting system of interest. Grand canonical Monte Carlo is the most advantageous methodology for adsorption studies because of the direct relationship between the chemical potential of the adsorbed fluid and the desired pressure of the system made with an equation of state. With zeolites and other porous materials, the phase space available to adsorbed gases within the framework is sampled by defining how the particles move within the system and the energetic interactions that define how the gas interacts with the framework. The trial moves include molecule translation and rotation (canonical moves) as well as the creation and destruction of the molecules within the framework. Using the previously outlined details, a very accurate picture of gas adsorption can be obtained using only simple classical dispersion and electrostatic interactions.

Recently, an impressive study was performed that screened 670,000 different known and hypothetical porous zeolites, MOFs, ZIFs, PPNs, and COFs for their selectivity at an initial loading of an 20:80 mixture of Xe:Kr at room temperature. Their results supported the conclusion that topologies with smaller pores and pockets that maximized interaction with Xe had improved Xe selectivities, and one of their top performers is SIZ-3 (CSD code: JAVTAC) which is an ALPO-11 (AEL) zeolite analogue.

Besides the mentioned concept of enhancing adsorbate-adsorbent interaction with zeolites, a study on high silica compositions can provide a reasonable approximation of the zeolite's behavior. While siliceous zeolites (containing only Si and O) are natural point to begin modelling

efforts, they may well represent practical adsorbents as well. As adsorbents, they may offer good selectivity through dispersive interactions for Kr and Xe, which have no standing multipolar moments to strongly interact with cations. A vital part of studying Kr/Xe adsorption in the vast family of zeolites is developing a transferrable description of adsorption into the pure TO2 frameworks. Here we develop such a model which we show can generally predict gas adsorption isotherms to excellent agreement with experiment. We then apply the model to all 229 siliceous zeolites to determine their ability to separate 90:10 Xe:Kr across the range of loadings relevant to an actual PSA process.

References:

1. Wolffis, J.J., *Improved Partial Charge Models in Siliceous Zeolites for the Simulation of Adsorption and Identification of Catalytic Sites*, in *Chemistry*. 2017, University of Nevada - Las Vegas
2. Chandler, D., *Introduction to Modern Statistical Mechanics*. 1987.
3. Daan Frenkel, B.S., *Understanding Molecular Simulation From Algorithm to Applications*.

Curriculum Vitae

Graduate College

University of Nevada, Las Vegas

Amit Sharma

sharma@unlv.nevada.edu

Degrees:

Bachelor of Technology – Nanotechnology, 2010

University of Rajasthan, Jaipur, INDIA

Masters of Technology – Nanotechnology, 2012

University of Rajasthan, Jaipur, INDIA

Publications:

1. A Sharma, KV Lawler, JJ Wolffis, CT Eckdahl, CS McDonald, JLC Rowsell, SA FitzGerald, PM Forster: Hydrogen Uptake of Coordinatively Unsaturated Metal Sites in VSB-5: Strong Binding Affinity Leading to High-Temperature D₂/H₂ Selectivity, 2017, *Langmuir*, 33 (51), 14586-14591.
2. KV Lawler, A Sharma, B Alagappan, PM Forster: Assessing Zeolitic Frameworks for Noble Gas Separations Through a Joint Experimental and Computational Approach, *Microporous and Mesoporous Materials*, 2016, 222, 104-112.1
3. A Dandia, V Parewa, SL Gupta, A Sharma, KS Rathore, A Jain: Microwave-assisted Fe₃O₄ Nanoparticles Catalyzed Synthesis of chemo[1,6]naphthyridines in Aqueous Media, 2015, *Catalysis Communications*, 61, 88-91.
4. A Dandia, A Sharma, V Parewa, B Kumawat, KS Rathore: Amidic C-N Bond Cleavage of Isatin: Chemoselective Synthesis of pyrrolo[2,3,4-kl]acridin-1-ones Using Ag NPs Decorated rGO Composites as an Efficient and Recoverable Catalyst Under Microwave Irradiation, *RSC Advances*, 2015, 5 (111), 91888-91902.
5. A Dandia, SL Gupta, V Parewa, A Sharma, KS Rathore: “On-water” Synthesis of 3-substituted Indoles via Knoevenagel/Michael Addition Sequence Catalyzed by Cu Doped ZnS NPs, *Tetrahedron Letters*, 2013, 54 (42), 5711-5717.

6. A Dandia, V Parewa, A Sharma, KS Rathore: Cobalt Doped ZnS Nanoparticles as a Recyclable Catalyst For Aqueous Mediated Synthesis of 2,4,5-Triaryl-1H-Imidazoles Under Ultrasonic Irradiation, *European Chemical Bulletin*, 2013, 2 (12), 971-974.

Dissertation Title:

Application of Nanoporous Materials in Gas Separation and Storage.

Dissertation Examination Committee:

Committee Chair: Paul Forster, Ph.D.

Committee Member: Kathleen Robins, Ph.D.

Committee Member: Jun Yong Yang, Ph.D.

Graduate College Faculty Representative: Satish Bhatnagar, Ph.D.